Université de Montréal

Applying Computational Approaches to the Understanding of the Consequences and Opportunities of Ion Channel Properties in Atrial Fibrillation

par Martin Aguilar

Département de pharmacologie et physiologie
Faculté de Médecine

Thèse présentée
en vue de l'obtention du grade de Philosophiæ Doctor (Ph.D.)
en Physiologie moléculaire, cellulaire et intégrative

Novembre 2019

Université de Montréal

Faculté des études supérieures et postdoctorales

Cette thèse intitulée:

Applying Computational Approaches to the Understanding of the Consequences and Opportunities of Ion Channel Properties in Atrial Fibrillation

Présentée par

Martin Aguilar

A été évaluée par un jury composé des personnes suivantes:

Dre. Teresa Kus, MD, Ph.D: Président- rapporteur

Dr. Stanley Nattel, MD: Directeur de recherche
Dr. Philippe Comtois, Ph.D: Co-Directeur de recherche

Dr. Leon Glass, Ph.D : Membre du jury
Dr. Rishi Arora, MD : Examinateur externe

Résumé

Les arythmies cardiaques représentent une famille de pathologies du système électrique cardiaque. La fibrillation auriculaire (FA), est l'arythmie cardiaque la plus fréquente dans la population générale et est associée à un fardeau de morbidité et mortalité cardiovasculaire important. Les médicaments antiarythmiques utilisées dans le traitement de la FA sont de vieilles molécules avec une efficacité sous-optimale et des effets secondaires importants. Les avancées récentes en électrophysiologie cardiaque fondamentale et le développement d'outils de modélisation mathématique ont le potentiel d'élargir notre compréhension des mécanismes pathophysiologiques en FA et contribuer au développement de nouveaux médicaments antiarythmiques optimisés pour le traitement de la FA. L'objectif global de cette thèse est d'utiliser les méthodes de modélisation mathématique pour étudier les conséquences et opportunités thérapeutiques de la modulation des canaux ioniques cardiaques, avec une emphase sur la FA.

Le potentiel d'action cardiaque est l'unité fonctionnelle de base du système électrique cardiaque ; il est le résultat du flux coordonné de courants électriques à travers de protéines spécialisées, les canaux ioniques. Les molécules antiarythmiques agissent à travers la modulation des canaux ioniques cardiaques. Nous avons posé l'hypothèse que des modèles mathématiques pourraient être utilisés pour étudier et optimiser les propriétés pharmacodynamiques d'un médicament antiarythmique pour le traitement de la FA. Nous avons démontré que les propriétés pharmacodynamiques (propriétés de liage et déliage) d'un bloqueur des canaux Na^+ état-dépendant modulent les effets anti- et pro-arythmiques de la molécule ; un bloqueur Na^+ sélectif pour l'état inactivé du canal serait maximalement FA-sélectif. Cette sélectivité pour la FA est la conséquence de la sélectivité pour la fréquence (effet thérapeutique plus important à des fréquences d'activation du cardiomyocyte élevées vs basses) avec une contribution relativement faible de la sélectivité auriculaire (effet thérapeutique plus important sur les cardiomyocytes auriculaires vs ventriculaires).

Par la suite, nous avons exploré des combinaisons de bloqueurs ioniques ayant des propriétés anti-FA synergiques. En utilisant des modèles mathématiques et des expériences en laboratoire, nous avons démontré que la combinaison d'un bloqueur des canaux Na^+ et d'un

bloqueur des canaux K^+ a des effets synergiques, augmentant de façon importante l'efficacité anti-FA pour un même degré de sélectivité vs un bloqueur des canaux Na^+ seul. Le mécanisme de synergie a été élucidé et consiste d'effets fonctionnels médiés par l'interaction du prolongement de la durée du potentiel d'action causé par le bloque des canaux K^+, les propriétés voltage-dépendantes du liage et déliage du bloqueur des canaux Na^+ ainsi que des propriétés d'inactivation des canaux Na^+, démontrant la nature hautement non-linéaire des dynamiques du potentiel d'action cardiaque.

Les courants K^+ ciblés par les médicaments antiarythmiques ont des effets proarythmiques ventriculaires importants. En utilisant des données expérimentales récentes, nous avons proposé une formulation mise à jour des dynamiques d'inactivation du courant K^+ I_{Kur}, un courant auriculo-sélectif. En utilisant ce modèle, nous avons démontré que, contrairement à ce qui avait été précédemment proposé, les propriétés fréquence-dépendantes du courant I_{Kur} dépendent de ses caractéristiques d'activation avec une contribution négligeable de ses propriétés d'inactivation, sous conditions physiologiques normales. Nous avons également démontré que la contribution de I_{Kur} à la repolarisation du potentiel d'action est maintenue, voir augmentée, dans le contexte de la diminution de I_{Kur} en situation de remodelage électrique induit par la FA. Finalement, nous avons décrit le mécanisme qui sous-tend les propriétés fréquence-dépendantes du bloque de I_{Kur}, l'unique courant K^+ avec de telles caractéristiques.

Jusqu'à très récemment, les fibroblastes cardiaques étaient considérés comme électriquement inactifs. Des travaux expérimentaux ont démontré la présence de canaux ioniques sur la surface de ces fibroblastes ainsi que la possibilité de couplage électrique entre cardiomyocytes et fibroblastes. Nous avons décrit un nouveau type de remodelage électrique en situation d'insuffisance cardiaque, le remodelage des courants ioniques des fibroblastes cardiaques. Ce remodelage est caractérisé par une diminution du courant K^+ voltage-dépendant $I_{Kv,fb}$ et une augmentation du courant K^+ $I_{Kir,fb}$. Nous avons par la suite incorporé ces trouvailles expérimentales dans un modèle mathématique simulant l'interaction électrique entre cardiomyocytes et fibroblastes et montré que le remodelage électrique des fibroblastes peut avoir un impact important sur les propriétés électrophysiologiques des cardiomyocytes. Dans

un modèle 2-dimensionel de FA, nous avons trouvé que la diminution de $I_{Kv,fb}$ a un effet antiarythmique alors que l'augmentation de $I_{Kir,fb}$ a des effets proarythmiques.

Les études ici présentées utilisent les méthodes de modélisation mathématique pour l'étude de systèmes non-linéaires en électrophysiologie cardiaque et aborder des avenues de recherche difficilement accessibles aux méthodes de laboratoire traditionnelles. Elles démontrent également comment des résultats théoriques peuvent orienter et trouver confirmation dans des travaux expérimentaux subséquents ou, à l'inverse, des trouvailles expérimentales peuvent être implémentées dans les modèles mathématiques pour investiguer les conséquences de celles-ci. La modélisation mathématique est un outil prometteur pour l'étude des effets complexes et non-linéaires de la modulation pharmacologique des canaux ioniques et ainsi contribuer au développement de médicaments antiarythmiques optimisés pour le traitement de la FA, un besoin clinique majeur.

Mots-clés : électrophysiologie cardiaque, modélisation mathématique, fibrillation auriculaire, médicaments antiarythmiques

Abstract

Cardiac arrhythmias are disorders of the electrical system of the heart and an often clinically-challenging group of disorders. Atrial fibrillation (AF) is the most common cardiac arrhythmia in the general population; it is associated with significant morbidity and mortality. Available antiarrhythmic drugs (AADs) for the treatment of AF are older molecules with sub-optimal efficacy and safety profiles. Recent advances in basic electrophysiology and the development of sophisticated mathematical modeling approaches could help in expanding our understanding of the basic mechanisms of AF and assist in the development of novel AF-selective AADs. The purpose of this thesis was to utilize computational approaches to the understanding of the consequences and opportunities of ion channel properties, with a special emphasis on AF.

The cardiac action potential is the basic functional unit of the electrical system of the heart and is the manifestation of coordinated current fluxes through specialized proteins known as ion channels. Antiarrhythmic drugs act through modulation of ion channel properties. We hypothesized that mathematical modeling could be used to study and optimize the pharmacodynamic properties of AADs for the treatment of AF. We demonstrated that the pharmacodynamic properties (binding/unbinding characteristics) of a state-dependent Na^+-channel blocker modulate the drug's anti-/proarrhythmic actions with inactivated-state blockers being optimally AF-selective. The optimized drug's selectivity for AF was the result of its rate-selectivity (stronger effects at fast vs slow cardiomyocyte activation rates) with relatively mild atrial-selective (stronger effects in atrial vs ventricular cardiomyocytes) actions. We found that the optimally AF-selective Na^+-channel blocker had sub-optimal anti-AF efficacy, but that slightly less selective drugs had favorable AF-termination rates.

We then sought to explore potential current-block combinations with synergistic AF-selective properties. Using mathematical modeling and laboratory experiments, we demonstrated that the combination of optimized state-dependent Na^+-channel block and K^+-channel block had synergistic effects, significantly augmenting AF termination rates for any level of AF-selectivity vs pure Na^+-channel block. The mechanisms of these synergistic effects were found to be mediated by the functional interaction between the action potential prolonging-

effects of K^+-channel block, the Na^+-channel blocker's voltage-dependent binding/unbinding properties and the Na^+ channel's inactivation characteristics, highlighting the non-linear nature of the cardiac action potential's dynamics.

Traditional K^+ currents targeted by AADs have significant ventricular proarrhythmic liabilities. Using recent experimental observations, we updated the mathematic formulation for the inactivation dynamics of the ultra-rapid delayed-rectifier K^+ current (I_{Kur}), an atrial-specific current. Using this model, we showed that, contrary to what had been proposed in the published literature, I_{Kur} rate-dependent properties are mediated by its activation properties with minimal contribution from inactivation, under physiological conditions. We also demonstrated that the contribution of I_{Kur} to action potential repolarization is preserved, or even increased, in the setting of electrical remodeling-induced I_{Kur} downregulation. Finally, we described the mechanisms of the forward rate-dependent of I_{Kur} block, mediated by functional non-linear interactions with the rapid delayed inward-rectifier K^+ current (I_{Kr}), the only K^+ current with such properties.

Until recently, fibroblasts were considered to be electrically inactive. More recently, experimental work demonstrated the presence of functional ionic current on the fibroblast and possible cardiomyocyte-fibroblast coupling. Here, we described a novel kind of heart failure-induced electrical remodeling involving the fibroblasts ion channels. This was characterized by downregulation of the fibroblast voltage-dependent K^+ current ($I_{Kv,fb}$) and upregulation of the fibroblast inward-rectifier K^+ current ($I_{Kir,fb}$). We then implemented our experimental findings into a mathematical model of cardiomyocyte-fibroblast coupling and found fibroblast electrical remodeling to have significant effects on the cardiomyocyte's electrophysiological properties. In a 2-dimension model of simulated AF, downregulation of $I_{Kv,fb}$ had an antiarrhythmic effect whereas $I_{Kir,fb}$ upregulation was found to be proarrhythmic.

The studies presented here utilized mathematical modeling to study non-linear systems in cardiac electrophysiology to tackle questions that would have been difficult to approach with traditional laboratory-based experimentation. They also showcased how theoretical results can help orient and receive confirmation with subsequent experimental work or, conversely, novel experimental findings results be implemented into a mathematical model to investigate potential consequences. Mathematical modeling is a promising tool to help in studying the complex and

non-linear effects of pharmacological modulation of ion channel properties and assist in the development of optimized antiarrhythmics for the treatment of AF, a major unmet need in clinical medicine. As models increase in sophistication to better represent the cardiomyocyte's electrophysiology, they will almost certainly play an ever-growing role in expanding our understanding of the mechanisms of complex arrhythmias.

Keywords : cardiac electrophysiology, mathematical modeling, atrial fibrillation, antiarrhythmic drugs

Table of Contents

List of Tables

List of Figures

List of Abbreviations

AAD	Antiarrhythmic drug
ACh	Acetylcholine
AF	Atrial fibrillation
AF-CHF	Atrial Fibrillation and Congestive Heart Failure
AFFIRM	Atrial Fibrillation Follow-Up Investigation of Rhythm Management
APD	Action potential duration
APD_x	Action potential duration at *x*% repolarization
AVN	Atrioventricular node
B	Fractional I_{Na} block
B_A	Fractional activated-state I_{Na} block
B_I	Fractional inactivated-state I_{Na} block
B_{ss}	Steady-state I_{Na} fractional block
BCL	Basic cycle length
C_m	Cell membrane capacitance
$C_{m,fb}$	Fibroblast cell membrane capacitance
Ca^{2+}	Calcium ion
Cl^-	Chloride ion
CAST	Cardiac Arrhythmia Suppression Trial
CL	Cycle length
CV	Conduction velocity
[D]	Drug concentration
DAD	Delayed afterdepolarization
DOF	Dofetilide
E_x	Nernst equilibrium potential for *x*
EAD	Early afterdepolarization
ECG	Electrocardiogram
EG	Excitable gap
F	Faraday's constant

g_x	Conductance for ionic species *x*
g_{Na}	Conduction for I_{Na}
h	I_{Na} fast inactivation gate
I_x	Current for ionic species *x*
$I_{b,Ca}$	Background Ca^{2+} current
$I_{b,Cl}$	Background Cl^- current
$I_{b,Na}$	Background Na^+ current
I_{CaL}	L-type Ca^{2+} current
$I_{Cl,Ca}$	4-aminopyridine-resistant, Ca^{2+}-activated chloride current
I_{ion}	Total ionic current
$I_{ion,HRd}$	Total ionic current for the HRd
$I_{ion,RNC}$	Total ionic current for the RNC model
$I_{K,ACh}$	Acetylcholine-dependent K^+ current
I_{K1}	Inward rectifying K^+ current
$I_{Kir,fb}$	Ba^{2+}-sensitive fibroblast inward rectifier K^+ current
I_{Kr}	Repolarizing rapid delayed-rectifier K^+ current
I_{Ks}	Repolarizing slow delayed-rectifier K^+ current
I_{Kur}	Ultra-rapid delayed-rectifier K^+ current
$I_{Kv,fb}$	TEA-sensitive fibroblast K^+-current
I_{Na}	Rapid Na^+ current
I_{NaCa}	Na^+/Ca^{2+} exchange current
I_{NaK}	Na^+/K^+ pump current
I_{pCa}	Ca^{2+} pump current
I_{stim}	Stimulation current
I_{to}	4-aminopyridine-sensitive transient outward K^+ current
j	I_{Na} slow inactivation gate
k_x	Binding rate constant for state *x*
k_a	Binding rate constant for the activated state
k_i	Binding rate constant for the inactivated state
K^+	Potassium ion

KCB	K^+-channel blocker
λ	Reentry wavelength
l_x	Unbinding rate constant for the state *x*
l_A	Unbinding rate constant for the activated state
l_I	Unbinding rate constant for the inactivated state
LA	Left atrium
m	I_{Na} activation gate
Na^+	Sodium ion
NCB	Na^+-channel blocker
NCX	Na^+/Ca^{2+} exchanger
p_x	open probability for ionic species *x*
PI	Proarrhythmic index
PIL	Pilsicainide
R	Universal gas constant
R_x	Resistance for ionic species *x*
RA	Right atrium
RMP	Resting membrane potential
RP	Refractory period
SAN	Sinoatrial node
τ	Dissociation time constant
T	Temperature
TEA	Tetraethylammonium
V_{max}	Maximal rate of phase-0 depolarization
V_x	Voltage for ionic species *x*
VP	Vulnerable period
z	Charge

The Pale Blue Dot, Voyager 1, February 14, 1990.

Il faut imaginer Sisyphe heureux.

Albert Camus

Acknowledgements

First and foremost, I would like to thank my research director, Dr. Stanley Nattel. You have given me a chance when I was a first-year medical student with limited research experience. My clinical and scientific development has been largely thanks to your guidance and support. I will always be infinitely grateful for your mentorship. I would also like to thank my research co-director, Dr. Philippe Comtois, for his input and support over the course of the years.

I am beholden to Dr. Teresa Kus, Dr. Leon Glass, and Dr. Rishi Arora, for gracefully accepting to take part in my jury. Your time and expertise have greatly contributed making this experience instructive and rewarding.

From the Dr. Nattel laboratory, I would like to thank Dr. Xiao Yan Qi and Dr. Feng Xiong, with whom I had the pleasure of working directly, for their fruitful collaboration and Jennifer Bacchi for her continuous support.

From Bordeaux, I am indebted to Dr. Edward Vigmond for his generosity with his time and expertise, which were fundamental to making this work possible.

From Montreal, I would like to thank Dr. Quoc Hung Ly, cardiology fellowship director at the Université de Montréal, for his support during my training in cardiology. Also, many thanks to Dr. Mathieu Walker who instilled the passion for clinical cardiology in me and was instrumental in setting me up on this unique journey.

To my family, Lucia, Silvia and Nestor, thank you for your continuous love and encouragement through the years. To my sunshine, Rafael, seeing you grow and discover the world is an honor and fills my life with joy and meaning. Finally, I would like to thank “ma stratège”, my best friend, my wife and the love of my life, Laura, for her support through the trials and tribulations of this unbelievable adventure. None of this would have been possible without your love, encouragement and support.

Chapter 1. Introduction

1.1 Overview

Heart disease is a major source of morbidity and mortality in the developed world. A higher emphasis on primary prevention and advances in the management of coronary artery disease and heart failure have significantly improved outcomes in patients with heart disease. Cardiac arrhythmias, or abnormal heart rhythms, form a family of disorders affecting the electrical system of the heart. These abnormal rhythms range from benign, such as “skipped beats” or extrasystoles, to life-threatening ventricular arrhythmias causing hemodynamic collapse and sudden cardiac death. Cardiac arrhythmias are the result of altered cellular electrophysiology and myocardial substrate. Recent decades have seen tremendous advances in our understanding of the ionic basis of the cardiac action potential and the pathophysiology of abnormal heart rhythms. Atrial fibrillation (AF) is the most common cardiac arrhythmia in the general adult population; its prevalence is reaching epidemic levels. Antiarrhythmic drugs (AADs) used to treat AF are plagued with the sub-optimal operational characteristics of moderate efficacy and significant electrophysiological side-effects, making new AF-selective drugs highly desirable. Advances in the field of cardiac electrophysiology and computational physiology, as the result of intense collaboration between basic scientists and clinicians, have generated opportunities for greater understanding of arrhythmias and the development of novel therapeutics.

1.2 The Electrical System of the Heart

1.2.1 The Relationship Between the Electrical and Mechanical Cardiac Events

The heart is a four-chambered organ responsible for pumping blood through the pulmonic and systemic circulations. The atria, the upper chambers of the heart, act as reservoirs by receiving venous return during ventricular systole; end-diastolic atrial contraction, or the

atrial kick, contributes a variable fraction of the ventricular preload depending on ventricular diastolic characteristics. During systole, the blood-filled ventricles, the lower chambers of the heart, contract to generate cardiac output across the aortic (left ventricle) and pulmonic (right ventricle) valves. The mechanical function of the heart is the result of a phenomenon called *excitation-contraction coupling*, that is the transduction of an electrical signal into myocardial contraction.

The specialized electrical system of the normal heart is composed of the sinoatrial node (SAN), atrioventricular node (AVN) and His-Purkinje system. Additionally, the Bachmann bundle facilitate transmission of the activation wavefront from the right to left atrium; other specialized connections also exist but will not be discussed here. The SAN is a sub-epicardial structure located in the high right atrium (RA), near the RA-superior vena cava junction; it is the main pacemaker of the heart and is responsible for initiating each cardiac cycle during normal operation. Activation of the SAN spreads across the RA and left atrium (LA) leading to atrial contraction (represented by the P wave on the surface ECG). In the normal heart, the atria and ventricles are electrically insulated, forcing the atrial activation to wavefront transition through the AVN (inferred from the PR interval on the surface ECG), a complex structure with slow-conduction properties. The AVN relays the electrical impulse to the His bundle, which divides into the bundle branches and the Purkinje fibers forming an arborizing network of rapidly-conducting fibrils leading to synchronized activation of the ventricular myocardium (represented by the QRS on the surface ECG).

1.2.2 The Cardiac Action Potential

The cardiomyocyte cell membrane is a bilipid layer impermeable to charged ions; the flux of current through the membrane is dependent on specialized proteins in the form of ion channels and exchangers, typically selective for one of the ionic species (Na^+, K^+, Ca^{2+} and Cl^-). The flow of ions is driven by the *electrical gradient* and the *concentration gradient*; the overall magnitude and direction of ionic transfer is determined by the relative force of these gradients. The concentration gradient is based on the principle of diffusion which stipulates that a solute will distribute equally into a solvent over time. Applied to the cardiomyocyte, this means that a given ionic species will tend to equilibrate such that the intra- and extracellular concentrations

become equal for that ionic species. The electrical gradient refers to the electrical force generated by the unequal distribution of electrical charge across the cell membrane. As an ionic species flows down its concentration gradient, there will be a point at which the electrical gradient will be of the same magnitude but opposite direction, leading to a steady-state of no-net ion flow; this is referred to as the Nernst equilibrium potential for that ionic species. The Nernst potential for a channel carrying ionic species *x* can be calculated as

$$E_x = \frac{RT}{zF} \ln\left(\frac{[x]_o}{[x]_i}\right)$$

where E_x is the Nernst potential for species *x*, $[x]_o$ and $[x]_i$ are the extra- and intracellular concentration of *x*, respectively, *z* is the charge of *x*, *R* is the universal gas constant, *F* is Faraday's constant and *T* is the temperature. Under normal physiologic condition, the Nernst potential measured intracellularly for Na^+, K^+, Cl^- and Ca^{2+} are approximatively +60 mV, -94 mV, -85 mV and +129 mV, respectively.

The basic functional unit of the electrical system of the heart is the cardiac action potential, a representation of the cardiomyocyte transmembrane potential as a function of time. The changes in the cardiomyocyte's transmembrane potential are the result of coordinated opening and closing of ion channels. The morphology and functional characteristics of the action potential varies greatly across the cardiac electrical system, reflecting different ion channel compositions (Figure 1); they are functionally divided into rapidly-activating Na^+-dependent action potentials and slowly-activating Ca^{2+}-dependent action potentials. Even within Na^+-dependent action potential, there is substantial morphological and functional heterogeneity as exemplified by the differences between the atrial and ventricular action potential or between the endo-, mid- and epicardial layers of the ventricular myocardium.

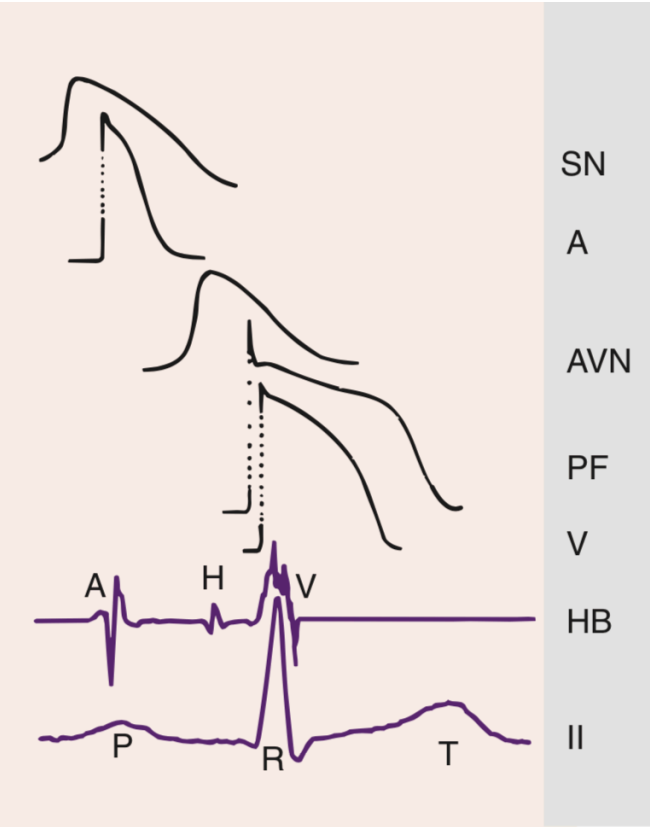

Figure 1. Representative action potential morphologies along the cardiac conduction system. The sinoatrial nodal (SN) and atrioventricular nodal (AVN) action potential depolarization is Ca^{2+}-dependent accounting for its slow upstroke. Atrial (A), Purkinje (PF) and ventricular (V) action potential depolarization is Na^{+}-dependent accounting for its sharp and rapid upstroke. The atrial, Purkinje and ventricular action potentials are morphologically distinct from one another. An intracardiac His-bundle recording (HB) with an atrial (A), His (H) and ventricular (V) electrogram and a surface electrocardiogram (lead II) is provided for relative timing of cardiac events.

The Na^{+}-dependent action potential is composed of 4 phases (Figure 2). Phase 4 of the action potential is the resting membrane potential; here, most channels are closed and the transmembrane potential is set by the inward rectifying K^{+} current (I_{K1}) at -90 to -80 mV. Depolarization of the transmembrane potential to the Na^{+}-channel activation threshold initiates phase 0, the rapid depolarizing phase, during which Na^{+} channels open leading to the upstroke of the action potential; Na^{+}-channels inactivate within 2 ms of opening. This is followed by phase 1, the early repolarization phase, during which the 4-aminopyridine-sensitive transient

outward K^+ current (I_{to}) opens bringing the transmembrane potential towards the K^+ Nernst potential; regional differences in I_{to} expression are important drivers of regional differences in action potential morphology and implicated in the Brugada syndrome. The ultra-rapid delayed-rectifier K^+ current (I_{Kur}) is atrial-specific, only functionally expressed in atrial cardiomyocytes, contributing to the early repolarization phase in humans. Other contributors to phase 1 of the action potential include the 4-aminopyridine-resistant, Ca^{2+}-activated chloride current ($I_{Cl,Ca}$) and the Na^+/Ca^{2+} exchanger (NCX). Phase 2 is one of the main features differentiating the cardiac from the neuron action potential. Here, the depolarizing forces carried via the L-type Ca^{2+} current (I_{CaL}) are in a dynamic equilibrium with the repolarizing rapid (I_{Kr}) and slow (I_{Ks}) delayed rectifier currents leading to little net change in transmembrane potential, hence this phase is referred to as the "plateau". Inactivation for I_{CaL} is time-dependent and, as this process takes place, the main repolarizing currents (I_{K1}, I_{Ks}, I_{Kr}) are no longer opposed, leading to a net exit of positive charges (mainly K^+) from the intracellular space down their concentration gradient into the extracellular space, repolarizing the cell membrane close to the K^+ equilibrium potential. The Na^+/K^+-ATPase pumps Na^+ out of and K^+ into the cell against their respective concentration gradients to restore the electric potential gradient necessary for the next action potential.

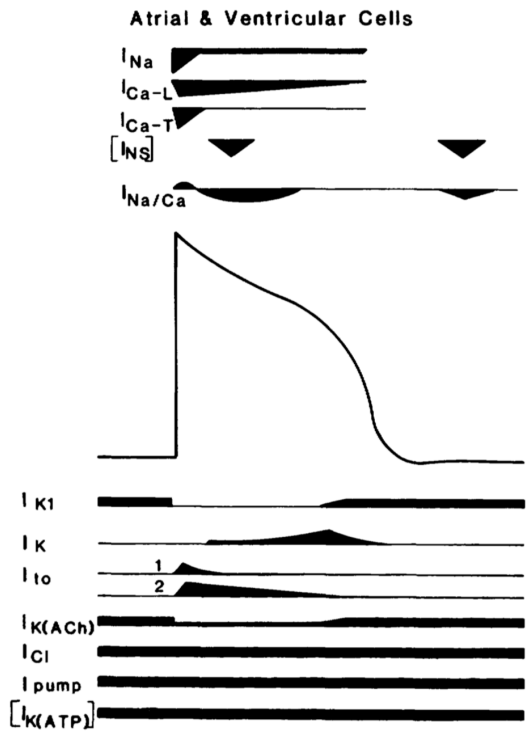

Figure 2. A representative fast-activating Na^+-dependent action potential. The time course of the main depolarizing (top) and repolarizing (bottom) currents as a function time are represented (1). I_{Na} and $I_{Ca,L}$ are depolarizing currents responsible for phase-0 and phase-2 of the action potential, respectively. Several repolarizing K^+ currents modulate the membrane potential, with I_{to} mediating the early phase-1 repolarization, I_{Kr} and I_{Ks} (I_K) responsible for phase-2 and -3 repolarization and I_{K1} setting the resting membrane potential and contributing the final repolarizing forces at the end of phase-3. Other background repolarizing currents include the ACh- and ATP-dependent K^+ currents (I_{ACh} and $I_{K,ATP}$). The T-type Ca^{2+} current ($I_{Ca,T}$) contributes depolarizing forces during phase-1 and the Na^+/Ca^{2+} exchanger is an electrotonic exchanger that plays an important role in intracellular Ca^{2+} homeostasis.

1.2.3 Basic Functional Electrophysiological Properties

The basic functional electrophysiological properties are the conduction velocity (CV) and refractory period (RP). The genesis of the resting membrane potential (RMP) was discussed above. The CV refers to the distance traversed by an electrical impulse per unit time (m/s). The rate of phase-0 depolarization, often quantified as the maximal rate of depolarization (V_{max}), is

one of the major determinants of CV in cardiac tissue; the larger the V_{max}, the faster the CV, all other conditions being equal. This accounts for the rapid conduction along the specialized His-Purkinje system (~2-3 m/s; Na^+-dependent rapid-upstroke action potential), intermediate conduction in atrial and ventricular myocardium (0.3-0.5 m/s; Na^+-dependent rapid-upstroke action potential) and slow SAN and AVN conduction (<0.05-0.1 m/s; Ca^{2+}-dependent slow-upstroke action potential). Other determinants of CV include the Na^+-channel activation potential, the RMP, the inter- and intracellular resistance to current flow, and the cell cross-sectional area. Changes in CV via modulation of I_{Na} and/or the myocardial substrate are important in the pathogenesis of cardiac arrhythmias.

The RP is the time between onset of repolarization to when the cardiomyocyte is capable of supporting propagated depolarization. The RP is sometimes further divided into the absolute (cell is unexcitable), effective (cell supports non-propagating depolarization) and relative RP (cell supports full depolarization with a supraphysiological stimulus). The cardiac action potential has a relatively long RP as compared to the neuron RP, likely to prevent excessively rapid activation rates which would be incompatible with the heart's mechanical function. The determinants of the RP are different in Na^+-dependent vs Ca^{2+}-dependent cardiomyocytes. In Na^+-dependent cardiomyocytes, the RP is determined by when Na^+ channels recover from inactivation. Because Na^+ channels are voltage-dependent, this usually takes place as the action potential completes phase-3 repolarization; hence, in Na^+-dependent cardiomyocytes, the RP is approximately equal to the action potential duration (APD). In Ca^{2+}-dependent cardiomyocyte, the RP is determined by the time-dependent recovery from inactivation of I_{CaL} and typically exceeds the APD. Action potential shortening and prolongation, through its effects on the RP, is important for arrhythmogenesis.

1.2.4 Mechanisms of Cardiac Arrhythmias

As described above, the cardiac action potential is a tightly regulated system; deviations from electrical homeostasis are responsible for the occurrence of cardiac arrhythmias. The cardinal mechanisms of arrhythmia are (i) automaticity, (i) triggered activity and (iii) reentry. A brief description of each of these mechanisms is provided here with their respective relevance to AF initiation/maintenance.

Automaticity. Automaticity is the property by which a cardiomyocyte can generate cyclical activation independent of external stimulation; automaticity can be physiological (such as in the normal sinus node function) or pathological (such as in ectopic atrial tachycardias). A cell's intrinsic automaticity can be increased by maneuvers that (i) depolarize the maximal diastolic potential, (ii) accelerate the rate of diastolic depolarization and/or (iii) hyperpolarize the action potential threshold potential. The reverse tends to suppress automatic rhythms. Automaticity does not appear to play a significant role in AF initiation and/or maintenance (2).

Triggered activity. Triggered activity is the mechanism by which a cardiomyocyte can spontaneously generate an action potential; triggered activity exists in two forms, early afterdepolarizations (EADs) and delayed afterdepolarizations (DADs).

Early afterdepolarizations occur mainly in the setting of bradycardia and/or prolongation of the QT interval (electrocardiographic correlate of the APD). These conditions are such that the depolarizing currents (I_{Na} and/or I_{CaL}) can recover from refractoriness and generate a phase-2 or -3 action potential (2). These afterdepolarizations are important in the genesis of Purkinje fiber-mediate arrhythmias (3) and in the long QT syndrome. However, EADs do not appear to play a significant role in AF pathogenesis (2).

Delayed afterdepolarizations are the consequence of intracellular Ca^{2+} overload and abnormal Ca^{2+} handling with spontaneous diastolic Ca^{2+} release-events from the sarcoplasmic reticulum (SR) into the cytosolic space. Diastolic intracellular Ca^{2+} is, in part, extruded to the extracellular space via NCX, which moves 3 Na^{+} ions for every Ca^{2+} ion. This generates a depolarizing current which can bring the transmembrane potential to the Na^{+}-channel activation potential, leading to a phase-4 action potential. Delayed afterdepolarizations tend to occur during rapid heart rates and form the basis for digoxin toxicity-associated tachyarrhythmias and catecholaminergic polymorphic ventricular tachycardia. DADs have been implicated in the initiation of episodes of paroxysmal AF.

Reentry. Reentry is a mechanism of arrhythmia by which a circuit leads to repetitive myocardial activation. Contrary to automaticity and triggered activity which are generated by mono-cellular events, reentrant arrhythmias, by definition, are multi-cellular phenomena. The pathogenesis and effects of pharmacological interventions on the former can be studied to a large extent in isolated cardiomyocytes whereas the latter, by virtue of their spatially-extended nature, tend to be more complex, with changes to the electrophysiological substrate leading to non-linear behaviors. Reentrant arrhythmias can be *anatomic* or *functional*.

Anatomic reentry. Anatomic reentrant arrhythmias are rhythms that depend on a fixed anatomical obstacle as their circuit. A necessary condition for the maintenance of anatomic reentry is that the pathlength of the circuit be sufficiently long to allow for recovery of cardiomyocytes at the leading edge of the activation front. The minimal pathlength is defined as the wavelength (λ) which is determined by the electrophysiological properties of the substrate, namely CV and RP as $\lambda = CV \times RP$. The difference between the anatomic obstacle pathlength and λ, is the excitable gap (EG). Simply put, the EG is the circuit-length between the activation front and its refractory tail; the longer the EG, the more stable the reentry.

The response of anatomically reentrant rhythms to changes to the electrophysiological substrate, especially with antiarrhythmic drugs, can be predicted on the basis of the relationship between λ, CV, and RP. Interventions that decrease λ via a slowing the CV or a shortening of the RP, will increase the EG and stabilize anatomic reentry. Conversely, interventions that increase λ via increase of the CV or prolongation of the RP, will shorten or even abolish the EG and lead to reentry termination. Anatomic reentrant arrhythmias are commonly encountered in clinical medicine and include rhythms such as atrial flutter, atrioventricular nodal reentrant tachycardia, bypass-tract mediated tachycardias and scar-related ventricular tachycardias; AF is not generally maintained by a macro-reentrant arrhythmia mechanism.

Functional reentry. Anatomic reentry has been the leading framework used to study reentrant cardiac arrhythmia until the early 1970's (4). Allesie and colleagues published a series of papers describing their observations on reentrant rhythms *without* anatomic obstacle in rabbit

atria; the *leading circle theory* was the first formal description of functional reentry in cardiac tissue (5-7). In the leading circle theory, a reentrant rhythm sets with the smallest circuit-size allowed by the substrate's electrophysiological properties; this is different than in anatomic reentry where the circuit size is determined by the obstacle's size. In this model, the circuit pathlength is exactly *equal to* the λ, once again given by λ = CV × RP (Figure 3). Potential circuits with pathlengths longer than λ are overridden by the faster leading circuit; potential circuits with pathlengths shorter than λ immediately encounter refractory tissue and annihilate. The core of the circuit is excitable tissue (vs non-excitable obstacle in anatomic reentry) maintained in a constant refractory state by centripetal activation from the leading circuit. Since the reentrant pathlength is equal to λ, there is no EG. A stable leading circle-type circuit with fibrillatory conduction has been proposed as a potential mechanism for certain forms of AF. However, others have demonstrated the presence of an EG during AF, which would be incompatible with the leading circle model (8).

Almost simultaneously, Zaikin and Zhabotinsky described emergent periodic dynamics in a chemical reaction, the Belousov-Zhabotinsky reaction, following perturbation of the equilibrium state (9). Winfree then formalized a mathematical construct to study the dynamics observed in the Belousov-Zhabotinsky reaction, which was, at a later time, expanded to the study of cardiac arrhythmias as the *spiral wave theory* (10).

A spiral wave or rotor is a spatially extended structure with a curved activation wavefront revolving around a point. This point is referred to as the *phase singularity* as all the phases of the action potential are represented at this singular point (Figure 3). The spiral wave's curved wavefront brings about emergent properties not represented in anatomic reentry or leading circle models. This is because the propagation velocity of a wavefront is dependent on the *source-sink ratio*, that is the relationship between the number of activated cardiomyocytes (source) to the number of upstream cardiomyocytes to activate (sink). At the phase singularity, the angle of curvature is high; here, a small number of source cells active a large number of sink cells, leading to slowing of propagation velocity. Conversely, far from the phase singularity, the wavefront curvature approaches that of a planar wave; here, the number of source cells is approximately equal to the number of sink cells, leading to a higher propagation velocity. In general, rotors are not stationary but meandering following more or less stable trajectories as directed by the

source-sink relationship along the wavefront. Moreover, spiral waves can interact with one another leading to the formation of new phase singularities. Contrary to anatomic and leading circle reentry, spiral wave reentry dynamics cannot be described by a simple relationship between the substrate's electrophysiological properties (i.e., $\lambda = CV \times RP$). Rotor dynamics and response to pharmacological interventions are complex and highly non-linear.

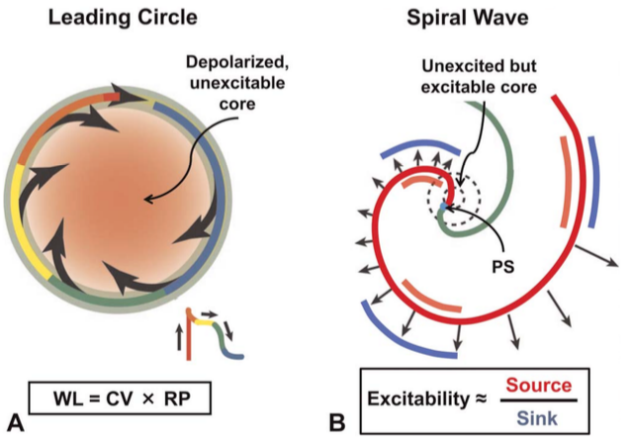

Figure 3. Schematic representation of the leading circle and spiral wave models of reentry. The size of the leading circle is determined by the reentry wavelength (WL), the shortest pathlength that can maintain reentry, given by the product of conduction velocity (CV) and refractory period (RP). A spiral wave is a curved wavefront of depolarization with a phase singularity (PS) revolving around an excitable but unexcited core. Propagation maintenance depends on excitability. The length of the arrows indicates the magnitude of conduction velocity.

1.3 Atrial Fibrillation

1.3.1 Epidemiology, Diagnosis and Clinical Relevance

Atrial fibrillation is the most common sustained cardiac arrhythmia in the general population (11). It is estimated that up to 1-2% of the population has AF and adult males have a life-time risk of developing AF of 25% (11). Despite significant advances in cardiac care, the prevalence and incidence of AF is increasing (12-14). These statistics likely under-estimate the true populational AF burden given that many patients remain asymptomatic, and therefore undiagnosed, for long periods of time (11). Most often, AF occurs in the setting of pre-existing

cardiovascular (e.g., hypertension, heart failure, coronary artery disease, valvular heart disease) and/or systemic risk factors (e.g., infection, sleep apnea, diabetes, thyroid disease, obesity) but can also take place in the absence of manifest cardiovascular or systemic disease (15).

This cardiac arrhythmia is an important cause of cardiovascular morbidity and mortality. First, AF is a common cause of heart failure with preserved or reduced left-ventricular ejection fraction. (16). Second, AF is a major risk factor for arterial thromboembolic events, namely stroke, as stagnant blood form thrombi in the fibrillating left atrial appendage (17, 18). Moreover, AF-related strokes tend to be larger and associated with worse neurological outcomes. (19-22). Third, AF can lead to a significant decrease in quality of life associated with decreased exercise tolerance and palpitations. In fact, AF is the most common cause for consultation with rhythm specialists in the emergency department (11, 23). Lastly, even after adjusting for competing risk factors, AF is associated with double the mortality rate as compared with a population without AF. (24).

Atrial fibrillation is diagnosed on the basis of the surface electrocardiogram (ECG) ; an irregularly irregular rhythm with no organized atrial activity is the typical electrocardiographic presentation (Figure 4). The clinical management of AF is divided into 3 components : (i) the identification of a trigger or reversible cause ; (ii) the management of the thromboembolic risk ; and (iii) the management of the arrhythmia. Items (i) and (ii) are clinical considerations with relatively stereotyped management strategies and will therefore not be further discussed.

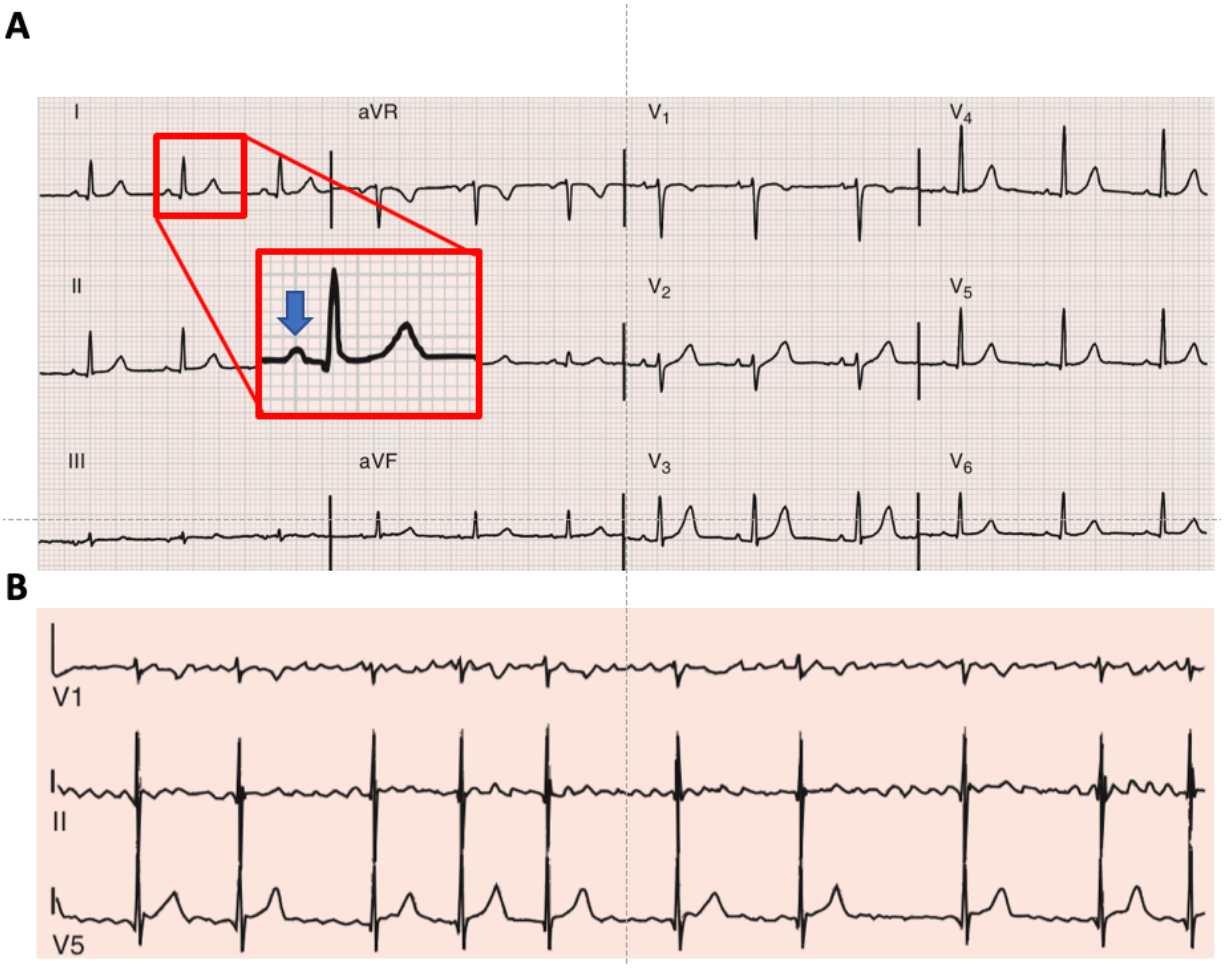

Figure 4. Surface electrocardiogram (ECG) during normal sinus rhythm (A) and in atrial fibrillation (AF; B). (A) Normal 12-lead ECG in sinus rhythm; atrial activation is represented by the P wave (blue arrow in inset). (B) 3-lead ECG of a patient in AF; there is no discernable organized atrial activity (no P waves) and the ventricular rate is irregularly irregular (QRS, high-amplitude sharp deflections).

Atrial fibrillation is categorized as paroxysmal, persistent and permanent based on its duration and rhythm-management goals. Paroxysmal AF is generally defined as self-terminating AF of duration 7-days or less, although most episodes of paroxysmal AF are much shorter. Persistent AF is any AF lasting for more than 7 days or requiring pharmacological or electrical cardioversion for termination. Finally, permanent AF refers to long-lasting AF for which sinus rhythm-restoration is no longer sought. The utility of this classification resides in the empiric

observation that therapies for AF have differential efficacy rates for different AF patterns. For example, AF catheter ablation is more effective in patients with paroxysmal AF and less effective in patients with persistent AF. Furthermore, the natural history of AF is characterized by short and infrequent episodes which progress over time to longer lasting persistent forms; some individuals never progress to persistent AF whereas others never have documented paroxysmal AF before presenting with sustained AF (25). The progression to more refractory forms of AF is the consequence of molecular changes and structural changes known as *remodeling.*

1.3.2 Atrial Fibrillation Rhythm-Control vs Rate-Control

There are two strategies for the management of AF the (i) rate-control strategy and (ii) rhythm-control strategy.

Atrial Fibrillation Rate-Control. Atrial fibrillation rate-control is an arrhythmia management strategy in which the ventricular response rate (i.e., the heart rate) is controlled while the atria remain in AF. The pharmacological agents used for rate-control are the beta-blockers (e.g., metoprolol, bisoprolol, nadolol), the non-dihydropyridine Ca^{2+}-channel blockers (e.g., diltiazem, verapamil) and digoxin; amiodarone, an antiarrhythmic drug, is sometimes used for rate-control (26). The goal of AF rate-control is to limit the number of electrical impulses conducted from the fibrillating atria, through the AVN to the ventricles to prevent excessively rapid heart rates (i.e., tachycardia) (26, 27). In refractory cases, it is also possible to ablate the AVN, causing complete and irreversible interruption of the electrical communication between the atria and the ventricles, of course, with prior implantation of a permanent pacemaker.

Atrial Fibrillation Rhythm-Control. In a rhythm-control strategy, the therapeutic goal is to restore normal sinus rhythm and prevent AF recurrence. Beyond the management of traditional risk factors, there are two main options for AF rhythm-control: (i) AADs and (ii) catheter ablation. Surgical AF ablation is available for patients undergoing cardiac surgery.

Whether AF rhythm-control is superior to rate-control has been, and continues to be, the object of significant debate and discussion in the cardiovascular community. From a physiological standpoint, it is reasonable to hypothesize that rhythm-control (sinus rhythm is restored) should be superior to rate-control (patient remains in AF). Atrial fibrillation eliminates atrial contraction leading to the loss of the end-diastolic atrial contribution to ventricular filling (preload). The atrial kick can represent up to 30% of the left-ventricular preload, a non-negligible fraction especially in patients with left-ventricular systolic or diastolic dysfunction. Moreover, the rapid and irregular heart rates during AF makes ventricular contraction less efficient and can ultimately lead to tachycardia-induced cardiomyopathy.

Several large clinical trials have compared rhythm- vs rate-control. The two largest, the Atrial Fibrillation Follow-Up Investigation of Rhythm Management (AFFIRM) trial and the Atrial Fibrillation and Congestive Heart Failure (AF-CHF) trial, are discussed here as representative of this literature. The AFFIRM trial randomized 4060 patients with preserved left-ventricular ejection fraction to a rate- vs rhythm-control strategy; the primary outcome was total mortality (28). After 5 years, the death rate in the rhythm-control group was 23.8% and 21.3% in the rate-control group with a hazard ratio of 1.15 (confidence interval 0.99-1.34). Hence rhythm-control was not superior to rate-control and was even associated with a trend towards higher mortality. Moreover, patients randomized to rhythm-control reported higher rates of drug-related adverse events as well as more electrical cardioversions and hospitalizations than patients in the rate-control group. The AF-CHF trial randomized 1376 patient with AF and heart failure with reduced ejection fraction (mean left-ventricular ejection fraction 27±6%) to a rate- vs rhythm-control strategy (29). At the end of the follow-up period, there were 182 deaths (27%) in the rhythm-control group vs 175 deaths (25%) in the rate-control group with a hazard ratio of 1.06 (confidence interval 0.86-1.30). Again, patients assigned to AADs had higher rates of drug side effects, electrical cardioversions and hospitalizations. Similar findings have been reported in a number of smaller trials (30-32). Hence, there is not definitive clinical evidence that (pharmacological) sinus rhythm-maintenance is superior to AF rate-control (33, 34).

Atrial fibrillation catheter ablation. Catheter ablation for AF was described by Haissaguerre and collegues, showing that pulmonary veins are common AF triggers and can

sometimes also act as drivers (35). The procedure has evolved significantly over the years, increasing the procedural success rates and decreasing complications. Virtually all AF ablation procedures include pulmonary vein isolation, the electrical disconnection of the pulmonary veins sleeves from the atrial myocardium (36). In patients with paroxysmal AF, current ablation techniques are associated with a success rate in the range of 65-75% at 1 year with a peri-procedural risk (e.g., cardiac tamponade, pulmonary vein stenosis, phrenic nerve injury, stroke, atrio-esophageal fistula) of <5% (15); the sinus rhythm-maintenance is less in patients in patients with persistent forms of AF (37). In brief, AF catheter ablation is commonly used for rhythm-control. However, it remains a relatively expensive procedure with non-trivial risks and imperfect long-term success rates performed only in a limited number of specialized centers; it is mainly indicated for symptomatic patients who recur on antiarrhythmic therapy or cannot tolerate AADs (33). Hence, the majority of patients with AF on a rhythm-control strategy are treated with AADs.

Antiarrhythmic drugs. The pharmacological properties of AADs will be discussed in more detail in Section 1.4. Antiarrhythmic drugs have been used to treat cardiac arrhythmias for over a century (38). However, despite major advances in our understanding of the basic pathophysiology of AF, most clinically available AADs are older molecules developed for indications other than the treatment of AF; their efficacy for sinus rhythm-maintenance is sub-optimal (39). As highlighted above, rhythm-control was not shown to be superior to rate-control in large randomized clinical trials. Several explanations have been offered to explain these findings; the sub-optimal antiarrhythmic efficacy and significant side effects associated with available AADs are the most commonly cited reasons for the failure to show benefit of rhythm-control. Hence, a safe and effective AAD for the treatment of AF is a major unmet need in clinical medicine.

1.3.3 Electrical and Structural Remodeling

Therapies for sinus rhythm-maintenance in patients with AF are generally more effective for paroxysmal forms of AF than in persistent AF. For example, in one study, the conversion to sinus rhythm-rate with amiodarone, the most effective AAD, was 85% in patients with AF of

less than 1 year duration but only 57% in patients with AF of more than 1 year duration (40). The progression from short-lasting paroxysmal forms of AF to persistent AF is the consequence of changes at the molecular level referred to as *remodeling.* The cardinal components of AF-induced remodeling are (i) electrical remodeling, (ii) structural remodeling, (iii) Ca^{2+}-handling abnormalities and (iv) autonomic nervous system dysregulation.

Electrical remodeling. In 1996, Wijffels and colleagues (41) published a study of 12 goats instrumented with epicardial atrial pacing wires ; AF could be induced by burst-pacing the atria. Without prior stimulation, a burst would induce non-sustained AF with a mean duration of 6±3 *seconds*. After 24 hours of rapid atrial stimulation, the same burst would induce AF with mean duration of 2.2±3.0 *minutes*. Finally, with 2 weeks of continuous rapid atrial stimulation, most goats were in sustained AF (duration >24 hours). As AF became longer-lasting, the authors also observed a corresponding (i) shortening of the mean atrial activation cycle length from 145±18 ms (no prior stimulation), to 108±8 ms (after 24 hours), to 99±10 ms (after 2 weeks) and (ii) shortening of the atrial refractory period from 146±19 ms (no prior stimulation) to <80 ms (sustained AF). These observations are the manifestation of *electrical remodeling*.

Electrical remodeling takes place as the homeostatic compensatory mechanisms of the cardiomyocytes are faced with intracellular Ca^{2+} overload during sustained rapid activation rates. One of the cardinal expressions of electrical remodeling is the shortening of the atrial APD, and consequently the RP, which then facilitate reentrant phenomena and AF maintenance (2). These changes to the cardiomyocyte electrophysiological properties are the consequence of alterations in ionic currents, with an overall upregulation of repolarizing currents and downregulation of depolarizing currents. The inward L-type Ca^{2+} current is the major depolarizing current during phase-2 of the action potential ; $I_{Ca,L}$ is strongly downregulated in response to increase cytosolic Ca^{2+} (42). The decrease in $I_{Ca,L}$ is through increased channel inactivation (acutely) and downregulation of transcription of the $I_{Ca,L}$ α-subunit (chronically) (43).

Looking, the density of I_{K1} is approximately doubled in the setting of AF vs sinus rhythm, mainly secondary to an increase in the expression of Kir2.1 (44, 45). The upregulation of I_{K1} leads to hyperpolarization of the cardiomyocyte resting transmembrane potential,

increasing the fraction of Na^+ channels available to activate, thereby stabilizing functional reentrant arrhythmias (46). The acetylcholine-dependent K^+ current ($I_{K,ACh}$), when activated, shortens the APD, facilitating reentry (47); $I_{K,ACh}$ exists in an agonist-dependent form and in an agonist-independent form. Electrical remodeling downregulates the agonist-dependent form of $I_{K,ACh}$ current but a proportionally larger upregulation of the constitutively active $I_{K,ACh}$ (44, 48, 49), principally secondary to an increase open probability of the channel (50). The ultra-rapid delayed rectifier K^+ current (I_{Kur}) has been reported to show no significant change in chronic AF in some studies (51-53) whereas other report downregulation of I_{Kur} (54, 55). The effects of I_{Kur} downregulation on the APD are non-linear and will be discussed in detail in Chapter 4. The rapid and slow components of the delayed rectifier K^+ current (I_{Kr} and I_{Ks}) are not significant down- or upregulated in chronic AF (56).

In summary, AF leads to remodeling in the expression/function of specific ionic currents resulting in an increase in repolarizing currents and a decrease in depolarizing forces, shortening the APD and RP and stabilizing reentrant arrhythmias.

Structural remodeling. Subsequent to the description of AF-induced electrical remodeling, Li and colleagues presented the electrophysiological and structural changes in a canine model of AF without (rapid atrial stimulation with controlled ventricular rates) and with (rapid ventricular stimulation) concomitant heart failure (57). Similar to what had been previously reported by Wijffels (41), the animals undergoing rapid atrial simulation experienced a shortening in the atrial APD and RP and mean activation cycle length. In the dogs with rapid ventricular stimulation and heart failure, these electrophysiological parameters were not significantly changed although AF maintenance was much more vs control. These important observations pointed to a different type of remodeling in the setting of heart failure than the electrical remodeling described by Wijffels. Histological examination of the atrial myocardium revealed extensive interstitial fibrosis, the basis for structural remodeling (57). These changes have an important impact on atrial electrophysiology, with overall pro-fibrillatory effects favoring AF maintenance.

A number of upstream pathways haven been described including inflammation, abnormal stretch conditions, autonomic signaling and oxidative stress/injury(58, 59). These are not only important for the understanding of the basic pathophysiology of AF but have also been proposed as potential therapeutic targets. The association between inflammation and cardiovascular disease has been a growing theme for basic and clinical research as it intersects with several other key pathophysiological pathways such as oxidative stress, fibrosis and thrombosis. For example, coronary artery disease (CAD) is now known to have a major inflammatory component and anti-inflammatory drugs such as colchicine are being investigated as treatment options. A similar relationship between inflammation and AF has been reported. Myeloperoxidase (MPO) has been found in higher levels in patients with AF and MPO knock-out rodent models have a decreased propensity for AF (60). Interleukin (IL)-6 and C-reactive protein, two inflammatory markers, were also found to be elevated in patients with AF vs control and associated with decreased success after AF catheter ablation (61). Tumor necrosis factor-α (TNF-α), IL-8, IL-10 have also been associated with AF (62-64).

The renin-aldosterone-angiotensin system (RAAS) has also been implicated as an upstream mediator of AF via local and systemic effects. Systemically, activation of the RAAS leads to hypertension, left-ventricular hypertrophy and congestive heart failure, all major clinical risk factors for AF. Locally, angiotensin II has direct pro-arrhythmic, pro-inflammatory and pro-fibrotic effects on the atrial myocardium (65, 66). Similarly, aldosterone and endothelin-1 have been associated with AF via a tumor growth factor β1-dependent signaling pathway (67, 68). Acute and chronic atrial stretch have also been implicated in AF pathogenesis. The pro-arrhythmic effects of stretch in part overlap with those associated with hypertension and left-ventricular hypertrophy such as activation of the RAAS and endothelin-1. Stretch was also found to have direct effects on atrial conduction velocity, likely mediated at least in part by stretch-sensitive channels.

There has been significant interest in targeting these upstream mechanisms for the prevention of AF using pharmacological agents such as angiotensin-converting enzyme inhibitors (ACEis), angiotensin receptor blockers (ARBs), statins, corticosteroids and poly-

unsaturated fatty acids (PUFAs). Initial experimental work and clinical trials reported positive findings using many of these agents. More stringent clinical studies have cast doubt on the value of available upstream therapies for AF beyond their primary clinical indication. As it stands today, upstream therapies are not routinely used for AF prevention(59).

1.3.4 Mechanisms of Atrial Fibrillation Arrhythmogenesis

Atrial fibrillation is a complex arrhythmia; our understanding of its basic functional pathogenesis is incomplete. Several mechanisms have been proposed for AF maintenance including a localized ectopic focus, an anatomic reentrant circuit with fibrillatory conduction and a functional reentrant circuit with fibrillatory conduction (Figure 5A) (69). More recently, other mechanisms have been proposed which include a small number of stable spiral waves, a larger number of dynamically unstable spiral waves and endo-/epicardium dissociation (Figure 5B) (69). These mechanisms are not mutually exclusive, and it is likely that they play a differential role in different patients and at different stages of the disease. Conceptually, AF requires a *trigger* for initiation of the arrhythmia and a pro-fibrillatory *substrate* for maintenance. Certain arrhythmia mechanisms are more susceptible to act as triggers (i.e., pulmonary vein ectopic depolarizations) whereas others are more likely to be important for AF maintenance (i.e., multiple interacting spiral waves). The specific arrhythmia mechanisms have important therapeutic implications. For example, a focal ectopic rhythm could be successfully treated with ablation whereas functional reentry may not, although some suggested otherwise.

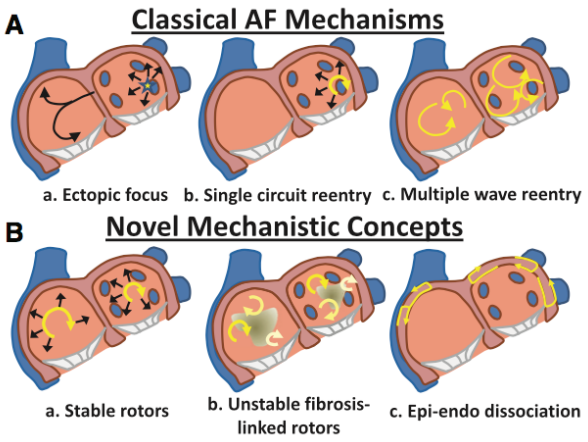

Figure 5. The classical and contemporary putative mechanisms of AF. (A-a) an ectopic focus ; (A-b) a stable anatomic reentry circuit ; (A-c) a stable functional reentry circuit. (B-a) A small number of spiral waves with fibrillatory conduction ; (B-b) a large number of spiral waves ; (B-c) epi-/endocardial dissociation (69).

1.4 Antiarrhythmic Drugs

1.4.1 Classification of Antiarrhythmic Drugs

Antiarrhythmic drugs are a heterogeneous group of molecules. Generally speaking, AADs include any medication with antiarrhythmic properties be it mediated by (i) blockade of a specific ion channel (e.g., block of the Na^+ channels by lidocaine), (ii) modulation of a membrane exchanger (e.g., block of the Na^+/K^+-ATPase by digoxin), interaction (iii) with adrenergic receptors (e.g., the use of beta-blockers) or (iv) with second-messengers in a signaling pathway (1). However, the operational definition of an antiarrhythmic in clinical medicine is restricted to molecules whose main electrophysiological action is via interaction with cardiomyocyte ion channels.

The AAD classification has significantly evolved over time paralleling our growing understanding of basic cardiac electrophysiology and pharmacology (38). The first classification was that of Hoffman and Bigger ; antiarrhythmics were divided into (i) drugs with CV-slowing and APD-prolongation properties (e.g., procainamide and quinidine) and (ii) drugs with APD-

shortening properties with no effect on CV (e.g., lidocaine) (70). Singh and Vaughan Williams later proposed a more detailed classification with drugs with anesthetic properties (class I; i.e., Na^+-channel blockers), drugs with anti-sympathetic effects (class II i.e., beta-blockers), drugs with APD-prolonging effects (class III; i.e., K^+-channel blockers) and (IV) Ca^+-channel blockers. (Table 1) (71, 72). Class I agents have been further subdivided into three sub-families based on their respective block kinetic properties with Ia (e.g., procainamide and quinidine), Ib (e.g., lidocaine, mexiletine) and Ic (e.g., flecainide, propafenone) agents having intermediate, fast and slow dissociation kinetics, respectively (73).

Table 1. The Singh and Vaughan William AAD classification.

Class	**Target**	**Representative examples**
I	Na^+ channels	a : quinidine, procainamide, disopyramide b : lidocaine, mexiletine c : flecainide, propafenone
II	Beta-adrenergic receptors	propranolol, metoprolol, nadolol
III	K^+ channels	sotalol, amiodarone, dofetilide
IV	Ca^{2+} channels	verapamil, diltiazem

The Singh and Vaughan William AAD classification has several limitations. For example, it includes ion channel blocker (classes I, III and IV) and non-ion channel blocker (class II) molecules. Moreover, most antiarrhythmics interact with more than one ion-channel species; amiodarone is a class III agent but has pharmacological properties of all four Singh and Vaughan William classes. Also, this classification does not include potentially clinically useful information such as anticholinergic (e.g., with the class Ia drug disopyramide) and/or negative inotropic effects (e.g., with the Ca^+-channel blocker diltiazem). Finally, drugs commonly used to treat arrhythmias (e.g., adenosine) are not represented in the Singh and Vaughan William classification. New and more comprehensive classifications have been proposed to address

some of these limitations (i.e., the Sicilian Gambit (1)); however, the operational simplicity of the Singh and Vaughan William classification is such that it remains the most commonly used antiarrhythmic taxonomy in clinical medicine.

The therapeutic goal of an AAD is to terminate and prevent the recurrence of a given abnormal cardiac rhythm; these effects are globally referred to as *antiarrhythmic.* Antiarrhythmic drugs can also modulate the electrophysiological substrate in ways that facilitate the occurrence of new arrhythmia, potentially more dangerous than the arrhythmia for which the drug was prescribed; these effects are globally referred to as *proarrhythmic.* The sub-optimal operational characteristic of currently-available AADs is a major limitation. For example, the Cardiac Arrhythmia Suppression Trial (CAST) studied the use of the class Ic-agents flecainide and encainide for ventricular ectopy-suppression post-myocardial infarction (74). The main finding of this study was that the use of class Ic agents *increased* total (and arrhythmic) mortality vs placebo. Similar results have been reported with the class Ib-agent mexiletine (IMPACT study) and the class III-agent d-sotalol (SWORD study) (75, 76). Safe and effective AADs for the treatment of cardiac arrhythmias in general, and AF in particular, are a major unmet need in clinical medicine.

1.4.2 Properties and Mechanisms of Action of Antiarrhythmic Drugs

Antiarrhythmic drugs modulate the flux of specific ionic species through their respective ion channel. As discussed above, Na^+-, K^+- and Ca^{2+}-channels constitute the main targets for currently-available AADs. More recently, novel ion channels with potentially antiarrhythmic properties, such as the small-conductance calcium-activated K^+ channel, have been described (77). Also, the role of altered Ca^{2+} homeostasis has been further implicated in the pathogenesis of AF, paving the way for new antiarrhythmic targets (i.e., the ryanodine receptor on the sarcoplasmic reticulum) (78). The papers presented in the thesis are centered around Na^+-channel blockers and K^+-channel blockers; these agents will be discussed in more detail.

Phamacological Properties of Na^+-Channel Blockers. This sub-section has been adapted from a review article published in parallel with the work presented in this thesis (39). The anti-

AF efficacy of clinically available Na^+-channel blockers depends on the drug's pharmacological properties and the population in which the drug is being used (i.e., paroxysmal vs persistent AF, comorbidities, etc.); they are sub-divided (Ia, Ib, Ic) on the basis of their binding/unbinding properties and effects on the APD. Class Ia agents (e.g., procainamide, disopyramide, quinidine) have intermediate Na^+-channel unbinding kinetics ($1 < \tau < 12$ s), a moderate V_{max}-lowering effect and prolong the APD via blockade of I_{Kr}. The anti-AF efficacy of procainamide, disopyramide and quinidine ranges from 43-66% (79-81), 48-60% (82-85) and 31-55% (86-93), respectively. Class Ia drugs are rarely used for AF rhythm-control, except in special populations such as in patients with AF and manifest pre-excitation (procainamide) and those with hypertrophic cardiomyopathy (disopyramide). Lidocaine and mexiletine are class Ib agents; these have rapid dissociation kinetics ($\tau < 1$ s) with minor effects on V_{max}; these drugs are second-line agents for ventricular arrhythmias and used for AF management. Finally, class Ic agents (e.g., flecainide, propafenone) have slow Na^+-channel dissociation kinetics ($\tau > 12$ s) associated with marked V_{max}-reduction and a neutral effect on the APD (mild affinity for I_{Kr}). Flecainide and propafenone have acute AF conversion rates to sinus rhythm in the range of 70% in patients with recent-onset AF (86, 93-97); their efficacity is substantially less in longer-lasting forms of AF (94, 98, 99). In patients with paroxysmal AF, these drugs can be prescribed for chronic daily use or as part of a "pill-in-the-pocket" strategy, that is to be used only when an AF episode occurs (100). Class Ic AADs are contra-indicated in patients with significant coronary artery disease, left-ventricular dysfunction or structural heart disease (74, 101).

1.5 Mathematical Modeling in Cardiac Electrophysiology

The cardiac action potential is the result of the coordinate flux of currents across the cardiomyocyte transmembrane potential. The ion channel dynamics are complex and highly non-linear making it challenging to predict the effects of perturbation to the electrophysiology of an isolated cardiomyocyte, let alone a group of interacting cells, on arrhythmia dynamics. Mathematical modeling of the cardiac action potential is a relatively new approach to the study of cardiac electrophysiology with a precision and resolution not achievable with currently-available experimental techniques (102). These models have already been successfully used in

this field, for example to predict the effect of specific ion-channel mutations and pharmacological interventions on action potential dynamics (102). Modeling can also predict new and unanticipated phenomena with subsequent experimental validation (e.g., the role of spiral wave in AF (103-105)) and help in delineating fundamental mechanisms of action potential dynamics. Contemporary applications of mathematical modeling in cardiac electrophysiology include prediction of the risk of sudden cardiac death in realistic ventricular geometries (106) and the *in silico* investigation of different ablation line patterns for AF ablation (107).

1.5.1 Mathematical Modeling of the Cardiac Action Potential

The first mathematical model of the action potential was proposed by Hodgkin and Huxley in their work on the propagation of electrical impulses along the axon of the giant squid (108). Their formalism was later extended to describe the cardiac action potential which, contrary to the neuron action potential, has a long phase-2 plateau. Over the years, models have evolved to better represent *in situ* electrophysiology by, for example, including detailed descriptions of intracellular Ca^{2+} handling (109) and the effects of neuro-hormonal modulation (110). Moreover, species-specific models were developed to account for the experimentally-observed differences in ion channel profiles (111). For example, the I_{Kur} current carried by the α-subunit Kv1.5 is functionally expressed in human atrial cardiomyocytes but relatively absent in dog cardiomyocytes.

A mathematical model of the cardiac action potential consists of a number of interacting sub-units. Each sub-unit describes the dynamics of a specific functional component of the model, for example, the dynamics of an ion channel, membrane exchanger, intracellular Ca^{2+} handling, etc. Sub-units are then assembled to recapitulate the global functional architecture of the cardiomyocyte's electrophysiology (Figure 6). Individual simulated cardiomyocytes can then be coupled to generate 1- (e.g., a cable), 2- (e.g., a slab of tissue) and 3- (e.g. an anatomically realistic atrial model) dimensional models.

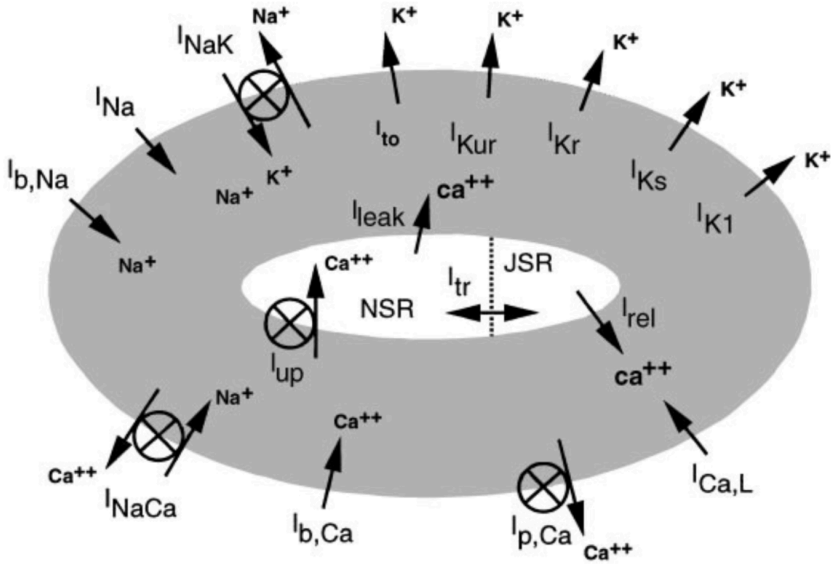

Figure 6. Schematic representation of the Courtemanche-Ramirez-Nattel human atrial cardiomyocyte model. Each ionic current, I_x, is represented by a system of differential equations. The different components of the model are assembled to recapitulate the virtual cardiomyocyte electrophysiology (112).

The action potential is the consequence of selective current fluxes across the cardiomyocyte membrane. The most commonly used mathematical formulation to represent an ionic current is the *ohmic* formulation (from Ohm's law) given by

$$I_{\mathrm{x}} = \frac{1}{R_{\mathrm{x}}} V_{\mathrm{x}} = g_{\mathrm{x}} V_{\mathrm{x}}$$

where I_x is the current for ionic species x, R_x is the resistance, V_x is voltage and g_x is the instantaneous conductance for species x (i.e., the inverse of R_x). The instantaneous conductance and transmembrane potential are then expanded as

$$I_{\mathrm{x}} = \bar{g}_{\mathrm{x}} p_{\mathrm{x}} (V - E_{\mathrm{x}})$$

where $\bar{g}_x$ is the maximal conductance for species x, p_x is the open probability for the channels of species x, V is the transmembrane potential and E_x is the Nernst equilibrium potential for x. This equation for I_x is generic and can be used to represent any current by specifying p_x, $\bar{g}_x$ and E_x. There are alternative generic expressions for I_x such as the Goldman-Hodgkin-Katz formulation, but these are less frequently used.

There are several possible formulations for p_x, the three main being (i) the instantaneous model, (ii) the Hodgkin-Huxley model and (iii) the Markov model (113). The main model used in this Thesis is the Courtemanche-Ramirez-Nattel which utilizes a Hodgkin-Huxley-type representation for p_x (112), in which the open probability has a phenomenological representation as a set of activation and/or inactivation "gates". For example, I_{Na} is described by the following equation

$$I_{Na} = \bar{g}_{Na} m^3 h j (V - E_{Na})$$

where m is the activation gate, h and j are the fast and slow inactivation gates respectively, $\bar{g}_{Na}$ is the maximal conductance, V is the transmembrane potential and E_{Na} is the Na^+ Nernst equilibrium potential. The time-evolution for each gate in the Hodgkin-Huxley formalism is provided by a differential equation of the form

$$\frac{dy}{dt} = \alpha_y (1 - y) - \beta_y y$$

where α_y and β_y are constants characterizing the transitions between the opened and closed state of gate y. Finally, the cardiomyocyte membrane is represented as a capacitor in parallel with the set ionic currents (Figure 7) mathematically expressed by

$$C_m \frac{dV}{dt} + I_{ion} - I_{stim} = 0$$

$$I_{ion} = I_{Na} + I_K + I_{Ca} + \cdots$$

where C_m is the membrane capacitance, V is the transmembrane potential, I_{ion} is the total ionic current and I_{stim} is a stimulation current. The full model consists of a set of differential equations; these equations are generally not solvable in closed form; they are solved numerically using different available computational algorithms.

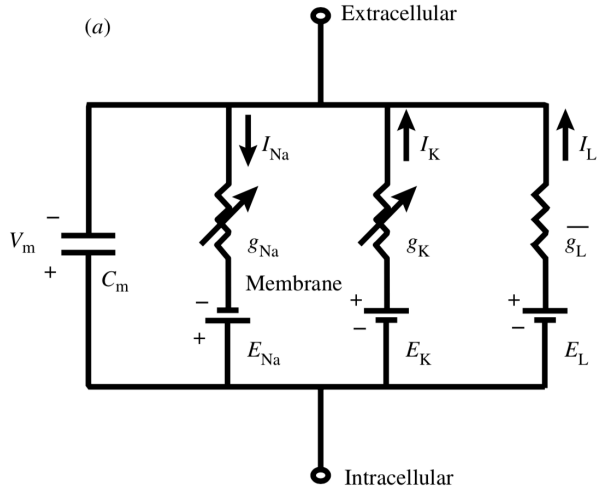

Figure 7. Schematic representation of the transmembrane potential as a capacitor (C_m) in parallel with the ion channel-mediated currents, I_x, with Nernst potential, E_x, and conductance, g_x.

1.5.2 Modeling of Antiarrhythmic Drug Action

A central theme of this thesis is the study of pharmacological interventions on the cardiac action potential and arrhythmias using computational methods. There are two main models used to describe the interaction between AADs and their target channel: (i) the modulated-receptor hypothesis and (ii) the guarded-receptor hypothesis.

The modulated-receptor hypothesis. The modulated-receptor hypothesis has been independently proposed by Hille, and Hondeghem and Katzung in the late 1970's (114-116); this model was developed to described the action of Na^+-channel blockers. The modulated-receptor model was an attempt to explain 3 cardinal observations on the electrophysiology of Na^+-channel blockers namely (i) the shift of the inactivation curve to more negative potentials ("*h*-curve shift"), (ii) the frequency-dependent effects of class I agents on V_{max} and (iii) the differential rate of recovery of V_{max} at hyperpolarized vs depolarized transmembrane potential.

The central hypothesis of the modulated-receptor formalism is that the affinity of a molecule for its target is *modulated* by the state of the channel (i.e., resting, activated, inactivated). In other words, the same drugs would have different affinities for the channel in its

rested vs activated vs inactivated conformation; a schematic representation of the modulate-receptor formalism is presented in Figure 8 (114).

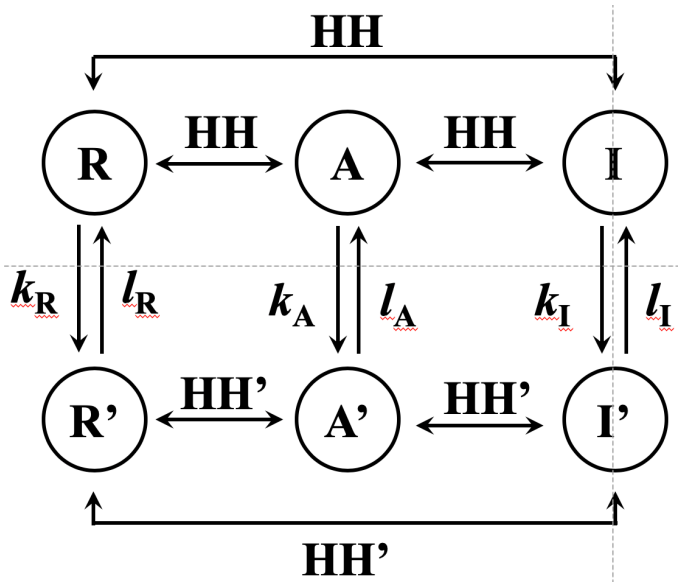

Figure 8. Schematic representation of the modulated-receptor formalism. The circles (R, I, A) represent the drug-free Na^+ channel in the resting (R), activated (A) and inactivated (I) state. The transitions between R, A and I are governed by the cardiomyocyte Hodgkin-Huxley model (HH). The X' circles represent drug-bound Na^+-channels. The transition between X and X' are characterized by a binding (k_x) and unbinding (l_x) rate constant. The transitions between R', A' and I' are governed by the modified HH equations (HH'; see text) (115).

In this model, the channel's transitions form resting (R), activated (A) and inactivated (I) state are governed by the Hodgkin-Huxley (HH) equations. The transitions between a drug-free channel in state X and its drug-bound state (X') is characterized by a set of binding (k_x) and unbinding (l_x) rate constants. The time-evolution of the total fractional block (B) is given by

$$\frac{\mathrm{d}B}{\mathrm{d}t} = (k_R R + k_A A + k_I I)D - (l_R R' + l_A A' + l_I I')$$

where B is the fractional block, R, A, et I, are the fractions of Na^+ channels in their resting, activated and inactivated state, respectively, R', A', and I' are the fractions of drug-bound Na^+-channels in the resting, activated and inactivated state, respectively, k_x and l_x are the binding and unbinding rate constants for state X, respectively and D is the drug concentration (115). A notable feature of the modulated-receptor hypothesis is that the mathematical expression for the

Na^+-channel' rapid inactivation gate, *h*, is explicitly modified to account for the experimentally observed *h*-curve shift as follows

$$\frac{\mathrm{d}h'}{\mathrm{d}t} = [\alpha_{\mathrm{h}'} I' + (k_{\mathrm{R}} R + k_{\mathrm{A}} A) D] - [\beta_{\mathrm{h}'} (R' + A') + l_{\mathrm{R}} R' + l_{\mathrm{A}} A']$$

where $\alpha_{h'}$ and $\beta_{h'}$ are functions of voltage used to incorporate the *h*-curve shift into the model. In summary, in the modulated-receptor hypothesis, the Na^+-channel blocker has differential affinities for the Na^+ channel in its different states and requires explicit modifications to the inactivation gate dynamics to account for experimental observations.

The guarded-receptor hypothesis. In 1984, Starmer and colleagues proposed an alternative formalism to model the interaction between class I AADs and the Na^+ channel, the *guarded-receptor hypothesis* (117). The main hypothesis of this model is that (i) the drug has a constant affinity for the different states of the channel but that the channel's gates (*m* and *h*) *guard* access to the drug binding site. Contrary to the modulated-receptor hypothesis, no changes to the *h* gate expression is required to account for the *h*-curve shift.

The transition between drug-free and drug-bound channel is given by a first-order transition of the form

$$U + D \underset{k_0, l_0}{\longleftrightarrow} B$$

where *U* is the drug-free channel, *D* represent the channel blocker, *B*, is the drug-bound channel and k_0 and l_0, are the binding and unbinding rate constants, respectively. The drug-bound channel population time-evolution is given by

$$\frac{\mathrm{d}b}{\mathrm{d}t} = k_0 [D](1 - b) - l_0 b$$

where *b* is the fractional block, k_0 and l_0 are the binding and unbinding rate constants, respectively and [*D*] is the drug concentration. The rate constants can be made to account for the energy required to displace a charged drug from the drug pool to its binding site on the Na^+ channel as follows

$$k_0 = k\mathrm{e}^{z\epsilon(V_{\mathrm{pool}} - V_{\mathrm{rec}})\mathrm{F/RT}}$$

$$l_0 = l\mathrm{e}^{-z(1-\epsilon)(V_{\mathrm{pool}} - V_{\mathrm{rec}})\mathrm{F/RT}}$$

where ε is a parameter partitioning the effect of the charge between binding and unbinding transitions, z is the drug charge, V_{pool} is the drug-pool potential, V_{rec} is the binding site potential, F if Faraday's constant, R is the universal gas constant and T is the temperature. The equation for the fractional block b can be generalized for an arbitrary number of channel states s as

$$\frac{db}{dt} = \sum_{s=1}^{s_{\text{u}}} f_{\text{s}} k_{\text{s}} [D](1-b)\, \text{e}^{z\epsilon\frac{(V_{\text{pool}}-V_{\text{rec}})\text{F}}{\text{RT}}} - \sum_{s=1}^{s_{\text{u}}} g_{\text{s}} l_{\text{s}}\, \text{e}^{-\frac{z(1-\epsilon)(V_{\text{pool}}-V_{\text{rec}})\text{F}}{\text{RT}}}$$

where k_{s} and l_{s} are the binding and unbinding rate constants for state s, $f_{\text{s}}(1\text{-}b)$ is the fraction of drug-free channels in state s and g_{s} is the fraction of drug-bound channels in state s ; the other parameters are as previously defined.

The guarded-receptor hypothesis is the drug-channel interaction model used in the original research papers presented in this thesis. We considered case of the 3-state Na^+ channel (resting, activated and inactivated) with a Na^+-channel blocker with affinities for the activated and inactivated states, as clinically relevant Na^+-channel blockers have trivial affinity for the resting state. The total fractional block, B_{T}, is then given by

$$B_{\text{T}} = B_{\text{A}} + B_{\text{I}}$$

$$\frac{\text{d}B_{\text{A}}}{\text{d}t} = k_{\text{A}}[D]m^3hj(1 - B_{\text{A}} - B_{\text{I}}) - l_{\text{A}}B_{\text{A}}e^{-zVF/RT}$$

$$\frac{\text{d}B_{\text{I}}}{\text{d}t} = k_{\text{I}}[D](1-h)(1 - B_{\text{A}} - B_{\text{I}}) - l_{\text{I}}B_{\text{I}}e^{-zVF/RT}$$

where B_{T}, B_{A}, are B_{I} are the total, activated-state and inactivated-state fraction block, respectively, k_{x} and l_{x} are the binding and unbinding rate constants for state x, respectively, m is the Na^+ channel activation gate, h and j are the fast and slow inactivation gates, respectively and V is the transmembrane potential. The Hodgkin-Huxley equation for I_{Na} is modified as follows to introduce the effect of the drug

$$I_{\text{Na}} = g_{\text{Na}}(1 - B_{\text{A}} - B_{\text{I}})m^3hj(V - E_{\text{Na}})$$

where g_{Na} is the Na^+ channel maximal conductance, E_{Na} is the Na^+ Nernst equilibrium potential and the other parameters are as previously defined. The guarded-receptor model has the advantage of reproducing a wide range of experimental observation without the need of

modifying the Na^+-channel inactivation gate dynamics, as is the case with the modulated-receptor model. (117).

1.6 Thesis Rationale

Cardiac arrhythmias are disorders of the electrical system of the heart, an often clinically-challenging group of disorders. Despite major advances in our understanding of the molecular basis of AF, the most common arrhythmia in the general population, currently available AADs are older molecules with sub-optimal operational characteristics. The complex non-linear nature of the cardiac action potential and emergent dynamics in anatomically-extended substrates make it difficult to rationally predict the effect of modulation of ion channels on arrhythmia dynamics. Mathematical modeling is a promising tool to help in studying the complex effects of pharmacological modulation of ion channel properties and assist in the development of optimized antiarrhythmics for the treatment of AF, a major unmet need in clinical medicine. The main objective of the thesis is to apply computational approaches to the understanding of the consequences and opportunities that derive from ion channel properties, especially as they relate to AF-selective AAD development.

Sodium-channel blockers (NCBs) are commonly-used antiarrhythmic agents for the treatment of AF. Currently-available NCBs have modest anti-AF efficacy and non-trivial proarrhythmic potential, limiting their clinical usefulness. The electrophysiological effect of I_{Na} blockade are non-linear and highly dependent on the NCB pharmacodynamic properties. In other words, how the drug interacts with the Na^+ channel determines its anti- and pro-arrhythmic profile. The main hypothesis of the first paper of this thesis is that the pharmacodynamic properties of a NCB can be optimized to maximize the drug's anti-AF efficacy while minimizing ventricular proarrhythmia risk.

Virtually all AADs interact with more than one ion channel species. For example, amiodarone, the most commonly-used antiarrhythmic drug, interacts with almost all ion channels. The electrophysiological effects of multi-channel blockade are highly non-linear and therefore difficult to predict. On the basis of the known effects on cardiomyocyte

electrophysiological properties of single-channel blockade, it is conceivable that specific multi-channel blocking combinations will have synergistic, neutral or even antagonistic antiarrhythmic properties. Mathematical models offer a unique opportunity to gain further insight into the dynamics of multi-channel blockade as an anti-AF strategy. The main hypothesis of the second paper of this thesis is that K^+-channel blockade (KCB) will have a synergistic AF-selective effect in combination with an optimized NCB. Understanding the dynamics of multi-channel blockade is crucial for the rational development of effective and safe antiarrhythmic agents.

The ultra-rapid delayed-rectifier K^+ current (I_{Kur}) is an attractive antiarrhythmic target for AF rhythm-control as it is only expressed in atrial cardiomyocyte, therefore circumventing the ventricular proarrhythmic effects of K^+-channel block-induced APD-prolongation. However, I_{Kur} has been shown (i) to inactivate at depolarized potentials [such as during rapid activation] and (ii) to be significantly downregulated in the setting of AF-induced electrical remodeling, potentially limiting the antiarrhythmic effects of I_{Kur} block. Moreover, currently-available mathematical models for I_{Kur} fail to reproduce the experimentally-observed channel inactivation dynamics. The main hypothesis of the third paper of this thesis is that I_{Kur} inactivation and AF-induced downregulation affect I_{Kur}-block anti-AF effects. To this end, we developed a new mathematical model of I_{Kur} with realistic inactivation properties and studied the effect of electrical remodeling on I_{Kur}-block antiarrhythmic properties.

Cardiac fibroblasts outnumber cardiomyocytes and play important roles in normal cardiac function. They also contribute to the pathogenesis of AF, in part by inducing conduction heterogeneity in the atrial substrate and anchoring reentrant circuits and there is evidence that they can affect cardiomyocyte electrophysiology via direct electrical coupling. More recently, fibroblasts have been shown to express ion channels with potentially significant electrophysiological properties. The main hypothesis of the fourth paper is that cardiac fibroblast ion-currents are subject to heart failure-induced remodeling, similar to their cardiomyocyte counterparts, and that this remodeling can affect atrial arrhythmogenesis via cardiomyocyte-fibroblast electrical coupling.

The various components of this thesis work in consort to test the overarching hypothesis that mathematical modeling of atrial ion channel function and remodeling can be used to gain

new insights into the determinants of AF maintenance and antiarrhythmic drug efficacy, thereby providing a potentially powerful approach to designing new antiarrhythmic strategies.

Chapter 2. The Pharmacological Determinants of Na^+-Channel Blockers Atrial Fibrillation-Selectivity

Atrial fibrillation is the most common cardiac arrhythmia in the general population. Currently available AADs for AF rhythm-control have limited efficacy and significant proarrhythmic side-effects. Most Na^+-channel blockers have state-dependent properties, that is that they have differential affinities for the channel in its different conformations (resting vs activated vs inactivated). In this paper, we explored the hypothesis that is possible to optimize a Na^+-channel blocker pharmacological properties to maximize its antiarrhythmic effects while minimizing proarrhythmia. In other words, we investigated the relationship between the drug's binding and unbinding rate-constant, antiarrhythmic efficacy and AF-selectivity.

2.1 In Silico Optimization of Atrial Fibrillation-Selective Sodium Channel Blocker Pharmacodynamics

Martin Aguilar-Shardonofsky, Vigmond Edward, Philippe Comtois and Stanley Nattel

Biophys J. 2012;102:951-960.

2.1.1 Abstract

Atrial fibrillation is the most common type of clinical arrhythmia. Currently available anti-AF drugs are limited by only moderate efficacy and an unfavorable safety profile. Thus, there is a recognized need for improved antiarrhythmic agents with actions that are selective for the fibrillating atrium. State-dependent Na^+-channel blockade potentially allows for the development of drugs with maximal actions on fibrillating atrial tissue and minimal actions on ventricular tissue at resting heart rates. On this study, we applied a mathematical model of state-dependent Na^+-channel blocking (class I antiarrhythmic drug) action, along with mathematical models of canine atrial and ventricular cardiomyocyte action potentials, AF and ventricular proarrhythmia, to determine the relationship between their pharmacodynamic properties and atrial-selectivity, AF-selectivity (atrial Na^+-channel block at AF rates versus ventricular block at resting rates), AF-termination effectiveness, and ventricular proarrhythmic properties. We found that drugs that target inactivated channels are AF-selective, whereas drugs that target activated channels are not. The most AF-selective drugs were associated with minimal ventricular proarrhythmic potential and terminated AF in 33% of simulations; slightly less AF-selective agents achieved termination rates of 100% with low ventricular proarrhythmic potential. Our results define properties associated with AF-selective actions of class-I antiarrhythmic drugs and support the idea that it may be possible to develop class I antiarrhythmic agents with optimized pharmacodynamic properties for AF treatment.

2.1.2 Introduction

Atrial fibrillation is the most common type of sustained cardiac arrhythmia (118). AF is associated with reduced quality of life and increased morbidity and mortality (119).

Antiarrhythmic drugs have long been used to treat AF (118), but the use of antiarrhythmic agents has markedly decreased because of limited drug efficacy and the risk of serious complications, particular ventricular proarrhythmia (29, 119-121). In animal and mathematical models, Na^+-channel blockers terminate AF by modulating the excitable gap and promoting the extinction of arrhythmia-maintaining rotors (122-124); however, they can also increase arrhythmic mortality (74). Recent experimental data suggest that Na^+-channel blockers can be atrial-selective (125, 126), causing minimal ventricular effects. Thus, there is a strong interest in the development of AF-selective antiarrhythmic drugs with optimized efficacy and safety profiles (120).

We hypothesized that we could maximize the atrial antiarrhythmic properties of Na^+-channel blockers and minimize their proarrhythmic potential by identifying pharmacodynamic parameters optimized for selective action on atrial tissue during AF. In this work, we address the question of how the Na^+-channel blocking kinetics influences atrial selectivity and the rate dependence of block, anti-AF efficacy, and ventricular proarrhythmic potential.

2.1.3 Materials and Methods

2.1.2.1 Guarded-receptor model

To simulate state-dependent sodium current (I_{Na}) block, we used the guarded-receptor model, in which a voltage-sensitive channel gate restricts drug access to and from a constant-affinity channel-binding site (117). We assumed that the Na^+-channel blocker could bind the Na^+-channel during either the activated (A) or inactivated (I) state. The drug's binding and unbinding kinetics are described by first-order transitions, with k_A and k_I being binding rate constants from activated and inactivated states, respectively, and l_A and l_I corresponding to the unbinding rate constants (Fig. 9). We computed the fraction of channels blocked in activated or inactivated states (B_A and B_I, respectively) using the following equations:

$$I_{\mathrm{Na}} = g_{\mathrm{Na}}(1 - B_{\mathrm{A}} - B_{\mathrm{I}})m^3hj(V - E_{\mathrm{Na}})$$

$$\frac{\mathrm{d}B_{\mathrm{A}}}{\mathrm{d}t} = k_{\mathrm{A}}[\mathrm{D}]m^3hj(1 - B_{\mathrm{A}} - B_{\mathrm{I}}) - l_{\mathrm{A}}B_{\mathrm{A}}e^{-\mathrm{zVF/RT}}$$

$$\frac{\mathrm{d}B_{\mathrm{I}}}{\mathrm{d}t} = k_{\mathrm{I}}[\mathrm{D}](1-h)(1-B_{\mathrm{A}}-B_{\mathrm{I}}) - l_{\mathrm{I}}B_{\mathrm{I}}e^{-\mathrm{zVF/RT}}$$

where g_{Na} is the Na^+ conductance; B_{A} and B_{I} are the fractional activated- and inactivated-state blocks, respectively, m is the activation variable; h and j are inactivation variables; V is the membrane potential; E_{Na} is the Na^+ equilibrium potential; z is the drug charge; F is Faraday's constant; R is the universal gas constant; T is the temperature; and [D] is the drug concentration (117). We assumed that z = 0 (uncharged drug) for the main analysis, but also considered a positively charged molecule (z = +1) in the single-cell analyses. We studied a wide range of binding and unbinding characteristics at a drug concentration of 60 μM.

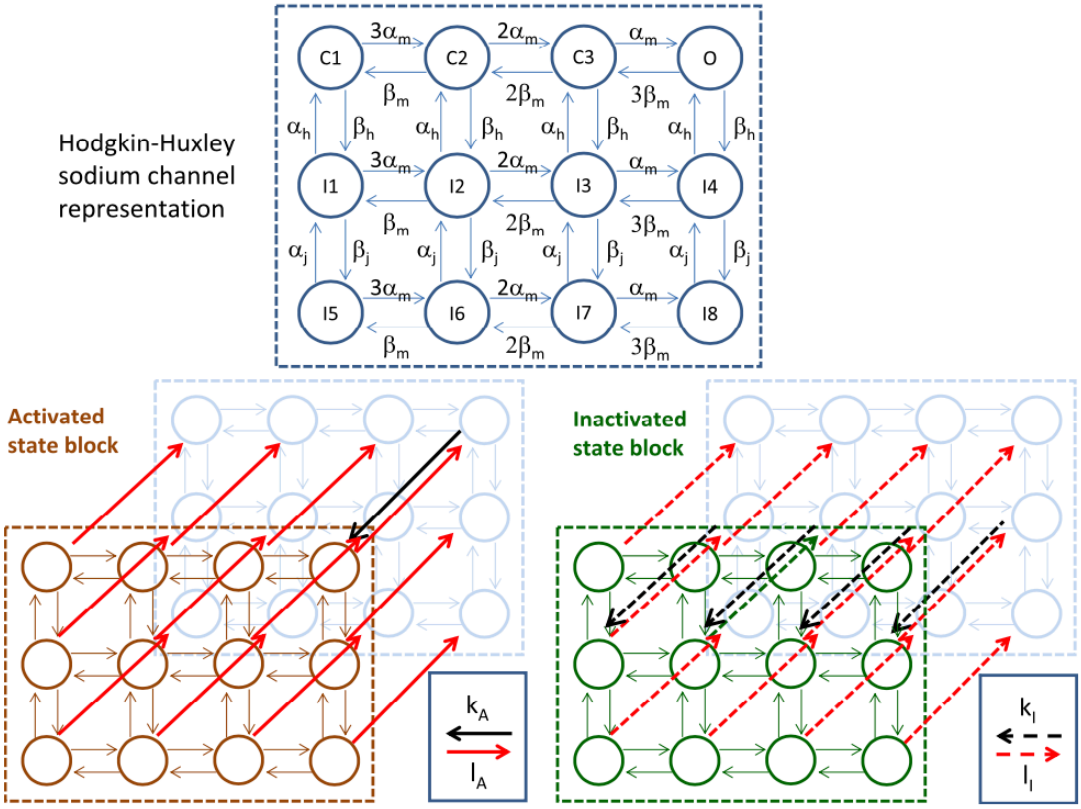

Figure 9. Schematic representation of the guarded-receptor model of Na^+-channel-blocking action. Transitions between the closed, activated (A), and inactivated (I) states are governed by Hodgkin-Huxley equations with rate constants α_x and β_x. Transitions between unblocked and blocked states are governed by binding-rate constants, k_{A} and k_{I}, and unbinding-rate constants, l_{A} and l_{I}.

2.1.2.3 Single-cell simulations

The Ramirez-Nattel-Courtemanche (RNC) ionic model of atrial cardiomyoctes (127) and the Hund-Rudy (HRd) ionic model of ventricular cardiomyocytes (128) were implemented.

The total ionic current for the RNC model ($I_{ion,RNC}$) is

$$I_{ion,RNC} = I_{Na} + I_{K1} + I_{to} + I_{Kur,d} + I_{Kr} + I_{Ks} + I_{Ca,L} + I_{ClCa} + I_{K,ACh} + I_{pCa} + I_{NaCa} + I_{NaK} + I_{b,Na} + I_{b,Ca} + I_{b,Cl}$$

where I_{K1}, I_{to}, $I_{Kur,d}$, I_{Kr}, I_{Ks}, and $I_{K,ACh}$ are the inward rectifier, treansient outward, ultrarapid delayed rectifier, rapid and slow delayed rectifiers, and acetylcholine (ACh)-activated K^+ currents respectively; $I_{Ca,L}$ is the L-type Ca^{2+} current; I_{ClCa} is the Ca^{2+}-activated Cl^- current; I_{pCa} is the Ca^{2+} pump current; I_{NaCa} is the Na^+/Ca^{2+} exchange current; I_{NaK} is the Na^+/K^+ pump current; and $I_{b,Na}$, $I_{b,Ca}$, and $I_{b,Cl}$ are the background Na^+, Ca^{2+}, and Cl^- currents, respectively (47).

The total ionic current for the HRd model ($I_{ion,HRd}$) is

$$I_{ion,HRD} = I_{Ca,t} + I_{Na,t} + I_{K,t} + I_{Cl,t}$$

With

$$I_{Ca,t} = I_{Ca,L} + I_{b,Ca} + I_{pCa} - 2I_{NaCa}$$

$$I_{Na,t} = I_{Na} + 3I_{NaK} + I_{CaNa} + 3I_{NaCa} + I_{Na,L}$$

$$I_{K,t} = I_{Ks} + I_{Kr} + I_{K1} + I_{CaK} + I_{to1} + I_{to2} - 2I_{NaK}$$

$$I_{Cl,t} = I_{to2} + I_{b,Cl}$$

where I_{CaNa} is the Na^+ current thought the L-type Ca^{2+} channel, $I_{Na,L}$ is the slowly inactivating late Na^+ current, I_{CaK} is the Ca^{2+}-dependent K^+ current, I_{to1} is the 4AP-sensitive transient outward K^+ current, and I_{to2} is the Ca^{2+}-dependent transient outward Cl^- current (with other terms as defined above) (128).

RNC and HRd cardiomyocytes at 37^{oC} were stimulated at 1 Hz (sinus rhythm frequency) and 6 Hz (AF equivalent frequency) for 3 min for each set of rate constants by numerical integration with MATLAB ODE23s ordinary differential equation solver (The MathWorks, Natick, MA). The stimuli were 30 pA/pF 2-ms square pulses. A Na^+-channel blocker was added after 1 min and the drug effect was quantified based on a reduction in peak I_{Na} ($B_{ss} = I_{Na,CTL} -$

$I_{Na,drug}$ / $I_{Na,CTL}$). We changed the rate constants one at a time to study the effect of each parameter. For a fixed set of k_A and k_I, l_A and l_I were varied from 10^{-7} to 10^{0} ms^{-1} in $10^{0.5}$ ms^{-1} intervals, generating 225 simulations for each k_A-k_I combination. The binding rate constants were then varied over k_A-k_I parameter space (k_A = {10^0, 10^1, 10^2, 10^3, 10^4, 10^5} $ms^{-1}mol^{-1}$, and k_I = {1, 20, 100, 500, 2500} $ms^{-1}mol^{-1}$) and for each k_A-k_I combination, l_A and l_I were varied, generating 4500 simulations each for the atrial cell paced at 1 Hz, the atrial cell paced at 6 Hz, and the ventricular cell paced at 1 Hz (for a total of 13,500 single-cell simulations). Rate-constant combinations with B_{ss} < 50% were excluded from optimization because at least 50% Na^+-channel blockade is required for AF termination (124).

We defined rate-selectivity as the ratio of B_{ss} in an atrial cell paced at 6 Hz and an atrial cell paced at 1 Hz (B_{ss} atrial 6 Hz / B_{ss} atrial 1 Hz). Atrial-selectivity was defined as the ratio of B_{ss} in an atrial cell paced at 1 Hz and a ventricular cell paced at 1 Hz (B_{ss} atrial 1 Hz / B_{ss} ventricular 1 Hz). We defined overall AF-selectivity as the product of rate-selectivity and atrial-selectivity (B_{ss} atrial 6 Hz / B_{ss} ventricular 1 Hz).

We repeated the analysis for four clinically used Na^+-channel blockers (lidocaine, procainamide, ranolazine, and flecainide) with rate constants from the literature over a clinically relevant concentration range, as follows: lidocainde: k_A = 5173 $ms^{-1}mol^{-1}$, k_I 4998 $ms^{-1}mol^{-1}$, l_A = 0.0128 ms^{-1}, and l_I = 0.0384 ms^{-1} (129); procainamide: k_A = 260 $ms^{-1}mol^{-1}$, k_I = 0.0 $ms^{-1}mol^{-1}$, l_A = 0.000058 ms^{-1}, l_I = 0.0 ms^{-1} (130); ranolazine: k_A = 2970 $ms^{-1}mol^{-1}$, k_I = 0.0 $ms^{-1}mol^{-1}$, l_A = 0.0053 ms^{-1}, l_I 0.0 ms^{-1} (126); and flecainide: k_A = 5830 $ms^{-1}mol^{-1}$, k_I = 0.0 $ms^{-1}mol^{-1}$, l_A = 0.31 ms^{-1}, l_I = 0.0 ms^{-1} (131).

2.1.2.4 Ventricular vulnerability simulations

We explored the vulnerable period (VP) and proarrhythmic index (PI) on a one-dimensional (1D) cable of ventricular myocytes as indices of proarrhythmic potential (132). We constructed a 10-cm cable of HRd ventricular myocytes by linking excitable segments with a 250 Ω cm axial resistivity, 100 μm length, and 11 μm radius. We stimulated the cable at 1 Hz at one end to achieve pseudo-steady-state Na^+-channel blockade after Na^+-channel blocker addition.

To measure the VP, we applied a conditioning stimulus (S1) at one end and a 3-cm test stimulus (S2) 3 cm from one end. The VP was the range of S1-S2 delays that caused unidirectional propagation (133). We defined the PI as VP/(CL-RP), where CL is the pacing cycle length and RP is the refractory period (134).

2.1.2.5 Two-dimensional simulations

Two-dimensional (2D) simulations were performed on a 6.5 x 7.0 cm sheet of RNC atrial cells. The tissue contained cardiomyocytes cables (radius 5 μm, resistivity 75 Ω cm coupled by resistors (300 k Ω), length 100 μm, inserted in a brick-wall manner). Fiber resistivity and interfiber resistance values were chosen to match experimental results (47, 135). AF was started by a cross-shock protocol, with S1 applied at one edge and S2 applied on a square area. The ACh effect simulated vagal tone, following a sinusoidal distribution with peak [ACh] of 15 nM, as previously described (47, 124). We refer to the AF that continued for the full simulation (10 s) as sustained AF. Na^+-channel blockers were added at six time points (t_{DRUG} = {948, 974, 1000, 1050, 1065, 1075} ms) for every optimal rate constant combination defined by single-cell optimization, generating 120 simulation (six different t_{DRUG} values for 30 k_A-k_I combinations). Drug efficacy was expressed as the percentage of successful AF terminations for each rate-constant combination.

2.1.2.6 AF-selectivity optimization

We optimized AF-selectivity, the product of rate- and atrial-selectivity, using the single-cell analysis. We identified the l_A-l_I with maximal AF-selectivity ($l_{A,max}$, $l_{I,max}$) for each k_A-k_I combination, yielding 30 (k_A, k_I, $l_{A,max}$, $l_{I,max}$) combinations. We then used this {k_A, k_I, $l_{A,max}$, $l_{I,max}$} set to study AF termination efficacy for each of the 30 (k_A, k_I, $l_{A,max}$, $l_{I,max}$) combinations. The optimized set of binding parameters {k_A, k_I, $l_{A,max}$, $l_{I,max}$} generated little variation in the PIs because the rate-constants combinations had been selected to minimize ventricular actions. We therefore repeated the proarrhythmia analysis by fixing $l_A = 10^{-3}$ ms^{-1} and $l_I = 10^{-2}$ ms^{-1} (optimally AF-selective values in single-cell analysis), and systematically varying k_A and k_I.

2.1.4 Results

2.1.4.1 Selectivity and binding rate constants

We first computed the drug-induced reduction in peak I_{Na} (B_{ss}) as a function of the binding rate constants, l_A and l_I, for a fixed set of binding rate constants, $k_A = 10^4$ ms^{-1}mol^{-1} and $k^I = 20$ ms^{-1}mol^{-1} (Fig. 10, A-C). B_{ss} was frequency-dependent and reached almost 100% at low l_A and/or l_I. The l_A-l_I parameter space for high B_{ss} was largest for the atrial myocyte at 6 Hz, producing a region with B_{ss} that was clearly greater in atrial cells at 6 Hz than at 1 Hz. Fig 10D shows the rate-selectivity, which was greater than unity over a small region of l_A-l_I space. The values for atrial-selectivity were considerable smaller than those for rate-selectivity (Fig. 10E), and is no case exceeded 1.5. AF-selectivity (Fig. 10F) showed a discrete area of large values, with a maximum of 5.8 at $l_{A,max}$ and $l_{I,max}$ of $10^{-3.5}$ ms^{-1} and 10^{-2} ms^{-1}, respectively.

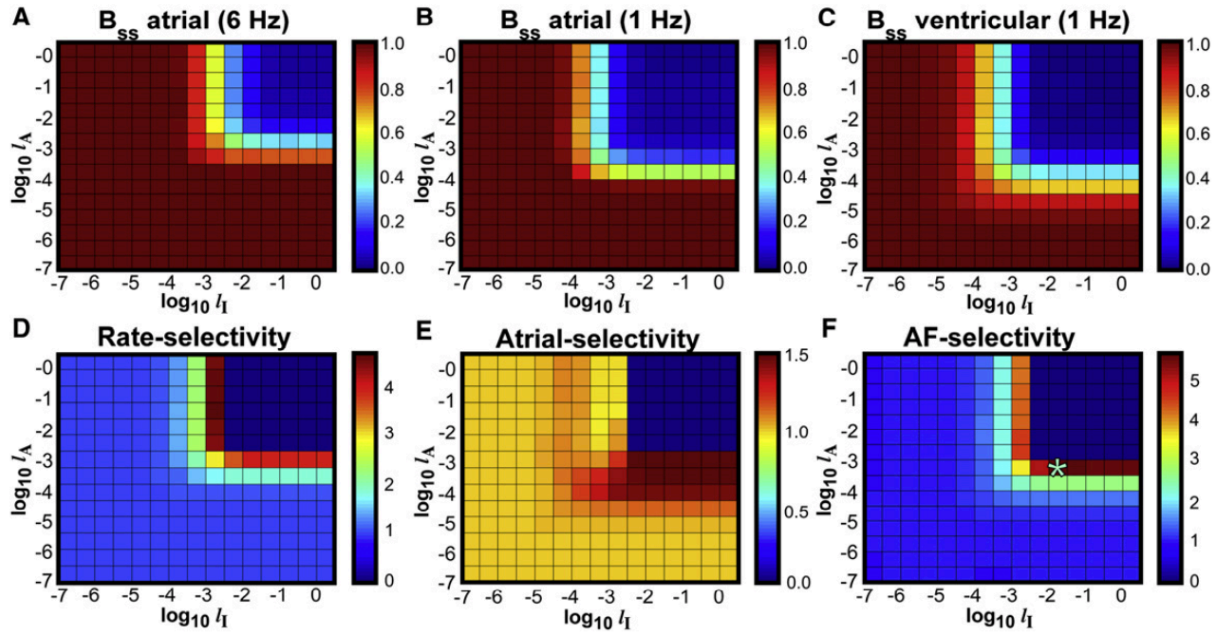

Figure 10. Optimization of l_A and l_I for fixed k_A and k_I. (A-C) Reduction in I_{Na} (B_{ss}) for an atrial myocyte paced at 6 Hz (A) and 1 Hz (B), and a ventricular myocyte paced at 1 Hz (C) as a function of l_A and l_I for $k_A = 10^4$ and $k_I = 20$ ms^{-1}mol^{-1}. (D and E) Rate- and atrial-selectivities. (F) AF-selectivity. Maximum AF-selectivity is shown by the asterisk. Color scales are at the right of each panel.

After examining the role of unbinding (l_A and l_I), we assessed the dependency of block on binding (k_A and k_I). We first defined $l_{A,max}$ and $l_{I,max}$ as the values of l_A and l_I that maximize the AF-selectivity for a fixed k_A and k_I by varying l_A and l_I independently from 10^{-7} to 10^0 ms^{-1} in $10^{0.5}$ ms^{-1} intervals. We defined AF-selectivity$_{max}$ as the AF-selectivity index at ($l_{A,max}$, $l_{I,max}$)

for each k_A and k_I, varying k_A and k_I independently (k_A = {10^0, 10^1, 10^2, 10^3, 10^4, 10^5} $ms^{-1}mol^{-1}$, k_I = {1, 20, 100, 500, 2500} $ms^{-1}mol^{-1}$ to compute AF-selectivity$_{max}$ over k_A-k_I parameter space. Fig. 11, A-C, shows the resulting rate-selectivity, atrial-selectivity, and AF-selectivity$_{max}$. In general, rate-selectivity and AF-selectivity increased with increasing inactivated-state affinity and decreased with activated-state affinity. However, AF-selectivity fell off with increases in k_I beyond a maximum at 500 $ms^{-1}mol^{-1}$. The rate constants with the greatest AF-selectivity (k_A = 1 $ms^{-1}mol^{-1}$, k_I = 500 $ms^{-1}mol^{-1}$, $l_A = l_I = 10^{-2}$ ms^{-1}) had a rate-selectivity of 12.8, atrial-selectivity of 1.93, and AF-selectivity$_{max}$ of 24.6. Fig. 11F shows B_A and B_I as a function of AF-selectivity$_{max}$. High AF-selectivity$_{max}$ values were associated with low B_A and high B_I, confirming preferential targeting of the inactivated state. The l_A and l_I values corresponding to the data in Fig. 11, A-E, are shown in Fig. 11, G and H, with l_A showing more variation that l_I for different k_A-k_I combinations. For comparison, results for four clinical Na^+-channel blockers are shown in Supplemental Table 2.1 in the Supporting Material. Rate-selectivities were highest for low-dose lidocaine and procainamide, with flecainide and ranolazine being the least rate-selective. Atrial-selectivities were relatively low except for ranolazine, which had an atrial-selectivity of ~3 compared with 1.1-1.9 for the other compounds. AF-selectivities ranged from 7.8 to 15.6 for lidocaine, 7.2 to 9.5 for procainamide, 1.0 to 1.1 for flecainide, and 5.2 to 6.6 for ranolazine, and dropped off at higher concentrations for all drugs.

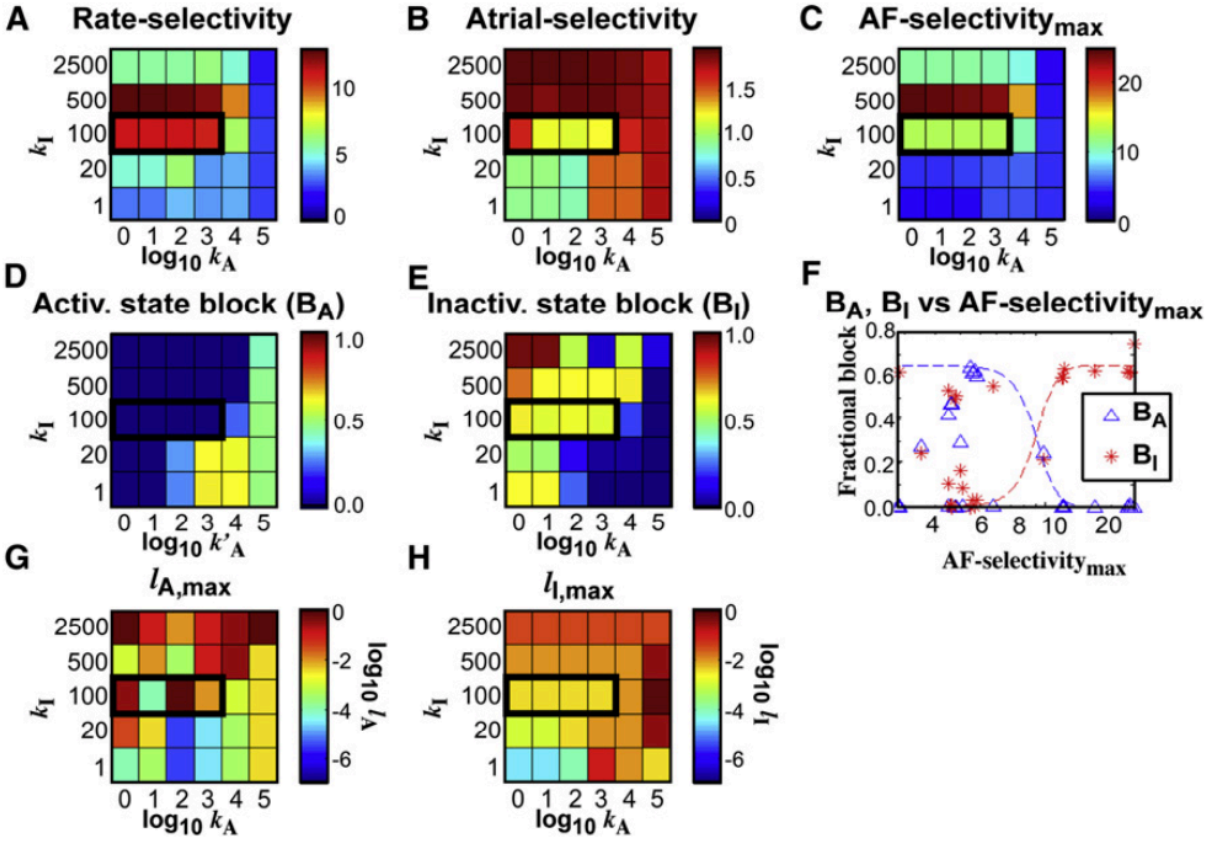

Figure 11. Na^+-channel blocker optimization over k_A-kI space. (A-C) Rate-selectivity, atrial-selectivity, and AF-selectivity$_{max}$ as a function of the binding-rate constants k_A and k_I. (D and E) Fractional block for activated (B_A) and inactivated (B_I) states. (F) Fractional block (B_A and B_I) versus AF-selectivity$_{max}$, with schematic curves (dashed lines). (G and H) Unbinding-rate constants ($l_{A,max}$ and $l_{I,max}$) corresponding to k_A-k_I parameter space. An area of large AF-selectivity (at $k_A = 10^1$-10^3 $ms^{-1}mol^{-1}$ and $k_I = 100$ $ms^{-1}mol^{-1}$) with low proarrhythmic risk and high AF-termination rates (see Figs. 10 and 11) is shown in black boxes.

Finally, because ventricular proarrhythmia can arise at rates higher than normal sinus rhythm, we repeated the simulations and computed atrial-selectivity as the ratio of drug-induced reduction in $I_{Na,max}$ of an atrial cell at 6 Hz versus a ventricular cell at 2.5 Hz (Supplemental Figure 2.1). Optimal AF-selectivity continued to occur with inactivated-state blockers, albeit with a shift in optimal rate constants and a decrease in maximal AF-selectivity.

Fig. 12 shows atrial and ventricular action potentials (A-C), Na^+-current (D-F) and fractional block (G-I) in activated (B_A) and inactivated (B_I) states pre- and postdrug for the optimally AF-selective blocker ($k_A = 10$ ms^{-1}mol^{-1}, $k_I = 500$ ms^{-1}mol^{-1}, $l_A = l_I = 10^{-2}$ ms^{-1}). Effects were largest for the atrial cardiomyocyte at 6 Hz (Fig. 12, A and D). At 6 Hz, activated-state block was almost zero, whereas inactivated-state fractional block varied between 60% and 75% over the cycle (Fig. 12 G). At slower frequencies, inactivated-state block declined to zero over each cycle (Fig. 12, H and I).

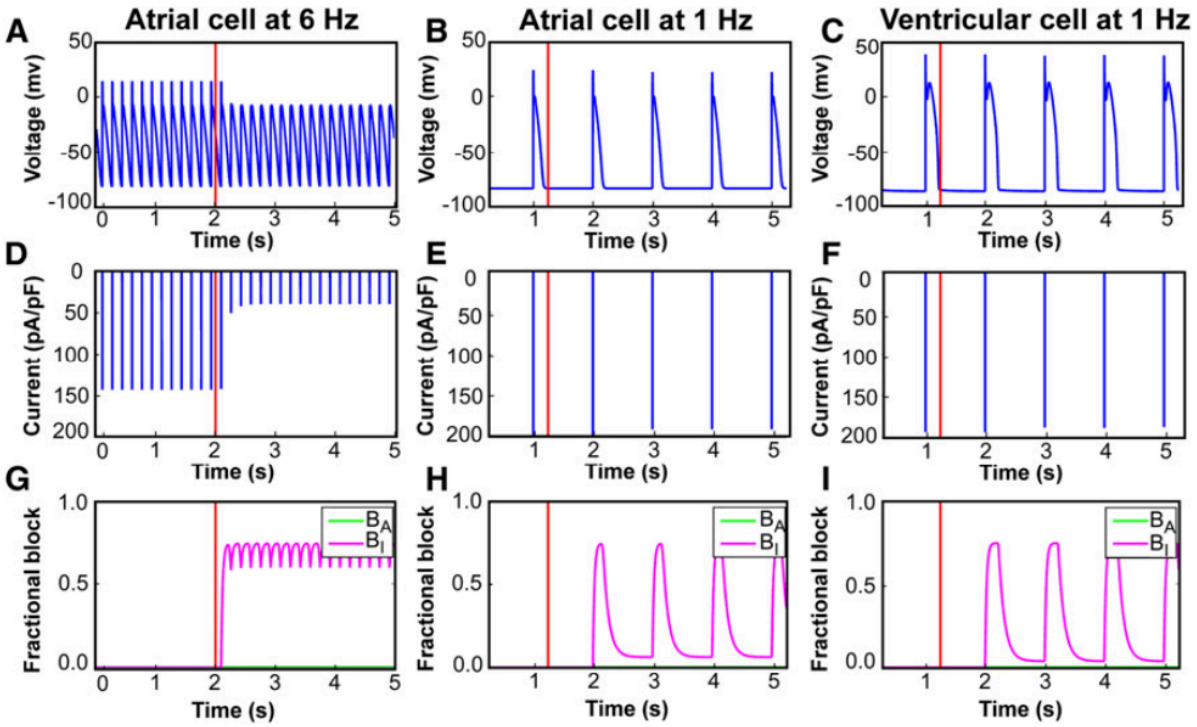

Figure 12. Action potentials, Na^+ current (I_{Na}), and fractional block for the optimally AF-selective Na^+-channel blocker ($k_A = 10$ ms^{-1}mol^{-1}, $k_I = 500$ ms^{-1}mol^{-1}, $l_A = l_I = 10^{-2}$ ms^{-1}). (A-C) Effects on an atrial cell paced at 6 Hz, an atrial cell paced at 1 Hz, and a ventricular cell paced at 1 Hz. In all panels, the vertical red line corresponds to t_{DRUG}, the time at which the drug was added. (D-F) Corresponding values of I_{Na}. (G-I) Fractional block in the activated (B_A, green) and inactivated (B_I, lavender) states. Panels H and I illustrate the temporal dynamics of block: B_I rises sharply just after the action potential upstroke, corresponding with the onset of inactivation. It then reaches a plateau and starts to decrease at the end of the action potential, when the Na^+ channels recover from inactivation. B_A is negligible. The atrial cell paced at 6 Hz

had a much larger B_I then atrial and ventricular cells paced at 1 Hz, because of the reduced unbinding time between action potentials.

We expanded our analysis (Supplemental Figure 2.2) by repeating the single-cell optimization with a positively charged molecule ($z = +1$) instead of a neutral molecule ($z = 0$). Optimal AF-selectivity continued to be associated with higher k_I and lower k_A values, but rate-selectivity and AF-selectivity were higher for the charged molecules, with maximal AF-selectivity = 89.1 vs 24.6 for the uncharged molecule.

2.1.4.2 Ventricular proarrhythmia

We initially analyzed the proarrhythmic potential with the optimized rate constants, but found very little variation in CV and VP (Supplemental Figure 2.3). Because l_A and l_I had been selected to maximize AF-selectivity, ventricular effects were minimized. We therefore repeated the analysis, fixing the unbinding rate constants (l_A, l_I) at optimally AF-selective values ($l_A = 10^{-3}$ ms^{-1} and $l_I = 10^{-2}$ ms^{-1}), varies k_A and k_I, and recomputed CV, VP, and PI. For k_A from 100 to 10^4 ms^{-1}mol^{-1}, CV was preserved, and VP and PI were minimal (Fig. 13, A-C). There was a sharp drop in CV (from ~55 to 39 cm/s) and increase in PI and VP (maximum increase = 55% and 32% respectively) at $k_A = 10^5$ ms^{-1}mol^{-1}. There was little effect of k_I variations on CV, VP, and PI. Fig. 13, D and E, show B_A and B_I at action-potential onsets a function of k_A and k_I. Proarrhythmic regions with increased PI were associated with parameters that preferentially blocked the activated state (high B_A and low B_I). Fig. 13 F shows values of B_A and B_I at action-potential onset as a function of PI, indicating the association with B_A. CV values were little affected by the clinical drugs (Supplemental Table 2.1) except for high-dose flecainide (39.7 cm/s). VP was similarly little affected except for high-dose flecainide (41% increase).

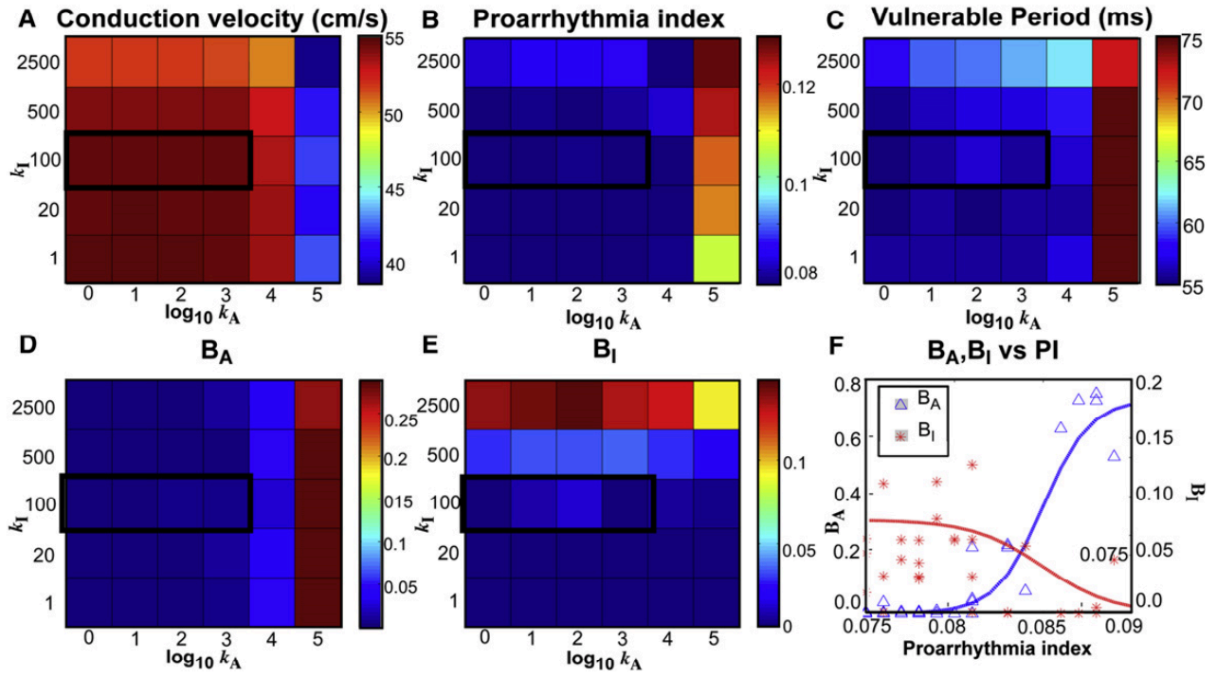

Figure 13. One-dimensional CV as a function of k_A and k_I for Na^+-channel blockers with l_A and l_I fixed at 10^{-3} ms^{-1} and 10^{-2} ms^{-1}, respectively. (B and C) PI and VP for the same parameters. (D and E) Fractional Na^+-channel block for activated (B_A) and inactivated (B_I) states in a ventricular cell at 1 Hz as a function of rate constants k_A and k_I. (F) Fractional block of Na^+ current in a ventricular cell at 1 Hz versus PI, with schematic curves showing that minimally proarrhythmic rate-constant combinations (low index) are associated with inactivated-state blockers, whereas proarrhythmic rate-constants combinations are associated with activated-state block. An area or large AF-selectivity with low proarrhythmic risk and high AF-termination rates is shown in the black boxes in A-E.

Supplemental Figure 2.4 shows blocking dynamics for a cell in the 1D cable for four representative cases. For AF-selective k_A-k_I combinations, inactivated-state effects predominate and activated-state block is negligible, whereas activated-state block was associated with nonselective combinations.

2.1.4.3 AF termination

Termination time was shortest at high k_A and k_I (Fig. 14 A). Termination rates of 100% (Fig. 14 B) were achieved with high k_A, but also with relatively AF-selective regions (AF-selectivity ratio averaging 12.81 ± 0.07) with sub-maximal k_I and low k_A values, in the regions

shown by a black box in Figs. 11, 13, and 14. Parameter combinations in this region produced little conduction slowing (Fig. 13 A) or PI increase (Fig. 13 B). The most AF-selective area was relatively inefficient, terminating only 33% of simulations. For comparison (Supplemental Table 2.1), lidocaine, procainamide, flecainide, and ranolazine terminated 50-67%, 0%, 16-33%, and 33-100% of AFs, respectively, over the concentration range tested. The properties of an agent with maximally AF-selective pharmacodynamics (NCB1) and an agent with submaximal AF selectivity but high AF-termination efficacy (NCB2) are also shown in Supplemental Table 2.1 for reference.

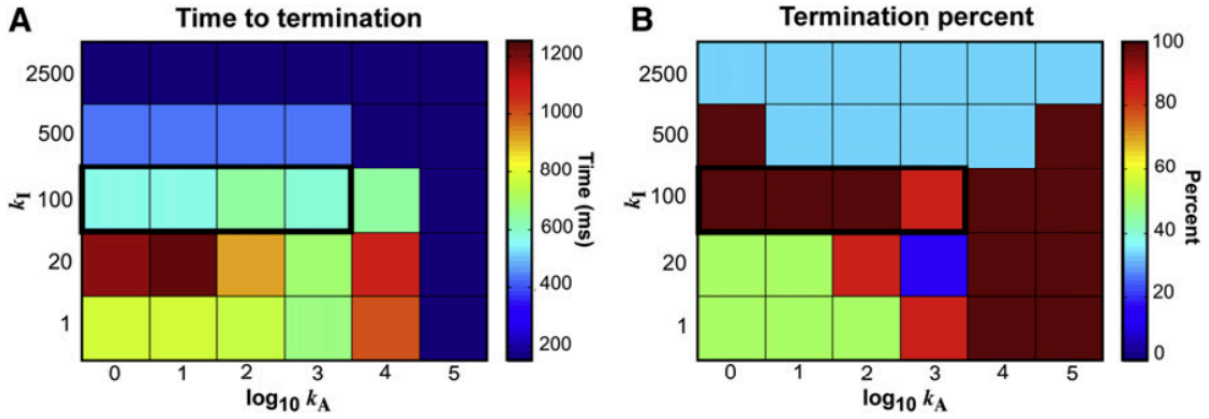

Figure 14. AF time to termination and termination percent for optimized NCBs. (A) Time to termination after Na^+-channel addition on a 2D sheet of atrial cells for the same rate-constant combinations as in Fig. 11. (B) Percentage of successfully terminated AF episodes. The optimally AF-selective area terminated the arrhythmia quickly (average of 429 ms), although the percentage of successfully terminated simulations was lower than in the non-AF-selective region (33 vs. 100%). An area of large AF-selectivity with low proarrhythmic risk and high AF-termination rates is shown in the block boxes (k_A = 10^1-10^3 $ms^{-1}mol^{-1}$; k_I = 100 $ms^{-1}mol^{-1}$).

The AF-termination mechanisms were similar to those observed in previous studies (74, 132). Fig. 15 shows one example. Generators anchored in areas of low ACh concentration ([ACh]) and high action potential duration (APD; Fig. 15 A). Annihilation events terminated the generators but produced counter-rotating wavefronts with new generators (Fig. 15, B and C). Drug block was largest in long-APD areas (Fig. 15 D). The ratio of depolarized cells (R_{APD}) decreased along with the number of generators, leading to termination (Fig. 15, D and E). Fig.

16 shows AF-termination for a slightly less AF-selective but more AF-termination-efficient blocker. The mechanisms of AF-termination are qualitatively similar. A notable difference is the block dynamics, with the less-effective combination in Fig. 15 showing more beat-to-beat variation in B_T (peak-to-trough variation of 0.33) than the more-effective combination in Fig. 16 (peak-to-trough variation 0.07).

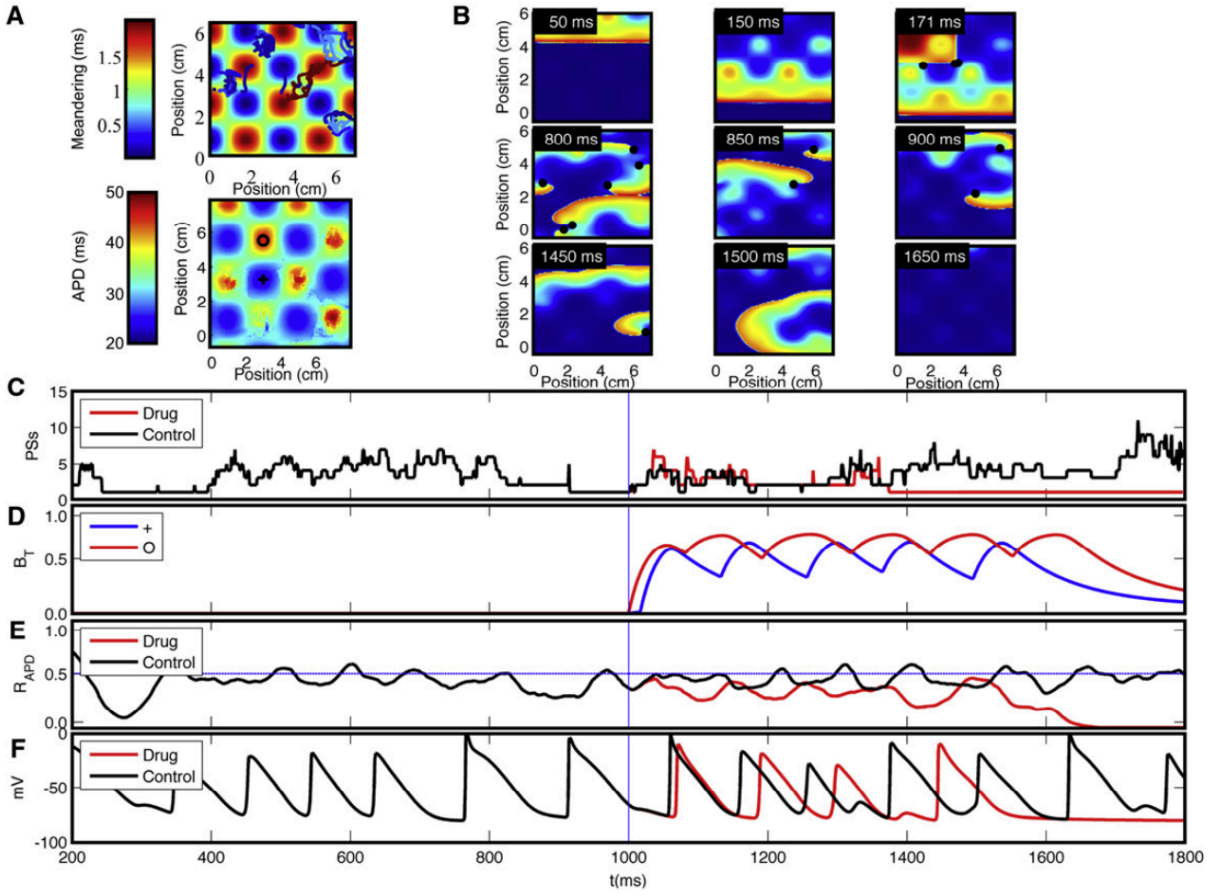

Figure 15. Termination of AF after addition of maximally AF-selective Na^+-channel blocker (AF-selectivity ratio = 23.9, k_A = 10 $ms^{-1}mol^{-1}$, k_I = 500 $ms^{-1}mol^{-1}$, $l_A = l_I = 10^{-2}$ ms^{-1}). (A) Top left: Position of generators from the time of drug application (t_{DRUG} = 1000 ms). Bottom left: Mean APD at -60 mV (APD_{-60}) distribution. (B) Transmembrane potential snapshots of the 2D sheet at time points indicated at the upper left of each frame; black dots denote phase singularities. (C) Number of phase singularities over time in control (black curve) and with drug (red curve). (D) Fraction of Na^+-channels blocked at two sites (positions indicated in A); larger fractional block is in the region with longer APD. (E) Ratio of depolarized cells (R_{APD}) over

time for control (black curve) and with Na^+-channel blockade (red curve). (F) Transmembrane action potentials over time before and after drug addition. Time of drug addition is shown in C-F by a vertical blue line.

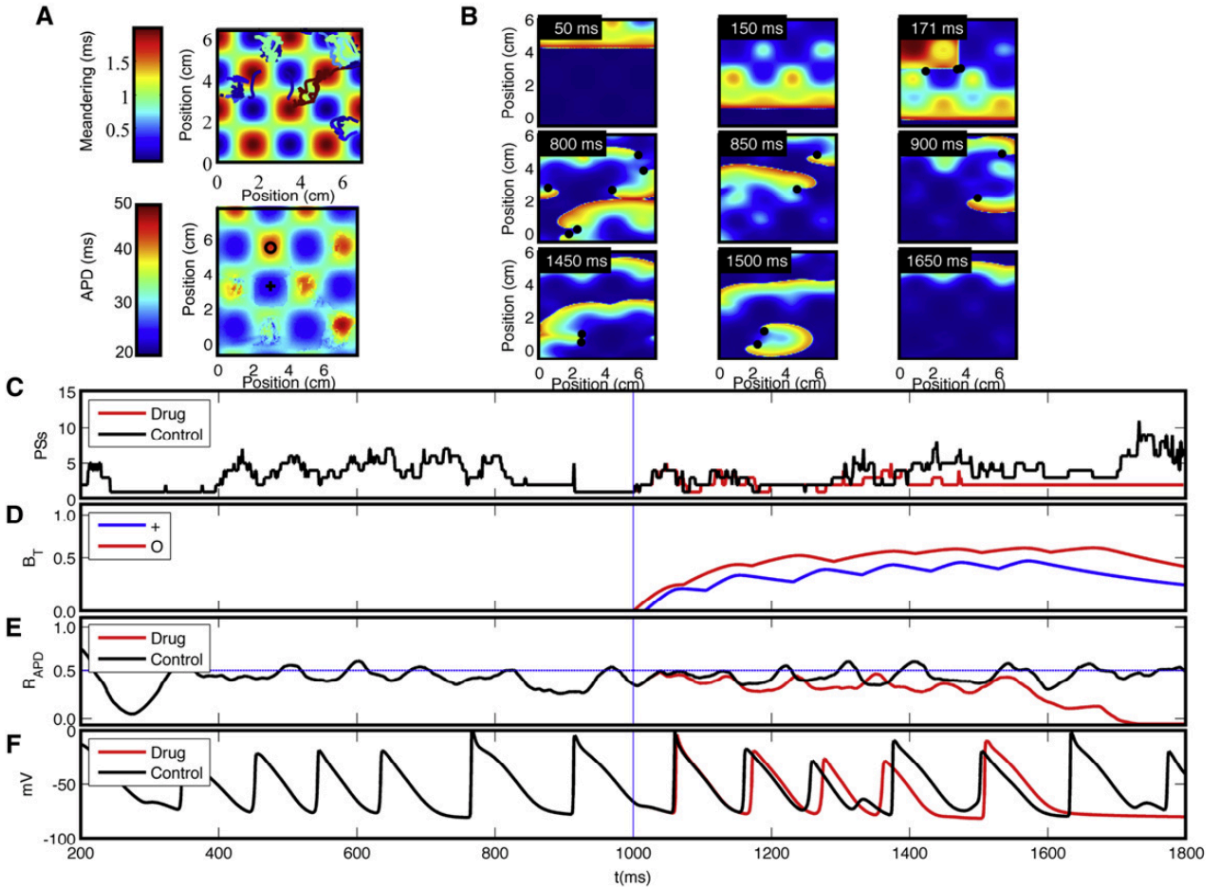

Figure 16. Termination of AF after addition of a slightly less AF-selective but more effective Na^+-channel blocker (AF-selectivity ratio = 12.8, $k_A = 10^2$ $ms^{-1}mol^{-1}$, $k_I = 100$ $ms^{-1}mol^{-1}$, $l_A = 10^0$ ms^{-1}, $l_I = 10^{-2.5}$ ms^{-1}). (A) Top left: Position of generators from the time of drug application (t_{DRUG} = 1000 ms). Bottom left: Mean APD at -60 mV (APD_{-60}) distribution. (B) Transmembrane potential snapshots of the 2D sheet at time points indicated at the upper left of each frame; black dots denote phase singularities. (C) Number of phase singularities over time in control (black curve) and with drug (red curve). (D) Fraction of Na^+-channels blocked at two sites (positions indicated in A); larger fractional block is in the region with longer APD. (E) Ratio of depolarized cells (R_{APD}) over time for control (black curve) and with Na^+-channel blockade (red curve). (F) Transmembrane action potentials over time before and after drug addition. Time of drug addition is shown in C-F by a vertical blue line.

2.1.5 Discussion

Antiarrhythmic drugs currently used for the treatment of AF have limited efficacy and insufficient safety. The potential benefits of sinus rhythm maintenance motivate a search for better antiarrhythmic drugs. Here, we used mathematical models to investigate the relationship between the pharmacodynamic properties of Na^+-channel-blocking antiarrhythmic drugs and their selectivity for atrial cells at rapid rates such as observed during AF versus ventricular cells at sinus rhythm rates. To our knowledge, this is the first study to systematically investigate the AF-selectivity of Na^+-channel blockers as a function of pharmacodynamic properties.

We found that drugs with selective binding affinity for the inactivated state are AF-selective, although selectivity is lost at very high inactivated-state affinities. We defined an optimally AF-selective region associated with maintained CV and low PI, which is relevant because decreased CV facilitates reentrant proarrhythmia (135, 136). We also defined a non-AF-selective region (high k_A) associated with decreased CV and increased PI (Fig. 13).

The optimally AF-selective drug terminated simulated AF in only 33% of cases (NCB1 in Supplemental Table 2.1); however, a slightly less-AF-selective drug had 100% AF-termination efficacy and low proarrhythmic potential (NCB2 in Supplemental Table 2.1). The decrease in AF-selectivity reflects less beat-to-beat unblocking, which was important for AF-termination because, as Na^+-channel block slowed AF, beat-to-beat unblocking became pronounced and prevented termination for the most selective drugs. As tissue excitability decreases, rotor frequency and stability decrease (124, 135); hence, drugs that retain efficacy at lower frequencies are able to destabilize lower-frequency rotors more effectively compared with drugs that are ineffective at lower frequencies.

One important finding is that AF selectivity does not increase monotonically with increasing inactivated-state block. Thus, drug pharmacodynamics may need to be fine-tuned to a narrow range. A possible explanation for this finding is that as k_I increases to very high values, block accumulation at lower frequencies decreases rate-selectivity and AF-selectivity.

According to the classical leading-circle theory, Na^+-channel blockade promotes reentrant arrhythmias by decreasing the wavelength, whereas spiral-wave theory predicts that I_{Na} blockade is antiarrhythmic (137). Previous work showed that a constant reduction in Na^+

current terminated AF by destabilizing AF-maintaining rotors (124). Comtois et al. (135) took this concept one step further by showing that a rapidly unbinding Na^+-channel blocker (lidocaine) terminates AF in a concentration-dependent manner. Here, we expand on that work by considering the relationship between Na^+-channel-binding properties and AF selectivity/efficacy. Irrespective of AF-selectivity, we found that termination occurred by previously described mechanisms, with decreased Na^+-channel availability reducing CV preferentially for wavefront with high radius of curvature, therby decreasing the number of generators, and increasing meandering (122, 124, 135, 138).

To compare our optimized drugs with clinically used Na^+-channel blockers, we repeated our analysis with reported rate constants for lidocaine, procainamide, flecainide, and ranolazine (Supplemental Table 2.1). Lidocaine displayed the highest AF-selectivity, and flecainide displayed the lowest. Flecainide strongly decreased CV and increased VP, consistent with its known proarrhythmic potential (74). Ranolazine was the most efficacious drug and procainamide was the least efficacious, consistent with their reported clinical efficacies (139). In our single-cell analysis, the rate-constant combination with the highest AF-selectivity (NCB1 Supplemental Table 2.1) displayed larger AF-selectivity than the four clinical drugs but limited efficacy. A combination with slightly lower AF-selectivity (NCB2), which was twice as AF-selective as ranolazine, had 100% AF-termination efficacy.

Our findings for ranolazine are in line with the experimental observations of Burashnikov et al. (139). The non-AF-selective drug propafenone terminated vagotonic AF faster and in 100% of experiment (139), consistent with the faster and more efficacious AF-termination by non-AF-selective drugs in our simulations. Our results are also consistent with the idea that increased efficacy for AF-termination can come at the price of increasing proarrhythmic potential: flecainide is effective for AF but has significant proarrhythmic potential (140).

Ranolazine was recently shown to be an atrial-selective open-state blocker instead of an inactivated-state blocker (126). Ranolazine's atrial selectivity is thought to be based on atrial action potential characteristics, such as a more negative steady-state I_{Na} inactivation voltage dependence and gradual phase-3 repolarization, as well as the rapid dissociation kinetics a steep voltage dependence of unbinding from the Na^+ channel (126, 141). Of interest, we found that

ranolazine, with more open-state blocking properties, was more atrial-selective than rate-selective, whereas our optimized inactivated-state blocker was more rate-selective than atrial-selective. This observation points to different mechanisms for atrial- versus rate-selectivity, which may be an interesting avenue to pursue in the future.

Overall, rate-selectivity was the major contributor to AF-selectivity in our pharmacodynamic analysis. Atrial-selectivity at 1 Hz, the ability to block the Na^+ current preferentially in atria over ventricles, ranged around unity. This finding points to a limitation of our modeling: we assumed that the drug affinities for the Na^+ channel in the atria and ventricles were identical. However, recent work suggests that Na^+ channels may differ intrinsically between the atria and ventricles (125). Our findings support recent suggestions that carefully selected class I antiarrhythmic drugs may emerge as a valid AF-selective therapeutic strategy (125, 142).

Moreno et al. (131) recently investigated the in silico proarrhythmic potential of flecainide and lidocaine. Using a Markov model, they reproduced the clinically observed proarrhythmic potential for flecainide and a relatively safe profile for lidocaine, in similarity to what we found here. Of importance, in our study we did not assume any a priori pharmacodynamic properties for the compound under investigation. Instead, we analyzed Na^+-blocking drug for AF-termination and ventricular proarrhythmia as a function of the pharmacodynamic parameter space. Thus, we were able to determine the relationship between Na^+-channel blocking properties and indices of anti-AF efficacy/ventricular proarrhythmia. Our method had the potential to contribute to rational approaches to define optimized Na^+-channel blocker properties for effective AF termination with minimized ventricular proarrhythmic potential. It is now possible, with contemporary drug-design methods, to create candidate agents with Na^+-current blocking kinetics within a predicted range. This then raises the question: What types of pharmacodynamic properties are likely to produce the greatest likelihood of clinical efficacy with the least likelihood of proarrhythmic adverse effects? Our study provides an initial approach for identifying such optimized pharmacodynamic properties.

2.1.5.1 Study limitations

This study has a number of limitations. First, we principally considered an uncharged ($z = 0$) molecule. Use-dependent blockers are usually charged molecules (116). Because our goal in this study was to explore how the binding and unbinding characteristic of Na^+-channel blockers affect drug-selectivity, we did not analyze in detail the role of drug charge. We did repeat the single-cell simulations for a positively charged molecule ($z = +1$; Supplemental Figure 2.2). The results were qualitatively similar to those obtained with the uncharged drugs, except that introduction of charge allowed for greater rate-, atrial-, and AF-selectivity. Further consideration of the charge dependence of AF-selectivity would be an interesting extension of this study.

Second, we considered a single inactivated state for the Na^+ channel. Previous work suggested that the Na^+ channel may have multiple inactivated states, and that transitions between states may not be strictly sequential; for example, a channel could transition not only from the open to the inactivated state after activation, as assumed in our study, but also directly from the resting to the inactivated state without opening (closed-state inactivation) (143). Such features could play important roles in the dynamic interaction between class I antiarrhythmics and the Na^+ channel. However, the fundamental conclusion of our study, i.e., that inactivated-state blockers are optimally AF-selective, would likely be unaffected by the inclusion of multiple inactivated states. If anything, it should be possible to achieve even greater AF-selectivity by optimizing drugs for different inactivated states, an idea that is worthy of further exploration.

Third, we used a squared-pulse stimulus to pace the simulated cells. Although this is a standard stimulus that is widely used in modeling and experimental work, a square pulse does not reproduce the stimulus current shape and amplitude sensed by a cell in situ during in situ propagation, particularly during AF, where the input current waveform would likely be of longer duration and lower amplitude compared with the waveform in normal sinus rhythm. However, our findings correlate well with experimental work, and therefore we believe that our main findings would hold even if we used a more realistic stimulus.

Fourth, we used a 2D sheet with sinusoidal [ACh] variation and nonconducting boundaries to study AF-termination efficacy. This choice has the limitation of introducing geometrical biases to conclusions regarding drug efficacy (144). Indeed, the addition of Na^+-channel blocker increases meandering, leading to rotor termination on boundaries. Full

exploration of this issue would require detailed analyses in accurate 3D models and is beyond the scope of this study. However, we did perform limited 3D simulations in an established model (Supporting Material), which support the main conclusions of the 2D work.

Fifth, ionic drift is an intrinsic component of mathematical action potential models that precludes true steady-state calculations (145). We ran our simulations over a relatively large number of cycles to minimize transient effects, and refer to the final state as the pseudo-steady-state to make this limitation explicit.

Sixth, we used a Hodgkin-Huxley model to simulate drug-channel interactions. However, the choice of ionic model can affect the dynamics of use-dependent block (146). We were unable to identify a canine atrial action potential model based on a Markov model formulation in the literature. Full development of such a model is beyond the scope of this work. Nevertheless, a limited analysis with a ventricular-cardiomyocyte Markov model modified to reproduce our atrial action potentials at 1 and 6 Hz was consistent with our general conclusions (Supporting Material).

Seventh, we based our analysis of inactivated-state block only on interaction with the fast-inactivated state (h). However, it is possible for drugs to interact with the slow-inactivated state represented by j. To assess the impact of the j interaction, we repeated our single-cell simulations with inactivated-state block depending on combined inactivation (hj). Although there were some small quantitative differences, our overall findings remained unchanged (Supporting Material).

Finally, the pathophysiological significance of our measure of ventricular proarrhythmia, the PI, is controversial. We chose the PI because it was previously used to study proarrhythmic drug determinants (134), and it is relatively simple to define and analyze. However, the PI in a cable of normal ventricular cardiomyocytes does not reproduce potentially important components of arrhythmogenic environments in vivo, such as tissue heterogeneity and diseased myocardium, and might therefore underestimate the proarrhythmic potential in our study. It would be interesting in future work to explore the relationship between Na^+-channel blocking pharmacodynamics and more complex and clinically relevant proarrhythmia indices

(e.g., arrhythmia promotion) in geometrically and physiologically realistic simulations (e.g., ischemic conditions).

2.1.6 Conclusions

The development of efficacious and safe antiarrhythmic agents for the prevention and treatment of AF is an important unmet need in clinical medicine. Using realistic mathematical models of atrial and ventricular cardiomyocytes, we found that Na^+-channel blockers targeting the inactivated state are more AF-selective and less proarrhythmic than those targeting the activated state. Our findings may contribute to the effort to optimize class I antiarrhythmic drug state-dependent interactions with Na^+ channels and develop selective, safer, and effective anti-AF agents.

2.1.7 Supplemental Material

2.1.7.1 Three-dimensional simulations

To verify the applicability of our 2-dimensional results to more geometrically-accurate models, we performed 3-dimensional simulations on an anatomically realistic model of canine atria. Briefly, a set of cables representing cardiac fibers was layed out in three dimensions and connected to each other via gap junctions. The left and right atria were connected by three distinct pathways: Bachmann's bundle, the muscular sheath of the coronary sinus, and the rim of the fossa ovalis. The atria measured 4 cm across, approximately canine dimensions. The mono- domain equation was solved with conductivity values resulting in a physiological activation time of 75 ms. Reentry was initiated by applying an ectopic beat to the pulmonary vein region after sinus-activation. Fibrillation was implemented by distributing islands of high [ACh] and allowed to proceed for ≥700 ms before drug application uniformly over the atria.

Reentrant AF in the absence of Na^+ channel blockade is shown in Supplemental Figure 2.5 (first column). The most AF-selective compound did not terminate AF, but reduced the frequency from 7.8 Hz to 4.9 Hz (third column) and created flutter-like activity. Consistent with the 2-dimensional simulations, a slightly less AF-selective drug successfully terminated reentry.

2.1.7.2 Markov model simulations

To compare our Hodgkin-Huxley (HH) model to a Markov (MK) model, we modified a published Na^+-current formulation of a canine ventricular MK model for its action potential properties to fit the properties of our atrial HH model at 1 and 6 Hz (Supp. Fig 2.6). This was done by iteratively scaling the drug-free transition rates to maximize concordance between the HH and MK upstroke at both test frequencies under control condition, i.e. [D] = 0 μM (Supp. Table 2.2). We also removed the background sodium and calcium currents ($I_{b,Na}$ and $I_{b,Ca}$) from the model and considered only binding to the open and inactivated Na^+ channel, as was assumed in our original analysis.

We computed rate-selectivity (B_{ss} atrial 6 Hz / B_{ss} atrial 1 Hz) for the optimized rate constants (k_A, k_I, $l_{A,max}$, $l_{I,max}$; the same rate constants as in Fig. 11) using the HH and MK models (Supp. Fig. 2.7). We found that the rate-selectivities obtained with the HH and MK models correlated to a reasonable extent, with MK selectivities being generally lower than HH selectivities. Supplemental Figure 2.8 shows the drug-induced action potential and I_{Na} changes for the HH and MK models for a representative example ($k_A = 1$ $ms^{-1}mol^{-1}$, $k_I = 2500$ $ms^{-1}mol^{-1}$, $l_A = 10^0$ ms^{-1}, $l_I = 10^{-1.5}$ ms^{-1}), which are in qualitative agreement.

2.1.7.3 Inactivated state block formulation with affinities to both fast and slow inactivation variables

In our main analysis, we defined the time evolution of the inactivated state block (B_I) as

$$\frac{dB_I}{dt} = k_I[D](1-h)(1-B_A-B_I) - l_I B_I e^{-\frac{zVF}{RT}}$$

where B_A and B_I are fractional activated and inactivated state block, h is an inactivation variable, V is membrane potential, E_{Na} is the Na^+ equilibrium potential, z is the drug charge, F is Faraday's constant, R is the universal gas constant, T is temperature, and [D] is drug concentration (3). In this definition B_I depends on the fast inactivation variable h but not the slow inactivation variable j.

To investigate the effect of including the slow inactivation variable *j*, we repeated all of our single cell analysis with B_I depending on the product *hj*

$$\frac{\mathrm{d}B_\mathrm{I}}{\mathrm{d}t} = k_\mathrm{I}[\mathrm{D}](1-hj)(1-B_\mathrm{A}-B_\mathrm{I}) - l_\mathrm{I}B_\mathrm{I}e^{-\mathrm{zVF/RT}}2$$

Supplemental Figure 2.9 shows the action potential (AP) and block variables (B_A, B_I) for the atrial cell paced at 1 and 6 Hz, as well as the ventricular cell paced at 1 Hz, using *h* or *hj* for a representative case. There are negligible differences in AP and block dynamics at 1 Hz pacing for both the atrial and ventricular cells. At 6 Hz, using *hj* led to slightly longer-lasting inactivated- state block, although absolute block values were in the same range as with *h* only, consistent with the idea that including the slow inactivation variable *j* prolongs the period over which the drug can bind to the inactivated state. Overall (Supp. Fig. 2.9), we found that the main observation of our primary analysis, that inactivated-state blockers are optimally AF-selective over a narrow range of k_I values, is unchanged by the use of *hj*, although maximal AF-selectivity was slightly lower with *hj* than with *h* alone.

Supplemental Table 2.1. Rate-, atrial- and AF-selectivity, proarrhythmic potential and termination efficacy for four prototypical Na^+-channel blockers at different concentrations compared to optimized Na^+-channel blocker (NCB). NCB 1 refers to the rate constant combination with the highest AF-selectivity but limited AF-termination efficacy. NCB 2 is a different optimization with lower AF-selectivity but higher termination efficacy (2/6 vs 6/6).

	Control	NCB 1	NCB 2	Lidocaine*		Procainamide			Flecainide		Ranolazine		
Concentration [µM]	0	60	60	10	60	10	60	120	5	30	10	30	60
Rate-selectivity	-	12.8	11.1	8.9	4.1	8.1	5.6	5.1	0.94	0.90	2.2	1.9	1.8
Atrial-selectivity	-	1.9	1.2	1.8	1.9	1.2	1.4	1.4	1.2	1.1	3.0	3.0	2.9
AF-selectivity	-	24.6	13.0	15.6	7.8	9.5	7.8	7.2	1.1	1.0	6.6	5.8	5.2
CV [cm/s]	54.8	54.2	53.9	54.4	52.8	54.7	54.6	54.3	52.2	39.7	54.3	53.7	52.7
VP [ms]	54.7	56.4	57.1	55.1	56.2	54.8	54.9	55.1	58.5	77.2	55.0	56.1	57.9
AF-termination %	-	2/6	6/6	3/6	4/6	0/6	0/6	0/6	1/6	2/6	2/6	6/6	6/6
Average time [ms]	-	579	429	295	223	-	-	-	2327	600	698	961	549

Supplemental Table 2.2. Drug-free transition rates with their corresponding scaling factor for the modified Markov model. The transition rates have been defined previously. The scaling factors have been obtained by an optimization procedure on the drug-free transition rates to maximize concordance between the HH and MK upstroke and other action potential properties at 1 and 6 Hz.

Transition rate	Scaling
α_{11}	1.1158
α_{12}	1.1158
α_{13}	1.1158
β_{11}	2.0153
β_{12}	0.1608
β_{13}	0.7751
α_{2}	0.4706
α_{3}	0.3663
β_{2}	0.6429

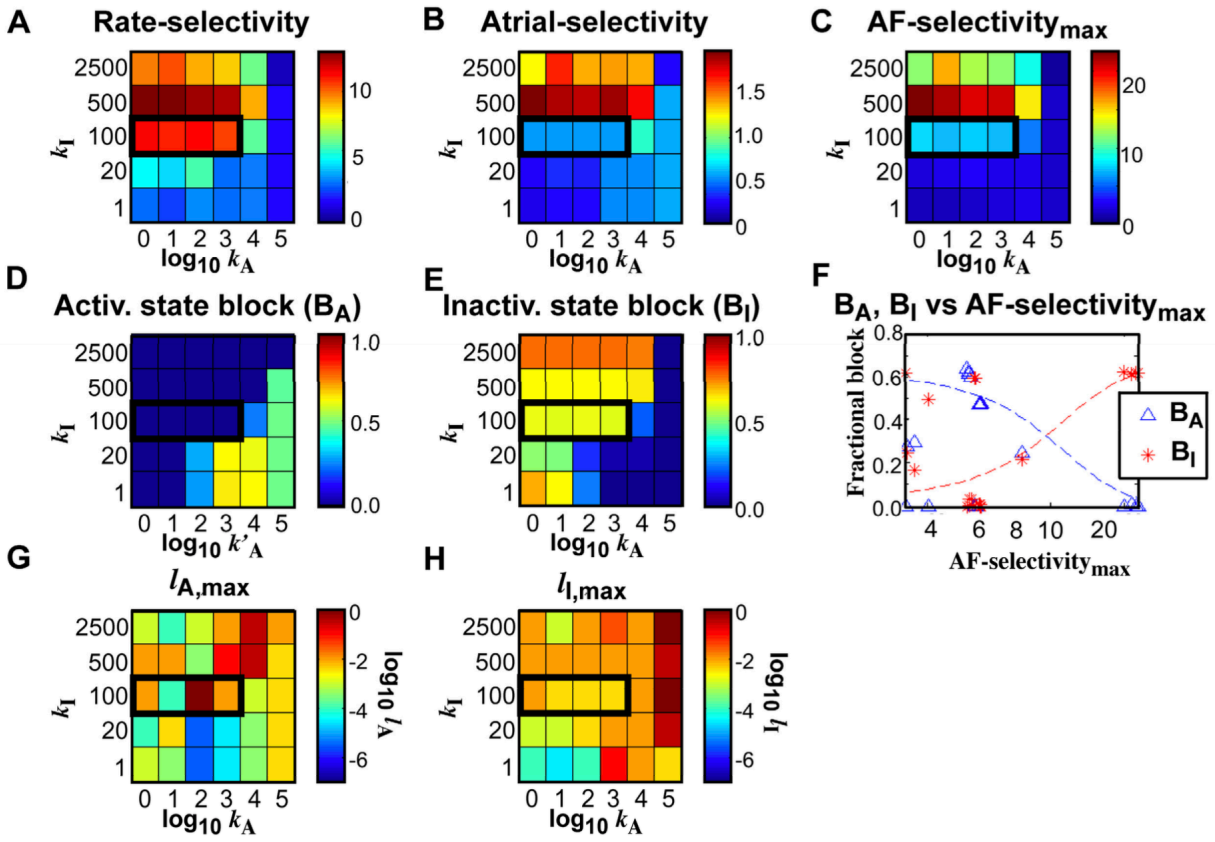

Supplemental Figure 2.1. Atrial-selectivity computed as the ratio of steady-state $I_{Na,max}$ reduction in an atrial cell paced at 6 Hz and a ventricular cardiomyocyte paced at 2.5 Hz. (A to C) Rate-selectivity, atrial-selectivity and AF-selectivity$_{max}$ as a function of the binding rate-constants k_A and k_I. (D to E) Corresponding fractional block for the activated (B_A) and inactivated state (B_I). (F) Fractional block (B_A and B_I) as a function of AF-selectivity$_{max}$, with schematic curves (dashed lines). (G and H) Values for the unbinding rate constants ($l_{A,max}$ and $l_{I,max}$) corresponding to the k_A and k_I values of the panels above. Maximal rate, atrial, and overall AF-selectivity are achieved at low k_A and high k_I. Note that the data points shown as a function of k_A and k_I do not all have the same $l_{A,max}$ and $l_{I,max}$ values, as shown in panels G and H. The area of large AF selectivity with low proarrhythmic risk and high AF termination rates in text Figs 11, 13 and 14 is shown in the black boxes.

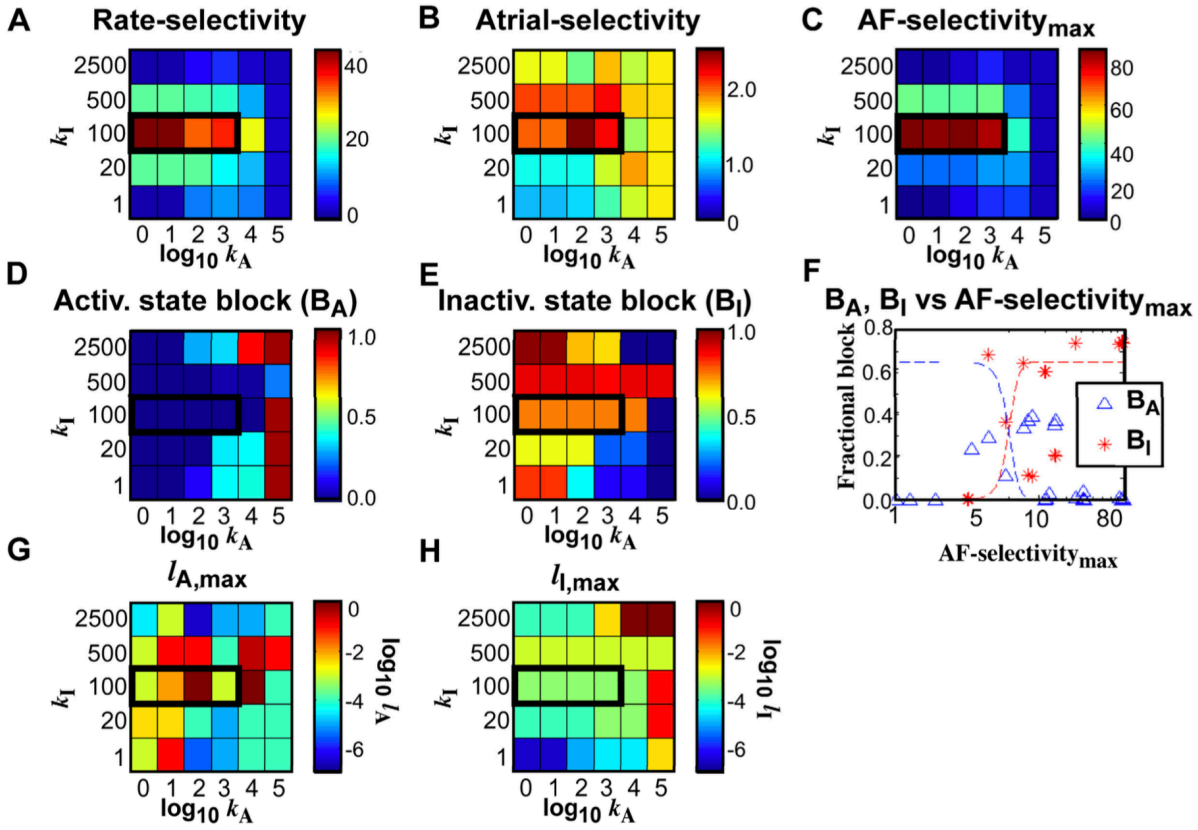

Supplemental Figure 2.2. (A to C) Rate-selectivity, atrial-selectivity and AF-selectivity$_{max}$ as a function of the binding rate-constants k_A and k_I for a positively charged molecule (z = +1). (D to E) Corresponding fractional block for the activated (B_A) and inactivated state (B_I). (F) Fractional block (B_A and B_I) as a function of AF-selectivity$_{max}$, with schematic curves (dashed lines). (G and H) Values for the unbinding rate constants ($l_{A,max}$ and $l_{I,max}$) corresponding to the k_A and k_I values of the panels above. Note that the data points shown as a function of k_A and k_I do not all have the same $l_{A,max}$ and $l_{I,max}$ values, as shown in panels G and H. The area of large AF selectivity with low proarrhythmic risk and high AF termination rates in text Figs 11, 13 and 14 is shown in the black boxes.

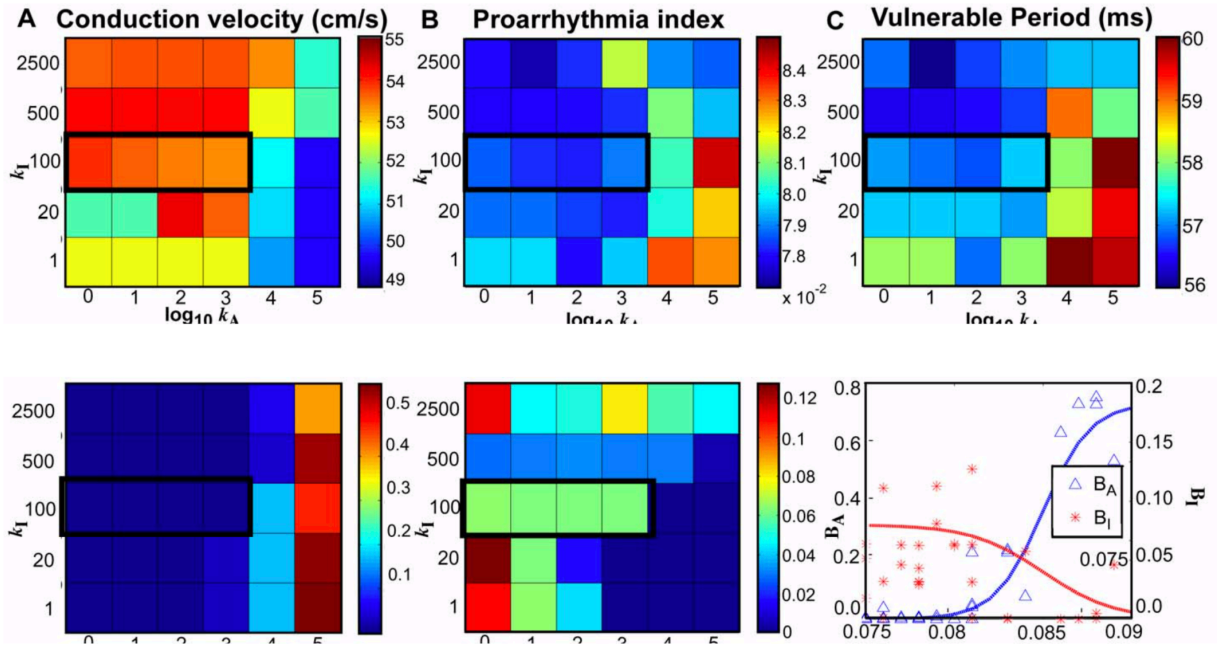

Supplemental Figure 2.3. (A) Conduction velocity on a 1-dimensional cable as a function of k_A and k_I with optimized l_A and l_I after Na^+-channel blocker addition (same rate constant combinations as in Fig. 11). (B-C) Proarrhythmic potential as indicated by the Proarrhythmia Index (PI) and vulnerable period (VP) for the same parameters as in (A). (D-E) Fractional Na^+-channel block for the activated state (B_A), fractional block for the inactivated state (B_I) in a ventricular cell at 1 Hz as a function of the binding rate constants k_A and k_I. (F) Fractional block of Na^+ current in a ventricular cell at 1 Hz as a function of the PI, with schematic curves showing that minimally proarrhythmic rate constant combinations (low index) are associated with inactivated- state blockers whereas the opposite is true for activated-state blockers. Variations in CV, VP and PI are small because these results were obtained with rate constant combinations optimized to minimize ventricular effects. The area of large AF selectivity with low proarrhythmic risk and high AF termination rates in text Figs 11, 13 and 14 is shown in the black boxes.

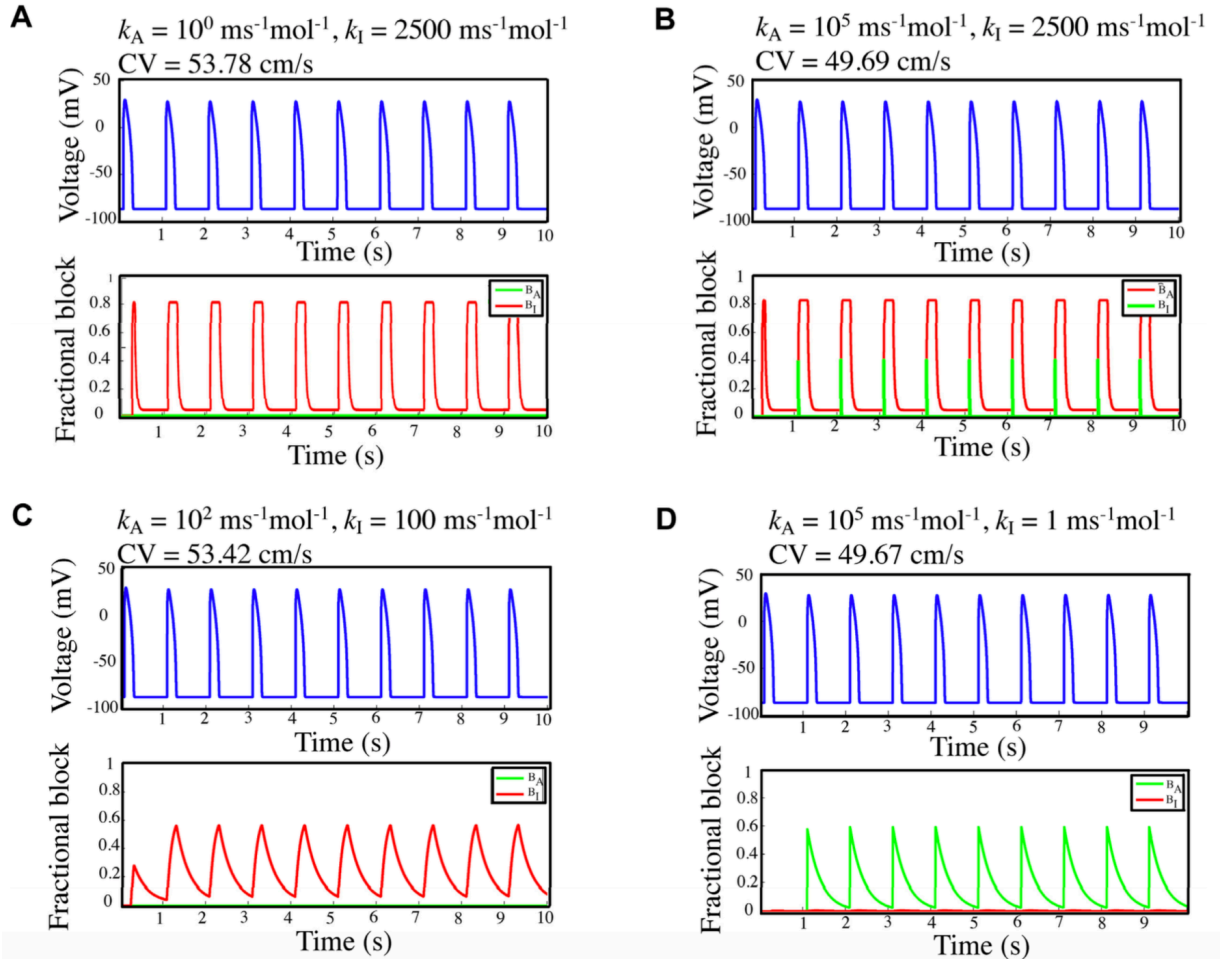

Supplemental Figure 2.4. Transmembrane potential, conduction velocity (CV) and activated- and inactivated-state block dynamics for a cell in the 1-dimensional ventricular-cell cable. (A) Low k_A and high k_I combinations shows negligible activated- state block (green) and slowly increasing inactivated-state effects (red). (B) High k_A and high k_I combination (non-selective) displays significant activated- and inactivated-state effects with almost complete unbinding between stimulation cycles. (C) Optimal combination displays negligible activated-state block but significant inactivated-state effects with near complete drug unbinding between cycles. (D) High k_A and low k_I combinations (non-selective) display significant block during the activated state and negligible inactivated effects.

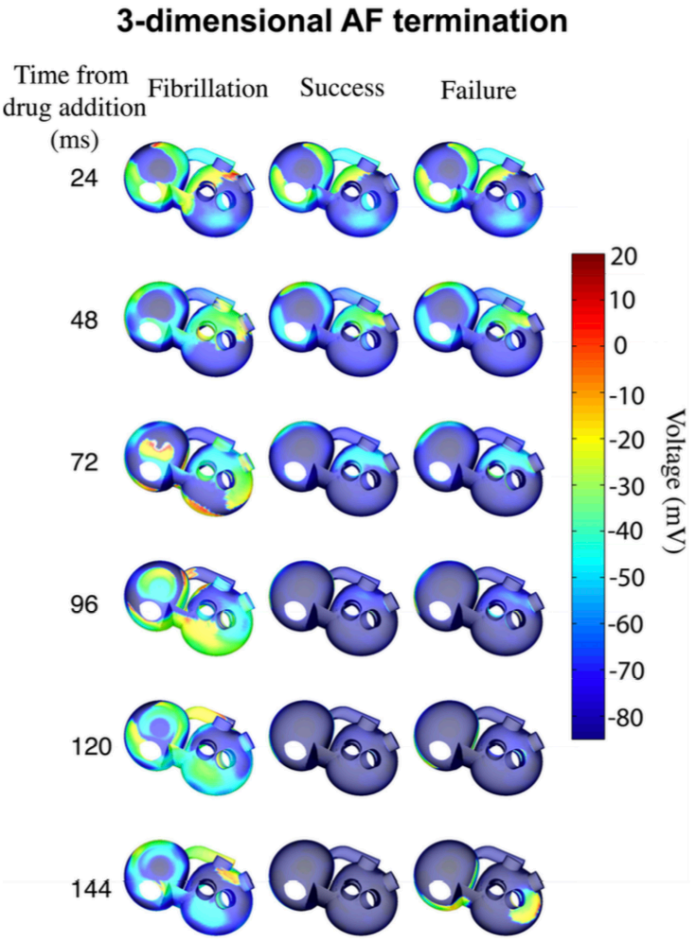

Supplemental Figure 2.5. Three-dimensional AF simulations with color-coded membrane potential at different time-points relative to drug-addition. The first column shows sustained AF in the absence of drug. The second column shows the effect of adding slightly less than optimally AF-selective drug ($k_A = 10^2$ ms^{-1} mol^{-1}, $k_I = 1000$ ms^{-1} mol^{-1}, $l_A = 10^0$ ms^{-1}, $l_I = 10^{-2.5}$ ms^{-1}). The third column shows the effect of adding optimally AF- selective drug ($k_A = 10^1$ ms^{-1} mol^{-1}, $k_I = 500$ ms^{-1} mol^{-1}, $l_A = 10^{-2}$ ms^{-1}, $l_I = 10^{-2}$ ms^{-1}). Consistent with the 2-dimensional simulations, the optimally AF-selective channel blocker (third column) did not terminate the arrhythmia, although it did reduce the reentry frequency. A slightly less AF-selective compound (second column) successfully terminated AF shortly after drug-addition.

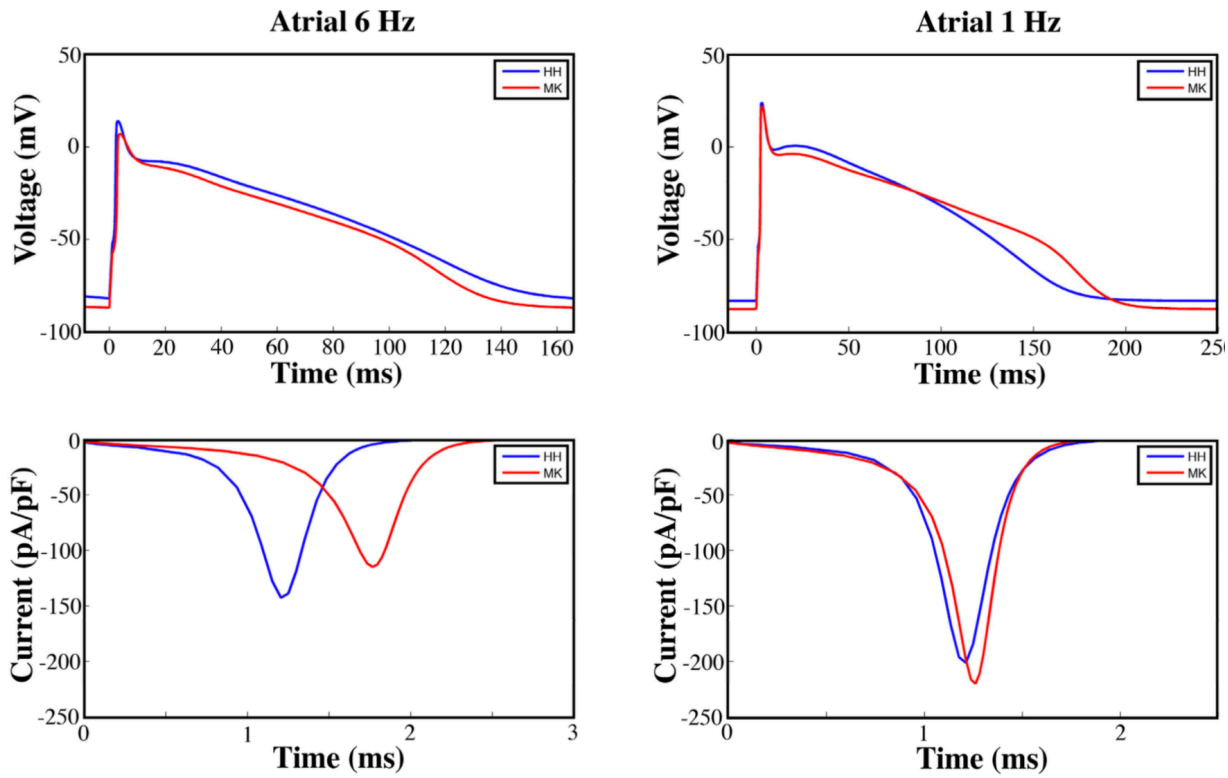

Supplemental Figure 2.6. Action potentials and Na^+ currents at 1 and 6 Hz for the Hodgkin-Huxley (blue) and Markov (red) model under control conditions ([D] = 0 μM). There is reasonably good agreement in action potential morphologies at 1 and 6 Hz, although the 1 Hz MK action potential has a somewhat longer phase 2 than the HH action potential. The Na^+ currents are also in qualitative agreement.

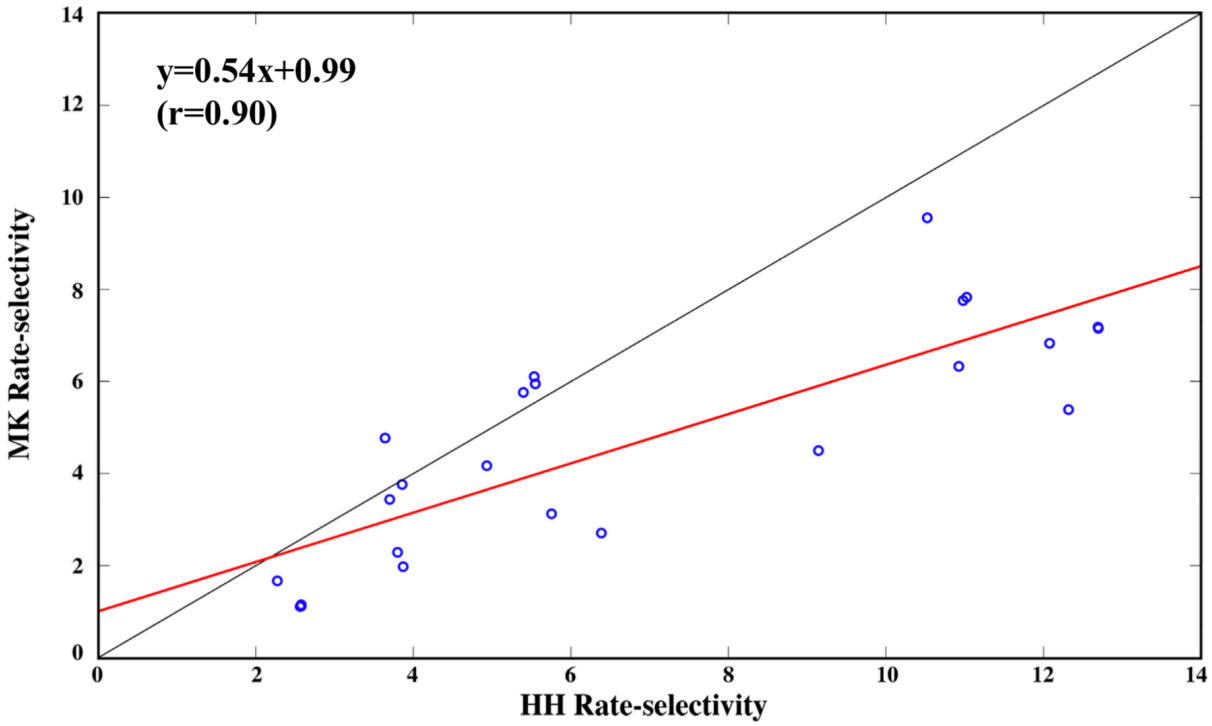

Supplemental Figure 2.7. Rate-selectivities for the optimized rate constants using the Hodgkin-Huxley (HH) versus Markov (MK) model. The red line is a least-squares linear fit of the data. The black line is the line of identity. We found that the rate-selectivities correlate well (r=0.90; r^2=0.66), although Markov selectivities were generally lower than the Hodgkin-Huxley selectivities.

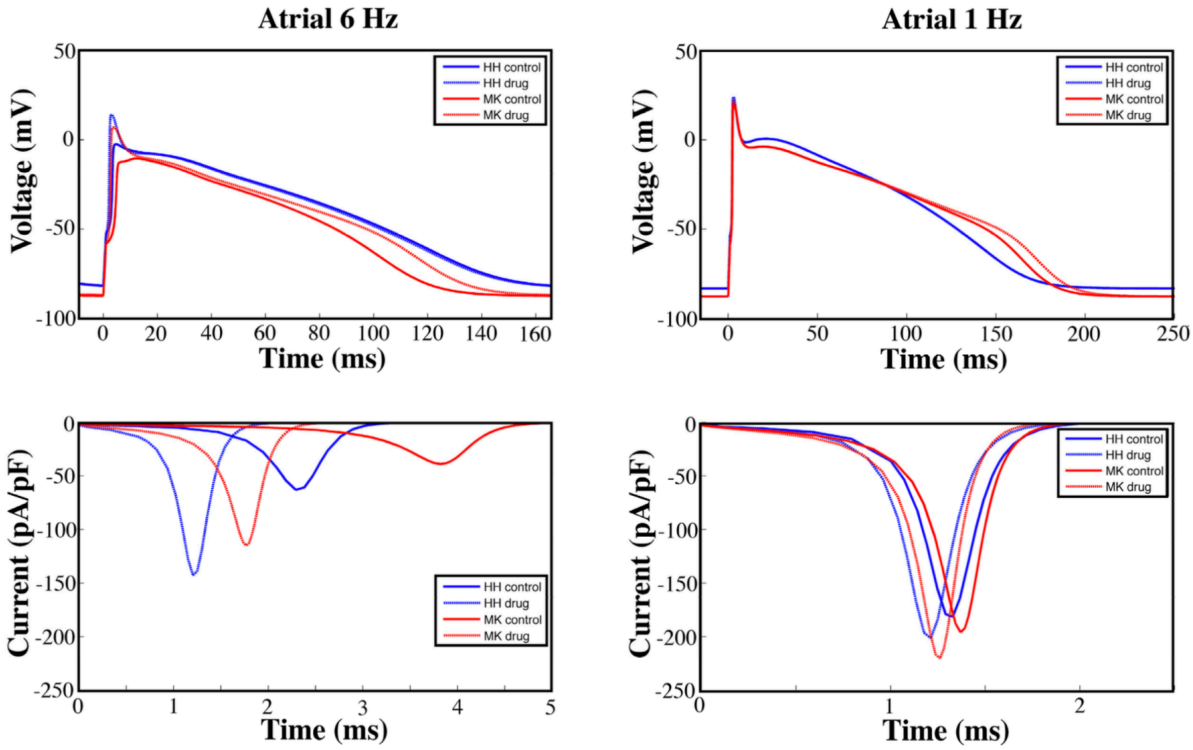

Supplemental Figure 2.8. Drug-induced action potential and Na^+ current changes for the Hodgkin-Huxley (blue) and Markov (red) model for a representative case ($k_A = 1$ $ms^{-1}mol^{-1}$, $k_I = 2500$ $ms^{-1}mol^{-1}$, $l_A = 10^0$ ms^{-1}, $l_I = 10^{-1.5}$ ms^{-1}). The solid curves represent control conditions and the dashed curves are at pseudo-steady-state with a drug concentration of 60 μM. Both the action potential and Na^+ current changes are in qualitative agreement, with a significant drop in $I_{Na,max}$ observed at 6 Hz but relatively minor effect on $I_{Na,max}$ at 1 Hz.

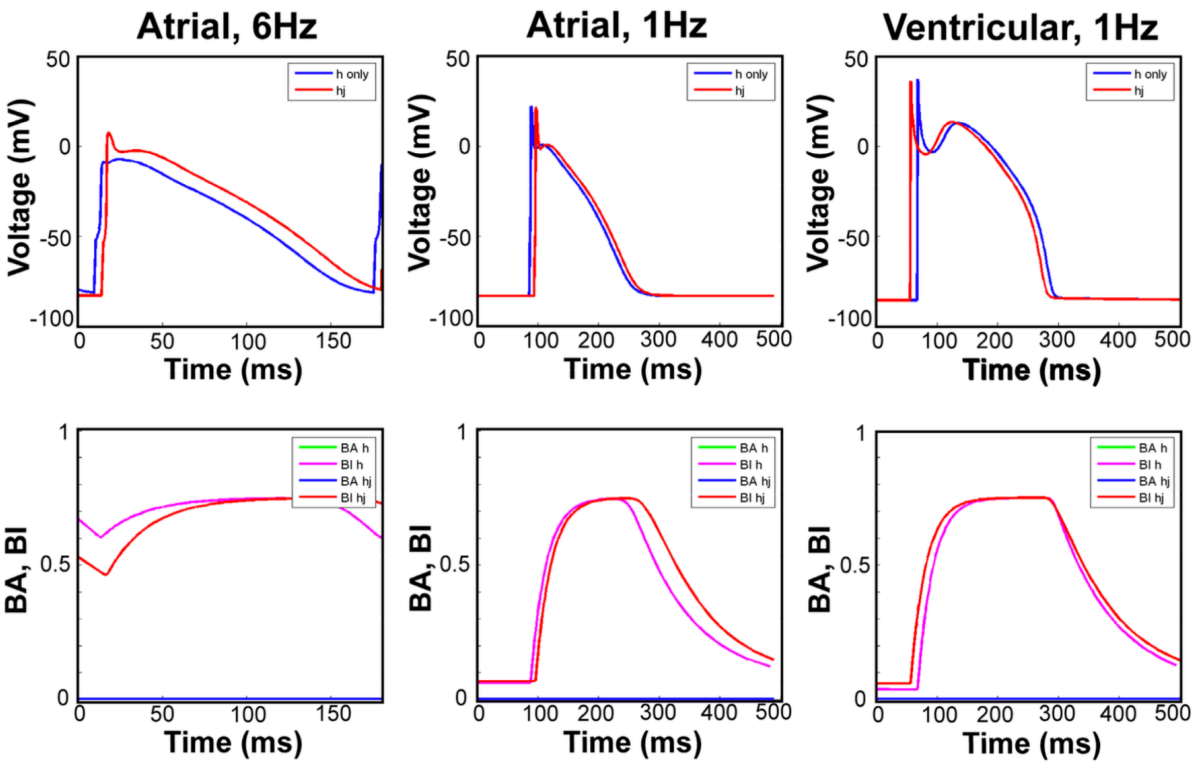

Supplemental Figure 2.9. Action potentials and block variables (B_A, B_I) using *h* only and the product of *h* and *j* at 1 and 6 Hz for a representative case. There are negligible differences in AP and block dynamics at 1 Hz pacing for both the atrial and ventricular cells. At 6 Hz, using *hj* led to slightly longer-lasting inactivated-state block, although absolute block values were in the same range as with *h* only, consistent with the idea that including the slow inactivation variable *j* prolongs the period over which the drug can bind to the inactivated state.

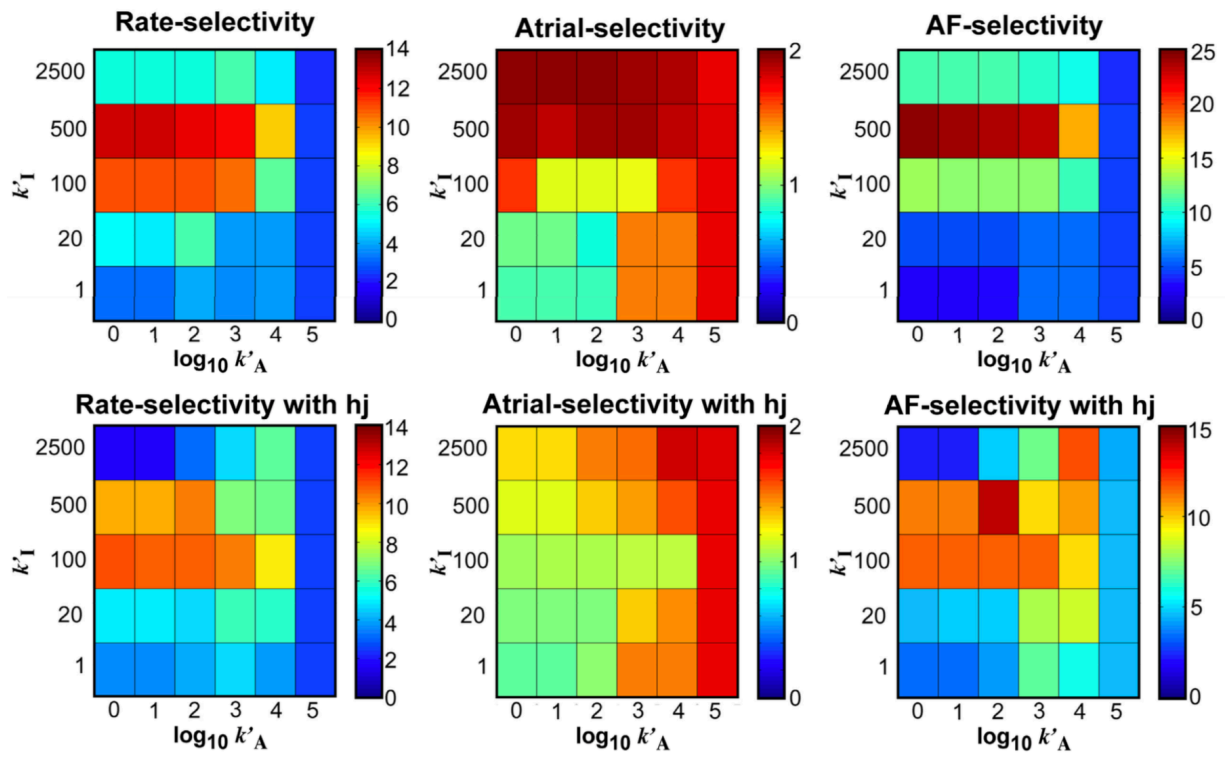

Supplemental Figure 2.10. Rate-, atrial- and AF-selectivity optimization using *h* only (top row) and the product *hj* (bottom row). There is good qualitative agreement in rate- and atrial-selectivity between the two formulations. Overall, we found that our main finding that inactivated-state blockers are optimally AF-selective over a narrow range of k_I values is unchanged, although maximal AF-selectivity was slightly lower with *hj* than with *h*.

Chapter 3. The Synergistic Atrial Fibrillation-Selective Effects of Combined Na^+- and K^+-Channel Block

Virtually all AADs target more than one ionic current. Given that the action potential is a highly non-linear system, the electrophysiological effects of multi-channel blockade are non-trivial. In Chapter 2, we showed that it is possible to optimize the pharmacodynamic properties of a state-dependent Na^+-channel blocker for AF-selectivity; the optimal drug had nevertheless limited anti-AF efficacy. In this paper, we hypothesized that adding an I_{Kr} blocker would have synergistic anti-AF effects to those of an optimized state-dependent Na^+-channel blocker.

3.1 Potassium Channel Blockade Enhances Atrial Fibrillation-Selective Antiarrhythmic Effects of Optimized State-Dependent Sodium Channel Blockade

Martin Aguilar, Feng Xiong, Xiao Yan Qi, Philippe Comtois et Stanley Nattel

Circulation. 2015;132(23):2203-11

3.1.1 Abstract

Background: A lack of effective and safe antiarrhythmic drugs for atrial fibrillation (AF) rhythm control is an unmet clinical need. Multichannel blockers are believed to have advantages over single-channel blockers for AF, but their development has been completely empirical to date.

Objectives: To test the hypothesis that adding K^+-channel blockade (KCB) improves the atrial-selective electrophysiological profile and anti-AF effects of optimized Na^+-channel blockers (NCB_os).

Methods: Realistic cardiomyocyte, tissue and state-dependent Na^+-channel block mathematical models, optical mapping and action potential recording were used to study the effect of Na^+-current (I_{Na}) blockade with or without concomitant inhibition of the rapid or ultra-rapid delayed rectifier K^+-currents (I_{Kr}, I_{Kur}, respectively).

Results: In the mathematical model, maximal AF-selectivity was obtained with an inactivated-state Na^+-channel blocker. Combining NCB_o with I_{Kr} block increased rate-dependent and atrial-selective peak I_{Na} reduction, increased AF-selectivity and more effectively terminated AF compared to NCB_o alone. Combining NCB_o with I_{Kur} block had similar effects but without I_{Kr} block-induced ventricular action potential prolongation. Consistent with the mathematical model, in coronary-perfused canine hearts the addition of dofetilide (selective I_{Kr} blocker; DOF) to pilsicainide (selective I_{Na} blocker; PIL) produced enhanced atrial-selective effects on maximal phase-0 upstroke and conduction velocity. Furthermore, PIL+DOF had higher AF termination efficacy than PIL alone. PIL alone had no statistically significant effect on AF inducibility while PIL+DOF rendered AF non-inducible.

Conclusions: K^+-channel block potentiates the AF-selective anti-AF effects obtainable with optimized Na^+-channel blockade. Combining optimized Na^+-channel block with blockade of atrial K^+-currents is a potentially valuable AF-selective antiarrhythmic drug strategy.

Keywords: anti-arrhythmic drugs, sodium channel blockers, potassium channel blockers, combination therapy, atrial fibrillation

3.1.2 Introduction

Atrial fibrillation (AF) is the most common sustained cardiac arrhythmia and is associated with significant cardiovascular morbidity and mortality (28, 30, 31, 118, 119, 147). The failure of large randomized clinical trials to demonstrate a benefit of AF rhythm control is often attributed to the poor efficacy and proarrhythmic potential of currently-available antiarrhythmic drugs (28-32, 147). The development of safer and more effective antiarrhythmic agents is a major unmet need.

There is growing interest in multiple-channel blockade as an anti-AF strategy, motivated by the empirical observation that multichannel blockers are generally more effective antiarrhythmics as exemplified by amiodarone, with actions of all antiarrhythmic classes (148). In recent experimental work, the combination of ranolazine (class I effect) and amiodarone or dronaderone (class III action) had superior antiarrhythmic efficacy compared to either drug alone (149-151). With the use of realistic mathematical models of cardiac electrophysiology, we previously analyzed the exploitation of state-dependent Na^+-channel blocking properties to produce channel-blockade that is selective for the fibrillating atrium, aiming to define pharmacodynamic properties that maximize therapeutic effects on the fibrillating atrium and minimize ventricular proarrhythmic actions at the much slower rate of resting sinus rhythm (152). Here, we tested the hypothesis that K^+-channel blockade might enhance the maximum AF-selectivity that can be obtained by optimizing the AF-selective properties of Na^+- channel blockers (NCBs).

We began by comparing the AF-selective actions that can be achieved with pure NCBs with those that are attainable with a combination of an NCB and a K^+-channel blocker (KCB). We then studied the effect of pilsicainide, a highly-selective NCB, alone and in combination with dofetilide, a specific KBC, on canine atrial and ventricular electrophysiology and AF inducibility/termination. Finally, we verified theoretical predictions by experiments on action potential properties of multicellular canine atrial-tissue preparations in vitro.

3.1.3 Methods

Principle methods are described here; for details see (online) Supplemental Methods.

3.1.3.1 Single-cell simulations

The Ramirez-Nattel-Courtemanche (RNC) ionic model of canine atrial cardiomyocyte (127) and the Hund-Rudy (HRd) ionic model of canine ventricular cardiomyocyte (128) action potentials (APs) were implemented. In brief, the mathematical model of the action potential consists of a set of equations (called "ordinary differential equations") that represent the evolution over time of the system's main electrophysiological variables (ion currents and intracellular ion fluxes) based on experimental recordings. Given the state of the system (i.e. transmembrane potential and starting points for all of the electrophysiological variables) at time t, the differential equations are used to calculate the changes in the electrophysiological variables for a small time increment Δt, the solution of which is the state of the system at time $t+\Delta t$. The same process is repeated (iterated) for a large number of successive time-steps, allowing for the precise calculation of the changes in transmembrane potential over time. This approach can be used to calculate a series of action potentials in a single cell, or by coupling model cells into a syncytium, the spread of electrical activity in model tissue over time. Equations for the total ionic current of the RNC model ($I_{ion,RNC}$) and the HRd model ($I_{ion,HRd}$) were composed as previously described (47, 128) and detailed in (online) Supplemental Methods.

RNC and HRd cardiomyocytes at 37°C were stimulated at 1 Hz (resting sinus rhythm-equivalent frequency) and 6 Hz (AF-equivalent frequency) for 1.5 min for each set of binding/unbinding constants by numerical integration with the MATLAB ODE23s ordinary

differential equation solver (The MathWorks, Natick, MA). The stimuli were 30 pA/pF 2-ms square pulses. An NCB and/or an I_{Kr}-blocker (Kr) was added after 30 s and the drug effect was quantified based on a reduction in peak I_{Na} (B_{ss}=[$I_{Na,CTL}$–$I_{Na,drug}$]/$I_{Na,CTL}$). Simulated NCB effects were state dependent, obtained with the guarded-receptor formalism (Supplementary Figure 3.1) (152). In brief, the NCB binds to the Na^+-channel in the activated (A) and/or inactivated (I) state; the binding and unbinding dynamics are characterized by binding and unbinding rate constants to the activated (k_A and l_A) and inactivated (k_I and l_I) states respectively. The fractional block in the activated (B_A) and inactivated state (B_I) as a function of time was obtained by iterative numerical integration (see Supplementary Methods).

AF-selectivity of Na^+-channel blockade was first optimized over binding and unbinding parameter-space in single-cell simulations. We defined rate-selectivity as the ratio of B_{ss} in an atrial cell paced at 6 Hz versus an atrial cell paced at 1 Hz (B_{ss} atrial 6-Hz/B_{ss} atrial 1-Hz) (152). Atrial-selectivity was defined as the ratio of B_{ss} in an atrial cell paced at 1 Hz versus a ventricular cell paced at 1 Hz (B_{ss} atrial 1-Hz/B_{ss} ventricular 1-Hz). We defined AF-selectivity as the product of rate-selectivity and atrial-selectivity (given B_{ss} atrial 6-Hz/B_{ss} ventricular 1-Hz). AF-selectivity was optimized over l_A-l_I parameter-space for fixed k_A and k_I by independently varying l_A and l_I from 10^{-5} ms^{-1} to 10^0 ms^{-1} in $10^{0.5}$ ms^{-1} intervals, generating 121 simulations for each (k_A, k_I). Subsequently, k_A and k_I were independently varied with k_A = [10^1, 10^2, 10^3, 10^4, 10^5] ms^{-1}•mol^{-1} and k_I = [1, 20, 100, 500, 2500] ms^{-1}•mol^{-1} to complete the optimization. Combinations with lower than 50% atrial I_{Na}-reduction at 6 Hz were excluded, as these were unlikely to terminate AF (124, 135). The NCB with maximal AF-selectivity is referred to as NCB_o. The optimization was performed for a NCB alone (NCB_o), a NCB with 25% I_{Kr} maximum-conductance reduction (NCB_o/Kr-25%), and a NCB with 50% I_{Kr} maximum-conductance reduction (NCB_o/Kr-50%). We performed detailed analyses with I_{Kr}-block to study the effects of combined Na^+/K^+-channel blockade, since virtually all clinically available K^+-channel blockers target I_{Kr}. There is, however, interest in developing novel K^+-channel blockers targeting atrial-selective K^+-channels, like the ultra-rapid delayed-rectifier K^+ current (I_{Kur}) (119). Therefore, we performed secondary analyses in which we studied NCBs optimized in the presence of 50% I_{Kur} reduction (NCB_o/Kur-50%).

3.1.3.2 Two-dimensional simulations

Two-dimensional (2D) simulations were performed on a 7×6.5 cm sheet of RNC atrial cardiomyocytes. The tissue contained cardiomyocyte cables (radius 5 μm, resistivity 75 Ω•cm) coupled by resistors ([300 kΩ], length 100 μm, inserted in a brick-wall manner). Fiber resistivity and interfiber resistance values were chosen to match experimental results (47, 135). AF was started by a cross-shock protocol, with S_1 applied at one edge and S_2 applied on a square area, as previously described (47, 124). For each (k_A, k_I), the NCB_o and NCB_o/Kr-50% was added at 8 different time points (t_{DRUG}=[975, 1000, 1050, 1075, 1100, 1250, 1500, 1750] ms). Time to termination, defined as the time from drug-application to the time at which membrane potential was negative to -70 mV for all myocytes in the substrate, was recorded and drug efficacy was expressed as the percentage of successful AF termination for each binding-constant set. Conduction velocity (CV) measurements were obtained by stimulating the 2D sheet at one edge at a fixed basic cycle length (BCL). Longitudinal CV was calculated as CV=L/δt, where δt is the time taken by the excitation front to travel across the sheet and L is the substrate length, at BCLs of 150, 160, 170, 175, 180, 185, 190, 195, 200, 225, 300, 400 and 500 ms.

3.1.3.3 AP recording

Hearts were excised from mongrel dogs (weight 24±2 kg, n=13) anesthetized with pentobarbital (30 mg/kg IV) and immersed in Tyrode's solution containing 2-mmol/L Ca^{2+} equilibrated with 100% O_2. The right atrium was opened and dissected, retaining a 3-cm rim of right ventricular tissue. The right coronary artery was cannulated and perfused with Krebs solution. The preparation was placed in a temperature-controlled bath (37°C) and the ventricular coronary branches were ligated. Atrial and ventricular tissues were paced at 2 and 4 Hz through a bipolar electrode (2-ms pulses, 2×diastolic threshold) and APs were recorded using floating microelectrodes filled with 3-mol/L KCl. The maximal phase-0 upstroke velocity (V_{max}) and AP-duration (APD) at 50%, 70% and 90% repolarization (APD_{50}, APD_{70} and APD_{90}) were

calculated from the AP-recordings. Measurements were taken under control conditions, with pilsicainide (PIL) 2 μmol/L (Sigma-Aldrich, St. Louis, MO, USA) and with pilsicainide 2 μmol/L and dofetilide 100 nmol/L (PIL+DOF). Results are expressed as mean±SEM.

3.1.3.4 Optical mapping

Hearts were excised, and right atria were dissected. After 10 minutes of stabilization and electrical-mechanical uncoupling with blebbistatin 15 μmol/L, the preparation was loaded with di-4-ANEPPS (Biotium, CA). Fluorescence images were recorded with a charge-coupled device camera (CardioCCD, Redshirt Imaging) at 0.5-2 kHz under control conditions and after a 20-min equilibration period with PIL or PIL+DOF. AF was initiated with 50-Hz burst-pacing under control, PIL and PIL+DOF conditions. Optical recording continued for about 4 seconds after the end of burst pacing. Inducible sustained AF (Supplementary Figure 3.2) was defined as spontaneously-maintained rapid (>300 bpm) irregular atrial rhythm lasting >1 s. Data were processed with a custom analysis-routine written in Matlab (The MathWorks, Natick, MA). Conduction velocity was calculated from the gradient of the scalar field of the isochronal activation maps. APD_{80} was calculated as the time from maximal upstroke velocity (dF/dt_{max}) to 80% repolarization.

3.1.3.5 Statistical analysis

Statistical analysis was performed with SPSS (IBM, Armonk, NY) and Graphpad Prism 5 (GraphPad Software, La Jolla, CA). Shapiro-Wilk tests were used to assess normality of distribution; non-parametric tests were used to compare data that did not follow normal distribution. Accordingly, CV and APD_{90} from optical mapping were compared with analysis of variance followed by Bonferroni-corrected t-tests; results are expressed as mean±SEM. AF duration, single-cell APD_{90} and V_{max} were compared with unpaired Mann-Whitney tests; results are expressed as median (IQR). When more than one measurement was available for the same

preparation (e.g. APD_{90} and V_{max} data), the mean value in each animal was used as a single representative measure. A p-value<0.05 was considered statistically significant.

3.1.4 Results

3.1.4.1 Effect of simulated Na^+- and K^+-channel block on cardiomyocyte electrophysiology

We first defined the binding and unbinding properties of NCB_o (optimized NCB) with the single-cell model (in the absence of any K^+-channel block) and examined its effects with and without added I_{Kr} block. Figure 17 shows the effect on simulated action potential morphology and I_{Na} of control (black; no drug), NCB_o alone (green) and NCB_o combined with 50% I_{Kr} reduction (NCB_o/Kr-50%; red). At 1 Hz (sinus rhythm-equivalent frequency), NCB_o or NCB_o/Kr-50% had no effect on I_{Na} in atrial and ventricular cardiomyocytes (Figure 17D and F; atrial and ventricular $I_{Na,max}$ were 201 pA/pF and 194 pA/pF, respectively, for all three conditions). Conversely, in the atrial cardiomyocyte paced at 6 Hz (AF-equivalent frequency), Na^+-entry was appreciably reduced compared to control (Figure 17B; control vs NCB_o; $I_{Na,peak}$ was 143 pA/pF vs 100 pA/pF, -30% vs control). Supplementary Figure 3.3 shows the corresponding blocking dynamics at 6 Hz; block with NCB_o and NCB_o/Kr-50% was exclusively in the inactivated state. The NCB_o/Kr-50% combination further reduced I_{Na} compared to NCB_o alone (Figure 17B; NCB_o/Kr-50% $I_{Na,peak}$ was 70 pA/pF, -30% vs NCB_o and -52% vs control).

One problem with I_{Kr}-blockers is the associated risk of Torsades de Pointes arrhythmias (119). As an alternate, possibly safer, approach to increasing NCB atrial-selectivity, we considered the effect of combining NCB with block of the atrial-specific ultra-rapid delayed rectifier K^+-current (119) (I_{Kur}; 50% I_{Kur} reduction, NCB/Kur-50%). Supplemental Figure 3.4 shows the simulated AP-morphology and I_{Na} of the atrial and ventricular cardiomyocytes for control (black), NCB_o alone (green) and NCB_o/Kur-50% (red). Similar to NCB_o/Kr-50%, $I_{Na,max}$ was unaffected by NCB_o and NCB_o/Kur-50% in atrial and ventricular cardiomyocytes paced at 1 Hz (sinus rhythm-equivalent frequency). In the atrial cardiomyocytes paced at 6 Hz (AF-equivalent frequency), I_{Kur} block potentiated $I_{Na,max}$ reduction in a rate-selective fashion (Supplemental Figure 3.4B; NCB_o vs NCB_o/Kur-50% $I_{Na,peak}$ was -99 pA/pF vs -72 pA/pF, -

27% vs NCB_o and -50% vs control). Contrary to NCB_o/Kr-50%, NCB_o/Kur-50% had no effect on the ventricular APD at 1 Hz (Supplemental Figure 3.3E).

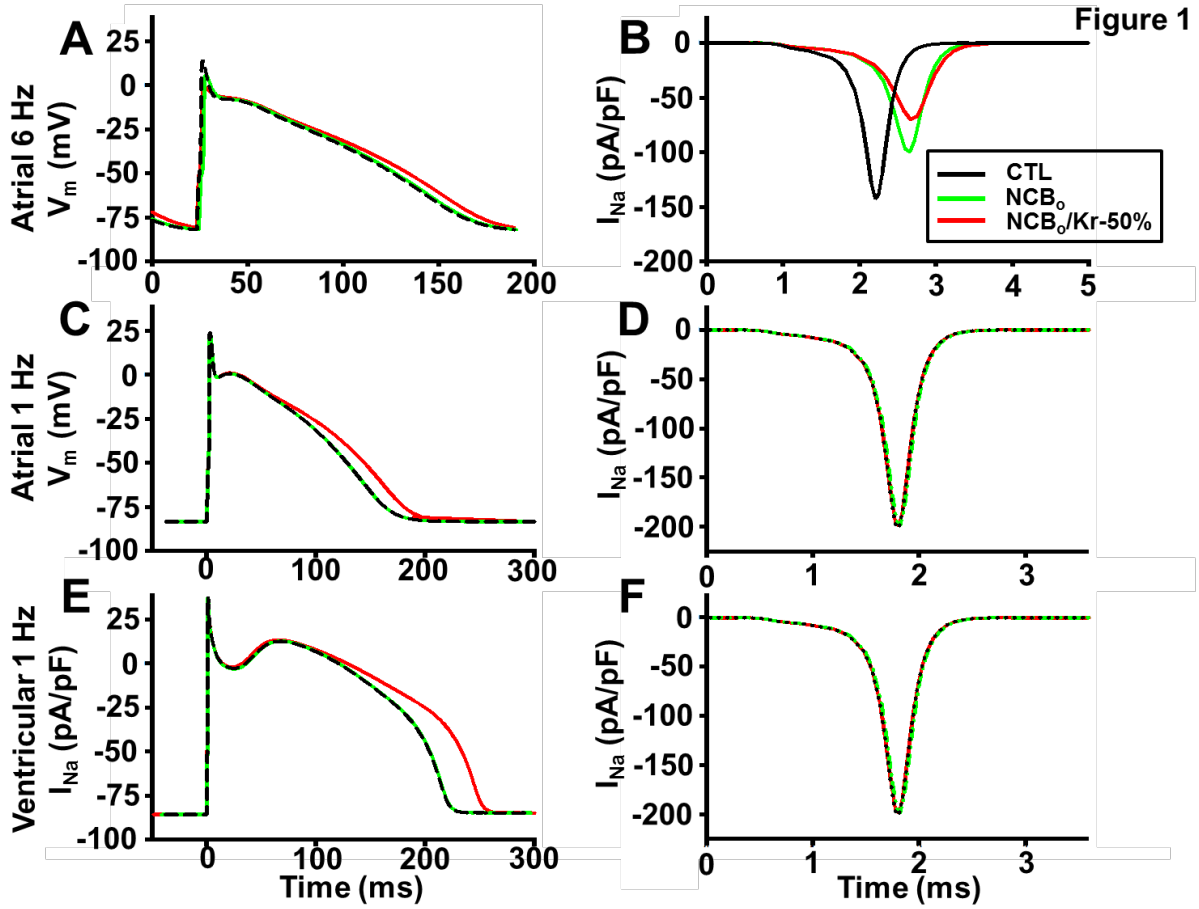

Figure 17. Simulated action potentials and I_{Na} for an atrial and a ventricular cardiomyocyte with and without channel blocker. Simulated action potentials (left) and I_{Na} (right) for control (black), optimal NCB alone (NCB_o; green) and optimal NCB/Kr-50% combination (NCB_o/Kr-50%; red) for an atrial cardiomyocyte paced at 1 Hz and 6 Hz and the ventricular cardiomyocyte paced at 1 Hz (rate constants for NCB_o: k_A = 100 $ms^{-1}\cdot mol^{-1}$, k_I = 100 $ms^{-1}\cdot mol^{-1}$, l_A = 0.1 ms^{-1}, l_I = 0.01 ms^{-1}).

Figure 18 shows the atrial APD, peak I_{Na}, and maximal phase-0 upstroke velocity (V_{max}) obtained from single cell simulations, along with conduction velocity (CV) obtained from pacing a 2-dimensional sheet of atrial cells at one edge of the substrate, as a function of the basic

cycle length (BCL) for control (black), NCB_o (green) and NCB_o/Kr-50% (red). As expected, I_{Kr} block prolonged APD whereas NCB_o alone had little effect (Figure 18A). Synergistic and rate-dependent reduction in peak I_{Na} and V_{max} at rapid pacing frequencies were observed (Figure 18B-C) whereas 1:1 conduction was lost at a slower BCL with NCB_o/Kr-50% compared to NCB_o and control (Figure 18D and inset). These data show that adding K^+-channel block enhances the rate-dependent effects of NCB_o on I_{Na} and I_{Na}-dependent properties like V_{max} and CV.

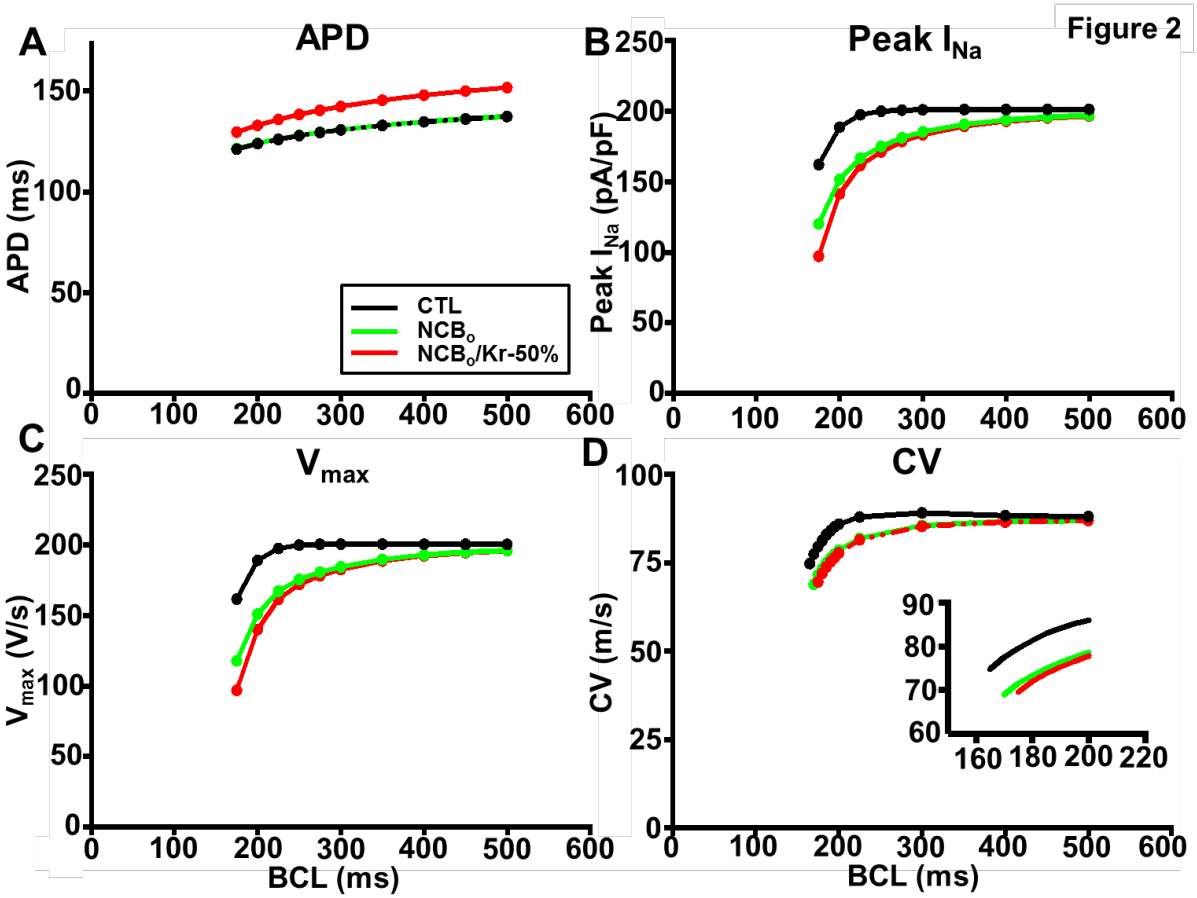

Figure 18. Action potential duration, peak I_{Na}, V_{max} and CV as a function of BCL. Single-cell action potential duration (APD, panel A), peak I_{Na} (panel B), and maximal phase-0 upstroke velocity (V_{max}, panel C) and 2-dimensional conduction velocity (CV, panel D) as a function of basic cycle length (BCL) for control (black), NCB_o (green) and NCB_o/Kr-50% (red). K^+-channel blockade prolonged APD in a reverse rate-dependent fashion whereas NCB_o had no effect on APD (panel A). Synergistic rate-dependent depression of peak I_{Na} and V_{max} with

NCB_o/Kr-50% versus NCB_o alone was observed (panels B-C). In 2-dimensional simulation, 1:1 conduction was lost at greater BCLs with NCB_o/Kr-50% (panel D, inset).

3.1.4.2 Rate-, atrium-, and AF-selectivity optimization

The data in Figures 17 and 18 show the effects on AF-selectivity of adding K^+-channel block to a Na^+-channel blocker optimized for AF-selectivity in the absence of K^+-channel block. We then examined the effect of added K^+-channel block on the properties of blockers optimized to maximize AF-selectivity of a NCB in combination with 50% I_{Kr} block over the full range of unbinding rate constants (l_A and l_I) for fixed values of the binding rate constants to the activated and inactivated state (k_A and k_I, respectively), versus a pure NCB under the same conditions. The (k_A, k_I, l_A, l_I) combination with maximal AF-selectivity was identified by computing AF-selectivity for all rate constant combinations in the k_A-k_I-l_A-l_I parameter-space, as detailed in the Methods. This procedure was repeated for a NCB alone (optimized NCB, NCB_o) and for a NCB in combination with 50% I_{Kr} block (optimized NCB/I_{Kr}-50%, NCB_o/Kr-50%). The results of this optimization are presented in Figure 19. The maximal attainable AF-selectivity was almost four-fold greater for NCB_o/Kr-50% versus NCB_o without K^+-channel block (Figure 19E-F; AF-selectivity$_{max}$ 108 vs 24). This increase in AF-selectivity was mainly driven by an increase in rate-selectivity (Figure 19A-B; rate-selectivity$_{max}$ 39 vs 13) and a smaller, but appreciable, increase in atrial-selectivity (Figure 19C-D; atrial-selectivity$_{max}$ 2.8 vs 1.9). The optimal inactivated-state binding rate constant (k_I) was smaller for NCB_o/Kr-50% than for NCB_o ($k_{I,max}$ 100 vs 500 $ms^{-1} \cdot mol^{-1}$). Qualitatively similar results, although of lesser magnitude, were found for NCB_o/Kr-25% (NCB_o with 25% I_{Kr}-block). Conversely, optimizing for NCB_o/Kr-50% and then removing I_{Kr}-block (NCB_o/XKr-50%) led to a marked decrease in selectivity compared to NCB_o/Kr-50% (Supplementary Figure 3.5; AF-selectivity$_{max}$ NCB_o/XKr-50% vs NCB_o/Kr-50% was 50 vs 108).

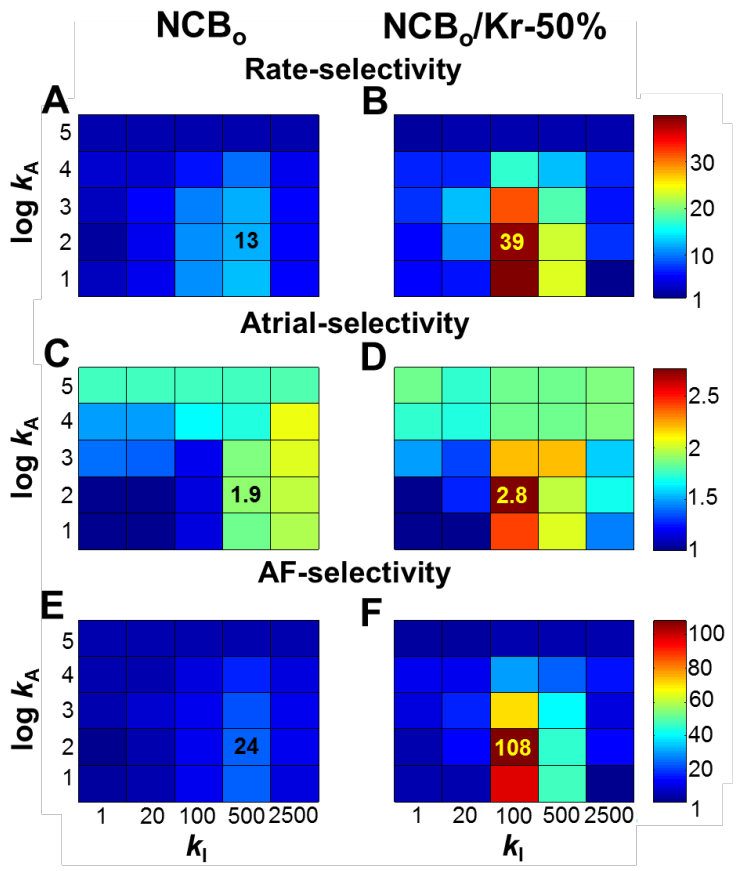

Figure 19. Rate-, atrial- and AF-selectivity as a function of k_A and k_I optimized for NCB (first column) and NCB/Kr-50% combination. Maximal rate-, atrial- and AF-selectivity for the NCB$_o$ were 13, 1.9 and 24, respectively, and 39, 2.8 and 108, respectively, for the NCB$_o$/Kr-50% combination. The optimal AF-selectivity was with the NCB$_o$/Kr-50% combination at k_A = 100 ms^{-1}mol^{-1}, k_I = 100 ms^{-1}mol^{-1}, l_A = 0.1 ms^{-1}, l_I = 0.01 ms^{-1}.

We repeated the AF-selectivity optimization for NCB$_o$ with 50% I_{Kur} reduction (NCB$_o$/Kur-50%); the results are presented in Supplemental Figure 3.6. The addition of I_{Kur} block to NCB increased AF-selectivity versus NCB$_o$ alone without ventricular APD prolongation (Supplemental Figure 3.6E-F; AF-selectivity$_{max}$ 86 vs 24). The increase in AF-selectivity was mainly driven by an increase in rate-selectivity (Supplemental Figure 3.6A-B; rate-selectivity$_{max}$ 42 vs 13), accompanying a marginal increase in atrial-selectivity (Supplemental Figure 3.6C-D; atrial-selectivity$_{max}$ 2.1 vs 1.9).

3.1.4.3 2-Dimensional simulated AF termination

Figure 20 shows the percent termination of simulated 2-dimensional AF (panel A) and average time to termination (panel B) as a function of k_I for independently-optimized NCB_o (green) and NCB_o/Kr-50% (red). Simulated AF was sustained under control conditions. Percent-termination increased with increasing k_I for both NCB and NCB/Kr-50%. The NCB/Kr-50% combination significantly increased termination-rates at low k_I (Figure 20A). The average time to termination was not significantly different between NCB and NCB/Kr 50% over the range of k_I under investigation (Figure 20B).

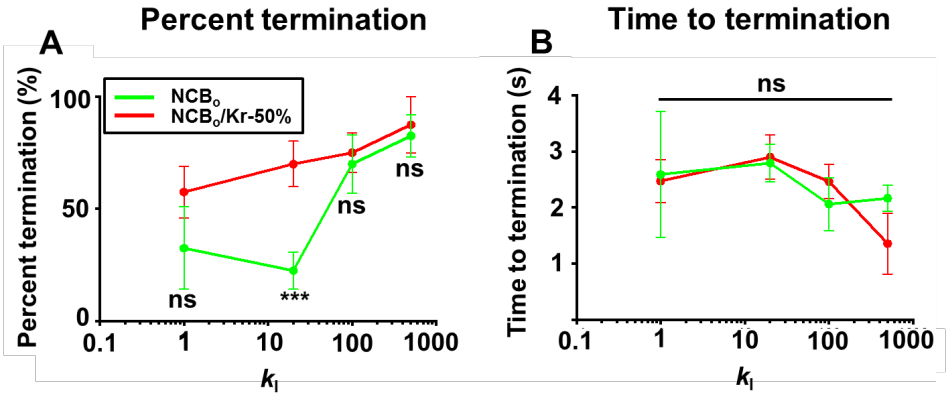

Figure 20. AF termination percent and termination time. Percent termination of simulated 2-dimensional AF (panel A) and corresponding average time to termination (panel B) as a function of k_I for the NCB_o and NCB_o/Kr-50% combination. ***p<0.001 versus NCB_o.

Figure 21 shows a representative example of successful AF-termination by the NCB/Kr-50% combination (with k_A = 1000 $ms^{-1}mol^{-1}$, k_I = 500 $ms^{-1}mol^{-1}$, l_A = 1 ms^{-1}, l_I = 0.01 ms^{-1}). Under control conditions, AF was sustained (Figure 21D, black). Qualitatively, re-entry was maintained by multiple unstable rotors, with a steady-state equilibrium between annihilation and generation of new rotors (Figure 21B, first two rows). The NCB/Kr-50% decreased membrane excitability and destabilized rotors leading to increased wavelet radius of curvature, meandering and termination against substrate boundaries (Figure 21B, bottom two rows). Na^+-channel block was predominantly in the inactivated state for both NCB and NCB/Kr-50% (Figure 21C, blue and orange) as in the single cell model (Supplementary Figure

3.1). Applying a NCB with the same rate constant but without I_{Kr}-block displayed similar I_{Na}-blocking dynamics but did not terminate re-entry, highlighting the synergistic anti-AF effect of combined I_{Na} and I_{Kr} block (Figure 21D, green vs red).

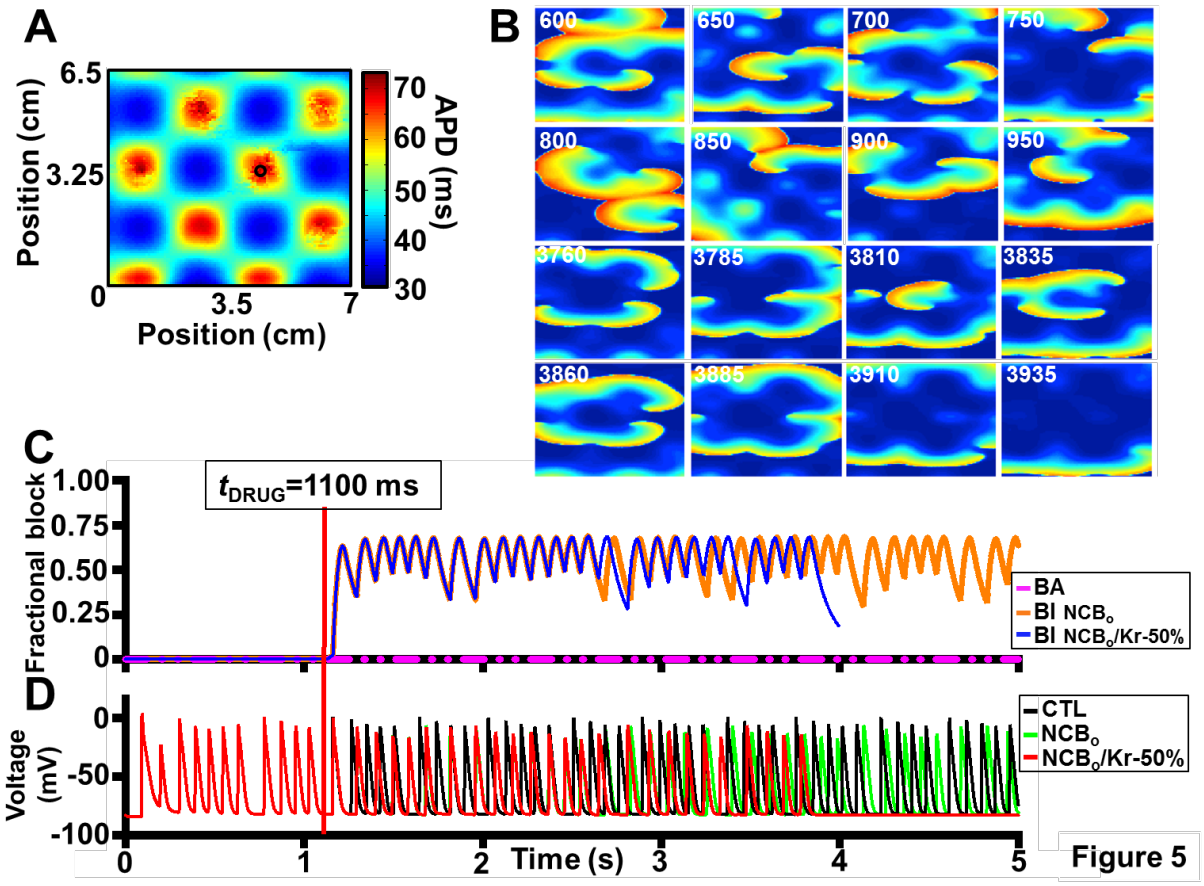

Figure 21. Representative example of simulated AF termination by the optimal NCB$_o$/Kr-50% (k_A = 100 ms^{-1}mol^{-1}, k_I = 100 ms^{-1}mol^{-1}, l_A = 0.1 ms^{-1}, l_I = 0.01 ms^{-1}). **A**: APD-distribution over the 2-dimensional sheet. **B**: Transmembrane potential as a function of time; the drug was applied at t_{DRUG} =1100 ms. Blocking dynamics are shown in **C**; block was exclusively in the inactivated state. **D**: transmembrane potential over time at the location marked "o" in A, for control (black), NCB (green) and NCB$_o$/Kr-50% (red). Under control and NCB conditions AF was sustained; NCB$_o$/Kr-50% terminated reentry 2894 ms after t_{DRUG}.

A representative example of simulated AF-termination by NCB/Kur-50% is shown in Figure 22 (with k_A = 100 ms^{-1}mol^{-1}, k_I = 100 ms^{-1}mol^{-1}, l_A = 0.1 ms^{-1}, l_I = 0.01 ms^{-1}). Termination-dynamics were qualitatively similar to NCB/Kr-50%. Again, block was almost exclusively in the inactivated state (panel C). Successful termination occurred 2850 ms after t_{DRUG} = 1000 ms (panel D).

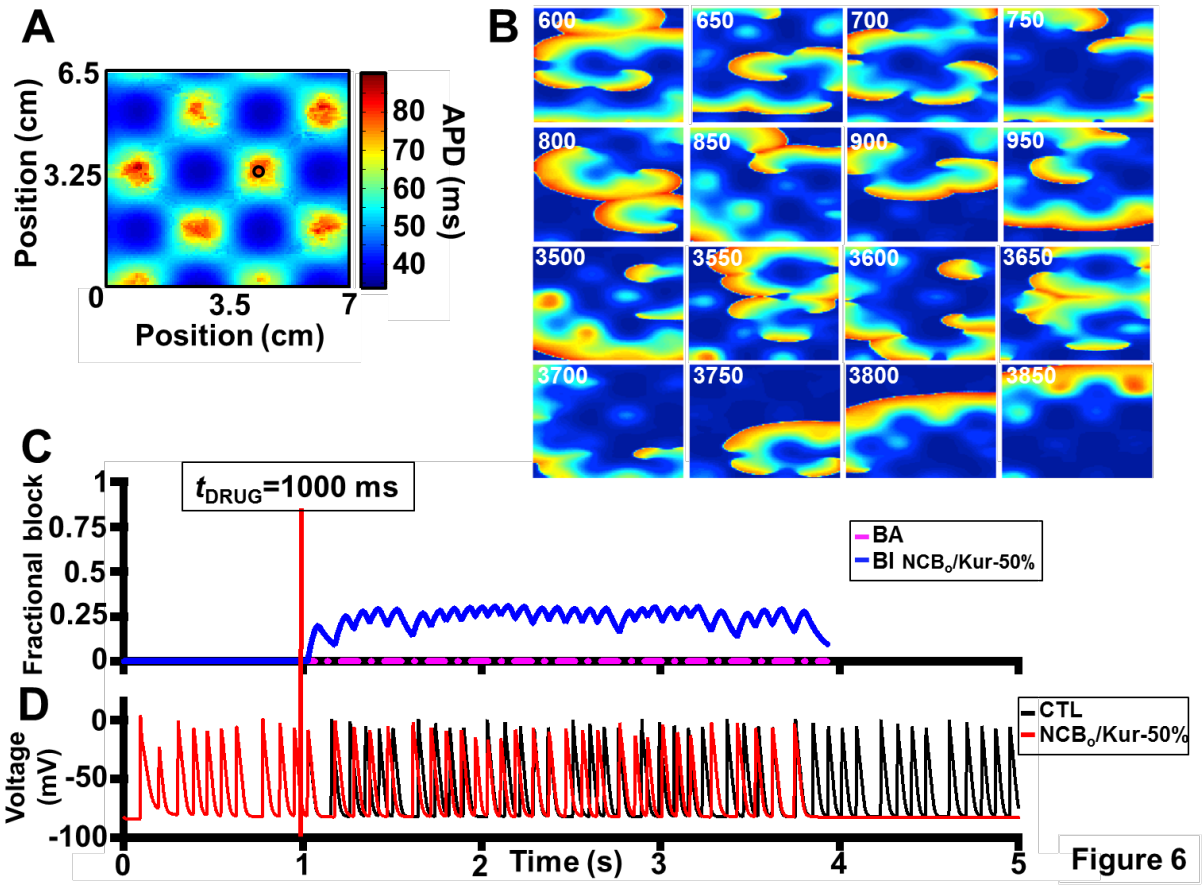

Figure 22. Representative example of simulated AF termination by the optimal NCB$_o$/Kur-50% (k_A = 100 ms^{-1}mol^{-1}, k_I = 100 ms^{-1}mol^{-1}, l_A = 0.1 ms^{-1}, l_I = 0.01 ms^{-1}). **A**: APD distribution over the 2-dimensional sheet. **B**: Transmembrane potential over time; t_{DRUG} =1000 ms. Blocking dynamics are shows in **C**; block was exclusively in the inactivated state. **D**: Transmembrane potential at location marked by "o" in A for control (black) and NCB$_o$/Kur-50% (red). Under control conditions AF was sustained; NCB$_o$/Kur-50% terminated reentry 2850 ms after t_{DRUG}.

3.1.4.4 Optical mapping

To examine the concept of favourable NCB-KCB interaction, we studied optically-mapped coronary-perfused dog right atria. As a test NCB, we chose pilsicainide, which unlike alternatives like flecainide and propafenone has negligible K^+-channel blocking activity at concentrations that produce substantial I_{Na}-inhibition (153). The addition of 2 μmol/L PIL reduced CV compared to control (Figure 23A-B; CV at 200 ms for CTL vs PIL was 94±4 vs 74±4 cm/s, -21%, $p<0.001$). Consistent with simulations, PIL+DOF caused a further decrease in CV compared to PIL alone (CV at 200 ms for PIL vs PIL+DOF was 74±4 vs 60±5 cm/s, -19%, $p<0.05$). PIL-alone had no effect on APD whereas PIL+DOF prolonged APD across the range of pacing cycle lengths under investigation (Figure 23C; APD_{80} at 200 ms for CTL vs PIL+DOF was 135±6 vs 176±8 ms, +30%, $p<0.01$). Furthermore, PIL+DOF synergistically decreased AF-duration compared to PIL-alone (Figure 23D). Finally, PIL-alone had no statistically significant effect on sustained-AF inducibility compared to control (Figure 23E; sustained-AF inducibility CTL vs PIL was 4/13 vs 2/13, ns), whereas PIL+DOF eliminated sustained-inducibility (sustained-AF inducibility CTL vs PIL+DOF was 5/13 vs 0/13, $p<0.05$).

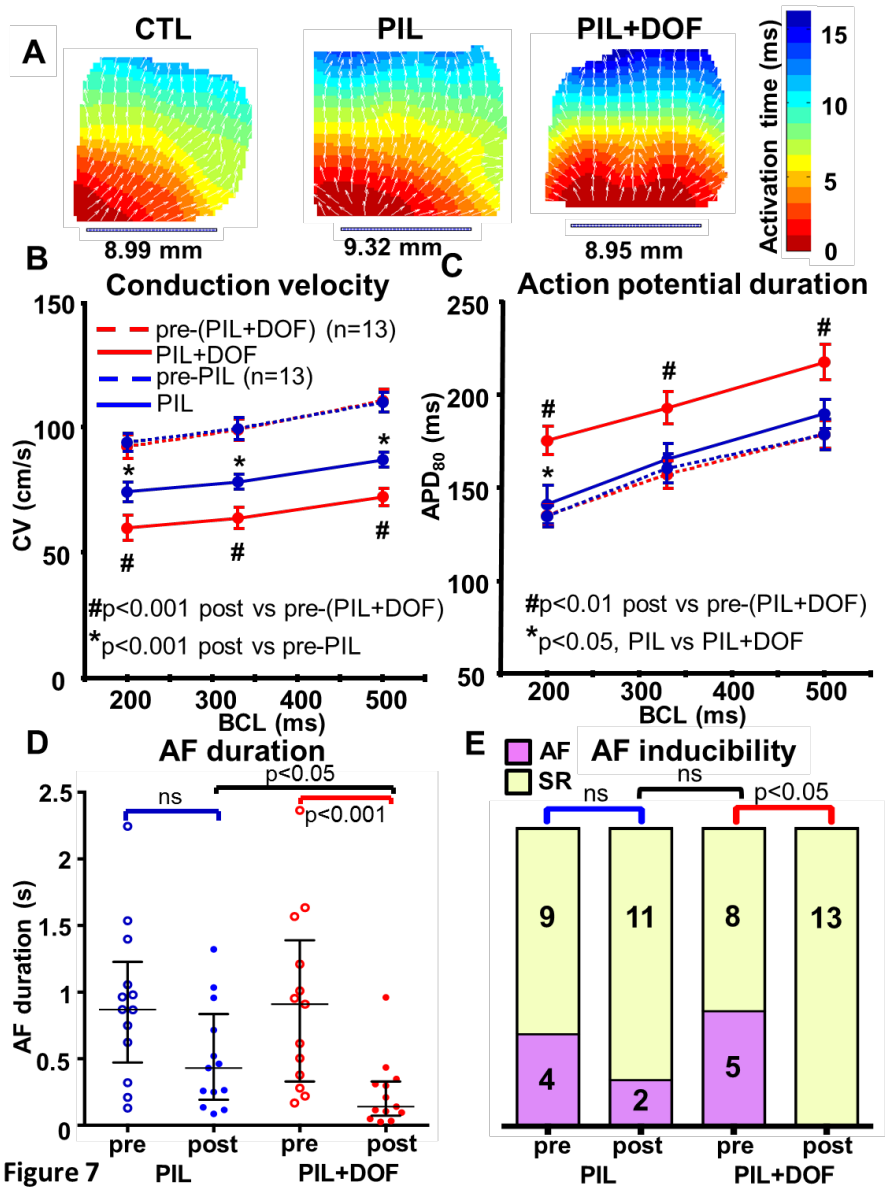

Figure 23. Optical mapping in coronary perfused dog right atria. **A**: Representative isochronal activation maps under control (CTL), pilsicainide 2 μmol/L (PIL) and pilsicainide 2 μmol/L and dofetilide 100 nmol/L (PIL+DOF). Conduction velocity (CV) and action potential duration (APD) at various basic pacing cycle lengths (BCLs) for PIL, PIL+DOF and their respective controls are shown in **B** and **C** respectively; PIL+DOF synergistically depressed CV versus PIL. Similar synergy with PIL+DOF compared to PIL was observed for atrial fibrillation (AF) duration (**D**). AF inducibility was not significantly affected by PIL, whereas PIL+DOF rendered AF non-inducible; results are median (IQR) (**E**).

3.1.4.5 AP recordings

The effects of PIL and PIL+DOF were studied on canine atrial cells (as an indicator of targeted action) and ventricular cells (as an indicator of selectivity/safety). Figure 24 shows representative atrial (panel A) and ventricular (panel B) AP-recordings at 2 (solid lines) and 4 (dashed lines) Hz for control (black), PIL (blue) and PIL+DOF (red). PIL had no significant effect on atrial (Figure 24C) or ventricular APD_{90} (Figure 24D). The addition of the I_{Kr}-blocker dofetilide to PIL (PIL+DOF) had a similar APD-prolonging effect in both atrial and ventricular cardiomyocytes (Figure 24C-D; atrial APD_{90} at 2Hz for CTL vs PIL+DOF was 197 (149-212) vs 232 (207-252) ms, +17%, $p<0.05$; ventricular APD_{90} at 2Hz for CTL vs PIL+DOF was 197 (182-203) vs 230 (221-262) ms, +17%, $p<0.001$).

Control atrial and ventricular V_{max} did not display statistically significant rate-dependence. PIL produced significant frequency-dependent V_{max} reduction (V_{max} PIL 2 Hz vs PIL 4 Hz was 143 (132-189) vs 96 (77-121) V/s, -33%, $p<0.05$). Consistent with the modeling results, PIL+DOF lead to a further rate-dependent decrease in V_{max} compared to PIL alone in atrial cardiomyocytes (Figure 24E: V_{max} PIL+DOF 2 Hz vs PIL+DOF 4 Hz was 144 (126-150) vs 53 (26-63) V/s, -63%, $p<0.001$). This synergistic effect was not observed in ventricular cardiomyocytes (Figure 24F). On the basis of these data, the experimental rate-, atrial- and AF-selectivity values for PIL NCB effects were 1.8, 1.3 and 2.4, respectively, and 3.0, 1.6 and 4.7, respectively, for PIL+DOF, indicating increased rate- and AF-selectivity with combined Na^+ and K^+-channel blockade as suggested by the mathematical model.

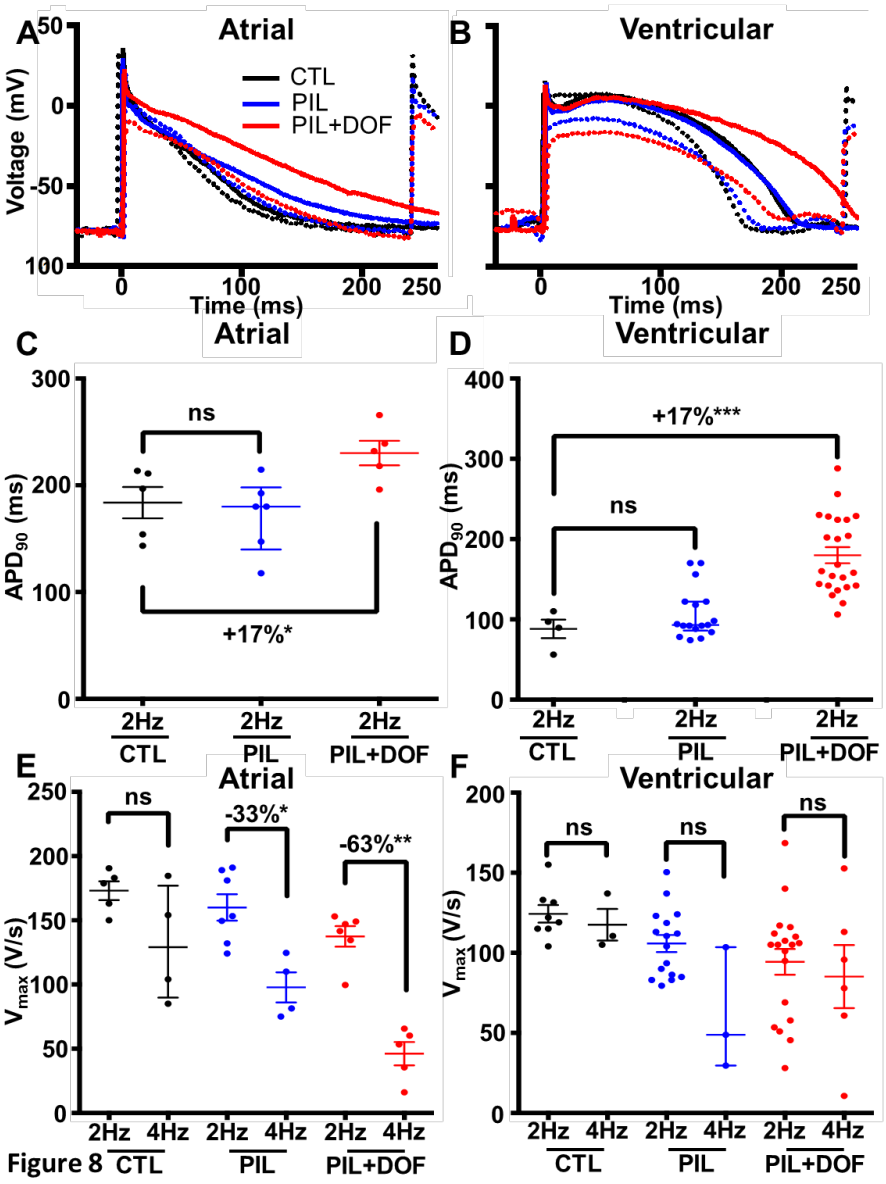

Figure 24. Coronary artery-perfused dog atrial and ventricular action-potential recordings. Representative atrial (**A**) and ventricular (**B**) action potentials at 2 and 4 Hz for control (CTL, black), pilsicainide 2 μmol/L (PIL, blue) and pilsicainide 2 μmol/L plus dofetilide 100 nmol/L (PIL+DOF, red). **C** and **D** show atrial and ventricular APD for control, PIL and PIL+DOF; PIL+DOF prolonged APD by a similar extent in atrial and ventricular cells. **E** and **F** show atrial and ventricular V_{max} at the two test frequencies under investigation. Synergistic V_{max} reduction with PIL+DOF compared to PIL alone was observed in atrial but not ventricular cardiomyocytes. Results are median (IQR). *p<0.05, **p<0.001, ***p<0.0001.

3.1.5 Discussion

Our theoretical results show that K^+-channel block potentiates the AF-selective antiarrhythmic effects of an optimized Na^+-channel blocker. Our experimental results support this favourable interaction. The combination of K^+-channel inhibition and optimized Na^+-channel block is therefore a potentially valuable approach to designing improved anti-AF drugs.

Na^+-channel blockers (NCBs), in particular class Ic drugs such as flecainide and propafenone, are effective agents for acute AF rhythm-control, with pharmacological cardioversion rates in excess of 70% in the setting of recent-onset AF (28, 86, 93, 100, 154). However, proarrhythmic effects, particularly in patients with ischemic heart disease, as well as poor long-term sinus rhythm maintenance, limit their clinical use (28, 74, 94, 98, 99, 101). Similarly, K^+-channel blockers (KCBs) such as dofetilide and ibutilide are moderately efficacious anti-AF drugs (155). Unfortunately, the risk of QT prolongation and ventricular tachyarrhythmias associated with KCBs, particularly in the setting of bradycardia and/or hypokalemia, are major limiting factors (148). Amiodarone, the most prescribed antiarrhythmic for AF, has several important extra-cardiac toxicities and is not approved for AF rhythm control (148). Therefore, a safe and effective AF-selective antiarrhythmic agent is an unmet need in clinical medicine.

Our experimental atrial and ventricular control AP-amplitude and APD measurements were consistent with previously-reported values (156). Pilsicainide is a class Ic antiarrhythmic drug with relatively pure inactivated-state Na^+-channel blocking properties and slow recovery dynamics approved in Japan for the treatment of ventricular and supra-ventricular tachycardias; it is not available in North America. In rabbit atrial cardiomyocytes at therapeutic concentrations (<3 μM), pilsicainide had no effect on the APD, the voltage-dependent Ca^{2+}-current, the delayed rectifier K^+-current and the inward-rectifier K^+-current, highlighting its selectivity for the Na^+-channel at the concentration used in this paper (2 μM) (153). In our experiments, pilsicainide decreased atrial and ventricular Na^+-dependent parameters in a rate-dependent manner with little effect on APD, consistent with previous animal studies in guinea-pig (157-160), dog right atrium and pulmonary vein (161, 162) and rat right ventricle (157, 161). The addition of dofetilide significantly prolonged APD in atrial and ventricular cardiomyocytes, in agreement with

previous work in canine right and left atrium (156) and ventricle (163) and guinea-pig and rat atria (164).

Using a realistic mathematical model, we found that an optimized I_{Na}/I_{Kr} blocker (NCB_o/Kr) compared to an optimized I_{Na} blocker alone (NCB_o) increased rate- and atrial-selectivity leading to a four-fold increase in AF-selective I_{Na} block (Figure 17). NCB_o/Kr AF-selectivity was achieved with an inactivated-state blocker, consistent with previously published work on pure NCBs (152). Removing the K^+-blocking properties from NCB_o/Kr combinations more than halved AF-selectivity and reduced peak I_{Na} block to less than 50% (Supplemental Figure 3.5), the critical level below which AF termination is very unlikely (124). Our theoretical and experimental results demonstrate a synergistic reduction in Na^+-dependent parameters ($I_{Na,peak}$, V_{max} and CV) with the combination of Na^+- and K^+- channel block (NCB/Kr and PIL+DOF) compared to isolated Na^+-channel block (NCB and PIL; Figures 17, 22 and 23). This synergistic effect was associated with more rapid and effective AF termination as well as reduced AF inducibility (Figure 21 and 22).

Given the proarrhythmic risks associated with ventricular I_{Kr} block, we investigated the effect of combining NCB with I_{Kur} block (NCB_o/Kur-50%), an atrial-specific current not expressed in ventricular cardiomyocytes (165). In simulations, we showed that NCB_o/Kur had a qualitatively similar AF-selectivity potentiating effect to NCB_o/Kr, but with no effect on ventricular APD during sinus rhythm (Supplemental Figures 3.4 and 3.6). NCB_o/Kur also effectively terminated simulated AF (Figure 22). Hence, combined I_{Na}/I_{Kur} block retained synergistic AF-selective action with minimal effect on ventricular cardiomyocytes.

Three mechanisms contribute to the synergistic effect of combining NCB with KCB on Na^+-dependent parameter reduction. First, prolongation of phase-2 of the action potential delayed recovery of the fast (*h*) and slow (*j*) inactivation gates of the Na^+-channel, decreasing phase-0 Na^+-channel availability in a rate-dependent fashion ($h \times j$; Supplementary Figure 3.7). Second, APD prolongation depolarized the action potential take-off potential at rapid rates, increasing the fraction of unavailable Na^+-channels at the onset of phase-0. Third, APD prolongation increased the average time spent at depolarized potentials, increasing drug binding, and shortened the diastolic interval, decreasing the time available for drug unbinding. As these effects are rate-dependent, NCB and KCB synergism had most of its impact on rate-selectivity relative to atrial-selectivity (Figure 19).

The experimentally derived rate-, atrial- and AF-selectivity were lower than those found using the mathematical model; three factors account for this discrepancy. First, in the mathematical model NCB was optimized to maximize AF-selectivity, whereas this was not possible experimentally. Second, the experimental AF-equivalent frequency (4 Hz) was lower than the simulation AF-equivalent frequency (6 Hz) and the experimental sinus rhythm-equivalent frequency (2 Hz) was higher than simulations (1 Hz). Third, although pilsicainide is an inactivated-state blocker, its experimentally-measured time constant is long (28.2±6.2 seconds), reflecting slow unbinding kinetics and limiting its rate-selectivity (157). We used pilsicainide because it is an inactivated-state NCB in clinical use for AF and is more selective for Na^+-channel blockade than alternative agents like vernakalant, ranolazine, flecainide or propafenone, all of which block K^+-channels in the Na^+-channel blocking concentration range. It would be interesting to test inactivated-state blockers designed to have faster unbinding kinetics closer to those of the predicted optimal NCBs. With modern pharmaceutical technology, the design of such agents should be an achievable goal (166).

The relatively high anti-AF efficacy of amiodarone has recently drawn attention to multichannel blockade as a valuable strategy to design anti-AF drugs. Intuitively, the partial block of several channels may reduce the undesired effects associated with strong inhibition of a single target while maintaining anti-AF efficacy. A key question then becomes which channels have synergistic, neutral or antagonistic effects on AF-selectivity and anti-AF efficacy. Theoretical considerations and recent experimental work motivated the choice of NCB and KCB as potentially synergistic targets. Sicouri *et al*., with ranolazine and chronic amiodarone, and Burashnikov *et al*., with ranolazine and dronedarone, showed that combination therapy depressed atrial V_{max} and AF inducibility more than either drug alone, similar to our findings (149, 150). The superior efficacy of combination therapy was attributed to the blockade of Na^+-channels in both their open-state by ranolazine and inactivated-state by amiodarone or dronedarone, an alternative anti-AF strategy (149, 150). Subsequently, preliminary results from a phase II clinical trial showed that the combination of ranolazine and dronedarone was superior to either drug alone in reducing AF burden (AFB), although only 45% of patients achieved >70% AFB reduction with combination therapy over the 12-week study period (151). Here, we used mathematical modeling to analyze and study the combination of pure I_{Na} and I_{Kr} blockade, permitting better compartmentalization of the effects of NCB and combined NCB/KCB on anti-

AF efficacy and AF-selectivity. Furthermore, our work provides a promising path to the development of combination-drugs including optimized Na^+-channel blockade and atrial-selective K^+-channel blockade.

3.1.6 Study Limitations

AF is a complex arrhythmia, often originating from the left atrium (LA). We performed experimental work to test model predictions using the right atrial (RA) free wall because of its favorable orientation for optical mapping in coronary artery-perfused preparations. There are known electrophysiological differences between the RA and LA (156). However, since one main difference between RA and LA electrophysiology is a larger I_{Kr} density in the LA (156), the I_{Kr}-block-mediated synergy reported in this paper might be of even greater magnitude in the LA, increasing AF-selectivity. Furthermore, recent work suggests that regional heterogeneity in $I_{Na\text{-}L}$ density may modulate the response of atrial and ventricular cardiomyocytes to class III antiarrhythmics (167). Further work on regional differences in the consequences of NCB-KCB interaction would be of interest.

We used V_{max} as an experimental indicator of peak I_{Na}. The relationship between peak I_{Na} and V_{max} is known to be non-linear (168). On the other hand, V_{max} can be measured experimentally under physiologically relevant conditions, whereas I_{Na} cannot.

Although dofetilide is thought to be a pure I_{Kr} blocker, recent experimental data suggests that dofetilide's proarrhythmic effects may, at least in part, be mediated by an increase in $I_{Na,L}$ (169). This off-class effect was not explicitly investigated in our experiments. Nevertheless, combining dofetilide with a NCB would antagonise the proarrhythmic effect of $I_{Na,L}$, potentially providing further antiarrhythmic action to this Na^+/K^+-channel combined block.

3.1.7 Conclusions

Restoration and maintenance of sinus rhythm is a desirable goal in many AF patients. However, currently available antiarrhythmic drugs have suboptimal efficacy and safety profiles. Using mathematical simulations and animal experiments, we found that K^+-channel blocker

potentiates the AF-selective anti-AF effects of an optimized Na^+-channel blocker. Thus, the combination of K^+-channel inhibition and optimized Na^+-blockade is a potentially valuable new approach to the design of improved atrial-selective anti-AF drugs.

3.1.8 Clinical Perspective

Atrial fibrillation is an extremely common clinical problem, and currently AADs have limited efficacy and proarrhythmic liability. We have shown previously that detailed mathematical analysis can be used to identify pharmacodynamics properties of Na^+-channel-blocking antiarrhythmic drugs to maximize action on atrial cells during AF (efficacy) and to minimize actions on ventricular cells during sinus rhythm (governing proarrhythmic risk), a property that can be called AF selectivity. Multichannel blocking antiarrhythmics have been found empirically to have a better efficacy/safety relationship. Here, we considered the hypothesis that the addition of K^+-channel blockade would enhance the AF selectivity of optimized Na^+-channel blockers. We first applied realistic mathematical models of canine cardiomyocyte and tissue electrophysiology, along with state-dependent Na^+-channel-blocking drug action, and found that adding block of either rapid delayed-rectifier (I_{Kr}) or ultrarapid delayed-rectifier K^+-current increased the AF selectivity achievable with optimized Na^+-channel blockers. We then used optical mapping and action potential recording in isolated coronary-perfused canine cardiac tissue preparations to study the effects of the highly selective Na^+-channel blocker pilsicainide, alone and along with the I_{Kr}-blocker dofetilide, to quantitatively test the predictions of the mathematical modeling and found them to be confirmed: Pilsicainide combined with dofetilide had selective rate-dependent atrial Na^+-channel blocking activity and enhanced AF-suppressing effectiveness compared with pilsicainide alone. We conclude that K^+-channel block potentiates the AF-selective antiarrhythmic effects obtainable with optimized Na^+-channel blockade. Combining optimized Na^+-channel block with blockade of atrial K^+ currents is a potentially valuable AF-selective antiarrhythmic drug development strategy, allowing the rationale design of multichannel blocking antiarrhythmics.

3.1.9 Supplemental Material

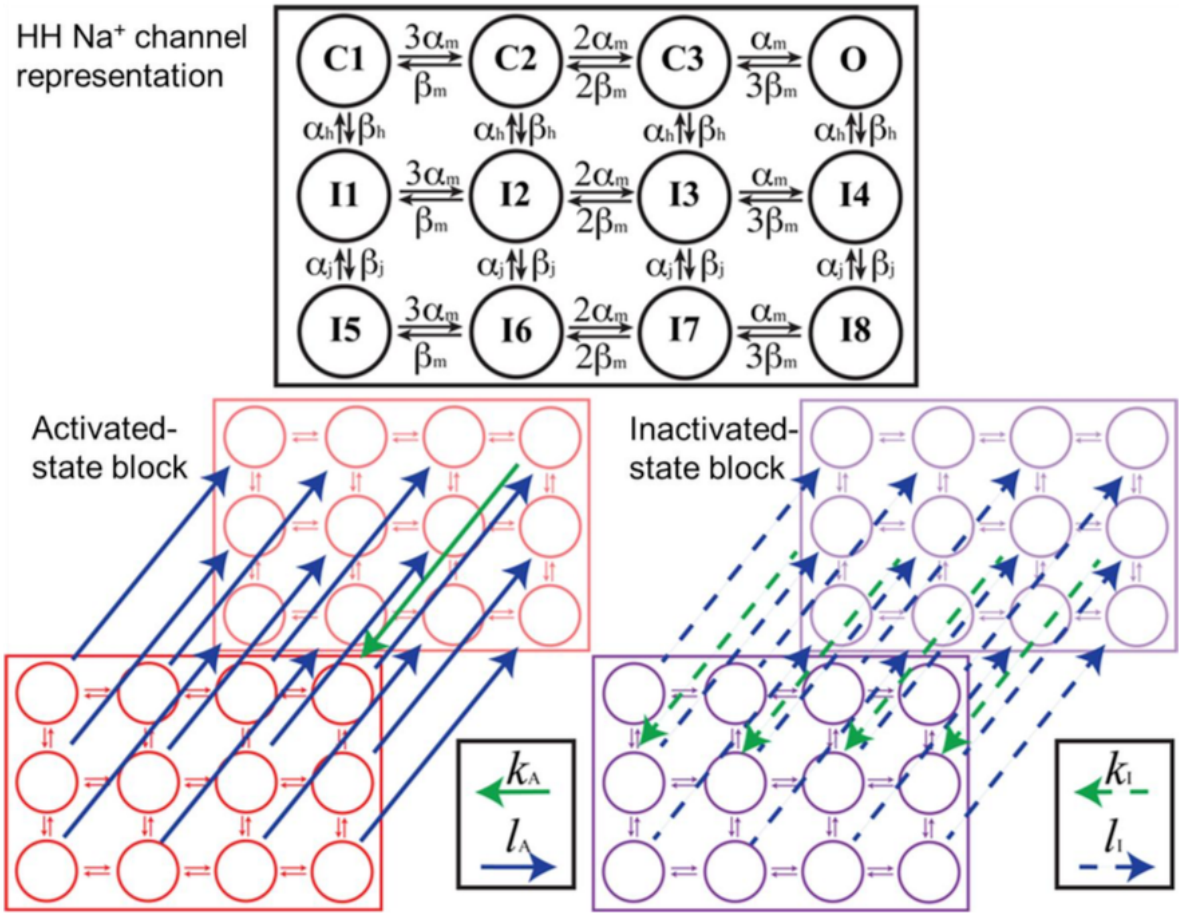

Supplemental Figure 3.1 Schematic representation of the guarded-receptor model of state-dependent Na^+-channel block. The Hodgkin-Huxley equations govern transitions between the closed, activated (A) and inactivated (I) states with rate constants α_x and β_x. The binding rate constants (k_A and k_I) and unbinding rate constants (l_A and l_I) govern drug binding and unbinding (see Methods).

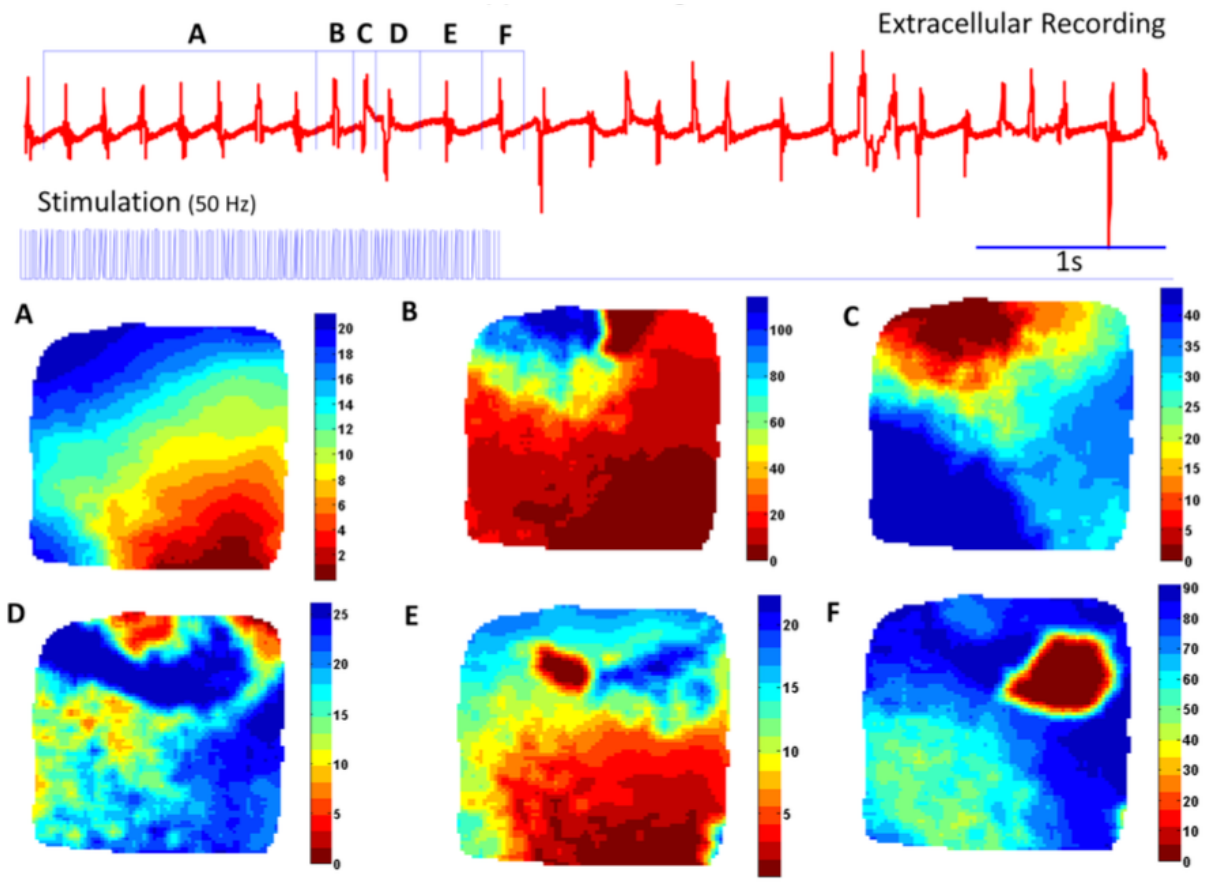

Supplemental Figure 3.2 Representative optical mapping recording at the onset of atrial fibrillation in a coronary-perfused right atrial preparation. An extracellular electrogram recording is shown at the top as a reference. Over the time designated by A, the response was regular and an average isochrones map for all beats over this interval is shown in A. Maps B through F show activation isochrones for the corresponding time window on the extracellular recording. The time scale for each map (in ms) is shown to the right of the map.

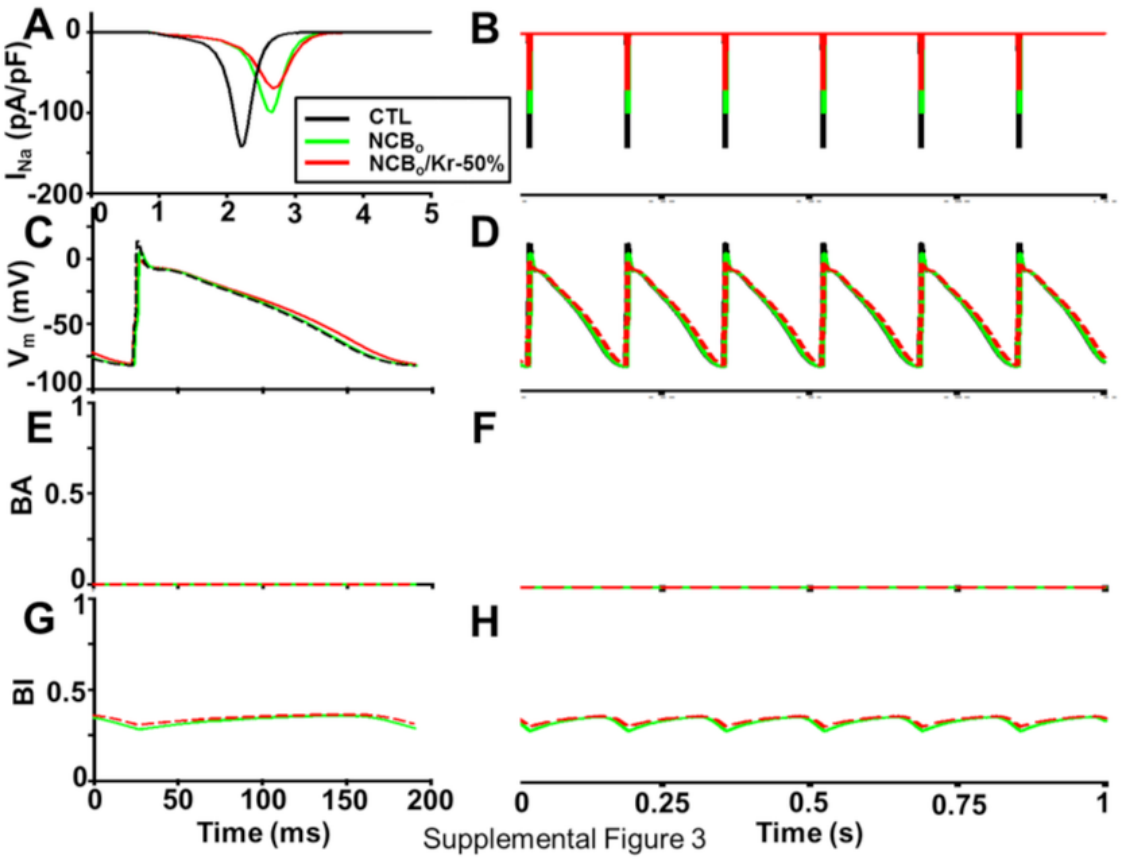

Supplemental Figure 3.3 I_{Na} blocking dynamics at 6 Hz for NCB_o and NCB_o/Kr-50%. Peak I_{Na} was synergistically reduced by NCB_o/Kr-50% (red) compared to NCB_o alone (green; panels A and B). Corresponding action potentials are shown in panels C and D. Activated-state block was virtually non-existent for NCB_o and NCB_o/Kr-50% (panels E and F); block was almost exclusively in the inactivated state (panels G and H). Percent block at the onset of depolarization for NCB_o and NCB_o/Kr-50% was 28% and 31%.

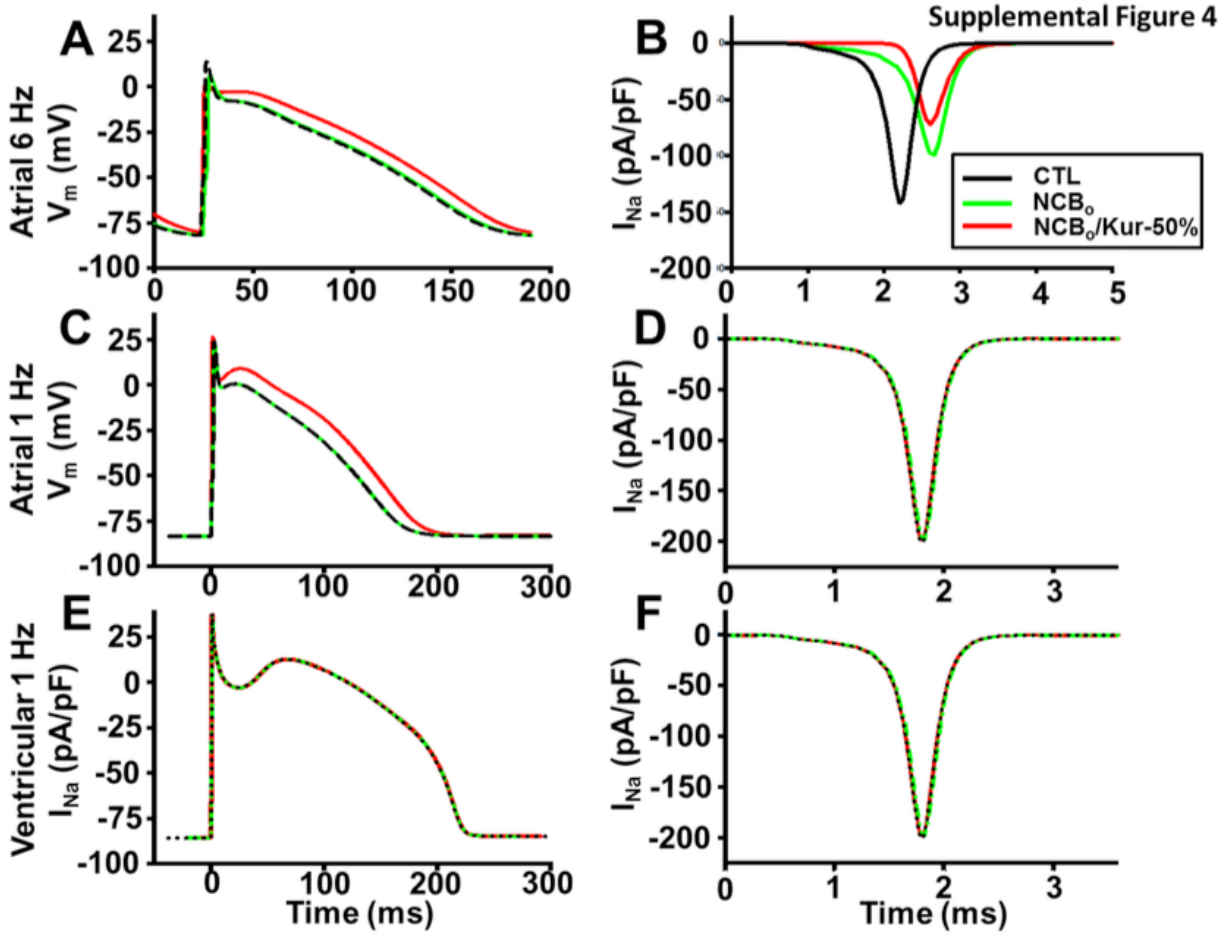

Supplemental Figure 3.4 Action potentials (left) and I_{Na} (right) for control (black), optimal NCB alone (NCB_o; green) and optimal NCB/Kur-50% combination (NCB_o/Kur-50%; ref) for the atrial cardiomyocyte paced at 1 Hz and 6 Hz and the ventricular cardiomyocyte paced at 1Hz (rate constants for NCB_o: k_A = 1 $ms^{-1}\cdot mol^{-1}$, k_I = 100 $ms^{-1}\cdot mol^{-1}$, l_A = 0.31623 ms^{-1}, l_I = 0.01 ms^{-1}). Peak I_{Na} was identical among all three conditions for the atrial and ventricular cardiomyocytes paced at 1 Hz (panels D and F). The NCB_o reduced peak Ina compared to control by 30% (panel B; 143 pA/pF vs 99 pA/pF). The NCB_o/Kr-50% combination further reduced peak I_{Na} compared to control by 52% (panel B; 143 pA/pF vs 72 pA/pF). NCB_o/Kur-50% had no effect on ventricular APD (panel E).

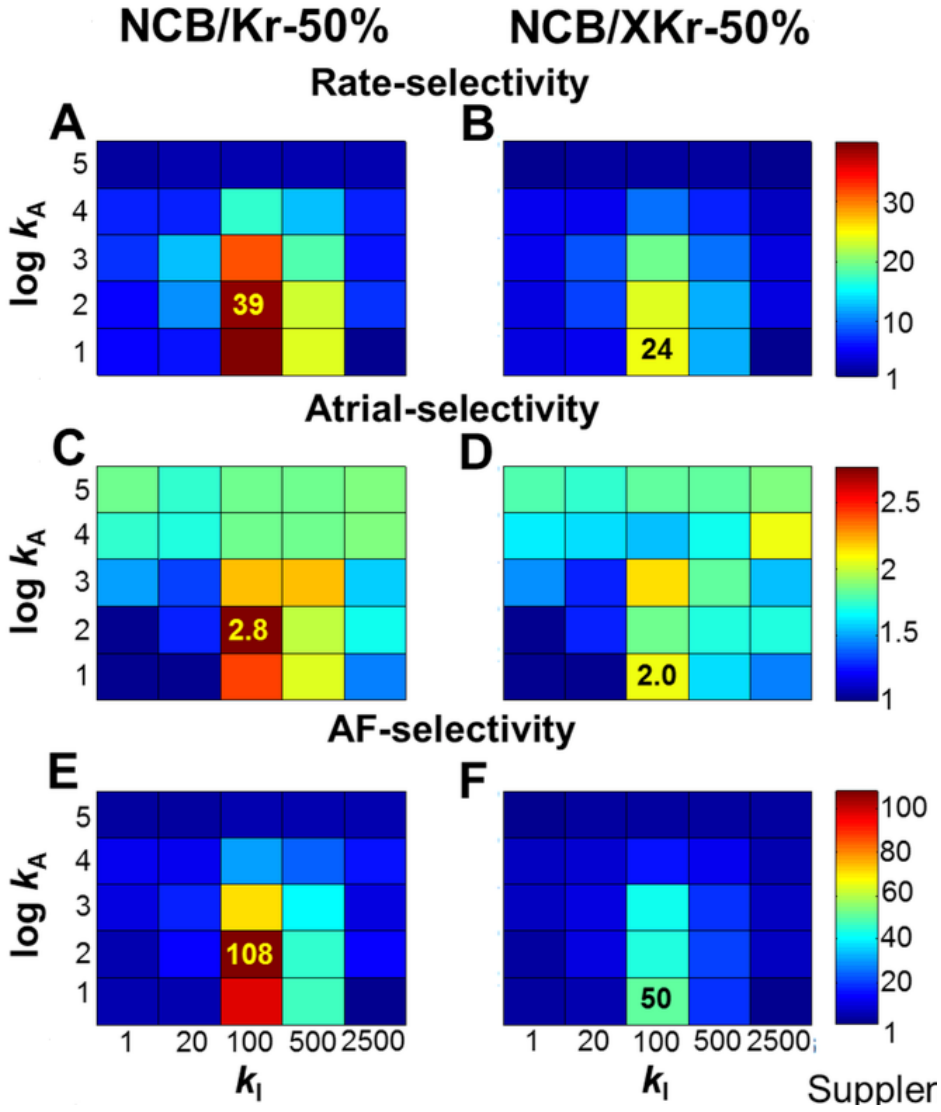

Supplemental Figure 3.5 Rate-, atrial- and AF-selectivity optimized for NCB/Kr-50% (left) and with the same rate-constants but removing I_{Kr} blocking properties from the combination (NCB_o/XKr-50%, right). AF-selectivity was halved with NCB_o/XKr-50% compared to NCB_o/Kr-50% (50 vs 108), mainly driven by a decrease in rate-selectivity (39 vs 24). Although the maximal AF-selectivity for NCB_o/XKr-50% was 50, percent I_{Na} reduction was less than 50%, making it unlikely for this drug to terminate AF.

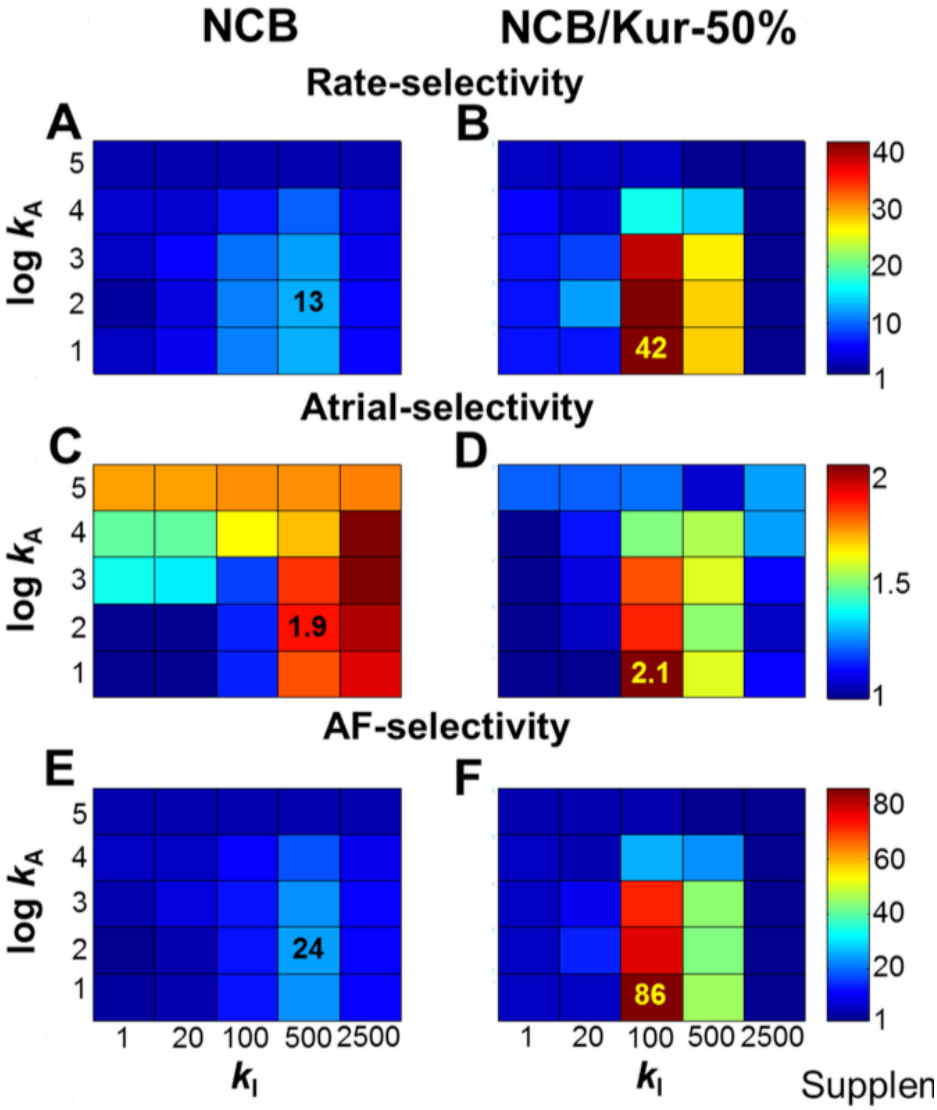

Supplemental Figure 3.6 Rate-, atrial- and AF-selectivity as a function of k_A and k_I optimized for NCB (left) and NCB/Kur-50% combination (right). Maximal rate-, atrial- and AF-selectivity for the NCB_o were 13, 1.9 and 24, respectively, and 42, 2.1 and 86, respectively, for the NCB_o/Kur-50% combination. The optimal AF-selectivity was seen with the NCB_o/Kur-50% combination at k_A = 1 $ms^{-1} \cdot mol^{-1}$, k_I = 100 $ms^{-1} \cdot mol^{-1}$, l_A = 0.31623 ms^{-1}, l_I = 0.01 ms^{-1}.

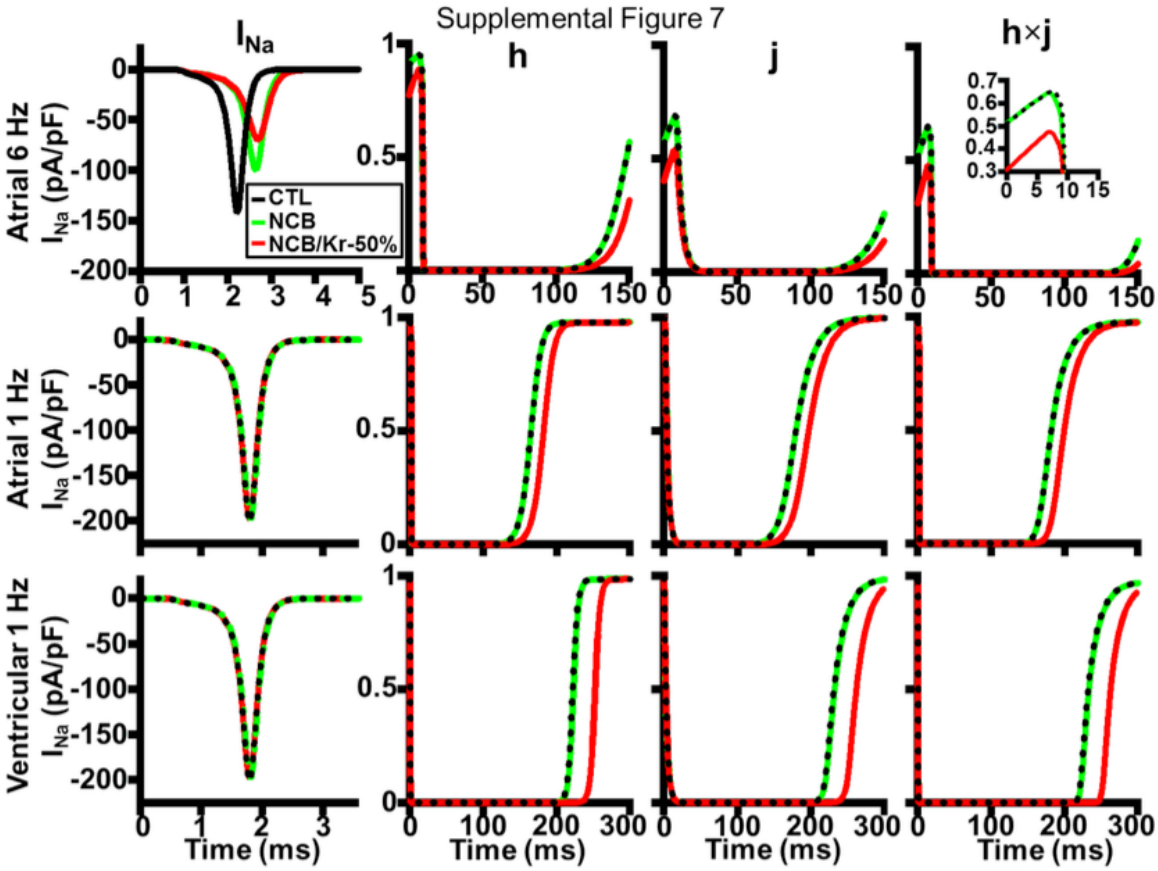

Supplemental Figure 3.7 Sodium current (I_{Na}), fast (*h*) and slow (*j*) inactivation variables of the Na^+ current and Na^+ channel availability (*h*×*j*) for the atrial cell paced at 6 Hz (top row) and the atrial and ventricular cells paced at 1 Hz (middle and bottom rows, respectively); *h*×*j* ranges from 0 (no channels available) to 1 (full channel availability). For the atrial and ventricular cardiomyocytes paced at 1 Hz, the inactivation variable *h* and *j* return to 1 within the diastolic interval, leading to full recovery of *h*×*j* and preserved I_{Na}. In the atrial cell paced at 6 Hz, only partial diastolic recovery of the inactivation gates is achieved, markedly reducing channel availability (*h*×*j*). This effect is more pronounced with NCB_o/Kr-50% compared to NCB_o (top right, inset).

Chapter 4. The Ionic Determinants of I_{Kur} Frequency-Dependent Properties

In Chapter 3, we have demonstrated that combining Na^+- and K^+-channel blockade had synergistic anti-AF effects. However, the K^+ current targeted in that study, I_{Kr}, is present in ventricular cardiomyocytes; I_{Kr} block leads to prolongation of the QT interval, the electrocardiographic correlate of the action potential duration, increasing the risk of malignant ventricular arrhythmias. The ultra-rapid delayed-rectifier K^+ current, I_{Kur}, is only functionally expressed in atrial cardiomyocytes, making it an attractive atrial-selective target. There is experimental data indicating that I_{Kur} inactivates completely at depolarized potential and is downregulated in chronic AF (electrical remodeling), casting doubts as to its value as an antiarrhythmic target. In this paper, we sought to update the mathematical formulation for I_{Kur} to account for experimentally-observed inactivation dynamics and then used this model to investigate the role of I_{Kur} inactivation and AF-induced downregulation on the action potential dynamics.

4.1 Rate-Dependent Role of I_{Kur} in Human Atrial Repolarization and Atrial Fibrillation Maintenance

Martin Aguilar, Jianlin Feng, Edward Vigmond, Philippe Comtois et Stanley Nattel

Biophys J. 2017;112:1997-2010

4.1.1 Abstract

The atrial-specific ultra-rapid delayed rectifier K^+ current (I_{Kur}) inactivates slowly but completely at depolarized voltages. The consequences for I_{Kur} rate-dependence have not been analyzed in detail and currently-available mathematical action-potential models do not take into account experimentally-observed I_{Kur} inactivation dynamics. Here, we developed an updated formulation of I_{Kur} inactivation that accurately reproduces time-, voltage- and frequency-dependent inactivation. We then modified the human atrial cardiomyocyte Courtemanche action-potential model to incorporate realistic I_{Kur} inactivation properties. Despite markedly different inactivation dynamics, there was no difference in action-potential parameters across a wide range of stimulation frequencies between the original and updated model. Using the updated model, we showed that, under physiological stimulation conditions, I_{Kur} does not inactivate significantly even at high atrial rates because the transmembrane potential spends little time at voltages associated with inactivation. Thus, channel dynamics are determined principally by activation kinetics. I_{Kur} magnitude decreases at higher rates because of action potential changes that reduce I_{Kur} activation. Nevertheless, the relative contribution of I_{Kur} to action potential repolarization increases at higher frequencies because of reduced activation of the rapid delayed-rectifier current I_{Kr}. Consequently, I_{Kur}-block produces dose-dependent termination of simulated AF in the absence of AF-induced electrical remodeling. The inclusion of AF-related ionic remodeling stabilizes simulated AF and greatly reduces the predicted antiarrhythmic efficacy of I_{Kur}-block. Our results explain a range of experimental observations, including recently-reported positive rate-dependent I_{Kur}-blocking effects on human atrial action-potentials, and provide insights relevant to the potential value of I_{Kur} as an antiarrhythmic target for the treatment of AF.

Keywords: atrial action potential model – potassium channel inactivation – human electrophysiology – antiarrhythmic drug therapy

4.1.2 Introduction

The ultra-rapid delayed rectifier K^+ current (I_{Kur}) was originally described as a rapidly activating, 4-aminopyridine-sensitive K^+ current with slow and limited inactivation (170). However, many of the original experiments used relatively short test pulses, typically less than 4 s long, which may have not been enough to observe the full extent of I_{Kur}'s inactivation. Feng et al., using longer 50-s test pulses, showed that I_{Kur} inactivates almost completely when depolarized to +40 mV, with a bi-exponential time course comprising fast (τ_f) and slow time constants (τ_s) of 1.0 s and 6.8 s, respectively (171). Based on these experiments, it has been hypothesized that I_{Kur} inactivation may play an important role under physiological conditions, specifically related to I_{Kur} frequency-dependent dynamics (171). The potential for full inactivation of I_{Kur} suggests that the contribution of the current would decrease at faster rates, as the total amount of time the cell is depolarized increases at faster rates and inactivation accumulates. However, recent experimental results using the I_{Kur}-selective blocker XEN-D0103 suggest the opposite, and indicate that the contribution of I_{Kur} to atrial repolarization increases at higher rates (172).

To our knowledge, none of the commonly used mathematical models of the human atrial cardiomyocyte action potential (AP) integrate the experimentally-defined I_{Kur} inactivation dynamics reported by Feng et al. In order to better understand the rate-dependent role of I_{Kur} and the effect of blocking it on the human atrial AP, it is necessary to use a model with accurate inactivation properties. In the present study, we sought to (i) quantify the kinetic features of the I_{Kur} inactivation properties defined by Feng et al.; (ii) update the Courtemanche human atrial AP model (112) to include realistic I_{Kur} inactivation parameters; (iii) investigate the rate-dependent properties of I_{Kur} inactivation over the course of the AP under physiological conditions; (iv) evaluate the contribution of I_{Kur} with realistic inactivation properties to human atrial repolarization at different frequencies; and (v) evaluate the potential consequences for effects of blocking I_{Kur} on atrial fibrillation (AF) in non-remodeled and AF-remodeled atrial tissue.

4.1.3 Materials and Methods

4.1.3.1 Mathematical modeling of I_{Kur} inactivation

The experimental data recorded by Feng et al. were used as the basis for model development in our study (171). A description of the experimental methods can be found in the original paper (171). The Courtemanche human atrial cardiomyocyte model was implemented (112). The original formulation of the I_{Kur} inactivation parameter is as follows

$$I_{\mathrm{Kur}} = C_{\mathrm{m}} \cdot g_{\mathrm{Kur}} \cdot u_{\mathrm{a}}^{3} \cdot u_{\mathrm{i}} \cdot (V - E_{\mathrm{K}})$$

$$g_{\mathrm{Kur}} = 0.005 + \frac{0.05}{1 + \exp\left(-\frac{V - 15}{13}\right)}$$

$$\alpha_{\mathrm{ui}} = \left[21 + \exp\left(-\frac{V - 185}{28}\right)\right]^{-1}$$

$$\beta_{\mathrm{ui}} = \exp\left(\frac{V - 158}{16}\right)$$

$$\tau_{\mathrm{ui}} = [\alpha_{\mathrm{ui}} + \beta_{\mathrm{ui}}]^{-1}/K_{\mathrm{Q10}}$$

$$u_{\mathrm{i},\infty} = \left[1 + \exp\left(\frac{V - 99.45}{27.48}\right)\right]^{-1}$$

$$\frac{\mathrm{d}u_{\mathrm{i}}}{\mathrm{d}t} = \frac{u_{\mathrm{i},\infty} - u_{\mathrm{i}}}{\tau_{\mathrm{ui}}}$$

where I_{Kur} is the ultra-rapid delayed rectifier K^+ current, g_{Kur} is the maximal I_{Kur} conductance, V is the transmembrane potential, E_K is the K^+ equilibrium potential, u_a and u_i are I_{Kur}'s activation and inactivation gating variables, respectively, α_{ui} and β_{ui} are the forward and backward rate constants for the inactivation gate variable, respectively, τ_{ui} is the time constant, $u_{i,\infty}$ is the steady-state relation for the inactivation gate variable, C_m is the membrane capacitance (100 pF) and K_{Q10} is a scaling factor (3).

To account for I_{Kur} inactivation dynamics we replaced the original inactivation gating variable u_i by fast ($u_{i,f}$) and slow ($u_{i,s}$) inactivation gating variables. The gating variables and time constant parameters were fitted by iteratively minimizing the mean error of the model time constants relative to experimentally-derived values obtained with a 50-s test-pulse at 0, 10, 20, 30, 40 and 50 mV (Supplemental Figure 4.1B-C); the modified inactivation gating variables and time constants are given by

$$\tau_{\mathrm{ui,f}} = 800 \cdot \left(2 - \frac{V}{40}\right)$$

$$u_{\mathrm{i,f}\infty} = \left[1 + \exp\left(\frac{V - 35}{20}\right)\right]^{-1}$$

$$\tau_{\mathrm{ui,s}} = 5800 \cdot \left[1 + \exp\left(-\frac{V + 80}{11}\right)\right]^{-1}$$

$$u_{\mathrm{i,s}\infty} = \left[1 + \exp\left(\frac{V + 5}{5}\right)\right]^{-1}$$

$$\frac{\mathrm{d}u_{\mathrm{i,x}}}{\mathrm{d}t} = \frac{u_{\mathrm{i,x}\infty} - u_{\mathrm{i,x}}}{\tau_{\mathrm{ui,x}}}$$

$$I_{\mathrm{Kur}} = C_{\mathrm{m}} \cdot g_{\mathrm{Kur}} \cdot u_{\mathrm{a}}^3 \cdot u_{\mathrm{i,s}} \cdot u_{\mathrm{i,f}} \cdot (V - E_{\mathrm{K}})$$

The activation gating variable and time constant were not modified and are given by

$$\tau_{\mathrm{ua}} = [\alpha_{\mathrm{ua}} + \beta_{\mathrm{ua}}]^{-1} / \mathrm{K}_{\mathrm{Q10}}$$

$$\alpha_{\mathrm{ua}} = 0.65 \left[\exp\left(-\frac{V + 10}{8.5}\right) + \exp\left(-\frac{V - 30}{59}\right)\right]^{-1}$$

$$\beta_{\mathrm{ua}} = 0.65 \left[2.5 + \exp\left(\frac{V + 82}{17}\right)\right]^{-1}$$

$$u_{a,\infty} = \left[1 + \exp\left(-\frac{V + 30.3}{9.6}\right)\right]^{-1}$$

The activation gate open probability is given by u_a^3. The inactivation gate open probability in the original model was given by u_i; in the modified model $u_{i,s} \times u_{i,f}$ was used to reflect the combined effects of slow and fast inactivation components. Open probabilities range from 0 (closed) to 1 (open). The charge carried by I_{Kur} in one cardiac cycle, given by the area under the I_{Kur} versus time curve (Kur AUC), was calculated by integrating I_{Kur} over one cardiac cycle. The activation gate open-probability area under the curve (u_a^3 AUC) was calculated by integrating u_a^3 over one cardiac cycle. The action potential amplitude (APA) was defined as the difference between the peak phase-0 overshoot potential and the resting membrane potential.

4.1.3.2 Mathematical simulations

The Courtemanche model of human atrial cardiomyocyte bioelectricity was implemented with the original and updated I_{Kur} inactivation formulations. The total ionic current for the model (I_{tot}) was given by:

$$I_{tot} = I_{Na} + I_{K1} + I_{to} + I_{Kur} + I_{Kr} + I_{Ks} + I_{Ca,L} + I_{p,Ca} + I_{NaK} + I_{NaCa} + I_{b,Na} + I_{b,Ca} + I_{K,ACh}$$

where I_{Na} is the fast inward Na^+ current, I_{K1} is the inward rectifier K^+ current, I_{to} is the transient outward K^+ current, I_{Kur}, I_{Kr} and I_{Ks} are the ultra-rapid, rapid and slow components of the delayed rectifier K^+ current, $I_{Ca,L}$ is the L-type inward Ca^{2+} current, $I_{p,Ca}$ is the sarcoplasmic Ca^{2+} pump current, I_{NaK} is the Na^+/K^+ pump current, I_{NaCa} is the Na^+/Ca^{2+} exchanger current, $I_{b,Na}$ is the background Na^+ current, $I_{b,Ca}$ is the backgroud Ca^{2+} current and $I_{K,ACh}$ is the acetylcholine-activated K^+ current (47). Isolated cardiomyocytes were simulated at 37 ºC by numerical integration with the MATLAB ODE23s ordinary differential equation solver with relative tolerance of 10^{-2} (The Mathworks, Natick, MA). For each condition, pacing was sustained for 280 cycles with 2-ms 3 nA stimuli and the last action potential was used for analysis.

Computer simulations of the effect of I_{Kur} block on AF were performed with the CARP simulator, which solves the mono-domain equation by the finite element method as described

previously (173) to solve the monodomain equation

$$\nabla \cdot \sigma_i \nabla V = \beta \left(C_m \frac{\partial V}{\partial t} + I_{tot} \right)$$

where σ_i is the tissue conductivity, β is the membrane surface to volume ratio (0.14 μm^{-1}), and C_m is the membrane capacitance (1 $\mu F/cm^2$). The updated Courtemanche ionic model was adapted and implemented in CARP. Conductivities were chosen to give a physiological conduction velocity in the longitudinal direction (47.9 cm/s). The tissue measured 7×6 cm with fibers oriented along the long dimension with an anisotropy ratio of approximately 6. The grid was discretized at 100-μm resolution and equations solved with a 25-μs timestep. Reentry was initiated by a standard S1-S2 cross-shock protocol with an S1-S2 interval of 170 ms.

Two-dimensional simulations were conducted using 3 different acetylcholine (ACh) distribution patterns (1 homogeneous ACh distribution and 2 sinusoidal distributions) and 3 peak ACh concentrations (1.875 nM, 3.75 nM, 7.5 nM) generating 9 conditions. I_{Kur} block was simulated by a fixed reduction in maximal I_{Kur} conductance (g_{Kur}). Dose-response curves were generated by introducing I_{Kur} block at 10 different time-points [t_{drug} = 1000 ms, 1100 ms, … 1800 ms, 1900 ms] for each percent I_{Kur} block [10%, 20%, …, 90%, 100%]; the average time to termination was quantified as the time from t_{drug} to reentry termination. Simulations were run using the control (non-remodeled) Courtemanche human atrial action potential model and repeated with an AF-remodeled action potential model consisting of the control model with the following modifications: I_{to} conductance reduced by 50%, I_{Kur} conductance reduced by 50%, $I_{Ca,L}$ conductance reduced by 70% and I_{K1} conductance increased by 100% (46).

4.1.4 Results

4.1.4.1 Experimentally observed time-dependent inactivation of I_{Kur}

The ultra-rapid delayed rectifier K^+ current (I_{Kur}) is often described as having slow and partial inactivation. Figure 25A shows normalized I_{Kur} during a 1000 ms test-pulse to +40 mV, 5 ms after a 100-ms pre-test pulse to +40 mV to inactivate I_{to}, as recorded experimentally (black) (171) and from the original Courtemanche human atrial model (blue). Using this relatively short test pulse, experimental I_{Kur} inactivates by about 45% (black). In contrast to experimental data, in the original Courtemanche model, I_{Kur} does not inactivate appreciably over the course of the pulse (blue). Figure 25B shows normalized I_{Kur} during a longer, 50 s test-pulse to +40 mV, 5 ms after a 100-ms pre-test pulse to +40 mV to inactivate I_{to}. With the longer pulse, the experimentally-recorded I_{Kur} (black) inactivated completely with a bi-exponential time-course characterized by fast and slow time constants of 702±7 and 5688±26 ms, respectively. Again, the original Courtemanche model (blue) fails to reproduce I_{Kur}'s inactivation dynamics, with 85% of peak current persisting at the end of the 50-s test-pulse.

4.1.4.2 Model inactivation kinetics modified according to experimental data

In order to accurately reproduce the experimentally-recorded I_{Kur} inactivation kinetics, we modified the Courtemanche model by introducing a set of slow ($u_{i,s}$) and fast ($u_{i,f}$) inactivation gating variables in place of the inactivation gating variable (u_i) in the original model. The voltage dependence of the inactivation gating variables for the original ($u_{i,original}$, blue line) and modified ($u_{i,f}$, red solid line; $u_{i,s}$, red dashed line) is shown in Supplemental Figure 4.1A. The major modification to inactivation gating is more complete inactivation at depolarized potentials; the complete mathematical formulation can be found in the Methods. We also replaced the inactivation time constant ($\tau_{ui,original}$) with a set of fast ($\tau_{ui,f}$) and slow ($\tau_{ui,s}$) inactivation time constants (Supplemental Figure 4.1B). Note that the updated inactivation time constants are of the order of 1 to 6 s. The voltage dependence of the activation gating variable (Supplemental Figure 4.1C; $u_{a,x}$) and activation time constant (Supplemental Figure 4.1D, $\tau_{ua,x}$) were not modified. The activation time constant is in the range of 1 to 6 ms.

The modified model (red line) closely reproduced the experimentally-recorded current inactivation (black line) during a prolonged pulse (Figure 25B) and the experimentally-recorded I_{Kur} inactivation kinetics (Figure 25C) at 37 ºC. Excellent agreement between experiments and the mathematical model was obtained across the spectrum of test potentials.

4.1.4.3 Time-, voltage-, and frequency-dependence of I_{Kur} inactivation

We then compared the time dependence of I_{Kur} inactivation in the model to experimental results obtained by varying the duration of the test pulse. Figure 25D (black) shows experimentally-recorded normalized I_{Kur} obtained with conditioning pulses to +40 mV of varying durations, followed by a 100-ms pre-pulse to +40 mV to inactivate I_{to} and then a 100-ms test pulse to +40 mV. I_{Kur} displayed complete inactivation with conditioning pulses >20 s. In contrast, the original Courtemanche model-derived data showed little inactivation even with the longest conditioning-pulse duration (Figure 25D, blue). Conversely, the modified model closely replicated the experimental data (Figure 25D, red); the half-inactivation conditioning pulse duration ($CPD_{1/2}$) was 1100 ms at +40 mV. The voltage dependence of I_{Kur} inactivation was then assessed by applying a 50 s pre-test pulse to various voltages followed by a 240-ms test pulse to +40 mV; the experimentally recorded normalized I_{Kur} is shown in Figure 25E (black). I_{Kur} inactivation is highly dependent on the pre-test pulse potential. The original Courtemanche model (blue) did not reproduce the experimentally observed voltage-dependent inactivation dependence (black, Figure 25E), whereas the modified-model generated data (red) closely matched experimental findings. The experimental and modified-model half-inactivation voltages ($V_{1/2}$s) were -7.5±0.6 and -6.5 mV, respectively.

The frequency dependence of I_{Kur} inactivation was studied by applying 100 pulses of 100-ms duration to +40 mV at various frequencies, followed by a 100-ms conditioning pulse to +40 mV to inactivate I_{to} and a 140-ms test pulse to +40 mV. Experimentally, I_{Kur} displayed marked frequency dependence with 84% reduction at 4 vs 0.1 Hz (Figure 25F, black data). In contrast, the original Courtemanche model showed virtually no frequency dependence (Figure 25F, blue). The modified model was consistent with the experimental findings (Figure 25F, red).

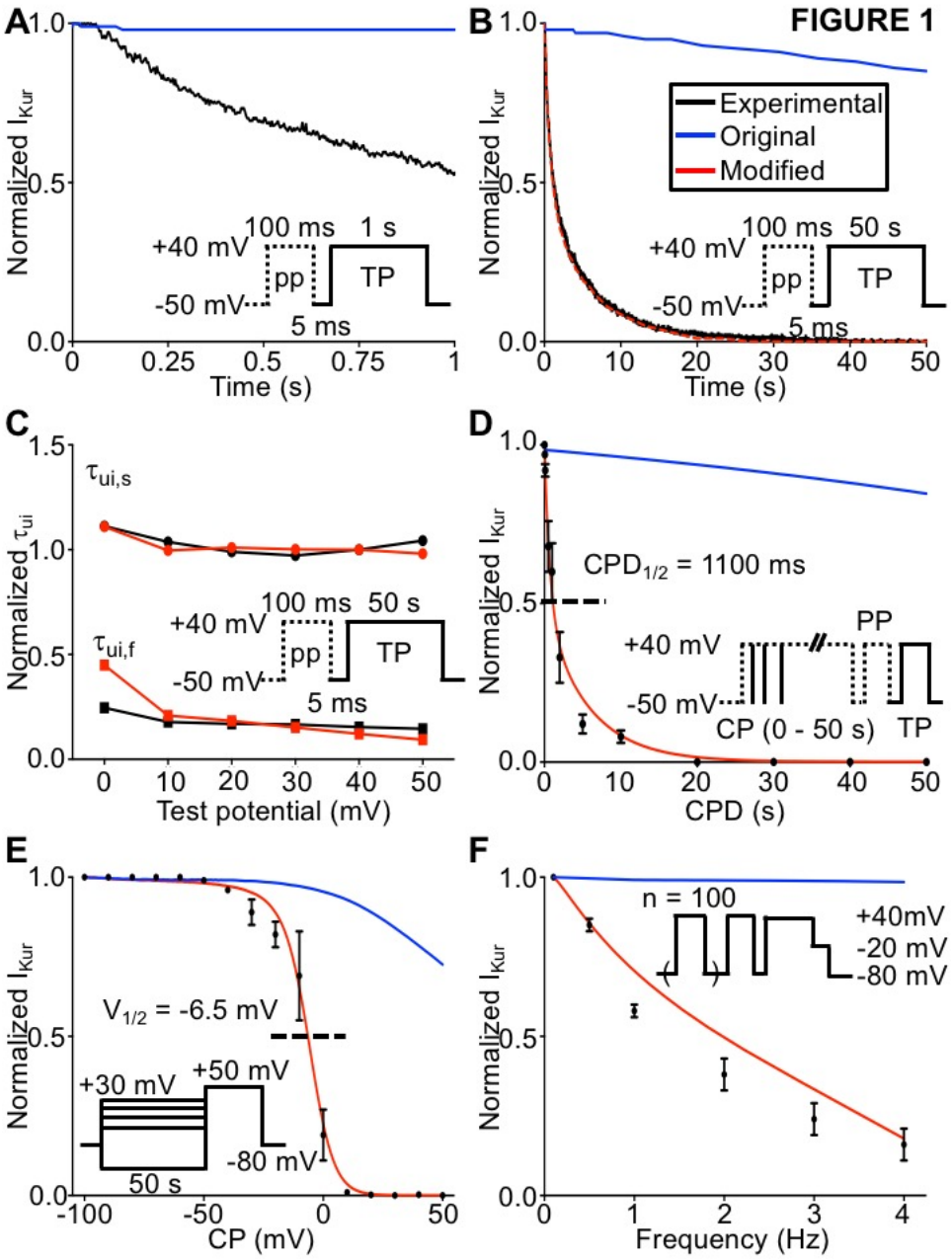

Figure 25. Time, voltage and frequency dependence of I_{Kur} inactivation. (A) Normalized I_{Kur} current during a 1000 ms test pulse (TP) at +40 mV, 5 ms after a 100 ms pre-pulse (PP) to inactivate I_{to} (inset) as recorded from the experimental preparation (black) and the original Courtemanche human atrial model (blue). (B) Normalized I_{Kur} current using a similar protocol but with test pulse duration of 50 s as recorded from the experimental preparation (black) and the original and modified Courtemanche model (blue and red, respectively). The experimental and modified model time constants are $\tau_{ui,f,exp}$ = 702 ± 7 ms and $\tau_{ui,s,exp}$ = 5688 ± 26 ms and

$\tau_{ui,f,model}$ = 713 ± 18 ms and $\tau_{ui,s,model}$ = 5848 ± 188 ms, respectively. (C) Normalized fast ($\tau_{ui,f}$) and slow ($\tau_{ui,s}$) time constants as a function of test pulse potential for the experimental preparation and the modified Courtemanche model at 37 ºC. (D) Normalized I_{Kur} current using a conditioning pulse of variable duration (CPD) to +40 mV, followed by a 100-ms pre-pulse (PP) to +40 mV to inactivate I_{to} preceding a 100-ms test pulse (TP) to +40 mV (inset) as recorded from the experimental preparation, original and modified models; the half-inactivation CPD ($CPD_{1/2}$) was 1100 ms. (E) Normalized I_{Kur} current using a 50 s-conditioning pulse (CP) to various voltages followed by a 240-ms test pulse to +40 mV (inset); the half inactivation voltage ($V_{1/2}$) was –6.5 mV in the model and –7.5 +/- 0.6 mV experimentally. (F) Normalized I_{Kur} current obtained by applying 100 pre-test stimuli of 100 ms duration at +40 mV at various frequencies followed by a 100 ms conditioning pulse to +40 mV to inactivate I_{to} and a 140-ms test pulse to +40 mV (inset); the normalized current at 4Hz was 16% of its value at 0.1 Hz. For all panels, experimental data are in black; original and modified models are in blue and red, respectively.

4.1.4.4 Incorporation of realistic I_{Kur} inactivation kinetics and AP dynamics

Supplemental Figure 4.2 shows the AP amplitude (APA, panel A), AP duration at 90% repolarization (APD_{90}, panel B), transmembrane potential at the time of maximum phase 0 overshoot (overshoot potential, panel C) and phase-0 peak Na^+ current (peak I_{Na}, panel D) as a function of cycle length (CL) for the original (black) and modified (red) Courtemanche models. Despite markedly different I_{Kur} inactivation kinetics, there were no significant differences in AP or Na^+-current dynamics between the two models across a wide range of physiologically-relevant cycle lengths. We then pursued the rate-dependent properties of I_{Kur} to understand why, despite much greater inactivation for both experimental and model pulse protocols than in the original Courtemanche model, there was no apparent effect on rate-dependent AP properties.

4.1.4.5 I_{Kur} activation and inactivation dynamics and mechanisms of rate-dependence

Figure 26A shows model APs at progressively shorter stimulation cycle lengths (750, 500, 300 and 265 ms). The AP duration is shortened and plateau potential becomes less positive

as the dome disappears when stimulation cycle length decreases. Figure 26B shows the corresponding I_{Kur} simulations. There is a rate-dependent decrease in I_{Kur} during phase-2 of the AP with little change in peak I_{Kur} (inset) except at the shortest cycle length (inset, red). Figures 26C and 26D show the corresponding activation and inactivation gate open probabilities (u_a^3; $u_{i,f} \times u_{i,s}$) as a function of time for the shortest (red) and longest (blue) cycle length. I_{Kur} activation decreases during phase 2 in a rate-dependent manner (Figure 26C), whereas inactivation is virtually rate-independent (Figure 26D). Therefore, I_{Kur} rate dependence is driven by its activation gate kinetics, with little contribution from inactivation. This is further detailed in Supplemental Figure 4.3 where the rate-dependence of the total I_{Kur} charge carried per cycle (panel B) is shown to be due to changes in rate-dependent activation-gate open probability (panel F), with no significant contribution from inactivation (panel D).

Figure 26E shows the steady-state activation gating variable as a function of transmembrane potential with the voltage for 50% ($V_{0.5}$ = -30 mV) activation marked with a purple dot; $V_{0.5}$ is shown in panel A as a purple dashed line. For membrane potentials negative to $V_{0.5}$, the activation gate starts to close, whereas for potentials positive to $V_{0.5}$, the activation gate is mostly open. The activation-variable (u_a^3; panel C) rate dependence can be understood based on the AP time course (panel A) and u_a's voltage dependence (panel E). At slower stimulation frequencies like a cycle length of 750 ms (blue curve), the plateau potential is positive to $V_{0.5}$ (dashed purple line in panel A) for the duration of phase-2 of the AP, keeping u_a largely open. It is only at the end of the AP plateau that the membrane potential falls below $V_{0.5}$ leading to appreciable decreases in u_a and return of the activation gate open probability towards 0 ($u_a^3 = 0$, closed, panel C). In contrast, at faster stimulation frequencies such as at a cycle length of 265 ms (red curve), the plateau potential is negative to $V_{0.5}$ starting at the end of phase-1 (panel A), leading to earlier and more rapid closure of the activation gate (red curve in panel C). The activation-gate time constant is in the range of 1 to 6 ms (Supplemental Figure 4.1D), which allows the activation gate to closely track changes in membrane potential.

Figure 26F shows the fast ($u_{i,f}$, solid black line) and slow ($u_{i,s}$, black dashed line) inactivation gating-variables as a function of test potential, with the slow inactivation-gating variable $V_{0.5}$ marked by teal dot. For membrane potentials positive to $V_{0.5}$ (teal dot), the slow

inactivation gate starts to close whereas for membrane potentials negative to $V_{0.5}$, the inactivation gates are mostly open. Figure 26D shows the inactivation gate open probability ($u_{i,f} \times u_{i,s}$) as a function of time at stimulation cycle lengths of 265 ms (red) and 750 ms (blue). The rate *in*dependence of $u_{i,f} \times u_{i,s}$ (panel D, blue vs red) can be explained from the AP time course (panel A) and u_i's voltage dependence (panel F). For the slow inactivation gate to close, the membrane potential needs to be positive to $V_{0.5}$ (-5 mV). For the fast inactivation variable, the voltage dependence is even more positive. However, the AP, both at cycle lengths of 265 and 750 ms, spends negligible time at potentials positive to the $V_{0.5}$ of either fast or slow inactivation (positive to the blue dashed line in panel E). Moreover, the inactivation time constants are > 1 s (Supplemental Figure 4.1B), at least 2 orders of magnitude longer than the time the membrane spends above $V_{0.5}$. Hence, because the membrane spends very little time positive to $V_{0.5}$ and the inactivation gate time constants are slow to close, the inactivation gating variables remain mostly in their open state (>0.93 fractional availability, Figure 26D) irrespective of activation frequency.

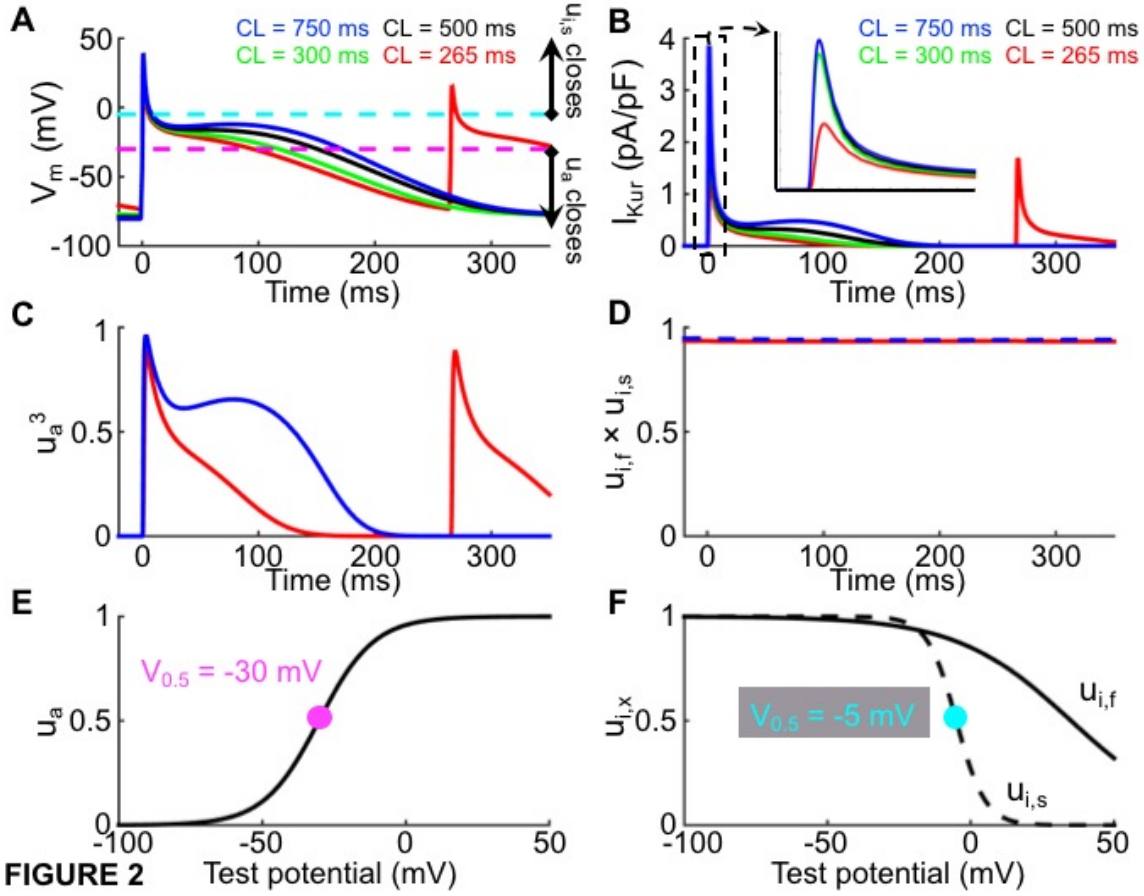

Figure 26. Mechanism of I_{Kur} rate dependence. (A) Action potentials at stimulation cycle lengths from 265 ms (red), 300 ms (green), 500 ms (black), and 750 ms (blue). The purple and teal dashed lines correspond to the activation and inactivation gating variable 50% ($V_{0.5,ua}$ = -30 mV and $V_{0.5,uis}$ = -5 mV) opening potentials, respectively. (B) Corresponding I_{Kur} tracings; there is a rate-dependent decrease in I_{Kur} during phase 2 of the action potential. (C) activation gate open probability (u_a^3) and (D) inactivation gate open probability ($u_{i,f} \times u_{i,s}$) as a function of time for cycle lengths (CLs) of 265 ms (red) and 750 ms (blue). The activation open probability is rate-dependent and the inactivation open probability is rate independent. (E) Activation gating variable (u_a) as a function of transmembrane potential (V_m); the purple dot corresponds to activation gating variable $V_{0.5}$ as transposed on panel A. (F) Fast ($u_{i,f}$; black solid) and slow ($u_{i,s}$; black dashed) inactivation gating variables as a function of transmembrane potential; the teal dot corresponds to the slow inactivation gating variable $V_{0.5}$ as transposed on panel A. The

inactivation open probability is rate independent because the action potential spends very little time positive to $V_{0.5,uis}$ (-5 mV; teal).

4.1.4.6 Rate-dependent effects of I_{Kur} block on AP properties and underlying mechanism

When I_{Kur} is blocked, the plateau voltage is raised and I_{Kr} is enhanced, counteracting the repolarization delays caused by I_{Kur}-block (174). Consequently, in order to understand the rate-dependent AP changes caused by I_{Kur}-block, it is essential to analyze the associated changes in I_{Kr}. Figure 27A shows the steady-state I_{Kr} activation-gate variable in the Courtemanche model as a function of test potential, with $V_{0.1}$ (-28 mV), $V_{0.5}$ (-14 mV), $V_{0.75}$ (-7 mV) and $V_{0.9}$ (0 mV) marked and transposed as dashed lines onto panel B. Panels B, C and D show the AP, I_{Kur} and I_{Kr} simulations obtained at a cycle length of 1000 ms under control conditions (blue) and with 75% I_{Kur} block (red). I_{Kur} block elevates the plateau potential, bringing the membrane potential positive to I_{Kr}'s $V_{0.5}$ (-14 mV; green dashed line in panel B) for the duration of phase-2 of the AP, leading to a 136% increase in I_{Kr}, an acceleration in phase 3 repolarization and no net change in overall APD (panel B; APD_{-60} control vs I_{Kur} block = 255 ms vs 256 ms, respectively). Panels E, F and G show the AP, I_{Kur} and I_{Kr} simulations at a cycle length of 250 ms under control conditions (blue) and with 75% I_{Kur} block (red). Because of the change in AP morphology at the short cycle length, I_{Kur} block-induced elevation of the plateau fails to keep the plateau potential in the I_{Kr} activation range (e.g. $V_{0.5}$ of -14 mV; green dashed line in panel E), hence, there is little I_{Kr} recruitment (ratio of total I_{Kr} with I_{Kur} block vs control = 1.40), leading to APD prolongation (APD_{-60} under control vs I_{Kur}-block conditions of 199 and 209 ms, respectively). Therefore, despite the fact that I_{Kur} is smaller at rapid frequencies, the ability of I_{Kur} block to prolong APD is enhanced.

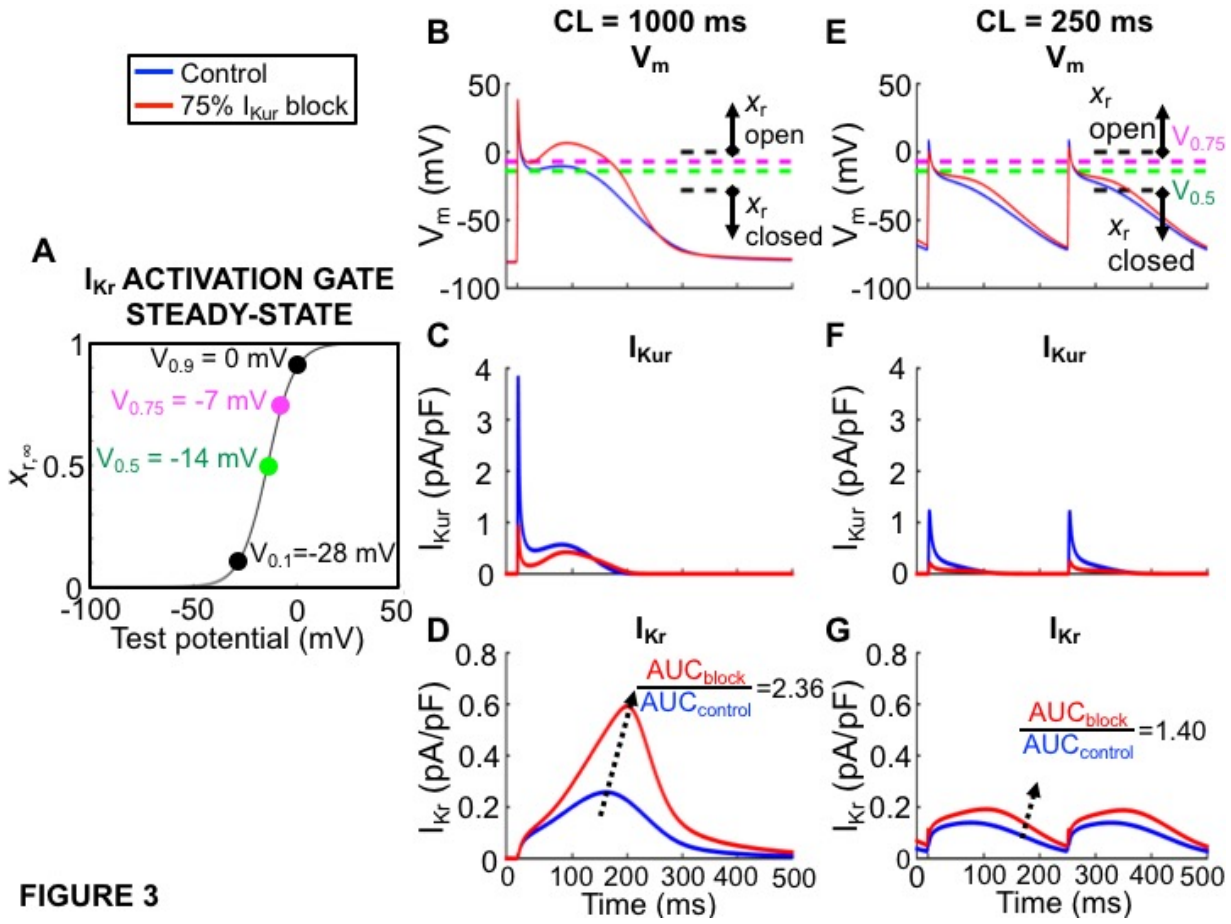

FIGURE 3

Figure 27. Rate-dependent effects of I_{Kur} block on the action potential. (A) I_{Kr} activation gate steady-state ($x_{r,\infty}$) as a function of test potential. The $V_{0.1}$, $V_{0.5}$, $V_{0.75}$ and $V_{0.9}$ are marked and transposed onto panels B and E as dashed lines. (B) Action potentials obtained at a cycle length of 1000 ms under control (blue) and with 75% I_{Kur} blockade (red); the action potential duration at -60 mV (APD_{-60}) was 255 ms for both. (C-D) Corresponding I_{Kur} and I_{Kr} tracings; the ratio of I_{Kr} with 75% I_{Kur} block to control was 2.36. (E) Action potentials obtained at a cycle length of 250 ms under control (blue) and with 75% I_{Kur} blockade (red); the APD_{-60} for control and 75% I_{Kur} block was 199 ms and 209 ms, respectively. (F-G) Corresponding I_{Kur} and I_{Kr} tracings; the ratio of I_{Kr} with 75% I_{Kur} block to control was 1.40.

4.1.4.7 I_{Kur} block and AF termination

The above analysis suggests that the APD-prolonging effect of I_{Kur} blockade is preserved at rapid rates and might result in an ability to suppress AF. We therefore studied the effect of

I_{Kur} block on simulated 2-dimensional cholinergic AF. We generated 9 acetylcholine (ACh) conditions (Supplemental Figure 4.4); re-entry was sustained for >5 seconds across conditions but displayed markedly different dynamics ranging from single spiral wave re-entry (Supplemental Figure 4.5) to multiple, short-lived wavelets (Figures 28 and Supplemental Figures 29-30 for representative examples). In line with our single-cell results, there were no significant differences in re-entry dynamics, APD_{-60} distribution and depolarized fraction between the original and modified I_{Kur} inactivation models (Figure 29 and Supplemental Figures 4.7-8 for representative examples). Using the non-remodeled Courtemanche human action potential model, we found a dose-dependent relationship between AF termination efficacy and percent I_{Kur} block (Figure 30). Re-entry termination was relatively infrequent with <50% I_{Kur} block but increased to over 90% of simulations at 100% I_{Kur} block for all conditions considered. We also found an inverse relationship between average time to termination and percent I_{Kur} block (Figure 30).

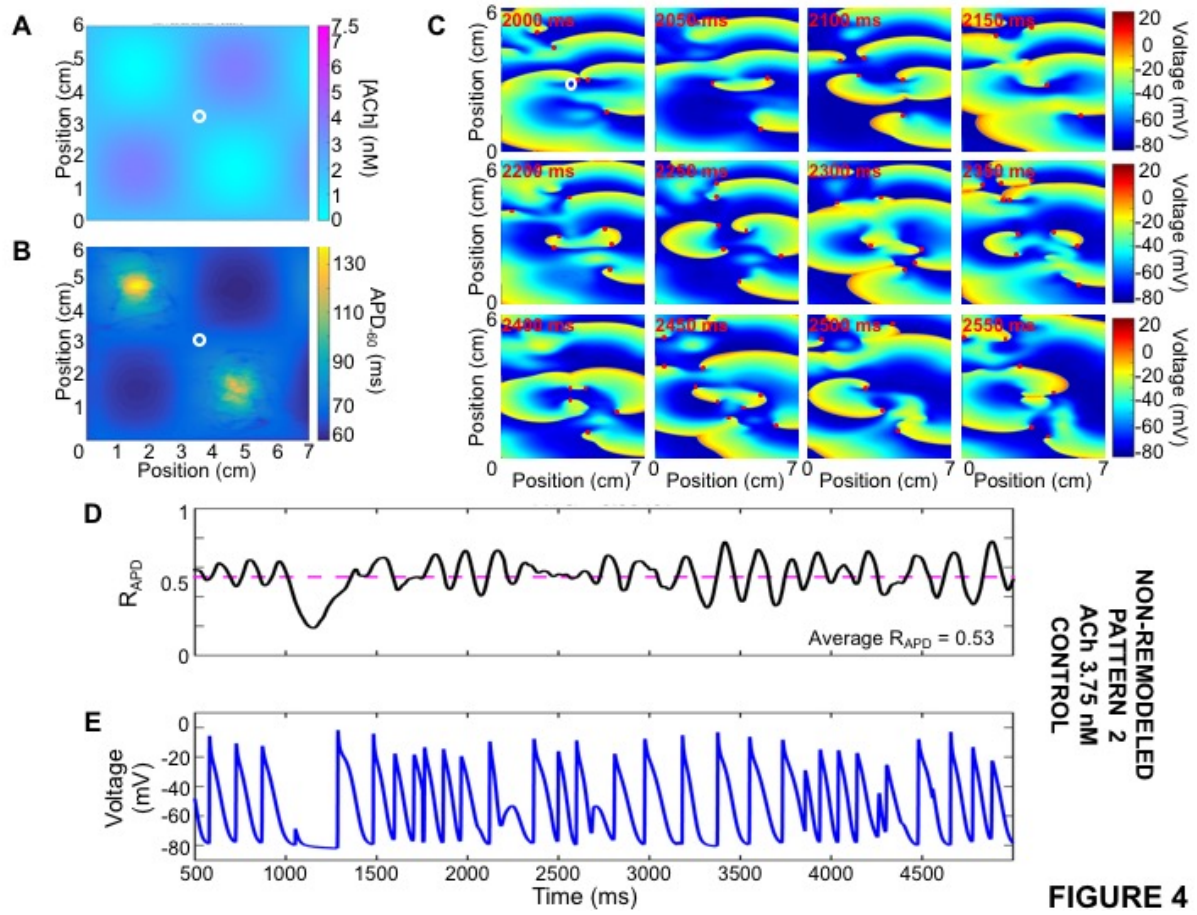

Figure 28. Representative example of simulated vagotonic AF using pattern #2 with peak ACh concentration of 3.75 nM and the non-remodeled cardiomyocyte model. (A) ACh distribution with peak concentration of 3.75 nM and (B) corresponding APD_{-60} distribution. (C) Transmembrane potential over time at 50 ms intervals; re-entry is maintained by multiple short-lived spiral waves. (D) Ratio of depolarized cells (ratio of cells with a voltage positive to -60 mV to the total number of cells) and (E) transmembrane potential over time for the cardiomyocyte marked with a white circle in panels A and B.

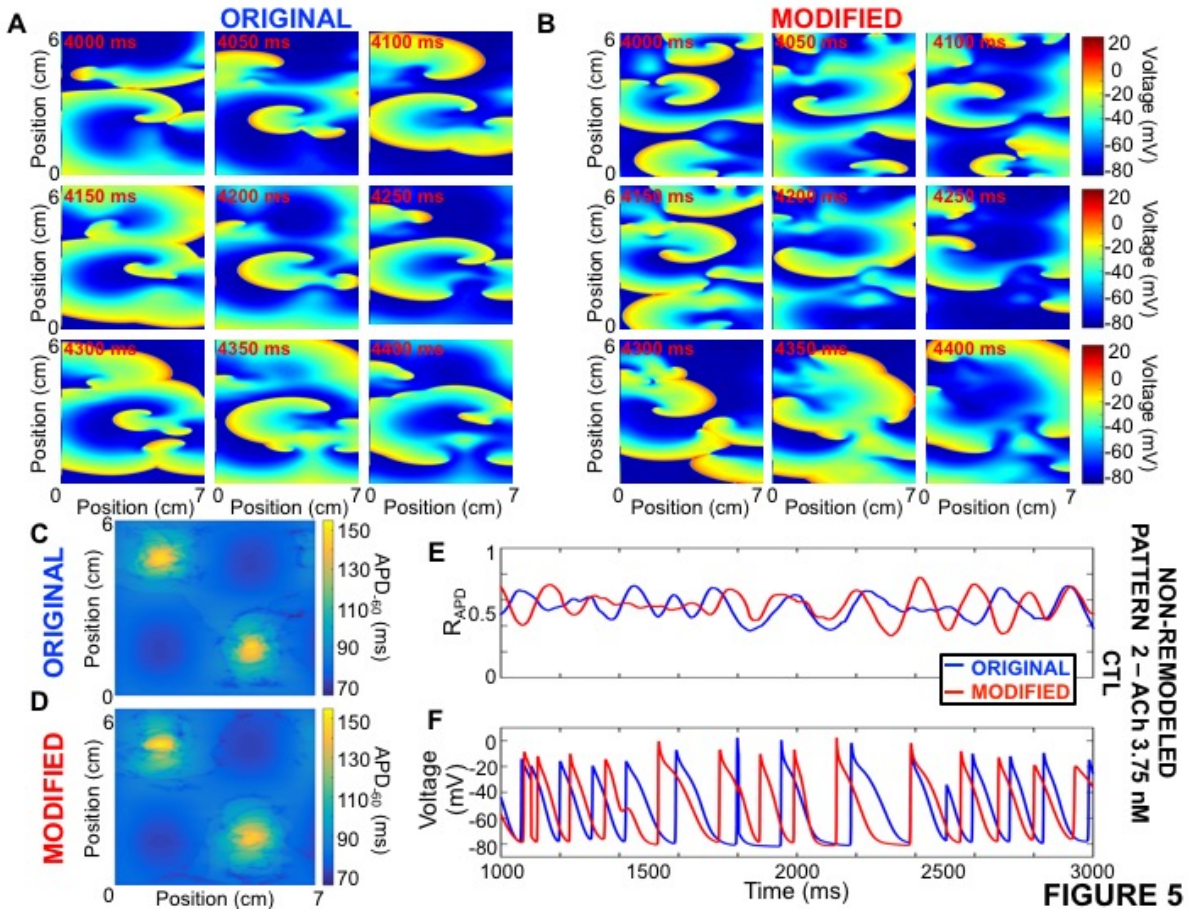

Figure 29. Representative example comparing re-entry dynamics in the original and modified models. (A-B) Transmembrane potential snapshots over time at 50 ms intervals for the original and modified models. (C-D) APD_{-60} for the original and modified models. (E-F) Ratio of depolarized cells (ratio of cells with a voltage positive to -60 mV to the total number of cells) and transmembrane potential for the original (blue) and modified (red) models. Non-remodeled cardiomyocyte model with ACh pattern #2 with peak concentration of 3.75 nM.

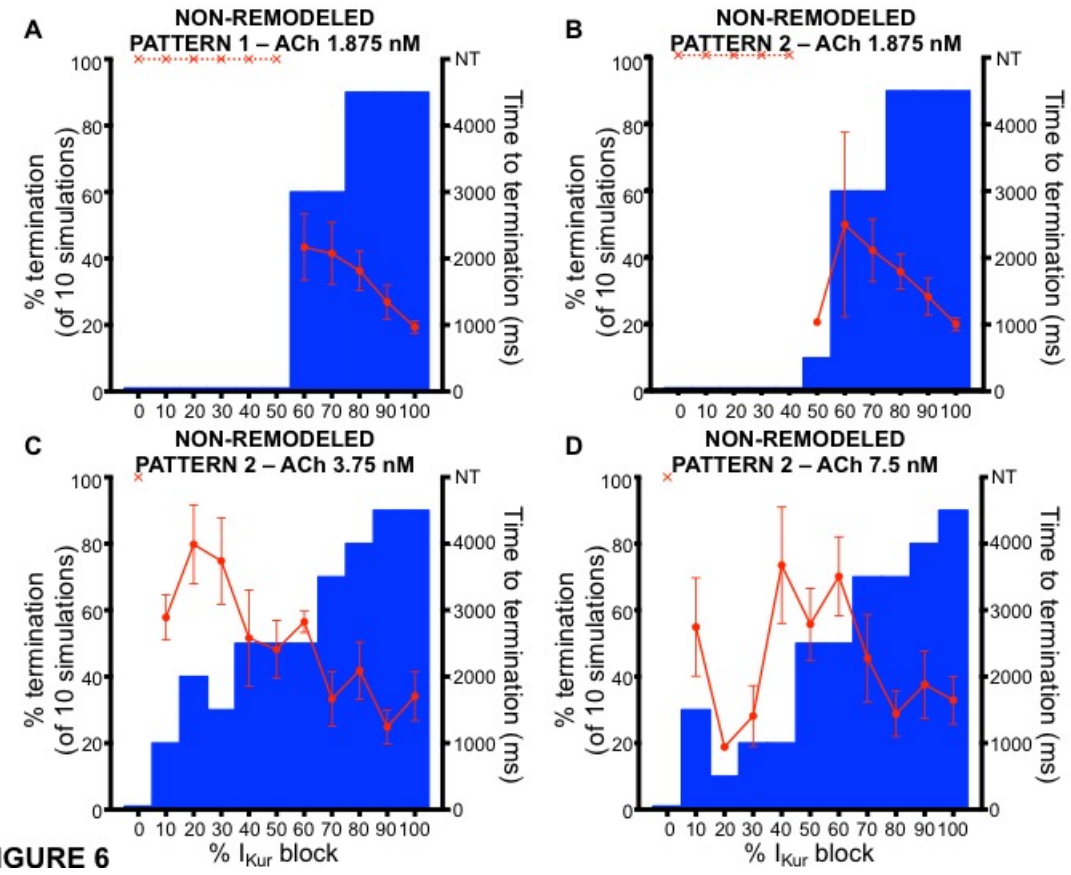

Figure 30. Dose-response and average AF termination time. Dose-response (bar-graphs) and average time to termination (red data) by I_{Kur} block using non-remodeled the non-remodeled cardiomyocyte model for (A) ACh pattern #1 with peak ACh concentration of 1.875 nM, (B-D) ACh pattern #2 and peak ACh concentration of 1.875 nM, 3.75 nM and 7.5 nM, respectively.

Figure 31 shows a representative example of successful AF termination by 50% I_{Kur} block with ACh pattern #2 and a peak concentration of 3.75 nM (panel A). The areas of largest ACh concentration had the shortest action potentials (panel B). I_{Kur} block prolonged refractoriness, increasing the excursion of the phase singularities, favoring wave-front collision, annihilation and re-entry termination (panels C-E). Supplemental Figure 4.9 shows the dynamics with the same ACh pattern/concentration but with 100% I_{Kur} block; the increased refractoriness is even more pronounced and termination more rapid. Consistent with a significant role of I_{Kur} in AP repolarization, the mean APD_{-60} increased from 85 ms under control conditions to 97 ms and 126 ms at 50% and 100% I_{Kur} block, respectively.

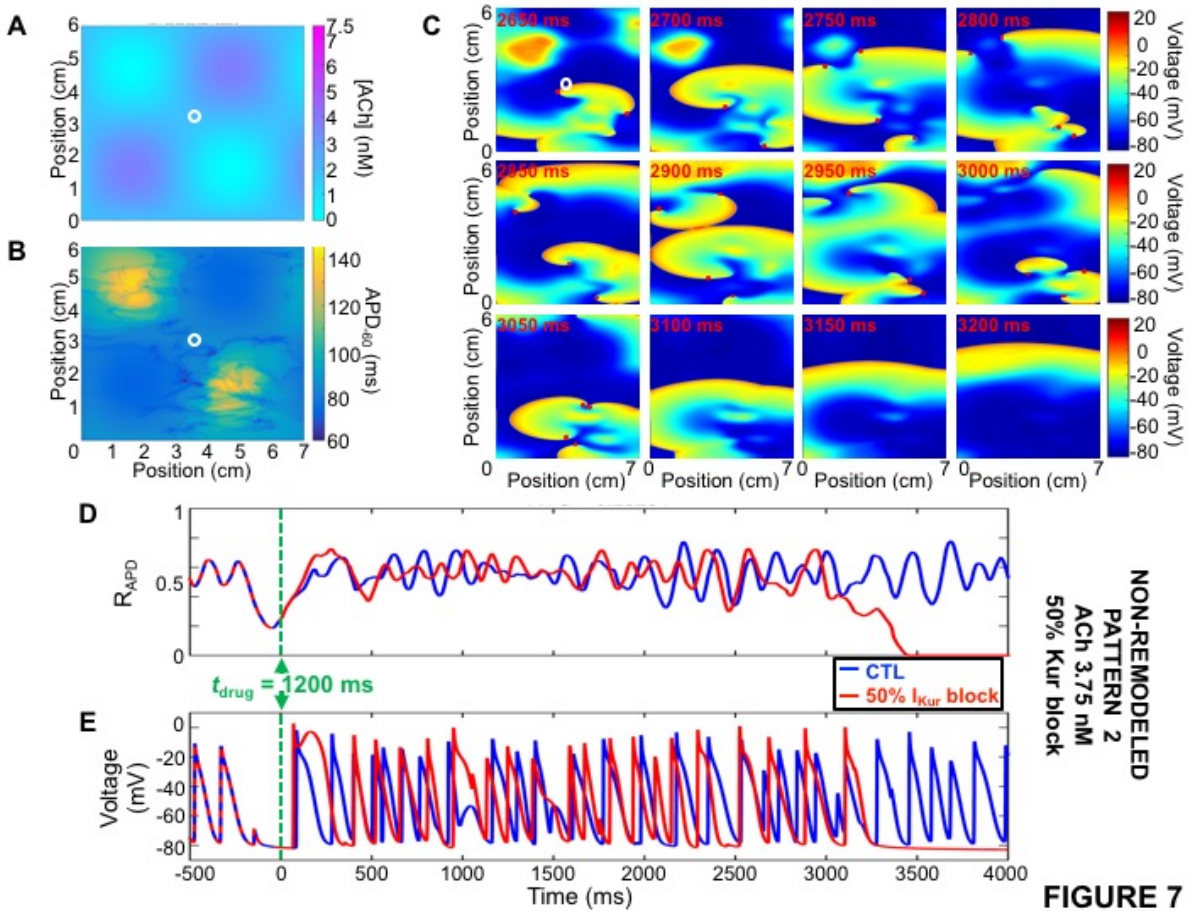

Figure 31. Representative example of re-entry termination by 50% I_{Kur} block using ACh pattern #2 with peak ACh concentration of 3.75 nM and the non-remodeled cardiomyocyte model. (A) ACh distribution with peak concentration of 3.75 nM and (B) corresponding APD_{-60} distribution. (C) Transmembrane potential snapshots over time at 50 ms intervals; 50% I_{Kur} block was introduced at t_{drug} = 1200 ms. (D) Ratio of depolarized cells (ratio of cells with a voltage positive to -60 mV to the total number of cells) and (E) transmembrane potential over time for the cardiomyocyte marked with a white circle in panels A and B for control (blue) and 50% I_{Kur} block (red).

We then sought to investigate whether I_{Kur} block could successfully terminate 2-dimensional AF under ionically remodeled conditions, such as in chronic AF. As previously reported (7), AF-remodeling conditions stabilize re-entry dynamics (Supplemental Figures 4.10-12) and ACh is no longer needed to maintain AF. Overall, the efficacy of I_{Kur}-block in

terminating AF in remodelled atria was very low, with no termination observed below 80% block and 10% termination at 90 and 100% block in the absence of ACh and across the 9 ACh conditions (see Supplemental Figure 4.13 for a representative example). At the cellular level, remodeling stabilized re-entry by (i) significantly shortening the APD_{90} (APD_{90} for non-remodeled vs remodeled was 283 ms vs 195 ms, respectively at CL 1000 ms; 204 ms vs 140 ms, respectively at APD_{90} at CL 250 ms) and (ii) hyperpolarizing the resting membrane potential (RMP) as compared to the non-remodeled cardiomyocyte (Figure 32A and B dashed vs solid) across a wide range of diastolic intervals (Figure 32C and 32D, blue). The I_{Kur} block-induced APD_{90} prolongation was preserved under remodeled conditions (Figure 32C vs 32D, red vs blue; ΔAPD_{90} at CL = 250 ms non-remodeled vs remodeled was 11 ms vs 10 ms, respectively). However, because the remodeled AP is of much shorter duration, the diastolic interval is long enough for the AP to return to the RMP before the next activation, even at rapid stimulation frequencies (Figure 32A, blue vs red dashed). Conversely, for the non-remodeled cardiomyocyte, even a small prolongation in APD encroaches on repolarization at short CLs (Figure 32A, blue vs red solid), and I_{Kur}-block causes APD alternans behavior at short CLs (Figure 32C). Hence, the differential efficacy of I_{Kur} blockade for AF termination in remodeled vs non-remodeled atria appears to be related to the remodeling-induced APD-abbreviation more than from I_{Kur} downregulation, since the APD prolongation caused by I_{Kur} block is preserved in remodeled cardiomyocytes.

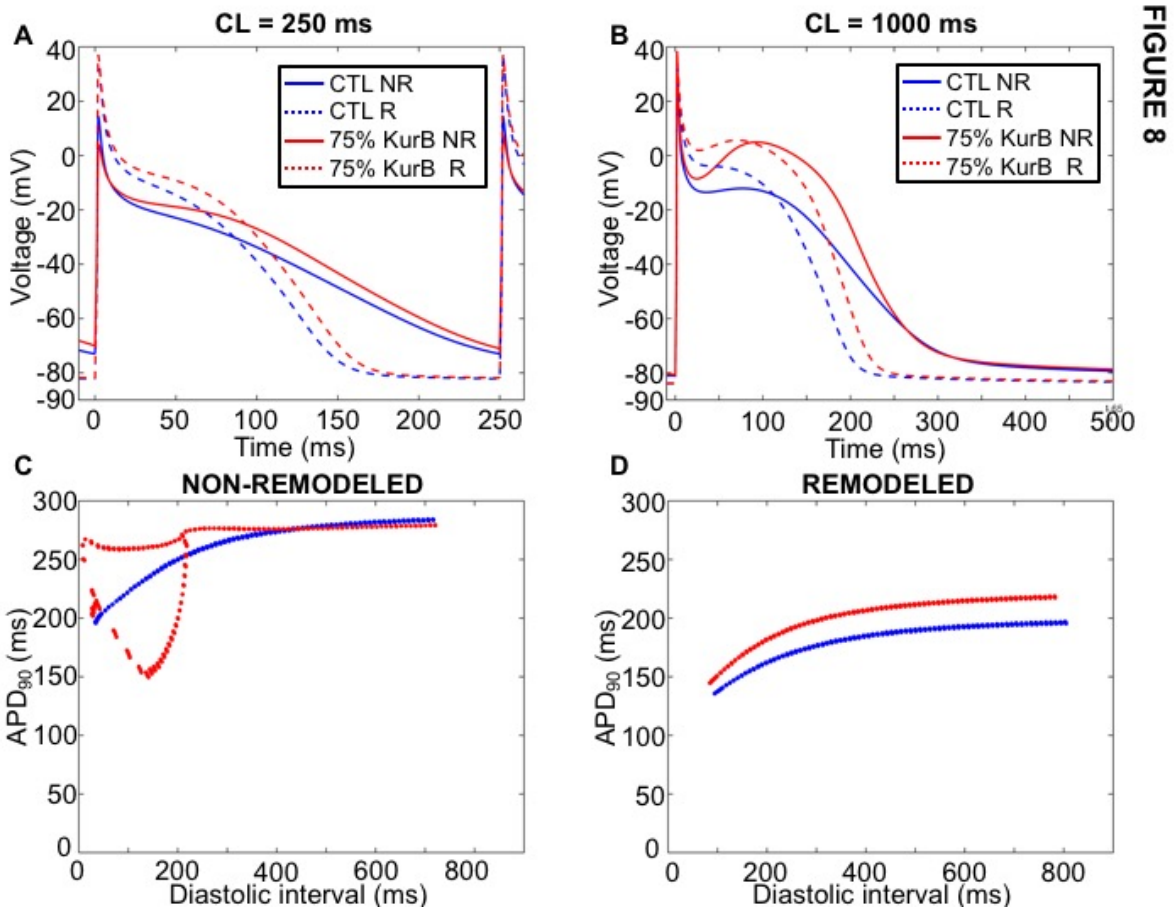

Figure 32. I_{Kur} blocking effects in remodeled cardiomyocytes. (A) Single cell action potential at a stimulation cycle length (CL) of 250 ms for a non-remodeled (NR; solid) and remodeled (R; dashed) cardiomyocyte without drug (blue) and with 75% I_{Kur} block (red). (B) Same as in (A) at CL of 1000 ms. (C) Action potential at 90% repolarization (APD_{90}) as a function of diastolic interval without drug (blue) and with 75 % I_{Kur} block (red) for a non-remodeled cardiomyocyte. (D) Same as in (C) but for a remodeled cardiomyocyte.

4.1.5 Discussion

4.1.5.1 I_{Kur} inactivation

In the present study, we have developed an updated formulation of I_{Kur} inactivation kinetics that reproduces experimentally observed I_{Kur} inactivation properties. Using the model, we have shown that, under physiological stimulation conditions, I_{Kur} dynamics are mainly

determined by its activation kinetics with relatively minor contribution from channel inactivation. Hence, (i) contrary to intuition, I_{Kur} inactivation does not accumulate at rapid stimulation frequencies, (ii) that despite a rate-dependent decrease in absolute I_{Kur} magnitude, the relative contribution of I_{Kur} to AP repolarization increases with increased activation frequency. We also found that I_{Kur} block terminates simulated cholinergic AF in a dose-dependent fashion in non-remodeled atrial tissue but is ineffective in the presence of simulated atrial remodeling. Since I_{Kur} is expressed in the human atrium but not ventricle (175), it is an interesting potential candidate for atrial-selective anti-AF therapy. Therefore, the demonstration that despite its potential for complete inactivation I_{Kur} maintains a significant contribution to repolarization dynamics and arrhythmia maintenance during AF is potentially significant.

4.1.5.2 Novel elements relative to prior in silico work

The initial reports characterizing I_{Kur} inactivation used relatively short test pulses, typically less than 5 s long, and therefore failed to observe the full scale of I_{Kur} inactivation (16, 176-180). Using 50-s test pulses, Feng et al. demonstrated that human atrial I_{Kur} inactivates fully, with a biexponential time-course characterized by rapid and slow time constants of 1.0 and 6.8 s, respectively (171). Moreover, I_{Kur} inactivation was found to be highly time-, voltage- and frequency-dependent. These observations raised the possibility that channel inactivation could accumulate at rapid activation frequencies, significantly decreasing I_{Kur}'s contribution to AP dynamics. If I_{Kur} inactivated completely at rapid activation frequencies, such as during AF, then I_{Kur} blockers would be predicted to have minimal antiarrhythmic effects. Paradoxically, and contrary to this intuitive expectation, recent work with the highly-selective I_{Kur} blocker XEN-D0103 found that I_{Kur} block prolongs the atrial APD and effective refractory period preferentially at rapid activation frequencies (172).

4.1.5.3 Mechanism of I_{Kur} rate dependence

To our knowledge, none of the commonly used human atrial *in silico* models correctly reproduces the experimentally-observed I_{Kur} inactivation kinetics. In the present investigation, we first analyzed experimental recordings of I_{Kur} inactivation in order to produce an accurate *in*

silico representation. We then studied I_{Kur} inactivation dynamics and rate-dependence with the updated model that accounted realistically for I_{Kur} inactivation (171) by introducing a set of fast and slow inactivation gating variables ($u_{i,f}$ and $u_{i,s}$) and corresponding time constants ($\tau_{ui,f}$ and $\tau_{ui,s}$). The modified model accurately reproduced I_{Kur} time-, voltage- and frequency-dependent inactivation across a wide range of physiological test potentials. Of note, the inactivation-gate time constants are three orders of magnitude slower than the activation-gate time constant (s vs ms). After including the updated I_{Kur} representation in the Courtemanche AP-model, we compared AP parameters as a function of stimulation cycle length and found no significant difference between the original and modified model results despite markedly different inactivation kinetics. We then applied our model to gain insight into the role of I_{Kur} activation and inactivation on I_{Kur} and its rate-dependent role in repolarization and arrhythmia maintenance.

4.1.5.4 Rate-dependent effect of I_{Kur} block on AP repolarization

We next sought to understand the mechanism underlying the positive rate-dependent effect of I_{Kur} block on the APD, as reported by Ford et al. (172). At slow stimulation frequencies, I_{Kur} block significantly elevated the AP plateau potential compared to control (no block), keeping the membrane at potentials for which I_{Kr}'s activation gate opens for the duration of phase-2 of the AP, leading to recruitment of I_{Kr} and compensating for I_{Kur} blockade with minimal effect on the APD. At rapid stimulation frequencies, the membrane potential is in negative to I_{Kr}'s half-activation potential leading to little I_{Kr} recruitment, limited compensation by I_{Kr} and I_{Kur} block-induced APD prolongation at rapid frequencies. Hence, although I_{Kur}'s absolute magnitude is less at rapid activation frequencies, the relative contribution of I_{Kur} to AP repolarization making I_{Kur} block a potentially interesting atrial-selective anti-AF strategy.

The mechanisms of reverse rate-dependency (RRD) of drug-induced APD changes have been a matter of substantial debate. Arguing from first principles, Zaza proposed that RRD is an intrinsic property of cardiac cells and that the same change in total transmembrane current will prolong long APs more than short ones (181). These predictions were supported by experimental work in which APD changes were shown to be proportional to the initial APD

using clinically available drugs like the class I agent lidocaine and class III agent dofetilide, as well as by applying inward or outward current pulses (182). The same group suggested that channel blockers may, at best, attenuate this intrinsic RRD but that forward rate-dependency (FRD) would be "difficult to attain" (182). In an elegant study using a series of ventricular cardiomyocyte models, Cummins et al. challenged this notion by suggesting that RRD can be overcome if rate-dependent AP morphological changes are large enough (183). In other words, the complex non-linear rate-dependent changes in current dynamics may be such that RRD could be offset, making FRD possible. For example, they showed that increasing $I_{Ca,L}$ ($g_{Ca,L}$) leads to FRD changes by elevating the AP plateau potential, leading to differential I_{Ks} activation at slow activation frequencies (183). Since I_{Kur} is not expressed in ventricular cardiomyocytes, the possible FRD properties of I_{Kur} block could not be evaluated. Our findings in atrial cardiomyocytes are however qualitatively in line with these observations, since we found that I_{Kur} block moves the AP plateau potential to more positive voltages, leading to differential I_{Kr} activation at slow vs rapid pacing rates and FRD APD-prolongation. Hence, FRD APD-prolongation, a highly desirable antiarrhythmic property, may be an attainable goal.

4.1.5.5 Relevance for antiarrhythmic drug development

We also found that I_{Kur} block terminates simulated cholinergic AF in a dose-dependent manner in non-ionically remodeled atrial tissue by prolonging refractoriness, increasing the re-entry wavelength, favoring rotor collision and annihilation. These findings are consistent with prior experimental work using relatively I_{Kur}-specific blockers in goats, rats, pigs, humans and *in silico* systems (184-188). Electrical remodeling shortened the APD and hyperpolarized the RMP, leading to very stable re-entry as previously described (46). The inability of I_{Kur} block to terminate simulated AF was greatly attenuated by remodeling, because the block-induced APD-prolongation was insufficient to counteract the strong effects of remodeling. The APD-prolonging effect of I_{Kur} block was not per se affected by channel downregulation. These observations are consistent with the report by Ford et al., in which APD_{90} prolongation induced by the I_{Kur}-selective blocker XEN-D0103's was maintained in chronic-AF human atrial cardiomyocytes (172). Scholz et al. found that I_{Kur} block was effective at terminating simulated AF, even in remodeled atria (188). However, they used slightly different remodeling parameters,

included gap junction remodeling, and did not incorporate I_{Kur} downregulation. The differential effectiveness of I_{Kur} block in non-remodeled vs remodeled atria is consistent with a prior randomized phase 3 clinical trial in which vernakalant, a mixed I_{Na}/I_{Kur} blocker, was much less effective at restoring sinus rhythm in patients with long lasting AF (4.0%) compared to recent-onset AF (51.7%) (189). Of note, recent experimental work demonstrated persistent antiarrhythmic efficacy of vernakalant in goats with remodeled atria owing to unaltered effects on Na^+-dependent parameters (conduction velocity and postrepolarization refractoriness) (190). Our findings suggest that the clinical efficacy of pure I_{Kur} block may be limited to recent-onset AF, in which remodeling has not taken place.

For the purposes of the present study, I_{Kur} block was simulated as a fixed reduction in maximal conductance (g_{Kur}). However, there is *in silico* and experimental evidence that the electrophysiological and antiarrhythmic effects of I_{Kur} blockade are modulated by the time- and voltage-dependent kinetics of block. Using a family of I_{Kur}-selective diphenyl phosphine oxide (DPO) compounds, Lagrutta et al. were able to show that I_{Kur} blocking potency and frequency dependence were a function of blocking kinetics, with open state blockers being the most effective I_{Kur} antagonists (191). Several other molecules, including vernakalant and experimental compounds like zatebradine, loratadine and bisindolylmaleimide, have also been shown to block I_{Kur} preferentially in the open-state (184, 192-194). Mathematical simulations support these findings and suggest that I_{Kur} blockers with rapid binding or slow unbinding kinetics have the strongest antiarrhythmic effects (188, 195). Further work is needed to analyze the effects (if any) on state-dependent drug block of adding realistic I_{Kur} inactivation kinetics.

Consistent with our present study, I_{Kur} block with XEN-D0101, a selective I_{Kur} blocker, prolonged the atrial effective refractory period (AERP) and decreased AF vulnerability in a dose- and rate-dependent manner in atrial tachycardia-induced remodeled canine atria. In human cardiomyocytes, XEN-D0101 prolonged AERP in AF-remodeled but not in non-remodeled tissue (196). However, experiments were conducted using a stimulation frequency of 1 Hz at which we predict no effect on APD and AERP based on the present study; rapid stimulation rates at which I_{Kur}-block induced prolongation of APD/atrial refractoriness would be expected were not reported. In coronary-perfused canine atria, 4-aminopyridine, a moderately-selective

I_{Kur} blocker, was found to shorten APD and to increase the propensity for AF, displaying only mildly antiarrhythmic effects in remodeled atrial (197). Again, the protocol employed a stimulation cycle length of 500 ms at which I_{Kur} block would not be expected to increase the APD or AERP. Furthermore, the mechanism of I_{Kur} in dog atrium is different from human and the magnitude is often very small (198). MK-0448 failed to prolong AERP in healthy human subjects using relatively slow stimulation cycle lengths of 400 and 600 ms at which I_{Kr} recruitment balances I_{Kur} block (199). I_{Kur} block rate-dependence, as described in the present study, along with species- and remodeling-related differences, likely account for these conflicting results. Finally, genetic studies reported both loss- and gain-of-function variants associated with the development of lone AF (200-203). Whether and how these observations in rare genetically-based forms of AF are applicable more broadly remains to be seen.

Na^+ channel blockers (NCBs) are moderately-effective antiarrhythmic drugs commonly used to control AF (39). It was recently reported that I_{Kr} block increases the anti-AF effects of an optimized NCB by delaying repolarization at rapid rates (204). However, I_{Kr} blockers have reverse-use dependent effects on APD, such that the APD-prolonging effect of I_{Kr} block is maximal at the slow rates of normal sinus rhythm (producing a serious risk of excess repolarization delay and ventricular proarrhythmia) and decreases markedly at rapid rates like those of AF. Given the positive rate-dependence of the APD-prolonging effect of I_{Kur} block, the addition of an I_{Kur} blocker to an optimized NCB would be expected to potentiate the NCB's anti-AF efficacy preferentially at rapid rates such as during AF. We have already shown evidence for this principle in a canine computational model (204). The work presented here provides tools and further rationale for testing this concept in human models.

4.1.5.6 Study limitations

The present study was performed in silico with extensive use of prior primary experimental patch-clamp data (171). The model predictions regarding the rate-dependent effects of I_{Kur} block on AP properties need to be tested prospectively in human tissue. Second, the model does not consider I_{Kur} modulation by adrenergic (205) or vagal tone, nor temperature dependence (171). However, the model was based on data obtained at normal body temperature

and should therefore be relevant to normal clinical conditions. Finally, as discussed above, we simulated I_{Kur} block with a fixed reduction in maximal conductance, whereas I_{Kur} block by antiarrhythmic drugs have been shown to depend on blocking kinetics and show state-dependent properties (188, 195, 206). Further computational analyses considering the state-dependent actions of specific I_{Kur} blockers might therefore be of interest.

Our simulations in remodeled atria have one major limitation. In order to compare remodeled results with those in non-remodeled conditions, we used the same I_{KACh} model and distributions. However, I_{KACh} is greatly reduced in remodeled atria (44). There are no realistic I_{KACh} models for remodeled atria. Future work is needed to create such models and use them to obtain a more accurate picture of I_{Kur}-blocking effects under these conditions.

4.1.6 Conclusions

An updated *in silico* model that accounts for experimentally-observed I_{Kur} inactivation kinetics shows that, contrary to possible intuitive inferences based on the potentially-complete inactivation shown by I_{Kur}, I_{Kur} inactivation is in fact negligible under physiologically-relevant conditions. On the contrary, the main determinant of I_{Kur} rate dependence is the response of its activation dynamics to frequency-dependent changes in AP-morphology. However, despite a smaller absolute I_{Kur} magnitude at rapid rates, the relative contribution of I_{Kur} to AP repolarization increases because of decreases in offsetting currents, particularly I_{Kr}. These positive rate-dependent effects allow I_{Kur} block to terminate AF and position it to have potentially valuable antiarrhythmic properties.

4.1.7 Supplemental Material

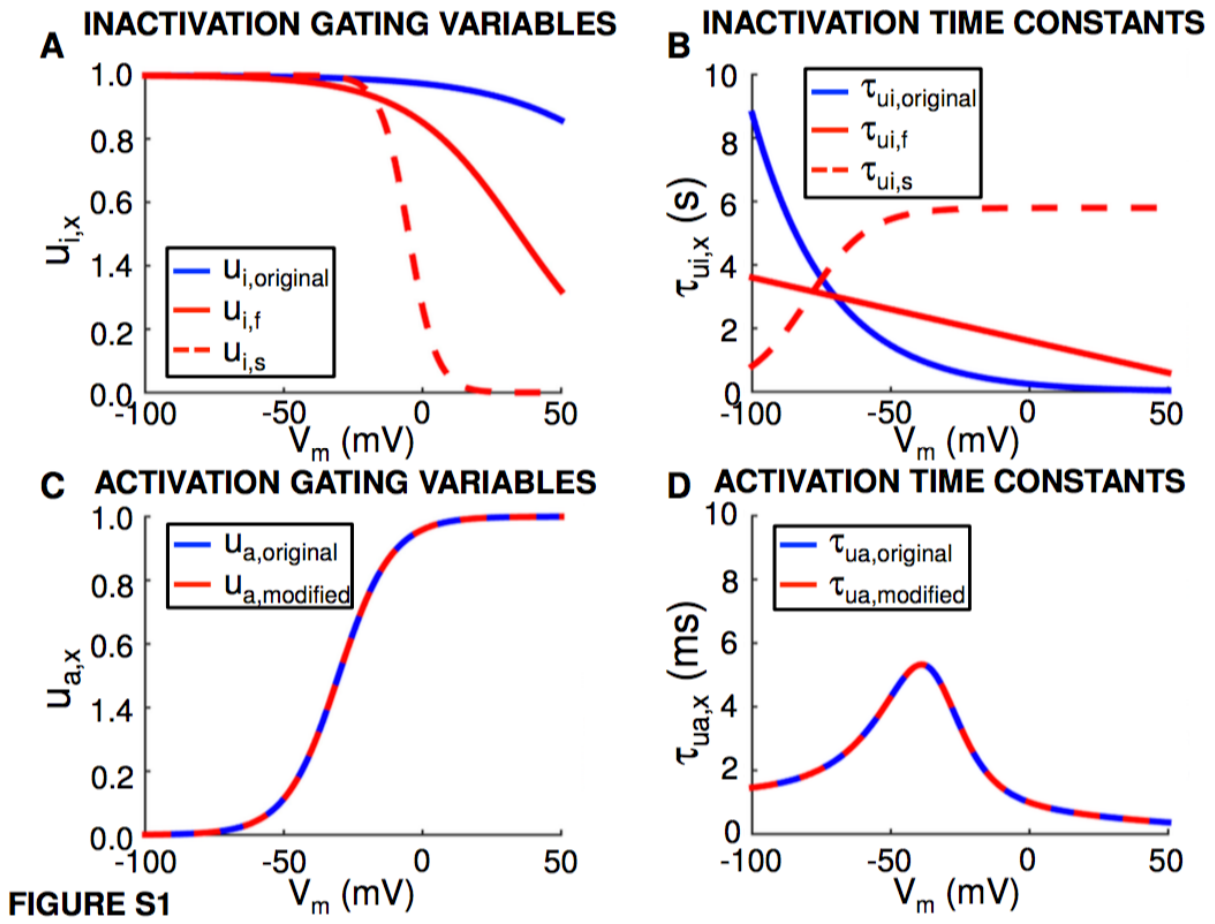

Supplemental Figure 4.1 Model inactivation and activation gating variables and time constants. (A) Inactivation gating variable as a function of transmembrane potential (V_m) for the original model ($u_{i,original}$; blue) and fast ($u_{i,f}$, red solid) and slow ($u_{i,s}$, red dashed) inactivation gating variables for the modified model. (B) Inactivation time constants as a function of transmembrane potential for the original ($\tau_{ui,original}$, blue) and modified ($\tau_{ui,f}$, red sold; $\tau_{ui,s}$, red dashed) model. (C) Activation gating variable as a function of transmembrane potential for the original ($u_{a,original}$, blue) and modified ($u_{a,modified}$, red) model. (D) Activation time constant as a function of transmembrane potential for the original ($\tau_{ua,original}$, blue) and modified ($\tau_{ua,modified}$, red) model.

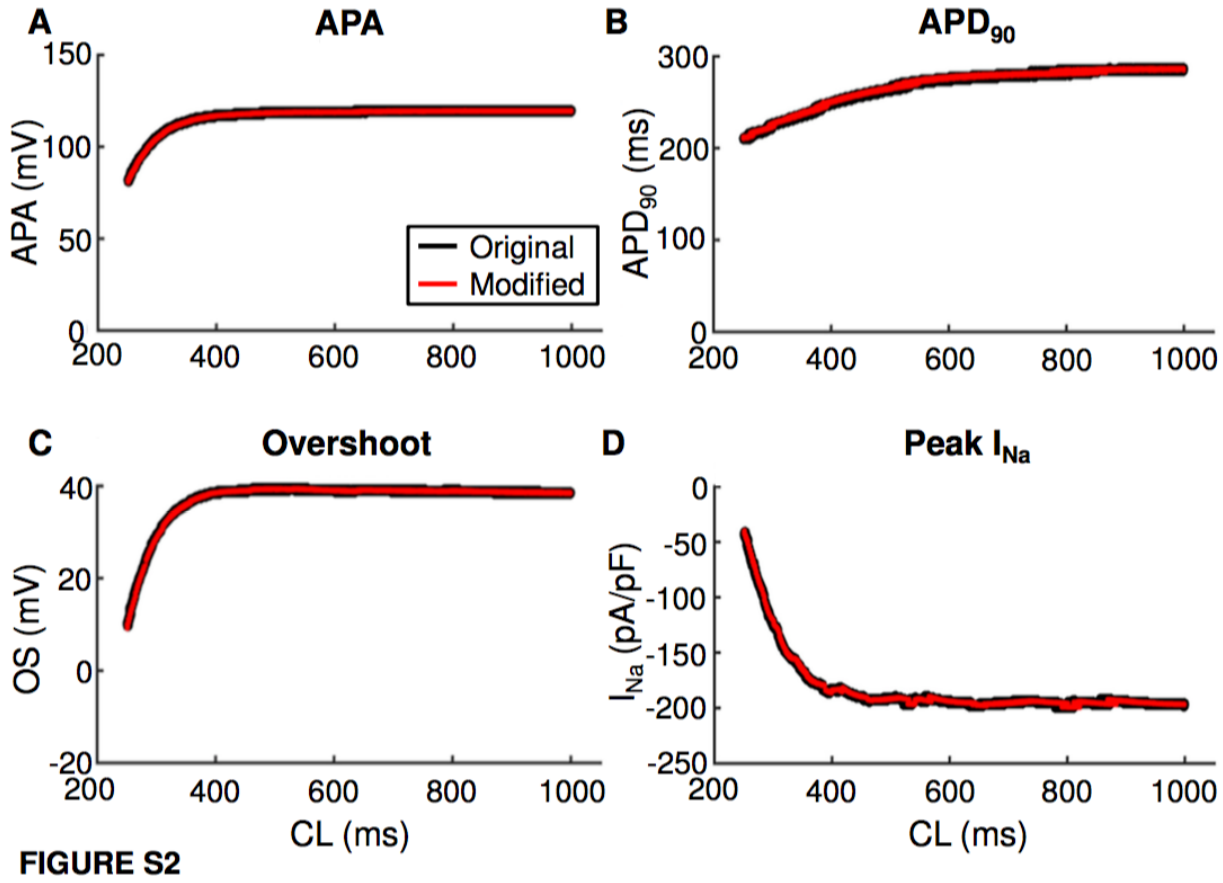

Supplemental Figure 4.2 I_{Kur} inactivation and action potential dynamics. (A) Action potential amplitude (APA), (B) action potential duration at 90% repolarizaton (APD_{90}), (C) maximal phase-0 overshoot potential (OS) and (D) peak Na^+ current (peak I_{Na}) as a function of stimulation cycle length (CL) for the original (black) and modified (red) Courtemanche models.

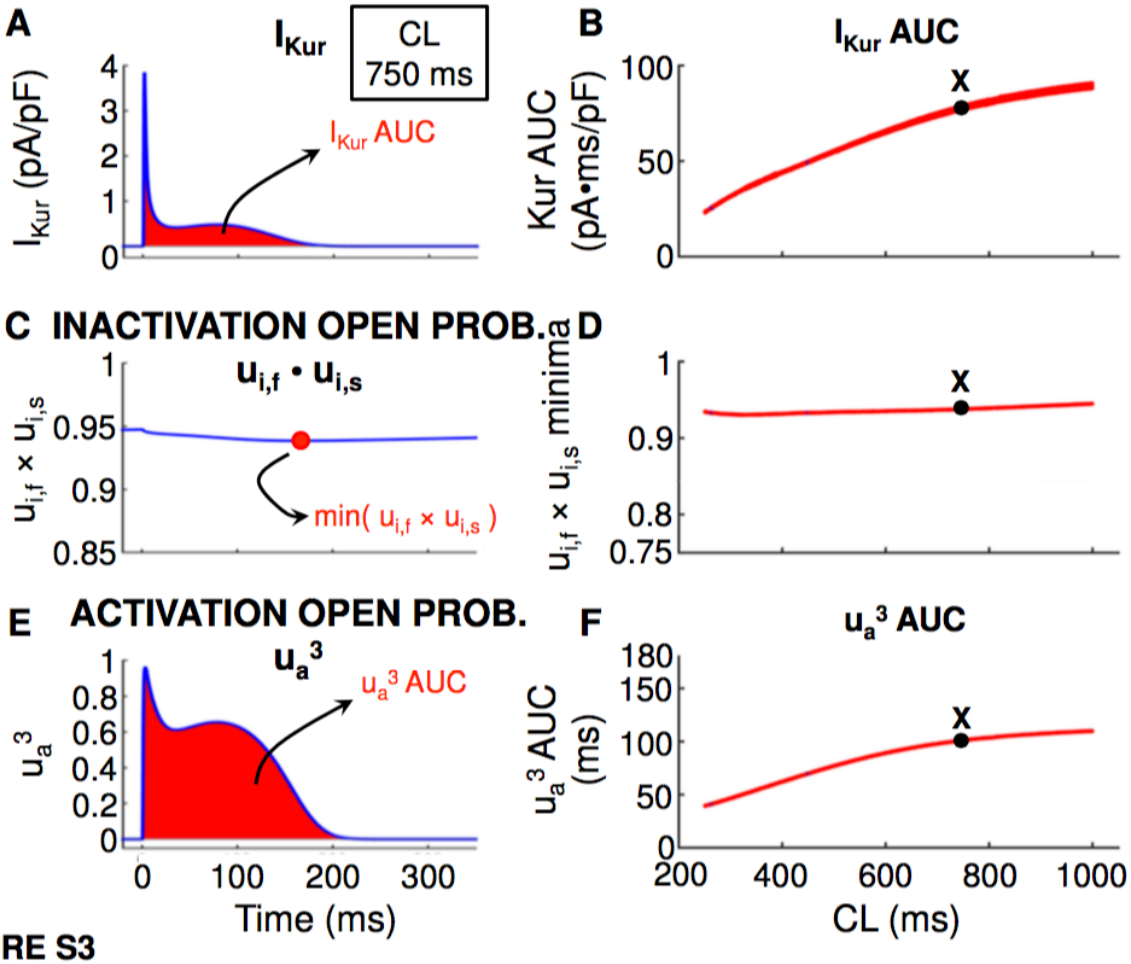

FIGURE S3

Supplemental Figure 4.3 Left panels: Kinetic determinants of I_{Kur} at a cycle length of 750 ms. Right panels: Cycle-length dependence of the same kinetic determinants (points corresponding to a cycle length of 750 ms indicated by an X). (A) Determinants of I_{Kur} rate dependence as a function of time for a stimulation cycle length (CL) of 750 ms. The area under the I_{Kur} curve (I_{Kur} AUC; shaded red) is calculated to determine charge carried per cycle. (B) I_{Kur} AUC as a function of stimulation cycle length. (C) Inactivation gate open probability ($u_{i,f} \times u_{i,s}$) as a function of time at CL = 750 ms. The open-probability minimum is marked by a red dot. (D) Inactivation gate open probability minima as a function of cycle length. (E) Activation gate open probability (u_a^3) as a function of time at CL = 750 ms. The area under the u_a^3 curve (u_a^3 AUC) is shaded in red). (F) Activation gate open probability AUC (u_a^3 AUC) as a function of stimulation cycle length.

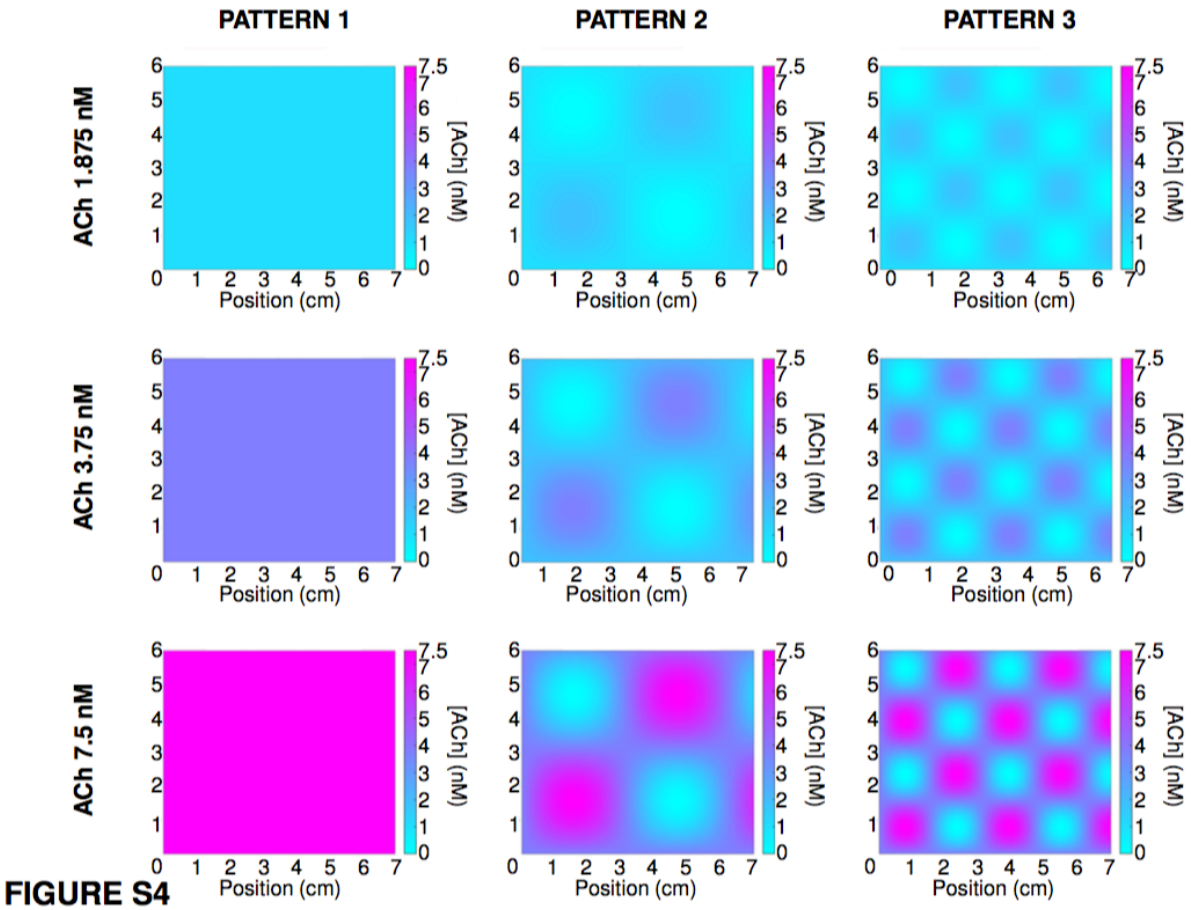

FIGURE S4

Supplemental Figure 4.4 ACh distributions used for the 2-dimensional AF simulations. Pattern #1 is a flat ACh distribution. Pattern #2 and #3 are sinusoidal ACh distributions. Three peak ACh concentrations (1.875 nM, 3.75 nM and 7.5 nM) for each pattern generated 9 different substrate conditions.

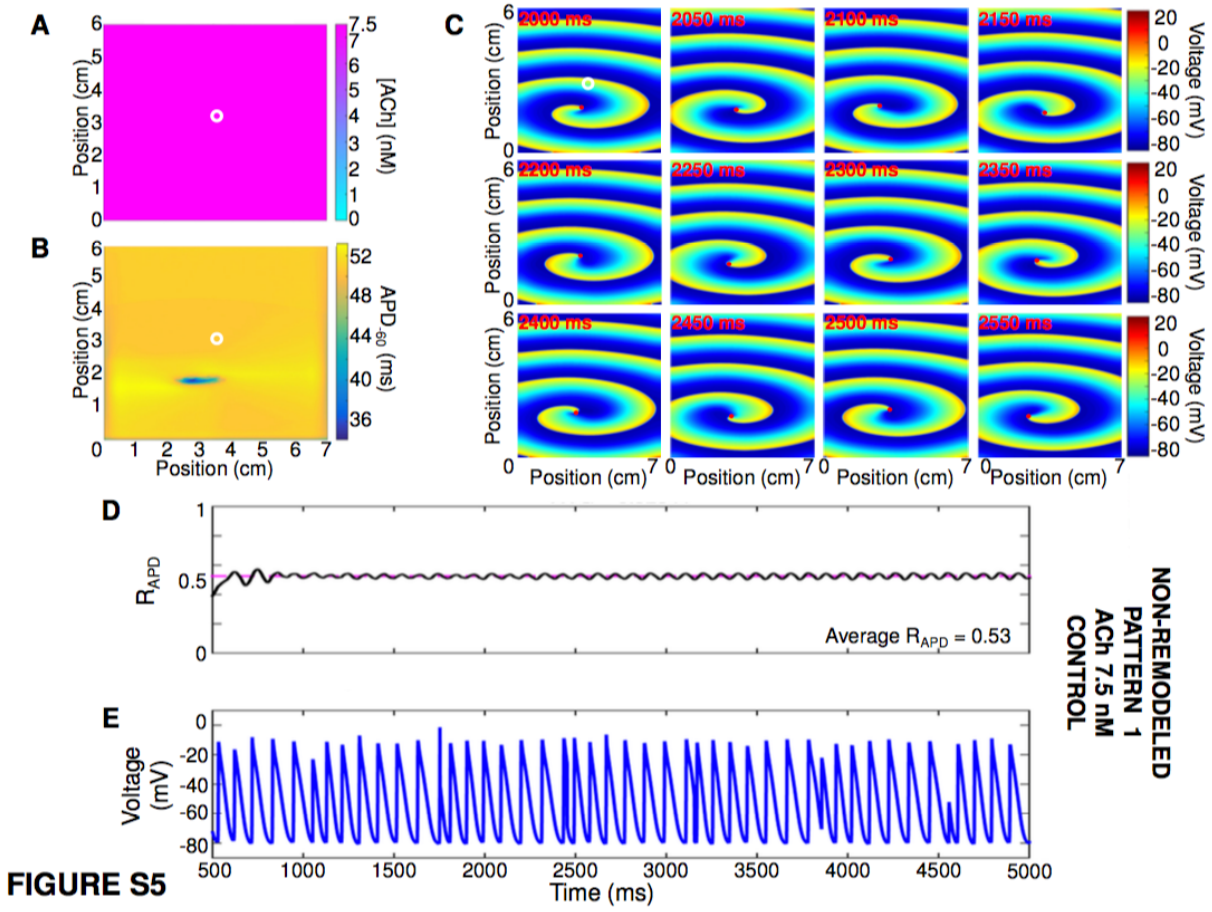

Supplemental Figure 4.5 Representative example of simulated cholinergic AF using pattern #1 with peak ACh concentration of 7.5 nM and the non-remodeled cardiomyocyte model. (A) ACh distribution with peak concentration of 7.5 nM and (B) corresponding APD_{-60} distribution. (C) Transmembrane potential over time at 50 ms intervals; re-entry is very stable and maintained by a single rotor. (D) Ratio of depolarized cells and (E) transmembrane potential over time for the cardiomyocyte marked with a white circle in panels A and B.

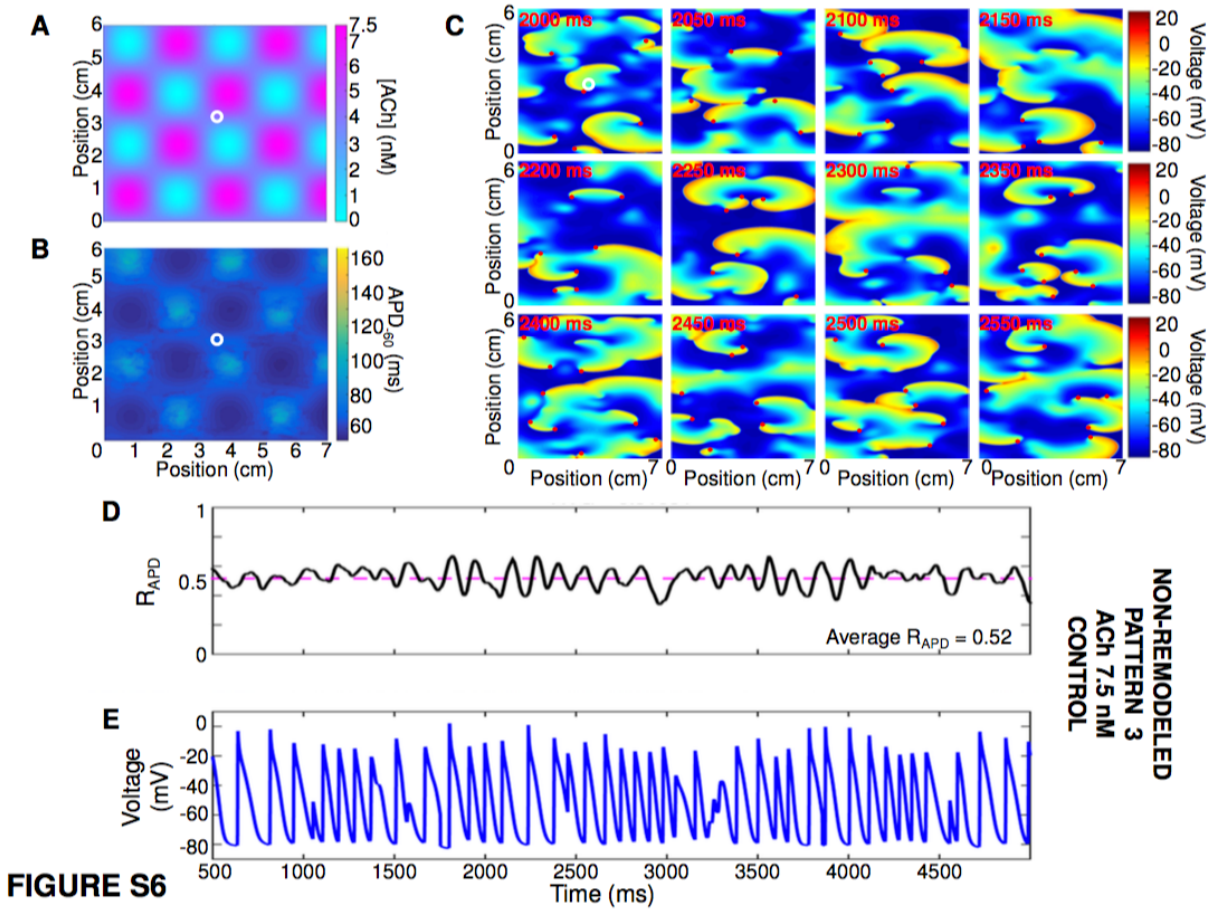

Supplemental Figure 4.6 Representative example of simulated cholinergic AF using pattern #3 with peak ACh concentration of 7.5 nM and the non-remodeled cardiomyocyte model. (A) ACh distribution with peak concentration of 7.5 nM and (B) corresponding APD_{-60} distribution. (C) Transmembrane potential over time at 50 ms intervals; re-entry is maintained by multiple short-live spiral waves. (D) Ratio of depolarized cells and (E) transmembrane potential over time for the cardiomyocyte marked with a white circle in panels A and B.

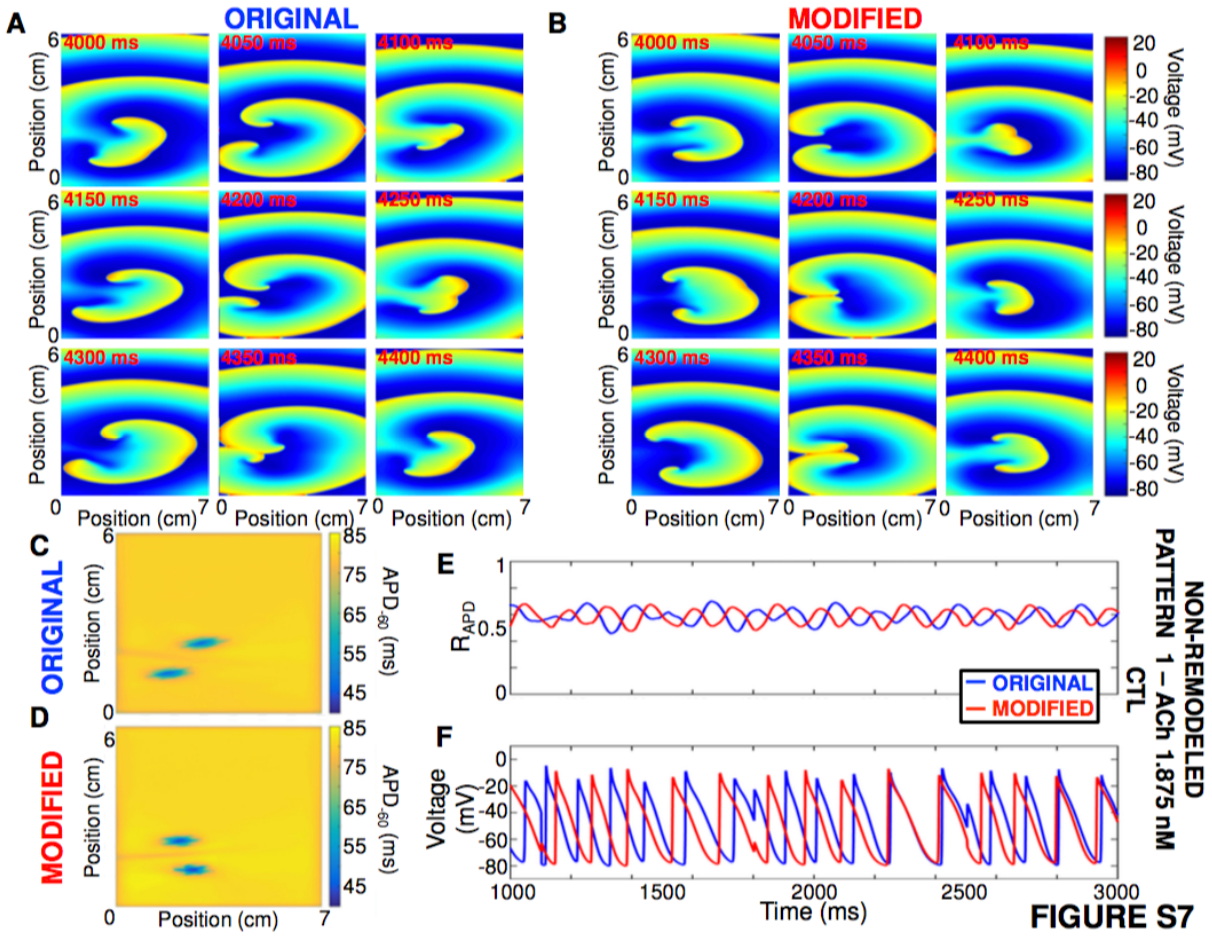

Supplemental Figure 4.7 Representative example comparing re-entry dynamics in the original and modified models. (A-B) Transmembrane potential over time at 50 ms intervals for the original and modified models. (C-D) APD-60 for the original and modified models. (E-F) Ratio of depolarized cells and transmembrane potential for the original (blue) and modified (red) models. Non-remodeled cardiomyocyte model with ACh pattern #1 with peak concentration of 1.875 nM.

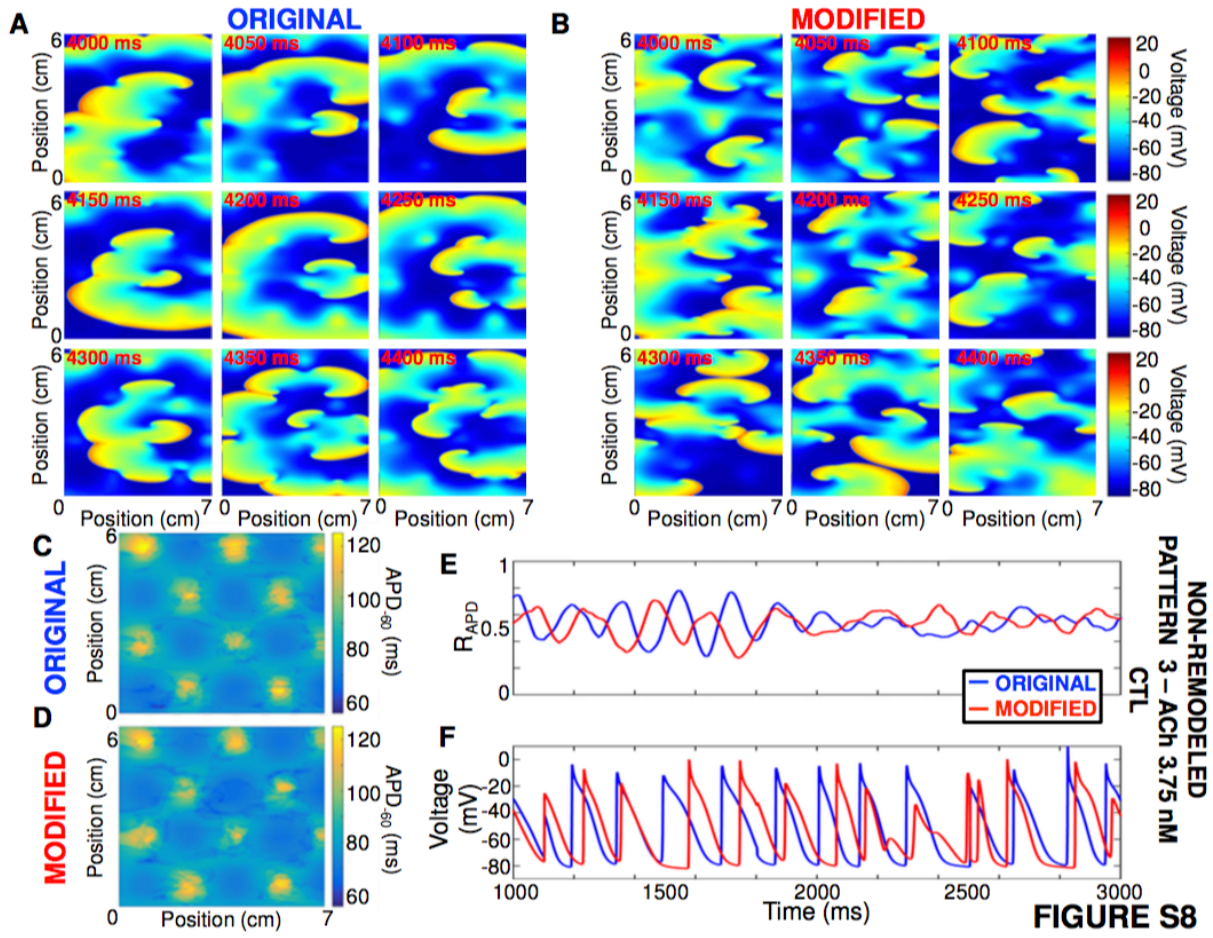

Supplemental Figure 4.8 Representative example comparing re-entry dynamics in the original and modified models. (A-B) Transmembrane potential over time at 50 ms intervals for the original and modified models. (C-D) APD-60 for the original and modified models. (E-F) Ratio of depolarized cells and transmembrane potential for the original (blue) and modified (red) models. Non-remodeled cardiomyocyte model with ACh pattern #3 with peak concentration of 3.75 nM.

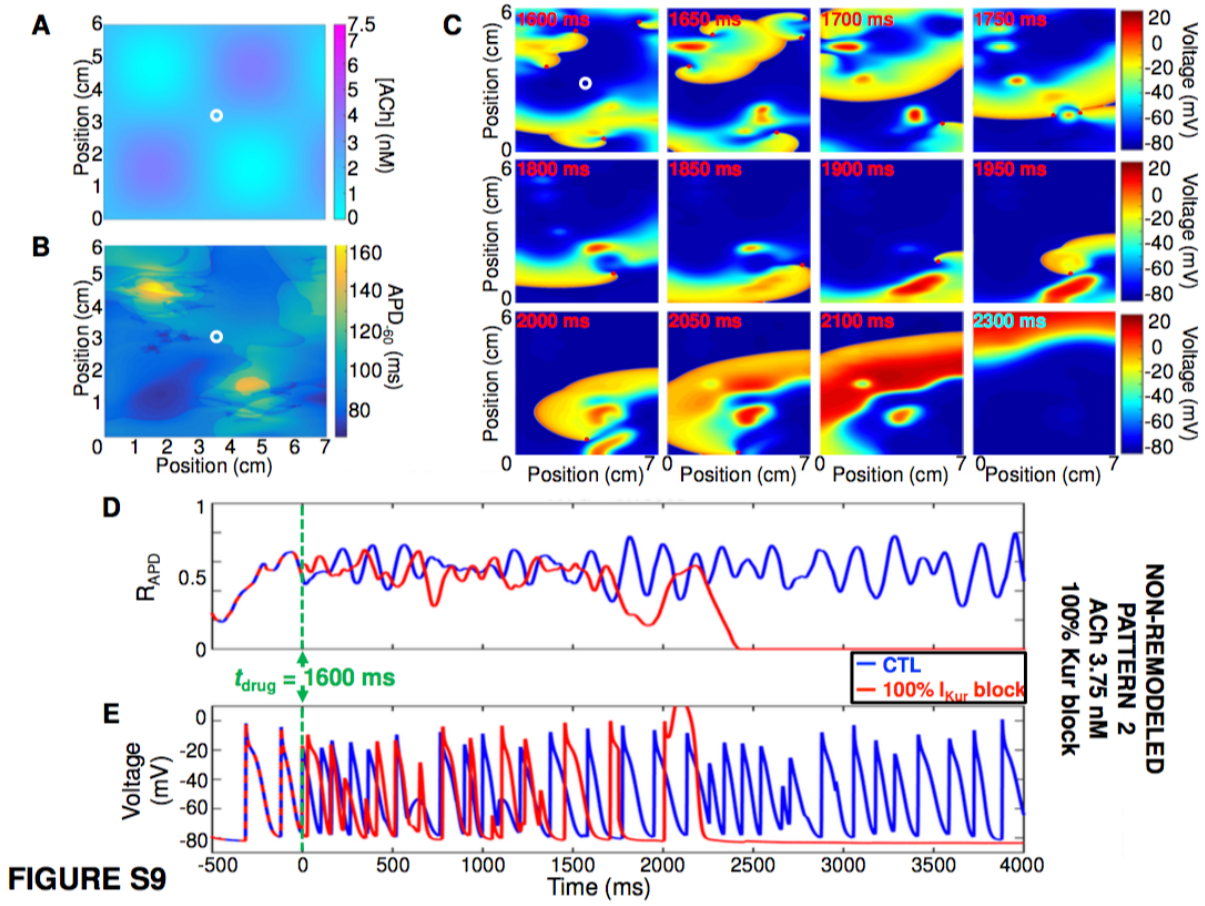

Supplemental Figure 4.9 Representative example of re-entry termination by 100% I_{Kur} block using ACh pattern #2 with peak ACh concentration of 3.75 nM and the non-remodeled cardiomyocyte model. (A) ACh distribution with peak concentration of 3.75 nM and (B) corresponding APD_{-60} distribution. (C) Transmembrane potential over time at 50 ms intervals; 50% I_{Kur} block was introduced at t_{drug} = 1600 ms. (D) Ratio of depolarized cells and (E) transmembrane potential over time for the cardiomyocyte marked with a white circle in panels A and B for control (blue) and 50% I_{Kur} block (red).

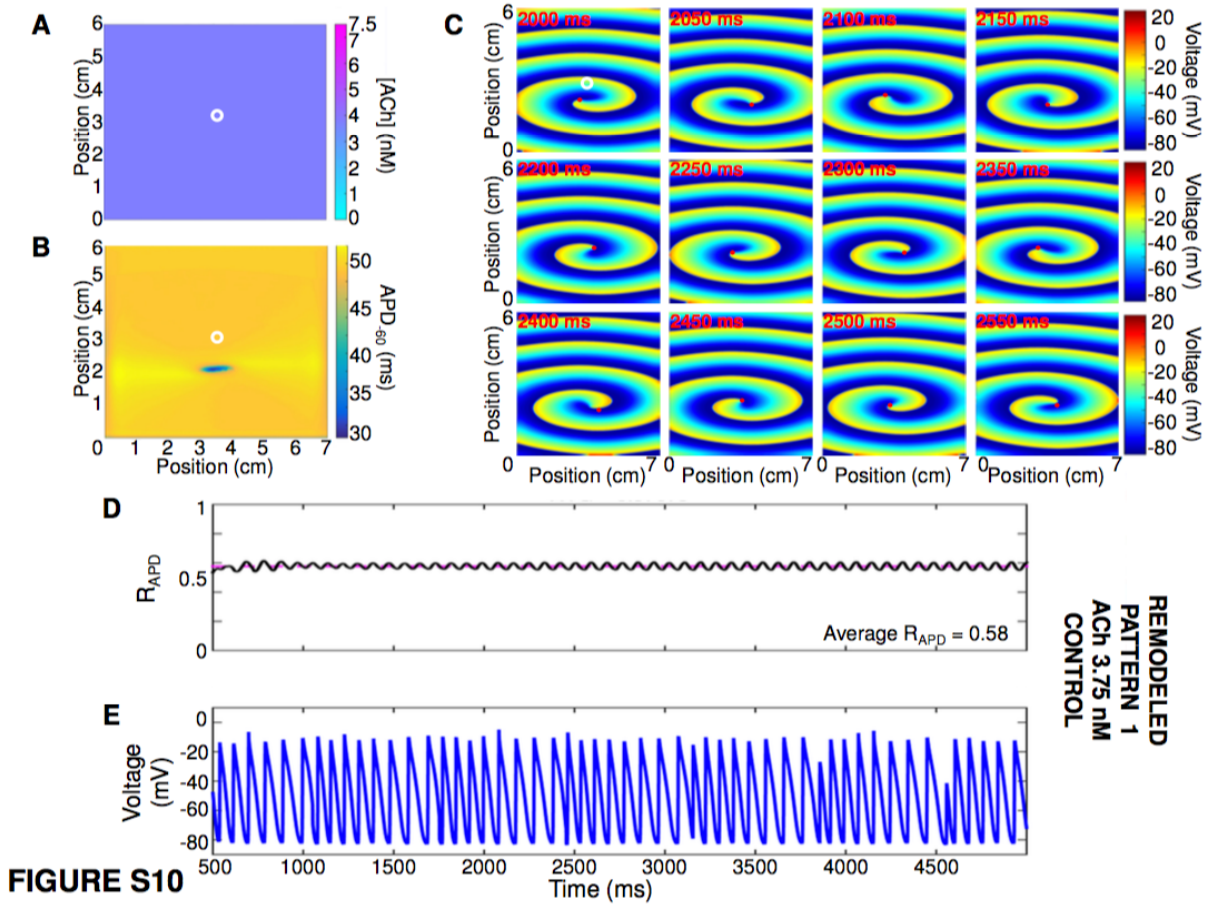

FIGURE S10

Supplemental Figure 4.10 Representative example of simulated cholinergic AF using pattern #1 with peak ACh concentration of 3.75 nM and the remodeled cardiomyocyte model. (A) ACh distribution with peak concentration of 3.75 nM and (B) corresponding APD_{-60} distribution. (C) Transmembrane potential over time at 50 ms intervals; re-entry is very stable and maintained by a single rotor. (D) Ratio of depolarized cells and (E) transmembrane potential over time for the cardiomyocyte marked with a white circle in panels A and B.

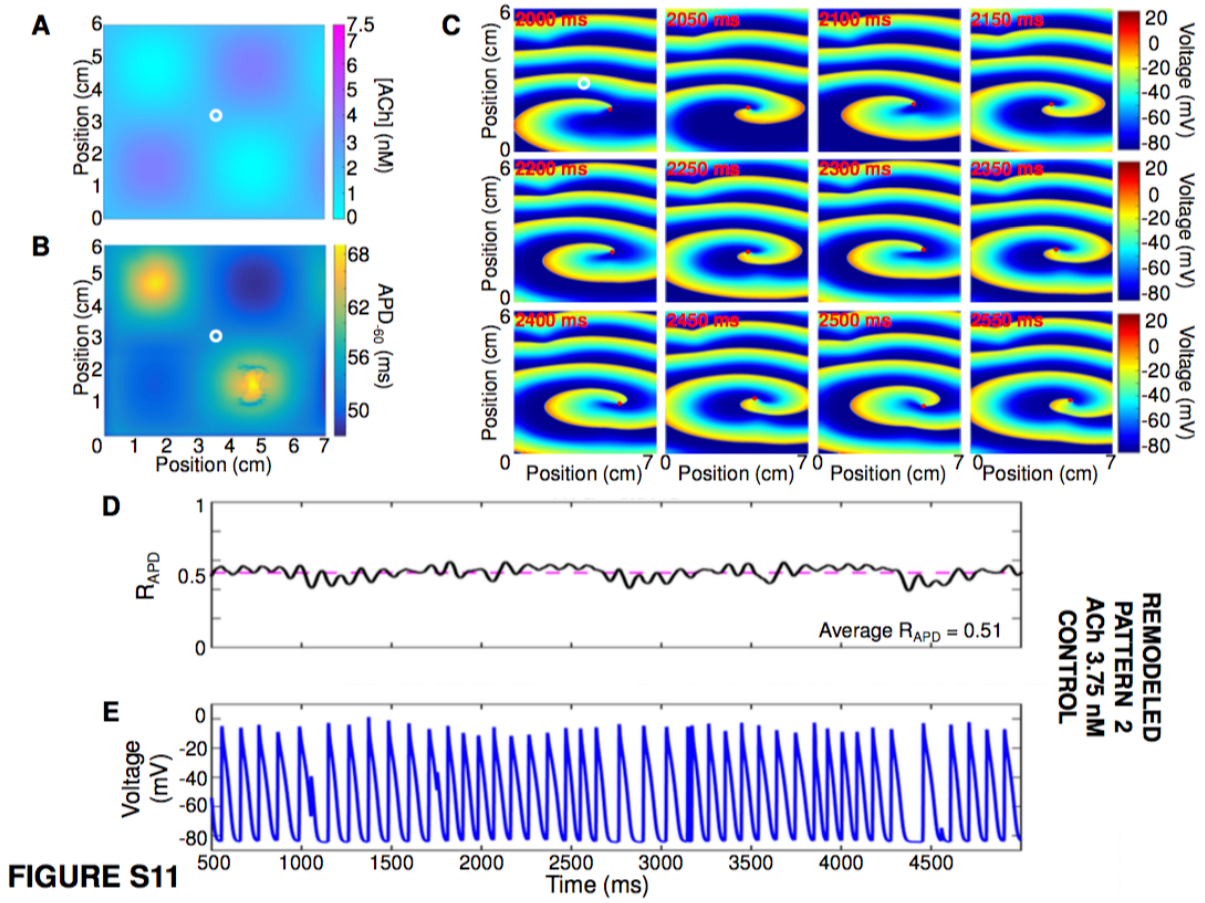

Supplemental Figure 4.11 Representative example of simulated cholinergic AF using pattern #2 with peak ACh concentration of 3.75 nM and the remodeled cardiomyocyte model. (A) ACh distribution with peak concentration of 3.75 nM and (B) corresponding APD_{-60} distribution. (C) Transmembrane potential over time at 50 ms intervals; re-entry is very stable and maintained by a single rotor. (D) Ratio of depolarized cells and (E) transmembrane potential over time for the cardiomyocyte marked with a white circle in panels A and B.

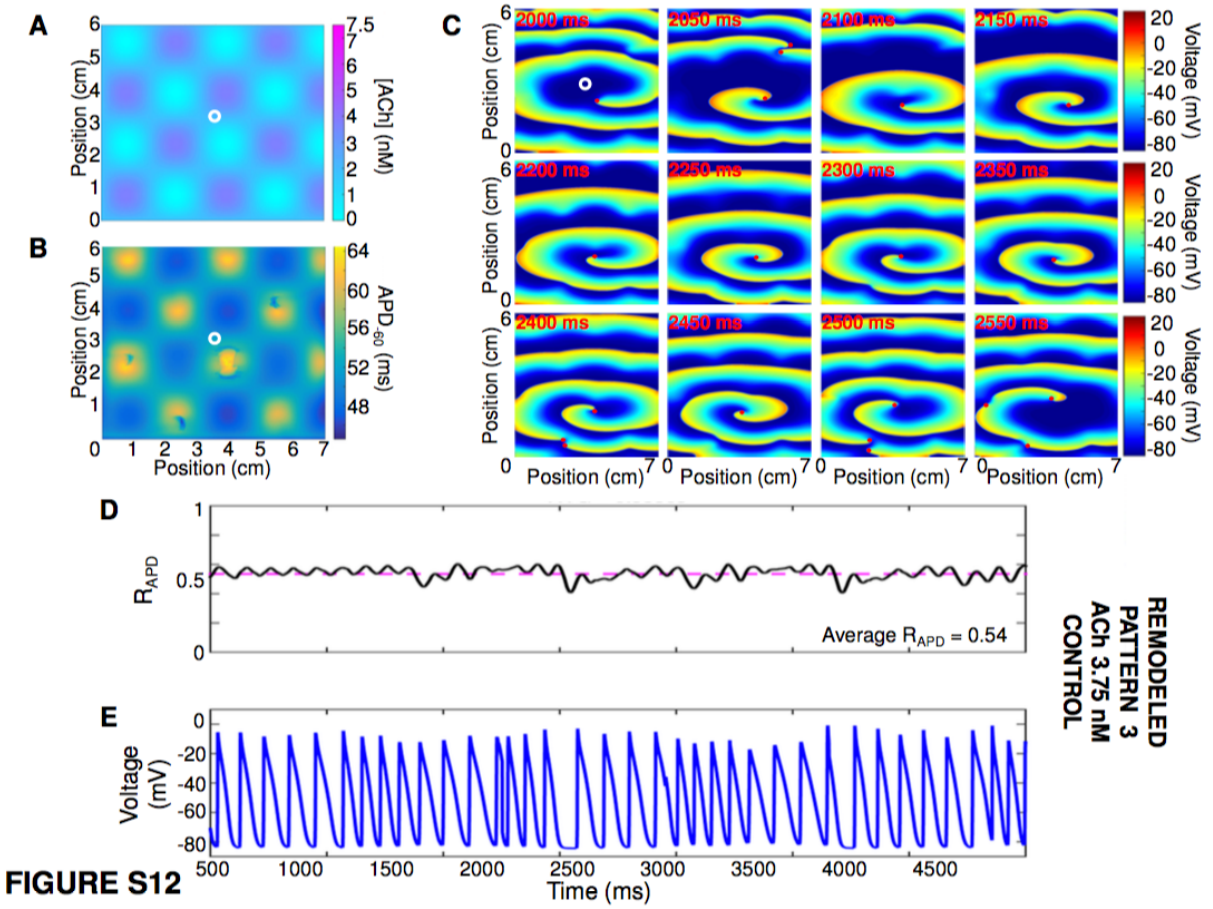

Supplemental Figure 4.12 Representative example of simulated cholinergic AF using pattern #3 with peak ACh concentration of 3.75 nM and the remodeled cardiomyocyte model. (A) ACh distribution with peak concentration of 3.75 nM and (B) corresponding APD_{-60} distribution. (C) Transmembrane potential over time at 50 ms intervals; re-entry is stable and maintained by a few rotors. (D) Ratio of depolarized cells and (E) transmembrane potential over time for the cardiomyocyte marked with a white circle in panels A and B.

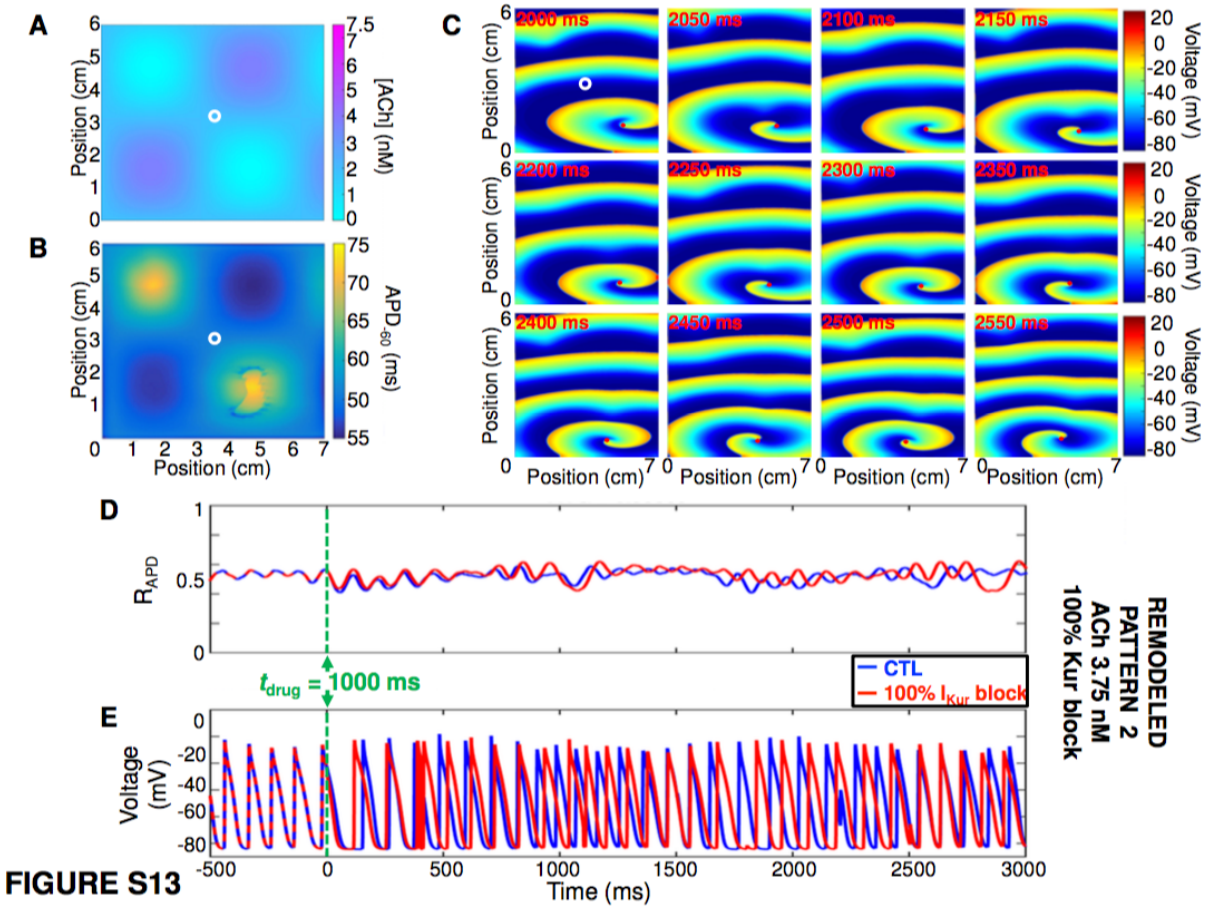

Supplemental Figure 4.13 Representative example of re-entry non-termination by 100% I_{Kur} block using ACh pattern #2 with peak ACh concentration of 3.75 nM and the remodeled cardiomyocyte model. (A) ACh distribution with peak concentration of 3.75 nM and (B) corresponding APD_{-60} distribution. (C) Transmembrane potential over time at 50 ms intervals; 100% I_{Kur} block was introduced at t_{drug} = 1000 ms. (D) Ratio of depolarized cells and (E) transmembrane potential over time for the cardiomyocyte marked with a white circle in panels A and B for control (blue) and 50% I_{Kur} block (red).

Chapter 5. The Effects of Heart Failure-Induced Fibroblast Electrical Remodeling on Cardiomyocyte Electrophysiology and Atrial Fibrillation Arrhythmogenesis

Cardiac fibroblasts are often considered electrically inactive. However, recent experimental studies have identified functional ionic currents on the fibroblast's membrane, giving them potentially active electrophysiological properties. There is also *in vitro* evidence that fibroblasts can electrically couple to neighboring cardiomyocytes and thereby play a direct role in arrhythmogenesis. In this study, we sought to investigate the changes to the fibroblasts' ionic currents induced by heart failure in an experimental canine model. We then implemented the experimentally-observed changed ion fibroblast currents in a mathematical model of cardiomyocyte-fibroblast coupling to study the effect of this new kind of remodeling on the cardiomyocyte's electrophysiology and AF arrhythmogenesis.

5.1 Fibroblast Electrical Remodeling in Heart Failure and Potential Effects on Atrial Fibrillation

Martin Aguilar, Xiao Yan Qi, Hai Huang, Philippe Comtois and Stanley Nattel

Biophys J. 2014;107(10):2444-2455.

5.1.1 Abstract

Fibroblasts are activated in heart failure (HF) and produce fibrosis, which plays a role in maintaining atrial fibrillation (AF). The effect of HF on fibroblast ion-currents and the potential role in AF are unknown. Here, we used patch-clamp to investigate the effects of HF on atrial fibroblast ion-currents and mathematical computation to assess the potential impact of this remodeling on atrial electrophysiology and arrhythmogenesis. Atrial fibroblasts were isolated from control and tachypacing-induced heart failure (HF) dogs. TEA-sensitive voltage-gated fibroblast current ($I_{Kv,fb}$) was significantly downregulated, by about 44%, whereas the Ba^{2+}-sensitive inward rectifier current ($I_{Kir,fb}$) was upregulated by 79%, in HF animals versus controls. The fibroblast resting membrane potential was hyperpolarized (-53±2 mV, vs -42±2 mV in control) and the capacitance was increased (29.7±2.2 pF, vs 17.8±1.4 pF, control) in HF. These experimental findings were implemented in a mathematical model including cardiomyocyte-fibroblast electrical coupling. $I_{Kir,fb}$ upregulation had a pro-fibrillatory effect through action potential duration shortening and hyperpolarization of the cardiomyocyte resting membrane potential. $I_{Kv,fb}$ downregulation had the opposite electrophysiological effects and was anti-fibrillatory. Simulated pharmacological blockade of $I_{Kv,fb}$ successfully terminated re-entry under otherwise pro-fibrillatory conditions. We conclude that HF induces fibroblast ion-current remodeling, with $I_{Kv,fb}$ downregulation and $I_{Kir,fb}$ upregulation, and that, assuming cardiomyocyte-fibroblast electrical coupling, this remodeling has a potentially important effect on atrial electrophysiology and arrhythmogenesis, with the overall response depending on the balance of pro- and anti-fibrillatory contributions. These findings suggest that fibroblast K^+-current remodeling is a novel component of AF-related remodeling that might contribute to arrhythmia dynamics.

5.1.2 Introduction

Atrial fibrillation (AF) is the most common sustained arrhythmia in the general population and is associated with significant cardiovascular morbidity and mortality (118, 119). The failure of randomized clinical trials to demonstrate a benefit from sinus rhythm maintaining antiarrhythmic therapy, a failure often attributed to the suboptimal efficacy and significant pro-arrhythmic potential of antiarrhythmic drugs (29), highlights our incomplete understanding of the basic pathophysiology of AF.

At the cellular level, it is well known that AF induces cardiomyocyte electrical remodeling and atrial fibrosis, forming the basis for longer lasting forms of AF (41, 57, 207, 208). Traditionally, fibroblasts were thought to be relevant to arrhythmogenesis primarily by virtue of the production of extracellular matrix that serves as a structural barrier affecting anisotropic conduction and creating conduction block (209-212). However, recent work has modified this paradigm by suggesting that cardiac fibroblasts may couple electrically to atrial cardiomyocytes and modulate their electrophysiological properties to promote various forms of arrhythmogenesis (213). Cardiomyocyte-fibroblast electrical interactions have been studied in co-cultured cell-systems (214-219) and mathematical models (220, 221), and postulated to contribute to the pathogenesis of AF (213, 220), although in vivo evidence of such interactions is lacking. Cardiomyocyte ion-channel remodeling is known to play an important role in AF pathophysiology (222). Fibroblasts also possess ion-channels, but their function is much less well understood than those of cardiomyocytes (213). The nature and potential significance of fibroblast ion-channel remodeling associated with AF remain to be evaluated. Here, we examined the remodeling of K^+-currents in fibroblasts freshly isolated from dogs with an AF substrate associated with heart failure (HF). Freshly isolated fibroblasts were used to preclude the effects of cell culture, which can obscure the fibroblast phenotype remodeling caused by HF (223). We then implemented these experimental findings in a mathematical model based on previous work (224) to investigate the potential effects of fibroblast electrical remodeling on atrial cardiomyocyte electrophysiological properties and arrhythmogenesis, assuming cardiomyocyte-fibroblast electrical coupling.

5.1.3 Materials and Methods

5.1.3.1 Animal model

Animal care procedures were approved by the Animal Research Ethics Committee of the Montreal Heart Institute and followed National Institutes of Health guidelines. A total of 20 adult mongrel dogs (20-30 kg) were studied, divided into control (n=10) and two week ventricular tachypacing-induced HF (n=10) groups. HF dogs were anesthetized under diazepam (0.25 mg/kg IV)/ketamine (5.0 mg/kg IV)/halothane (1% to 2% PI) anaesthesia so that two leads could be inserted under fluoroscopy into the right ventricular apex (via the left jugular vein) and connected to a pacemaker (St. Jude Medical, St. Paul, MN) implanted subcutaneously in the neck. After twenty-four hours for post-operative recovery, ventricular pacing was initiated at 240 bpm for two weeks. On study days, dogs were anesthetized with morphine (2 mg/kg SC) and α-chloralose (120 mg/kg IV, followed by 29.25 mg/kg per hour) and ventilated mechanically. The atrial effective refractory period (aERP) and mean AF duration were measured at basic cycle length (BCLs) of 150, 200 ms, 250 ms, 300 ms and 350 ms in the right atrium. aERP was determined with 10 basic stimuli (S1) followed by a premature extrastimulus (S2) with 5 ms decrements (the longest S1-S2 interval failing to capture defined the aERP). The mean of 3 aERP values at each BCL was used for analysis. AF was induced with atrial burst pacing at 10 Hz and 10 V. Mean AF duration was based on 10 AF inductions in each dog. If the mean duration of the first five episodes of AF was longer than 2 minutes, AF was only induced five times. After in vivo study, hearts were removed and immediately immersed in oxygenated Tyrode solution containing (mmol/L): NaCl 136, KCl 5.4, MgCl2 1, $CaCl_2$ 2, NaH_2PO_4 0.33, HEPES 5 and dextrose 10, pH 7.35 (NaOH). Atrial tissue was subjected to enzymatic digestion as described below for cell isolation.

5.1.3.2 Fibroblast isolation

Atrial fibroblasts were obtained from left atria of adult mongrel dogs as described previously (225). The heart was removed after intra-atrial injection of heparin (10,000 U),

immersed in Tyrode solution containing 2 mmol/L Ca^{2+}, and the left coronary artery was cannulated. The left atrial tissue was then perfused with 2 mmol/L Tyrode solution (37°C, 100% O_2), then with Ca^{2+} -free Tyrode solution (~10 minutes), followed by ~60-minute perfusion with the same solution containing collagenase (~0.48 mg/mL, CLSII, Worthington) and 0.1% bovine serum albumin (BSA, Sigma). Cells were dispersed by trituration in Kraftbrühe (KB) solution (for contents, see below). Filtration (500 μm micromesh) was used to remove debris and cells were centrifuged at 800 rpm for 5 minutes to pellet cardiomyocytes. The supernatant was collected and filtered through 30 μm nanomesh and centrifuged at 1500 rpm for 10 minutes to pellet fibroblasts. Pelleted, freshly isolated fibroblasts were then separated.

5.1.3.3 Ion current and membrane potential recordings

All *in vitro* recordings were obtained at 37°C. The whole cell perforated patch technique was used to record resting membrane potential (RMP) in current clamp mode and tight seal patch clamp was used to record K^+-current in voltage clamp mode. Borosilicate glass electrodes (Sutter Instrument) filled with pipette solution were connected to a patch clamp amplifier (Axopatch 200A, Axon). Electrodes had tip resistances of 6 to 8 MΩ. For perforated-patch formation, nystatin-free intracellular solution was placed in the tip of the pipette by capillary action (~30 s). Pipettes were then back-filled with nystatin-containing (600-μg/mL) pipette solution. Currents are expressed as densities (pA/pF). Junction potentials between bath and pipette solutions averaged 10.5 mV and were corrected for RMP measurements only. $I_{Kir,fb}$ was quantified as 300 μmol/L Ba^{2+}-sensitive current. $I_{Kv,fb}$ was quantified as current sensitive to 10 mmol/L tetraethylammonium (TEA) (24). The bath solution contained (mmol/L): NaCl 136, $CaCl_2$1.8, KCl 5.4, $MgCl_2$1, $NaH_2PO_4$0.33, dextrose 10, and HEPES 5, titrated to pH 7.3 with NaOH. The pipette solution contained (mmol/L): GTP 0.1, potassium-aspartate 110, KCl 20, $MgCl_2$1, MgATP 5, HEPES 10, sodium-phosphocreatine 5, and EGTA 0.005 (pH 7.4, KOH). KB solution contained (mmol/L): KCl 20, KH_2PO_4 10, dextrose 10, mannitol 40, L-glutamic acid 70, β-OH-butyric acid10, taurine 20, and EGTA 10 and 0.1% BSA (pH 7.3, KOH).

5.1.3.4 Atrial cardiomyocyte and fibroblast mathematical models

The Ramirez-Nattel-Courtemanche (RNC) ionic model of canine atrial cardiomyocyte action potentials (127) was implemented and electrically connected to a variable number (n) of MacCannell model fibroblasts (221) via gap junctions of conductance G_{gap}. The total ionic current for the RNC model ($I_{ion,RNC}$) is:

$$I_{ion,RNC}=I_{Na}+I_{Kir}+I_{to}+I_{Kur,d}+I_{Kr}+I_{Ks}+I_{CaL}+I_{ClCa}+I_{KACh}+I_{pCa}+I_{NaCa}+I_{NaK}+I_{b,Na}+I_{b,Ca}+I_{b,Cl}+nI_{gap}$$

where I_{Kir}, I_{to}, $I_{Kur,d}$, I_{Kr}, I_{Ks}, and I_{KACh} are the inward-rectifier, transient-outward, ultrarapid delayed-rectifier, rapid and slow delayed rectifier, and acetycholine (ACh) activated K^+-currents respectively; I_{CaL} is the L-type Ca^{2+}-current; I_{ClCa} is the Ca^{2+}-activated Cl^- current; I_{pCa} is the Ca^{2+} pump current; I_{NaCa} is the Na^+/Ca^{2+} exchange current; I_{NaK} is the Na^+/K^+ pump current; $I_{b,Na}$, $I_{b,Ca}$, and $I_{b,Cl}$ are the background Na^+, Ca^{2+}, and Cl^- currents respectively (47). I_{gap} is the gap-junction current and *n* is the number of fibroblasts coupled to each cardiomyocyte. The total ionic current for the MacCannell fibroblast model ($I_{ion,fb}$) is:

$$I_{ion,fb}=I_{Kv,fb}+I_{Kir,fb}+I_{NaK,fb}+I_{b,Na,fb}+I_{gap}$$

where $I_{Kv,fb}$ and $I_{Kir,fb}$ are the fibroblast delayed-rectifier and inward-rectifier K^+-currents respectively, $I_{NaK,fb}$ is the Na^+/K^+ exchange pump current, $I_{b,Na,fb}$ is the background Na^+ current and I_{gap} is the gap junction current (221).

Fibroblast electrical remodeling was simulated by scaling the fibroblast $I_{Kv,fb}$ and $I_{Kir,fb}$ maximal conductance, as follows: $G_{Kir,fb}'=f_{Kir,fb}\times G_{Kir,fb}$ and $G_{Kv,fb}'=f_{Kv,fb}\times G_{Kv,fb}$, where G_x is the baseline conductance, f_x is the remodeling factor and G_x' is the remodeled conductance. $G_{Kir,fb}$ and $G_{Kv,fb}$ were set at 0.4822 nS/pF and 0.14 nS/pF, as per Ashihara *et al* (224). We varied $f_{Kir,fb}$ and $f_{Kv,fb}$ independently with $f_{Kir,fb}$ = [1, 2.5, 5, 10] and $f_{Kv,fb}$ = [0.1, 0.25, 0.5, 0.75, 1].

5.1.3.5 Single cell and cable simulations

A single cardiomyocyte with capacitance 100 pF (127) was connected to a fibroblast through a gap junction with a gap junction conductivity (G_{gap}) of 3 nS. The cardiomyocyte was

paced at a basic cycle length (BCL) of 250 ms and the cardiomyocyte transmembrane potential, fibroblast transmembrane potential, gap junction current (I_{gap}) and total fibroblast potassium current ($I_{K,fb}$) were monitored under control and remodeled conditions. We then constructed a 1-dimensional monodomain cable of atrial cardiomyocytes connected to fibroblasts and simulated cardiomyocyte and fibroblast transmembrane potential, I_{gap}, $I_{K,fb}$ and relevant electrophysiological parameters under control and remodeled conditions. Numerical integration of the single cell model was performed using the MATLAB ODE23s ordinary differential equation solver (The MathWorks, Natick, MA).

5.1.3.6 2D sheet and fibroblast distribution

Two-dimensional (2D) simulations were performed on a 5×10 cm sheet of RNC atrial cells. The tissue contained cardiomyocyte cables (radius 5 μm, resistivity 75 Ω-cm; coupled by resistors of 300 kΩ length 100 mm, inserted in a brick-wall manner). Fiber resistivity and inter-fiber resistance values were chosen to match experimental results (47, 226). Supplementary Figure 5.1 shows the fibroblast distribution used; results presented in this manuscript are with intermediate density (0.250), but analyses have been conducted with all three fibroblast distribution-maps and produced qualitatively-similar results. Fibroblast-proliferation was generated through a recursive algorithm as described by Ashihara et al (224). Re-entrant spiral waves were initiated using an S1-S2 cross-shock protocol. Initiation, maintenance and termination dynamics were investigated; dominant-frequency analysis was performed by computing the frequency domain amplitude of the fast Fourier transform of the pseudo-ECG. Both the cable and 2D models were coded in C and calculations were performed with a time step of 25 μs using up to 8 processors with an SGI Altix XE high-performance parallel processor (Westgrid).

5.1.4 Results

5.1.4.1 In vivo measurements

In vivo electrophysiological data and hemodynamic indices are shown in Figure 33. HF significantly increased aERP at all BCLs (Figure 33A). Mean AF duration increased in HF dogs (745±287 vs 22±10 seconds in control, CTL; Figure 33B). Systolic and diastolic pressures were reduced in HF dogs, whereas left ventricular (LV) end-diastolic, left atrial (LA), and right atrial (RA) pressures were increased (Figure 33C-E), consistent with the HF phenotype.

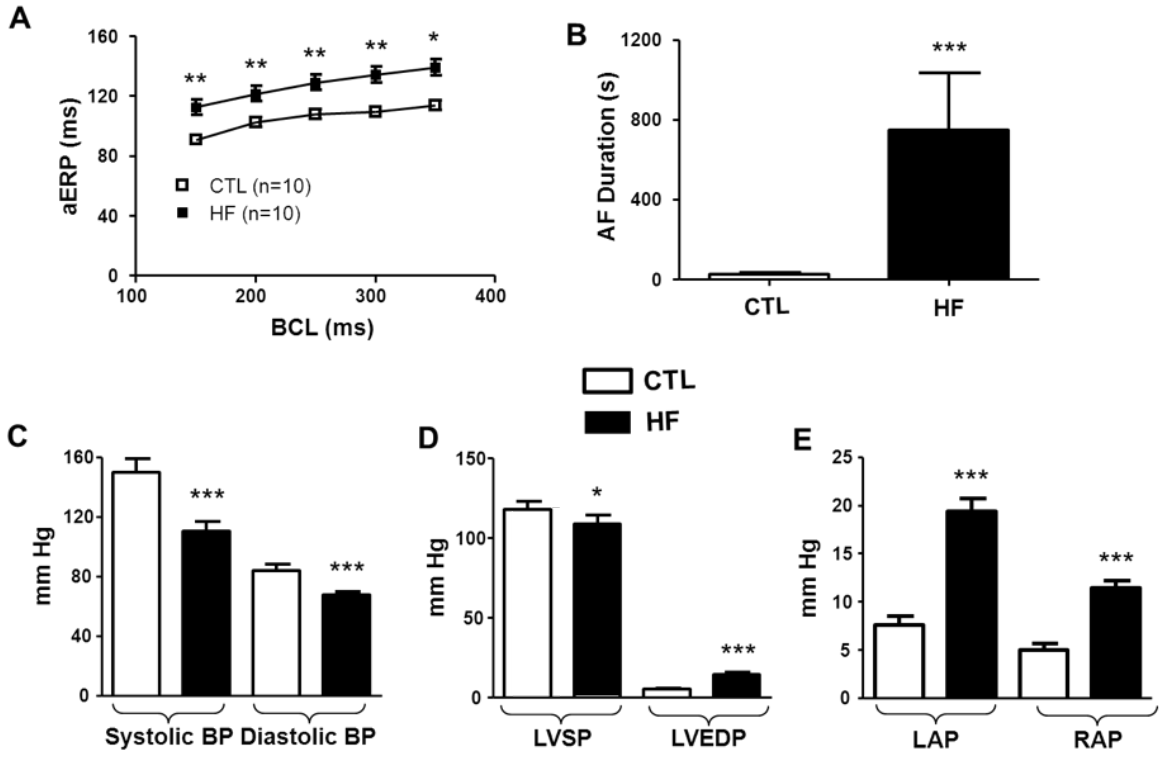

Figure 33. In vivo electrophysiological data and hemodynamic indices. (A) Atrial effective refractory period (aERP) as a function of basic cycle length (BCL). (B) AF duration. (C) Arterial blood pressure. (D) Left ventricular systolic (LVSP) and end diastolic pressure (LVEDP). (E) Left (LAP) and right atrial (RAP) pressures. *P<0.05, **P<0.01, ***P<0.001 vs. CTL.

5.1.4.2 Fibroblast Kv and Kir current remodeling in AF

Time- and voltage-dependent K^+-current ($I_{Kv,fb}$) was elicited by 500 ms voltage clamp steps to voltages ranging from -110 to +70 mV. $I_{Kv,fb}$ activated rapidly and showed little inactivation, and was reversibly suppressed by 30 mmol/L TEA (Figures 34A-B). HF strongly downregulated the TEA-sensitive K^+-current (Figure 34B). Mean current density-voltage relations (Figure 34C) showed statistically significant decreases in $I_{Kv,fb}$ by about 70% in HF fibroblasts over a wide range of voltages. LA fibroblasts had membrane capacitances of 17.8±1.4 (n=33) and 29.7±2.2 (n=33, P<0.001 vs CTL) pF in CTL and HF, respectively (Figure 34D).

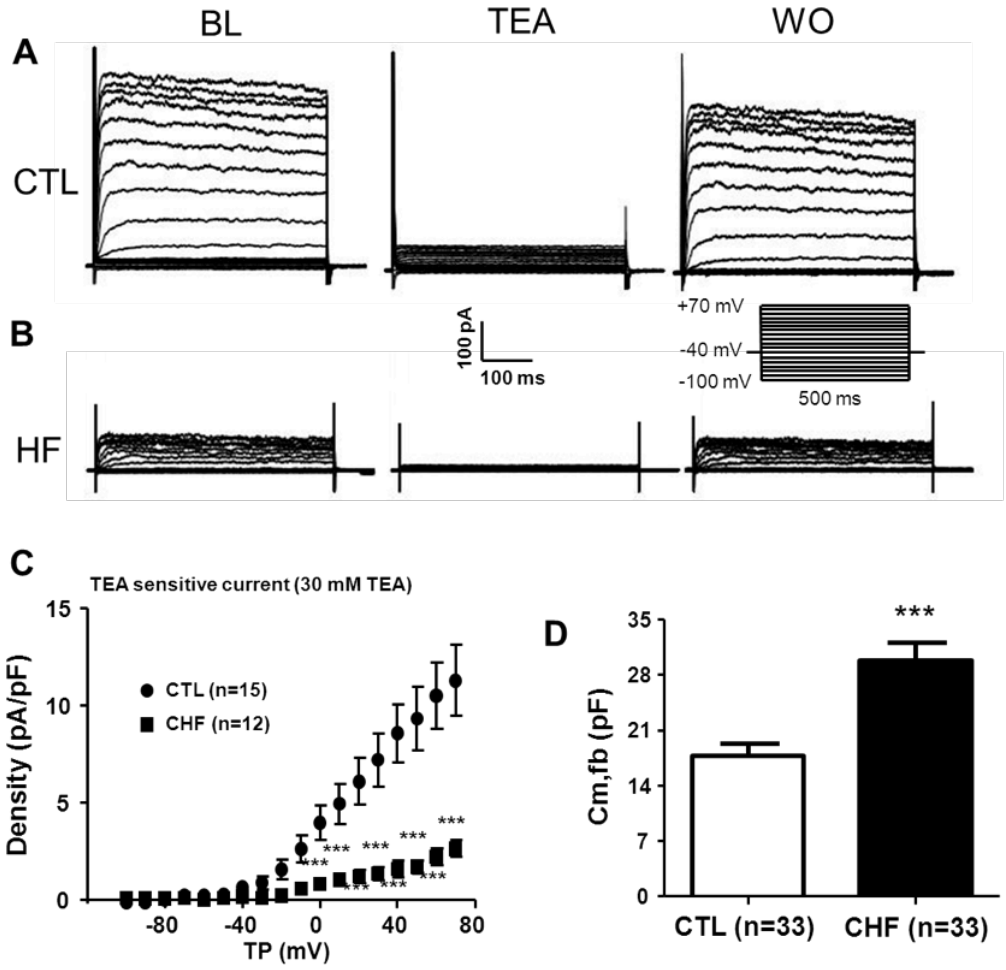

Figure 34. Experimental recordings of the TEA-sensitive current ($I_{Kv,fb}$). (A) Current densities at baseline (BL), after 30-mM TEA and upon washout (WO) in a control atrial fibroblast

(voltage protocol in inset). (B) Same as (A), but for HF-cell. (C) TEA-sensitive current-density as a function of test potential (TP), (D) Fibroblast membrane-capacitance ($C_{m,fb}$). Results are mean±SEM. ***P<0.001 vs. CTL.

Kir currents ($I_{Kir,fb}$) recorded from control and HF atrial fibroblasts are shown in Figure 35A. Current induced with a ramp depolarization at baseline before Ba^{2+} and current in the presence of 300 µmol/L Ba^{2+} are shown for individual cells obtained for each condition. Figure 35B shows the mean density of $I_{Kir,fb}$ as a function of test voltage. At -120 mV, $I_{Kir,fb}$ averaged -1.4±0.6 in CTL (n=15) and -2.6±0.3 (n=10) pA/pF in HF fibroblasts, an 86% increase (P<0.001). Consistent with inward-rectifier current upregulation in HF, RMP averaged -42±2 mV in CTL (n=16) and -53±2 mV in HF (n=19, P<0.01 vs CTL) fibroblasts (Figure 35C).

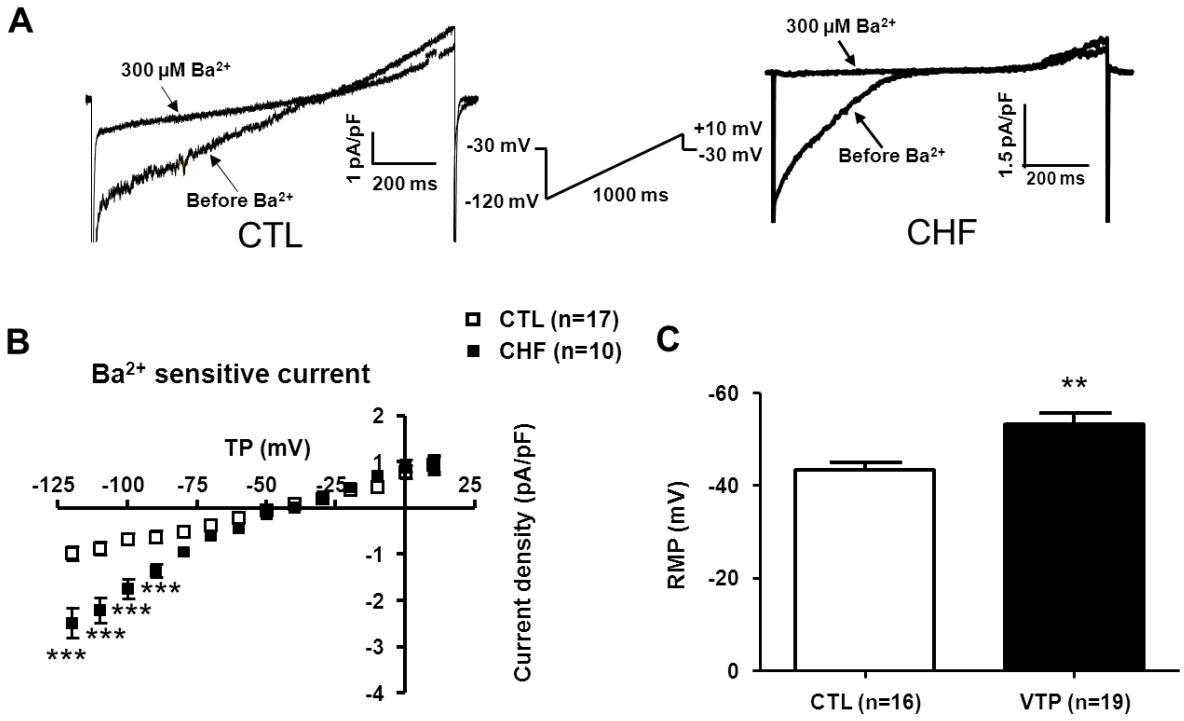

Figure 35. Experimental recordings for Kir current ($I_{Kir,fb}$). (A) Current-densities for control (left) and HF (right), obtained with a ramp-protocol before and after addition of 300-µM Ba^{2+}. (B) Current-densities as a function of test potential (TP). (C) Resting membrane potential (RMP). Results are mean±SEM. **P<0.01, ***P<0.001 vs. CTL.

5.1.4.3 Effects of fibroblast electrical remodeling on the atrial cardiomyocyte AP

Figure 36 shows the model-simulated cardiomyocyte transmembrane potential (V_m, panel A), fibroblast transmembrane potential ($V_{m,fb}$, panel B), gap junction current (I_{gap}, panel C) and total fibroblast K^+-current ($I_{K,fb}$, panel D) with progressive $I_{Kv,fb}$ downregulation for a cardiomyocyte paced at 4 Hz coupled to two fibroblasts by a gap junction conductivity of 3 nS. Downregulation of fibroblast $I_{Kv,fb}$ decreased the total fibroblast K^+ current (Figure 36D), reducing the fibroblast repolarizing current. This had the effect of increasing the gap junction current flow from the fibroblast to the cardiomyocyte during phases 2 and 3 of the cardiomyocyte action potential (Figure 36C), thereby making the fibroblast a source of depolarizing current. This depolarizing current led to progressive cardiomyocyte APD prolongation (Figure 36A). $I_{Kv,fb}$ downregulation also had a depolarizing effect on the cardiomyocyte RMP.

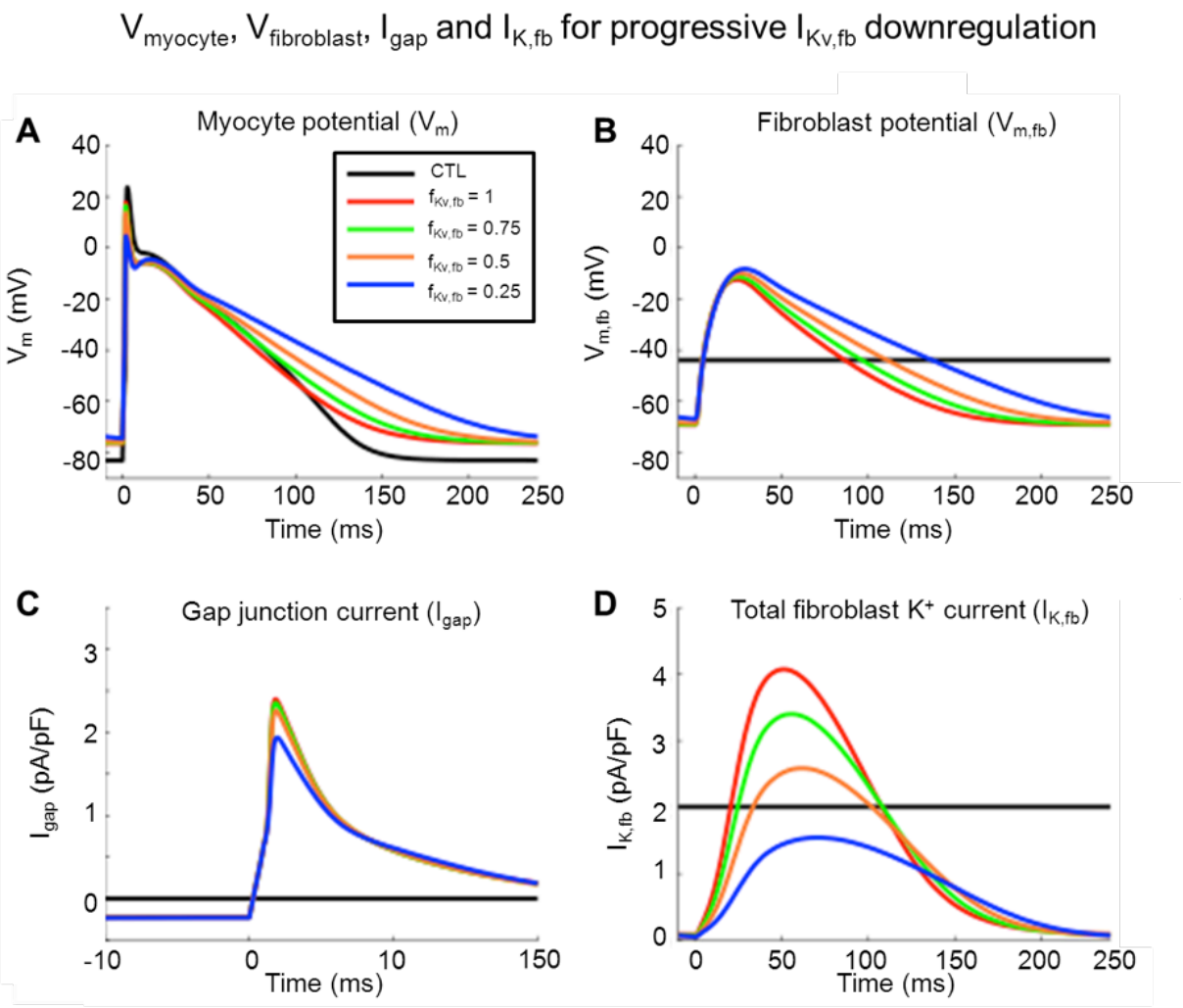

Figure 36. Effect of fibroblast $I_{Kv,fb}$-downregulation on action potential and relevant currents. Effect of fibroblast $I_{Kv,fb}$-downregulation on (A) cardiomyocyte transmembrane potential (V_m), (B) fibroblast transmembrane potential ($V_{m,fb}$), (C) gap junction current (I_{gap}), and (D) total fibroblast K^+-current ($I_{K,fb}$). Progressive $I_{Kv,fb}$ downregulation decreased the fibroblast repolarizing K^+-current density, making the fibroblast behave as a current source during phase 2 and 3 of the cardiomyocyte action potential leading to APD prolongation. The cardiomyocyte RMP was depolarized by $I_{Kv,fb}$-downregulation, leading to partial I_{Na} inactivation. Results were obtained with two fibroblasts connected to a cardiomyocyte paced at 4 Hz with a G_{gap} of 3 nS.

Figures 37A-D show the same variables as in Figure 36, but for graded $I_{Kir,fb}$ upregulation. Upregulation of $I_{Kir,fb}$ progressively increased the total fibroblast K^+ current (Figure 37D), thus

increasing the fibroblast repolarizing current. This effect increased the gap junction current from the cardiomyocyte to the fibroblast, thereby making the fibroblast a current sink for the cardiomyocyte, shortening the cardiomyocyte APD (Figure 37A). $I_{Kir,fb}$ upregulation also had a hyperpolarizing effect on the RMP, helping to maintain Na^+-current availability during phase 0 of the action potential.

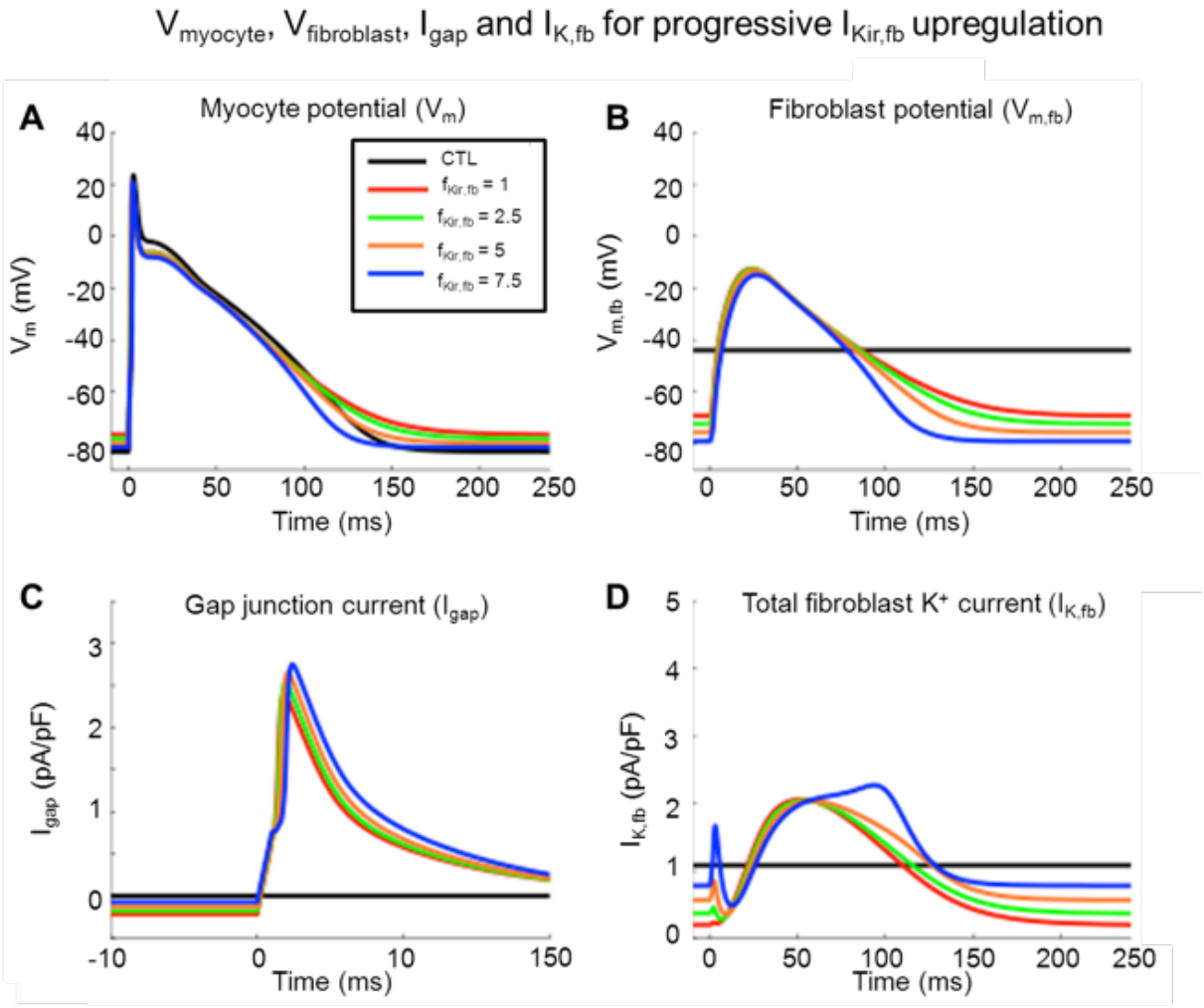

Figure 37. Effect of fibroblast $I_{Kir,fb}$-upregulation on the action potential and relevant currents. Effect of fibroblast $I_{Kir,fb}$-upregulation on (A) cardiomyocyte trans-membrane potential (V_m), (B) fibroblast transmembrane potential ($V_{m,fb}$), (C) gap junction current (I_{gap}), and (D) total fibroblast K^+-current ($I_{K,fb}$). $I_{Kir,fb}$-upregulation increases fibroblast repolarizing K^+-current density, making the fibroblast behave as a current sink during phase 2 and 3 of the myocyte

action potential leading to APD shortening. The cardiomyocyte was hyperpolarized by $I_{Kir,fb}$ upregulation, preserving Na^+ channel availability. R Results were obtained with two fibroblasts connected to a cardiomyocyte paced at 4 Hz with a G_{gap} of 3 nS.

5.1.4.4 Graded effects of fibroblast electrical remodeling on atrial tissue RMP, APD_{90}, and conduction velocity

The effects of fibroblast ion-current remodeling on cardiomyocyte cellular electrical properties was determined by simulating activation of a cable over a wide range of pacing frequencies to vary diastolic interval (DI). Supplemental Figure 5.2 shows the resting membrane potential (RMP; panel A), action potential duration at 90% repolarization (APD_{90}, panel B), and conduction velocity (CV, panel C) as a function DI for $I_{Kv,fb}$ downregulation (red) and $I_{Kir,fb}$ upregulation (green) over a 10-cm cable with 2 fibroblasts per cardiomyocyte with a G_{gap} of 3 nS. $I_{Kv,fb}$ downregulation had a small depolarizing effect on the cardiomyocyte RMP but substantially prolonged APD compared to control (e.g. APD_{90} at BCL = 500 ms for $f_{Kv,fb}$ = 1.0, 0.75, 0.5 and 0.25 were 162 ms, 175 ms, 194 ms, and 225 ms, respectively; RMP values were -76.9 mV, -76.8 mV, -76.6 mV, -76.4 mV, respectively). Conduction velocities paralleled the conduction velocities for the control condition over the spectrum of $f_{Kv,fb}$ under investigation.

$I_{Kir,fb}$ upregulation had the opposite effect on repolarization and resting potentials, significantly hyperpolarizing the cardiomyocyte RMP and shortening APD_{90} versus control (APD_{90} values at BCL = 500 ms for $f_{Kir,fb}$ = 1.0, 2.5, 5.0, and 10 were 162 ms, 152 ms, 137 ms, and 115 ms, respectively; corresponding RMP values were -76.9 mV, -78.22 mv, -79.7 mV and -81.2 mV). $I_{Kir,fb}$ upregulation reduced CVs at long DIs compared to control, but CVs were increased compared to control at DIs less than 150 ms, highlighting the biphasic effect of RMP on CV and the prolongation of the Na^+ channel recovery time constant at more positive RMP (226) (e.g. at DI ≈ 62 ms, CVs for $f_{Kir,fb}$ = 1.0, 2.5, 5.0, and 10 were 72.2 cm/s, 78.4 cm/s, 85.4 cm/s, and 89.5 cm/s, respectively). 1:1 conduction was sustained at progressively shorter DIs with increasing $f_{Kir,fb}$ (Supplemental Figure 5.2B).

5.1.4.5 Effect of fibroblast electrical remodeling on 2D spiral-wave dynamics

Figure 38 shows the APD_{90} distribution over a 2-dimensional sheet of atrial cardiomyocytes with moderate fibrosis density and 2 fibroblasts per cardiomyocyte, with a G_{gap} of 3 nS, for progressive $I_{Kir,fb}$ upregulation (Figure 38, top row) and $I_{Kv,fb}$ downregulation (Figure 38, bottom row). In accordance with the single cell and cable analyses, mean APD_{90} was progressively shortened by $I_{Kir,fb}$ upregulation (mean APD_{90} values for $f_{Kir,fb}$ = 1.0, 2.5, 5.0, and 10 were 121 ms, 116 ms, 107 ms, and 81 ms, respectively; Figures 38A-D). The APD_{90} dispersion, as quantified by the APD_{90} coefficient of variation, increased with $I_{Kir,fb}$ upregulation (e.g. coefficient of variation for CTL and $f_{Kir,fb}$ =10 were 0.8% and 6.2%, respectively). $I_{Kv,fb}$ downregulation (Figures 38E-H) prolonged mean APD_{90} (mean APD_{90} values for $f_{Kv,fb}$ = 1.0, 0.75, 0.5, and 0.25 were 121 ms, 134 ms, 154 ms, and 159 ms, respectively) and increased the coefficient of variation, to an extent similar to $I_{Kir,fb}$ upregulation (coefficient of variation for CTL and $f_{Kv,fb}$ = 0.25 were 0.8% and 6.2%, respectively). Supplemental Figure 5.3 illustrates the increasing spatial variability of APD due to heterogeneous distribution of fibroblasts as a function of ion-current remodeling, by showing results as a heat map of APD deviations around the mean under each condition.

Figure 6

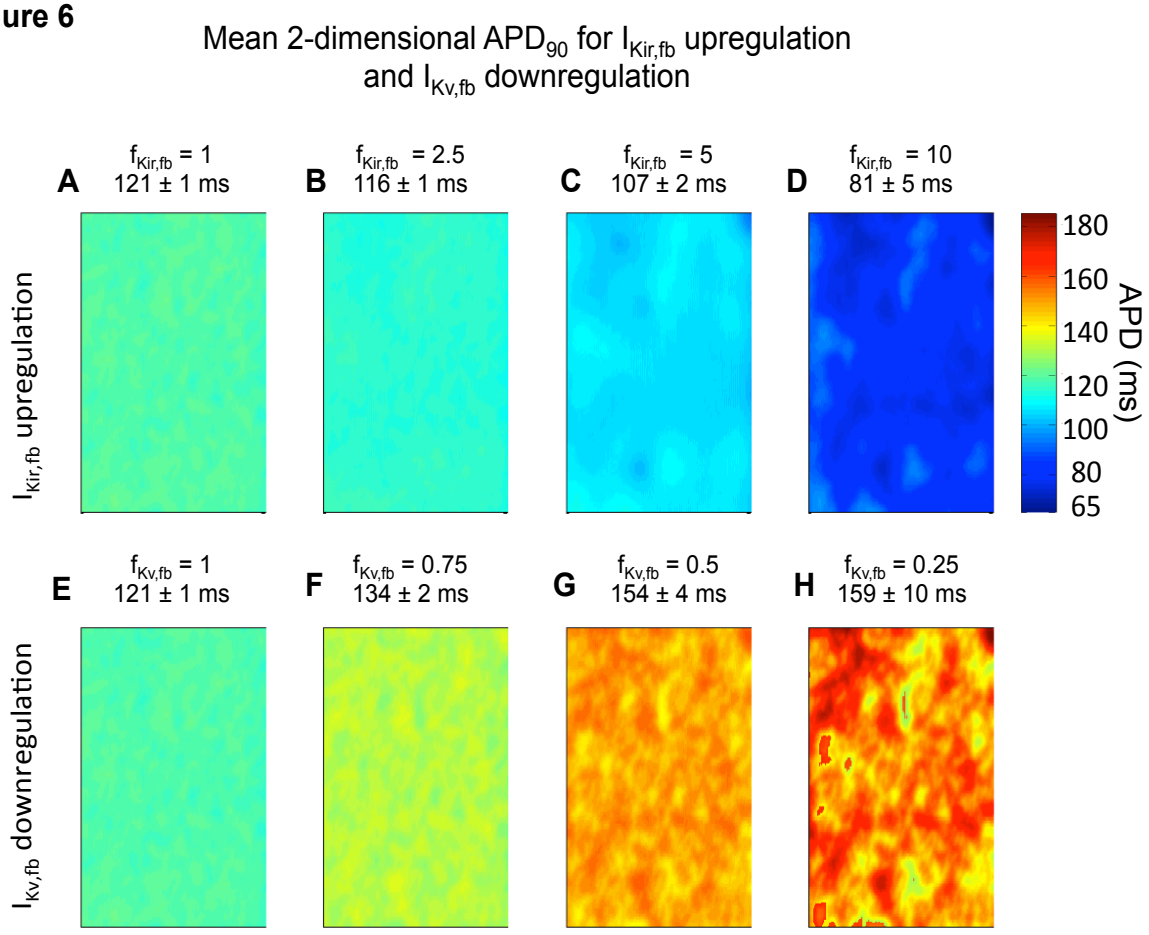

Figure 38. APD_{90}-distribution over a 2-dimensional sheet of cardiomyocytes with patchy fibrosis (two fibroblasts with a G_{gap} of 3 nS per cardiomyocyte) in the 2-dimensional model for $I_{Kir,fb}$-upregulation (top row, panels A-D) and $I_{Kv,fb}$ down-regulation (bottom row, panels E-H). APD_{90} was reduced by $I_{Kir,fb}$ up-regulation and increased by $I_{Kv,fb}$ downregulation. Values above each panel are mean±SD APD_{90} across the substrate.

Figure 39A shows snapshots of the cardiomyocyte transmembrane potential as a function of time over a 2-dimensional sheet of cardiomyocytes for progressive $I_{Kir,fb}$ upregulation with $I_{Kv,fb}$ at its control value. For the non-remodeled condition ($f_{Kir,fb}$ = 1, $f_{Kv,fb}$ = 1, first column), the wavefront quickly drifted out of the substrate and extinguished on the right boundary after completing a single revolution. For intermediate $I_{Kir,fb}$ upregulation ($f_{Kir,fb}$ = 2.5, second column), the wavefront completed about three revolutions before terminating. At higher levels

of $I_{Kir,fb}$ upregulation ($f_{Kir,fb}$ = 5 and 10), the wavefront was successfully contained within the substrate boundaries, leading to sustained re-entry. Panel B shows the rotor trajectories of the 2-dimensional substrate for the corresponding simulations; as $f_{Kir,fb}$ was increased, the rotor stabilized into a more compact, quasi-periodic rosette-like meandering pattern. Supplemental Figure 5.4 shows the power spectra analysis for $I_{Kir,fb}$ upregulation; the dominant frequencies of rotors progressively increased with increasing $f_{Kir,fb}$, passing from 5.7 to 6.1 and then 6.7 Hz. The non-remodeled condition ($f_{Kir,fb}$ = 1, $f_{Kv,fb}$ = 1) terminated after completing a single revolution, precluding the formal calculation of the spiral wave's dominant frequency; it was estimated to be 4.6 Hz.

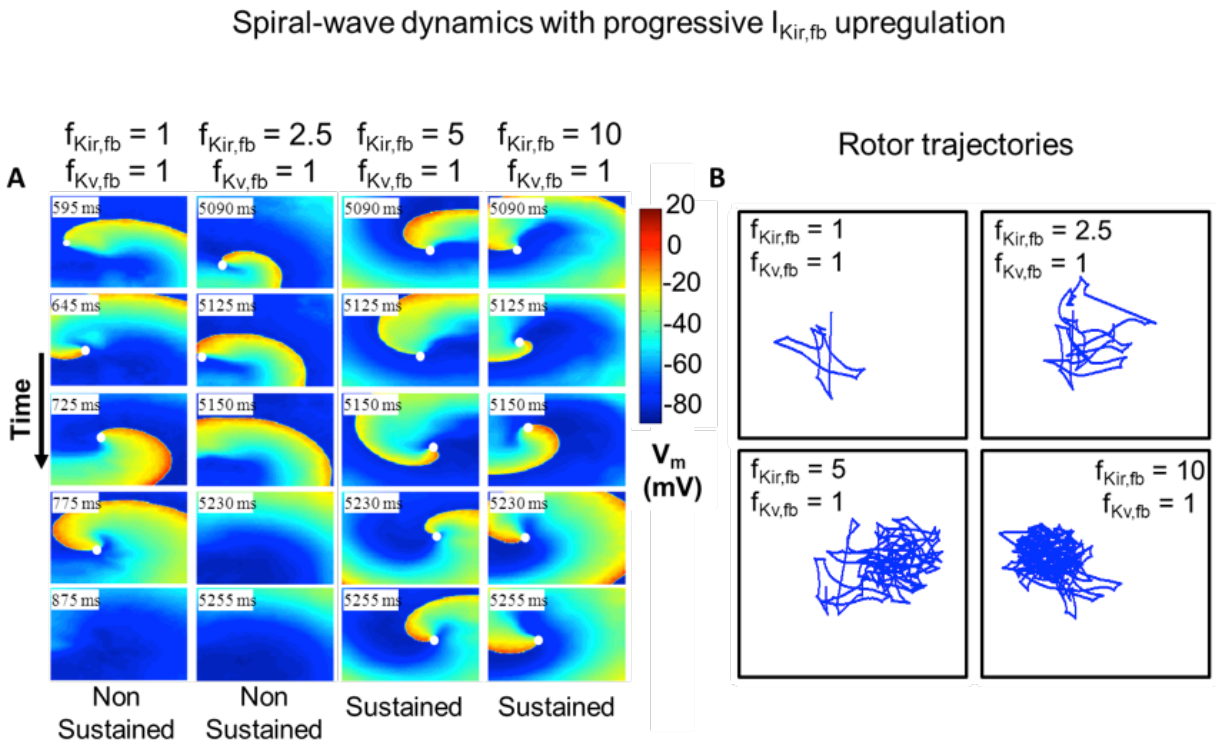

Figure 39. Spiral-wave dynamics with progressive $I_{Kir,fb}$ upregulation. (A) Spiral-wave dynamics over time for progressive $I_{Kir,fb}$ upregulation and fixed $I_{Kv,fb}$. White dots identify the rotor-tip phase-singularities. In the control condition ($f_{Kir,fb}$ = $f_{Kv,fb}$ = 1), the phase-singularity rapidly drifts and extinguishes on a boundary. With $f_{Kir,fb}$ = 2.5, the spiral-wave completes one complete revolution before extinguishing. With $f_{Kir,fb}$ = 5 and 10, re-entry is sustained. (B) Rotor trajectory for the corresponding simulations in (A).

Supplemental Figure 5.5A follows the same format as Figure 39 but for $I_{Kv,fb}$ downregulation while keeping $I_{Kir,fb}$ at the control value. As previously described, for the control condition ($f_{Kir,fb} = 1$, $f_{Kv,fb} = 1$, leftmost column) the wavefront rapidly extinguished on a substrate boundary. Similar dynamics are observed with $f_{Kv,fb} = 0.75$ ($f_{Kir,fb} = 1$, $f_{Kv,fb} = 0.75$, second column). With 2- and 4-fold $I_{Kv,fb}$ downregulation, the wavefront failed to depolarize neighboring cardiomyocytes, also leading to propagation failure and re-entry termination with qualitatively similar dynamics ($f_{Kir,fb} = 1$, $f_{Kv,fb} = 0.5$ and 0.25, third and fourth columns). Supplemental Figure 5.5B shows the rotor trajectories for the corresponding simulations; all three trajectories had the same morphology. Hence, $I_{Kv,fb}$ downregulation did not facilitate re-entry; re-entry was not sustained long enough to allow for determination of the dominant frequency.

We then investigated the effect of combined $I_{Kir,fb}$ upregulation and $I_{Kv,fb}$ downregulation on reentry dynamics. Figures 40A and B show representative examples of the dynamics observed under control conditions ($f_{Kir,fb} = 1$, $f_{Kv,fb} = 1$), with $I_{Kv,fb}$ downregulation ($f_{Kir,fb} = 1$, $f_{Kv,fb} = 0.25$), $I_{Kir,fb}$ upregulation ($f_{Kir,fb} = 5$, $f_{Kv,fb} = 1$), and $I_{Kir,fb}$ upregulation with the addition of $I_{Kv,fb}$ suppression ($f_{Kir,fb} = 5$, $f_{Kv,fb} = 0$), along with corresponding rotor trajectories. $I_{Kir,fb}$ upregulation stabilized the primary rotor, leading to sustained re-entry (Figure 40A, third column vs. first column). Keeping $I_{Kir,fb}$ at proarrhythmic conditions but simulating the addition of an $I_{Kv,fb}$ blocker by $I_{Kv,fb}$ downregulation (Figure 40A, fourth column) successfully terminated reentry, with rotor dynamics (Figure 40B) becoming qualitatively similar to the control condition. In summary, the arrhythmogenic effect of fibroblast remodeling is strongly dependent on the relative degree of $I_{Kv,fb}$ downregulation and $I_{Kir,fb}$ upregulation, and $I_{Kv,fb}$ suppression is able to terminate AF under proarrhythmic conditions.

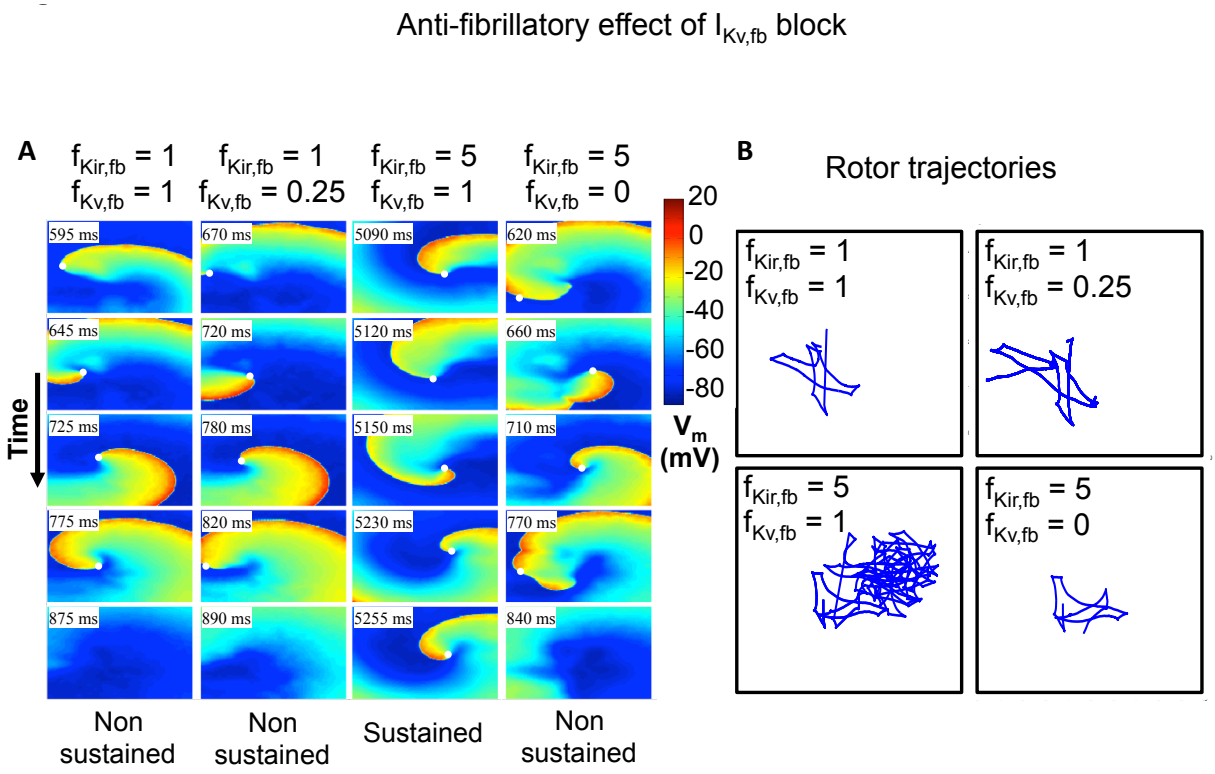

Figure 40. Spiral-wave dynamics for representative cases of mixed $I_{Kir,fb}$ up-regulation and $I_{Kv,fb}$ downregulation. Down-regulation of $I_{Kv,fb}$ terminates reentry after fewer revolutions under control-conditions. Conversely, $I_{Kir,fb}$-upregulation leads to sustained reentry. Simulating the addition of an $I_{Kv,fb}$-blocker under proarrhythmic conditions (last column) demonstrates the potential antiarrhythmic effect of $I_{Kv,fb}$-blockade, with reentry-termination occurring promptly where reentry had previously been sustained. (B) Trajectories of spiral wave rotor core-tip corresponding to cases in (A).

Supplemental Figure 5.6 shows the model-predicted effects of the average experimentally-observed change in $I_{Kir,fb}$ and $I_{Kv,fb}$ remodeling on AF-vulnerability. With 2 fibroblasts per cardiomyocyte, spiral-wave dynamics were similar to the non-remodeled condition, with reentry terminating shortly after initiation. However, with 4 fibroblasts per cardiomyocyte, the HF-induced fibroblast ionic remodeling effect was greater, leading to more complex reentry dynamics and greater spiral-wave persistence compared to control. HF also increases fibroblast capacitance ($C_{m,fb}$), at least in part by increasing fibroblast size (Supplemental Figure 5.7). This increase would be expected to enhance the electrotonic

influence of fibroblasts on coupled cardiomyocytes. The result of reproducing experimental HF-induced $C_{m,fb}$-increases is also shown in Supplemental Figure 5.6. The HF-induced $C_{m,fb}$ remodeling prolonged time to termination and qualitatively increased rotor trajectory complexity for 2 fibroblasts per cardiomyocyte, whereas it had the opposite effect with 4 fibroblasts per cardiomyocyte. These discrepant changes result from the fact that $C_{m,fb}$-increases enhance the effects of both profibrillatory $I_{Kir,fb}$-increases and antifibrillatory $I_{Kv,fb}$-decreases, with the net change determined by the balance between the two.

5.1.5 Discussion

The main findings from this study are that: 1) HF induces fibroblast ion-current remodeling by downregulating $I_{Kv,fb}$ and upregulating $I_{Kir,fb}$; 2) in the presence of appreciable cardiomyocyte-fibroblast electrical coupling, fibroblast ionic remodeling affects the electrophysiology of coupled cardiomyocytes; 3) atrial arrhythmogenesis is altered by fibroblast ion-current remodeling, with $I_{Kv,fb}$ downregulation having an anti-fibrillatory effect and $I_{Kir,fb}$ upregulation having a pro-fibrillatory effect. To our knowledge, this is the first report describing fibroblast ionic current remodeling in the setting of HF and investigating the potential effects of this remodeling on atrial arrhythmogenesis.

5.1.5.1 Relation to previous studies on fibroblast ion currents

The properties of $I_{Kir,fb}$ and $I_{Kv,fb}$ described in this paper are grossly similar to those reported in prior studies of rat (227), canine (223, 225) and human (228) fibroblasts. The downregulation of $I_{Kv,fb}$ reported here is similar to our observations in previous work, both in fibroblasts from HF animals and occurring spontaneously under cell-culture conditions (223, 225). We are not aware of prior reports of $I_{Kir,fb}$ remodeling in HF. The fibroblast RMP was hyperpolarized in HF compared to control (-53±2.1 vs -42±1.9 mV) because of upregulation of $I_{Kir,fb}$, as inward-rectifier current is the primary determinant of the fibroblast RMP (229). Our simulated non-remodeled fibroblast RMP closely matched the experimental measurements (experimental and simulated RMP were -42±1.9 vs -43.2 mV respectively). In our experiments, the baseline $C_{m,fb}$ was somewhat larger than previously reported for rat ventricular fibroblasts (17.8±1.4 vs 6.3 pF) (227) and greatly increased in HF animals (29.7±2.2 pF), closer to the value

of 53 pF reported for rat ventricular myofibroblasts (227) and passage 2-6 human fibroblasts (228). The differences may be due to species-, tissue- and study-conditions.

5.1.5.2 Potential role of fibroblast electrical remodeling in atrial arrhythmogenesis

There is extensive evidence from in vitro and simulation models that fibroblast coupling to cardiomyocytes can alter cardiac electrical activity and promote arrhythmogenesis (213), although clear in vivo evidence is lacking. Fibroblasts can couple cardiomyocytes over extended distances, producing arrhythmogenic coupling delays (216). Cardiac injury promotes fibroblast-cardiomyocyte interactions, enhancing their ability to contribute to arrhythmia formation (230). Co-culture of myofibroblasts with cardiomyocytes is associated with electrotonic coupling that is highly arrhythmogenic (219). Mathematical modeling work suggests that cardiomyocyte-fibroblast interactions contribute to conduction abnormalities in arrhythmogenic left atrial posterior walls from HF animals (212) and to complex fractionated electrogram patterns in patients (224).

Mathematical modeling has been applied extensively to assess the potential electrophysiological consequences of fibroblast-cardiomyocyte coupling. Key determinants include the size of individual fibroblasts relative to cardiomyocytes, the number of fibroblasts coupled to cardiomyocytes, and fibroblast density (220, 221, 231-233). Here, we introduced a determinant that has not been examined before: changes in fibroblast K^+-channel properties resulting from phenotypic alterations induced by cardiac pathology. The functional effect of fibroblast electrical remodeling on atrial arrhythmogenesis was investigated by independently upregulating $I_{Kir,fb}$ and downregulating $I_{Kv,fb}$. $I_{Kir,fb}$ upregulation proved to be pro-fibrillatory, whereas $I_{Kv,fb}$ downregulation was anti-fibrillatory. As summarized in Supplemental Figure 5.8, the pro-fibrillatory effect of fibroblast $I_{Kir,fb}$ upregulation was mediated through an increased fibroblast repolarizing current, making the fibroblast act as a current sink for the cardiomyocyte, leading to 1) hyperpolarization of the atrial cardiomyocyte RMP and increased cardiomyocyte I_{Na} availability, and 2) shortening of the atrial cardiomyocyte APD, thereby preserving cardiomyocyte excitability, facilitating conduction and reentry at higher frequencies like those of AF. In contrast, the anti-fibrillatory effect of $I_{Kv,fb}$ downregulation was mediated through a decrease in fibroblast repolarizing current, making the fibroblast act as a current source for the

cardiomyocyte, leading to 1) depolarization of the atrial cardiomyocyte RMP and decreased I_{Na} availability, and 2) prolongation of the APD, decreasing cardiomyocyte excitability and impeding reentry.

Our findings are conceptually consistent with previous work on AF-induced cardiomyocyte remodeling by Pandit et al (46), in which they described the rotor-stabilizing effects of atrial cardiomyocyte $I_{Kir,fb}$-equivalent (I_{K1}) upregulation. They found that cardiomyocyte I_{K1} upregulation hyperpolarized the RMP, increasing I_{Na} availability and shortening APD, similar to what we observed with $I_{Kir,fb}$ upregulation, facilitating reentry and maintenance of the rotor underlying AF. In our study, the cardiomyocyte was hyperpolarized through a novel indirect mechanism, that of fibroblast electrical remodeling and cardiomyocyte-fibroblast electrical interaction, in the absence of intrinsic cardiomyocyte I_{K1} upregulation.

To clarify their individual effects, most of our analyses of $I_{Kir,fb}$ and $I_{Kv,fb}$ remodeling were performed by independently up- or downscaling individual current conductance. However, the experimental data show that $I_{Kv,fb}$ and $I_{Kir,fb}$ remodeling occurred simultaneously. We therefore investigated the effect of simultaneous $I_{Kv,fb}$ downregulation and $I_{Kir,fb}$ upregulation (Supplemental Figure 5.6) and found that the balance between these opposing effects determines the consequences of fibroblast ion-current remodeling on AF properties. Using experimentally-obtained values for $I_{Kir,fb}$ upregulation and $I_{Kv,fb}$ downregulation, we found that HF-induced fibroblast ionic remodeling has the capacity to promote AF (Supplemental Figure 5.6) while prolonging the effective refractory period, as observed experimentally (Supplemental Tables 5.1 and 5.2). However, for a given upregulated $f_{Kir,fb}$, one could observe sustained reentry, non-sustained reentry or no reentry at all depending on the degree of $I_{Kv,fb}$ downregulation. With our first-order model, it is difficult to directly correlate the magnitude of the experimentally-observed remodeling with mathematical-model predictions regarding atrial arrhythmogenesis. Nevertheless, $I_{Kv,fb}$ had to be downregulated to extreme values before it could counterbalance modest $I_{Kir,fb}$ upregulation. Atrial cardiomyocyte ionic-current remodeling also occurs in HF (234). Implementing both cardiomyocyte and fibroblast ionic modeling (Supplemental Tables 5.1 and 5.2), we found that the cardiomyocyte ionic remodeling previously reported to prolong APD and ERP (234) makes reentry maintenance more difficult, but does not otherwise alter the qualitative properties of AF associated with fibroblast ionic remodeling as described here (Supplemental Figure 5.9).

5.1.5.3 Novelty and potential importance

The notion that atrial ion-current remodeling plays an important role in AF-promotion has been established for almost 20 years (42). Atrial ion-current remodeling has always been associated with cardiomyocyte ion-currents: here, we show for the first time that the fibroblast ion-current remodeling occurring with AF-promoting pathologies might affect AF-susceptibility. The remodeling of ion-currents in fibroblasts coupled to cardiomyocytes was able to contribute to the AF-maintaining substrate via electrotonic interactions that modified cardiomyocyte electrical function in profibrillatory ways. We also found that reducing $I_{Kv,fb}$ could counter the profibrillatory effect of $I_{Kir,fb}$ upregulation and lead to reentry termination, providing a proof-of-principle for the plausibility of targeting the ion-currents of cardiomyocyte-coupled fibroblasts for antiarrhythmic purposes. Conversely, one could target $I_{Kir,fb}$, as upregulation of this current was clearly found to facilitate reentry. Traditional cardiomyocyte K^+-channel blockers are moderately effective antiarrhythmic agents; however, their use is severely limited by ventricular proarrhythmic risk (e.g. Torsade des pointes), resulting from APD and QTc prolongation (235). A selective blocker of fibroblast Kv or Kir current with little action on corresponding cardiomyocyte currents might convey antiarrhythmic activity with the benefit of interacting with atrial tissue predominantly in areas of fibrosis, thereby theoretically avoiding the risk of K^+-channel blocker induced ventricular proarrhythmia. If significant atrial fibroblast-cardiomyocyte coupling is confirmed in vivo, it might be of interest to search for molecular and/or functional differences between cardiomyocyte and fibroblast K^+-channels, as a basis for developing fibroblast-selective pharmacological agents.

Targeting fibroblast ionic currents for antiarrhythmic drug therapy might have applications beyond rhythm control of AF. Ventricular tachyarrhythmias in patients with ischemic cardiomyopathies are a major source of cardiovascular morbidity and a leading cause of sudden cardiac death (236). These arrhythmias often originate in post-infarction scars with complex networks of viable and hibernating myocardium imbedded within the area of infarction, making such highly proarrhythmic lesions difficult to treat via catheter ablation (237). Targeting ventricular fibroblast ion-currents to produce antiarrhythmic electrophysiological changes in and around the infarct site may provide a new paradigm for the

management of complex ventricular arrhythmias (238). Evidence has been presented to suggest that modulating fibroblast ATP-regulated K^+-current may be exploited to alter border-zone electrophysiology in infarcted hearts (239).

5.1.5.4 Potential limitations

A significant limitation of this work is the lack of in vivo evidence of cardiomyocyte-fibroblast electrical coupling. Several studies have demonstrated the existence of cardiomyocyte-fibroblast electrical coupling in experimental co-cultured media. Nevertheless, with the exception of work on the sino-atrial node, it has not to date been technically possible to determine whether such coupling occurs in vivo. Despite extensive experimentation with a variety of in vitro systems, this fundamental question remains to be resolved to establish the in vivo relevance of cardiomyocyte-fibroblast electrical interactions in the heart. Establishing the significance of fibroblast electrical remodeling in the pathogenesis of AF remains critically dependent on experimental validation of electrical coupling between cardiomyocytes and fibroblasts in the atrium in situ.

We only considered cardiomyocyte-fibroblast coupling (single-sided connections in Kohl's terminology (240)), without considering that fibroblasts may couple to more than one cardiomyocyte at a time, creating electrical connections between previously disconnected cardiomyocytes (double-sided connections). We used a single specific value for G_{gap}, knowing that the magnitude of this parameter can have a significant impact on the dynamics of cardiomyocyte-fibroblast coupling (220). We selected a G_{gap} well within experimentally-reported values, which range from 0.31 to 8 nS (214, 215). In addition, we examined limited combinations of conditions of fibroblast-coupling and numbers of fibroblasts coupled to cardiomyocytes (N_{fb}). Supplemental Figure 5.10 shows a further examination of the parameter space, varying N_{fb}, G_{gap} and $C_{m,fb}$. Some of the parameter-manipulations had the expected effects (e.g. decreasing N_{fb} or $C_{m,fb}$ attenuated the effects of ionic remodeling, reducing $C_{m,fb}$, and reducing G_{gap} virtually eliminated the effect of $I_{Kv,fb}$-downregulation). Increasing these variables had no clear effect, perhaps because the default values were already sufficiently large that further increases produced little additional change. We also did not include the HF-induced cardiomyocyte ionic and capacitance remodeling. A limited set of simulations with remodeled

cardiomyocytes did not qualitatively change the nature of our results (Supplemental Figure 5.9). Furthermore, we used a 2D sheet to study the effect of fibroblast electrical remodeling on reentry dynamics. This choice has the limitation of introducing geometrical constraints that potentially bias arrhythmia sustainability in situations of increased meandering, leading to rotor extinction on substrate boundaries, with substrate size being an important determinant of reentry maintenance.

Finally, we used a fibroblast ionic model that was developed based on observations in ventricular fibroblasts (221). Burstein et al. showed that atrial and ventricular fibroblasts behave and proliferate differently (241). However, there were no ion-channel subunit expression differences identified on genome-wide analysis in the Burstein study (241), and recent work suggests that atrial and ventricular $I_{Kv,fb}$ differ significantly only at physiologically non-relevant voltages positive to +60 mV (225). In addition, there were no differences in $I_{Kv,fb}$ for atrial vs ventricular fibroblasts from HF-dogs (225).

5.1.6 Conclusion

HF induces fibroblast ion-current remodeling: fibroblast Kv current is downregulated whereas fibroblast Kir current is upregulated. Mathematical modeling indicates anti-fibrillatory effects of $I_{Kv,fb}$ downregulation and pro-fibrillatory effects of $I_{Kir,fb}$ upregulation, and reveals the underlying electrophysiological mechanisms. The outcome of fibroblast electrical remodeling in atria with a disease-induced AF substrate will therefore critically depend on the balance between pro- and anti-fibrillatory changes. If efficient electrical coupling between atrial fibroblasts and cardiomyocytes can be confirmed in vivo, pharmacological modulation of fibroblast K^+-currents might be useful as a potential AF-selective target for antiarrhythmic drug therapy. These findings provide new insights into the potential role of fibroblasts in the pathogenesis and treatment of AF.

5.1.7 Supplemental Material

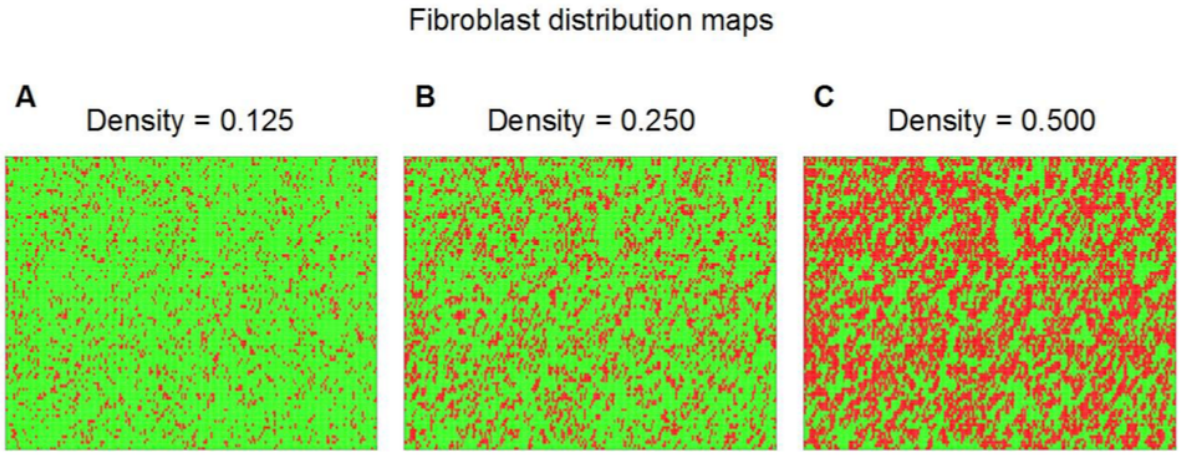

Supplemental Figure 5.1 Fibroblast distribution maps. Three different fibroblast were investigated : low, medium and high densities corresponding to 12.5%, 25% and 50% of cardiomyocytes coupled to 2 fibroblasts. The red patches represent areas of fibrosis.

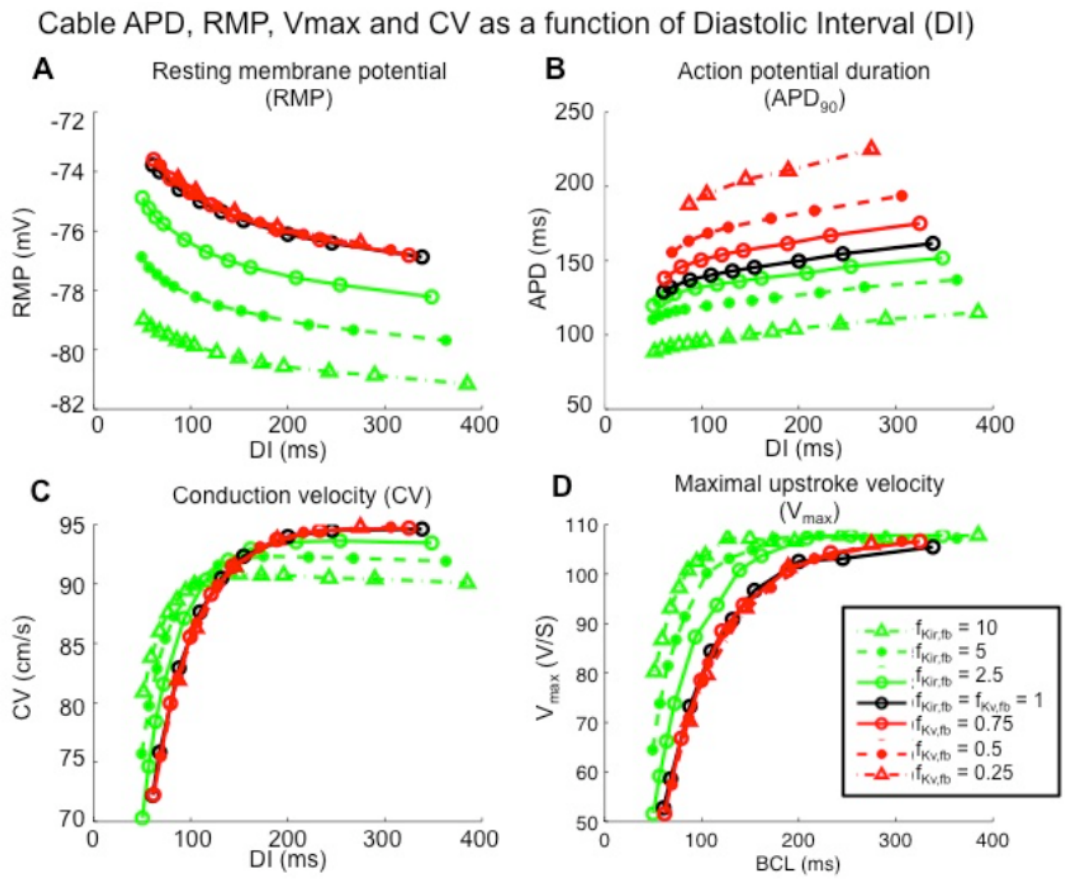

Supplementary Figure 5.2 Effect of progressive $I_{Kv,fb}$ downregulation (red curves) and $I_{Kir,fb}$ upregulation (green curves) on the cardiomyocyte resting membrane potential (RMP), action potential duration (APD_{90}), conduction velocity (CV) and maximal upstroke velocity (V_{max}) as a function of the diastolic interval (DI) for a 10-cm cable of cardiomyocytes with 2 fibroblasts per cardiomyocyte with G_{gap} of 3 nS. The control curve in black is for $f_{Kv,fb} = f_{Kir,fb} = 1$. $I_{Kv,fb}$ downregulation had a small depolarizing effect on the RMP, prolonged APD90, with negligible effect on CV. $I_{Kir,fb}$ upregulation had the opposite effect; it significantly hyperpolarized RMP, shortened APD_{90} and preserved CV and 1:1 conduction at progressively shorter DIs with increasing $f_{Kir,fb}$.

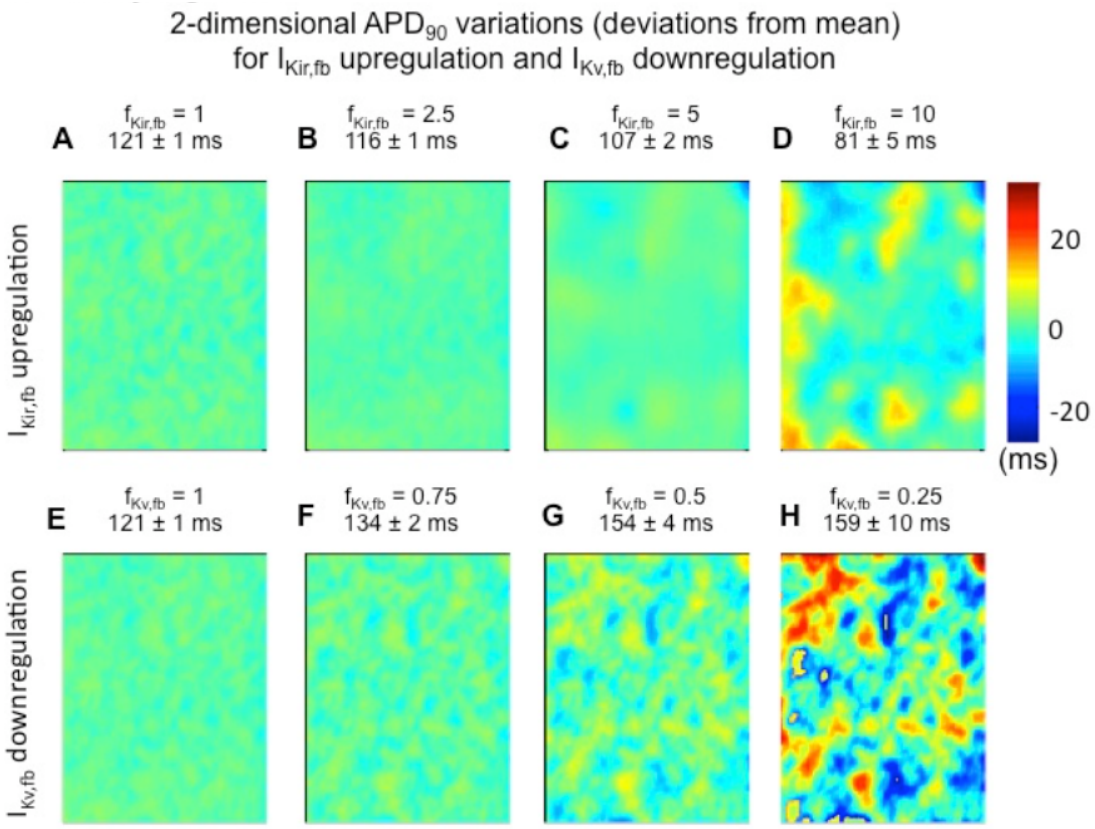

Supplemental Figure 5.3 Distribution of APD_{90}-deviations from mean-values over a 2-dimensional sheet of cardiomyocytes with patchy fibrosis (2 fibroblasts per cardiomyocyte with a G_{gap} of 3 nS) in the 2-dimensional model for progressive $I_{Kir,fb}$ upregulation (top row, panels A-D) and $I_{Kv,fb}$ downregulation (bottom row, panels E-H). APD_{90} dispersion, as indicated by the standard deviation, increases with both $I_{Kir,fb}$ upregulation and $I_{Kv,fb}$ downregulation from <1% to 6%. Values above each panel are mean±standard deviation APD_{90} across the substrate.

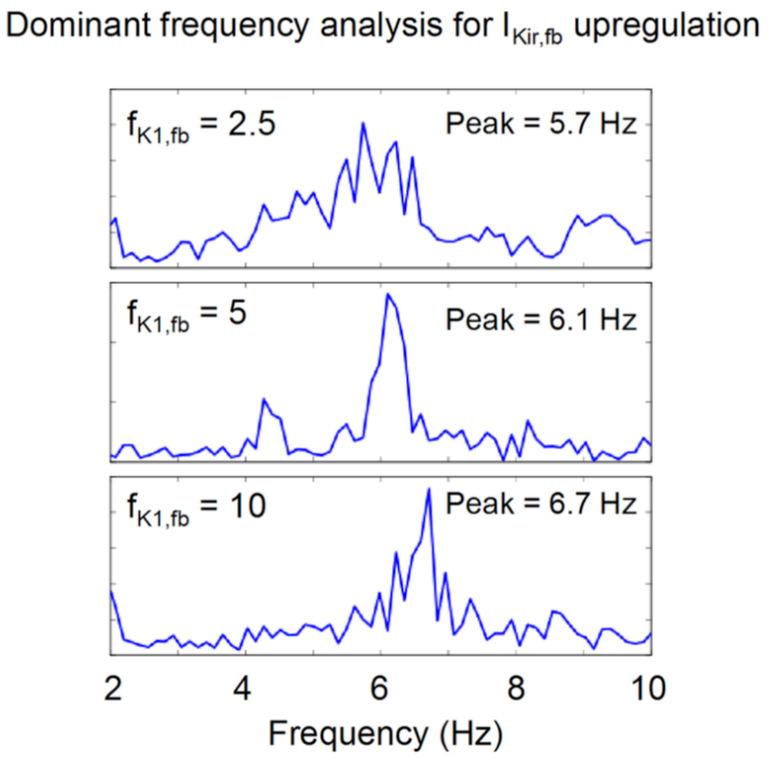

Supplemental Figure 5.4 Power spectrum analysis for $f_{Kir,fb}$ = [2.5, 5, 10]. $I_{Kir,fb}$ upregulation progressively increased the spiral-wave dominant frequency from 5.7 to 6.7 Hz. For $f_{Kir,fb}$ = 1, reentry was non-sustained, precluding precise computation of the dominant frequency, but it was estimated at 4.6 Hz.

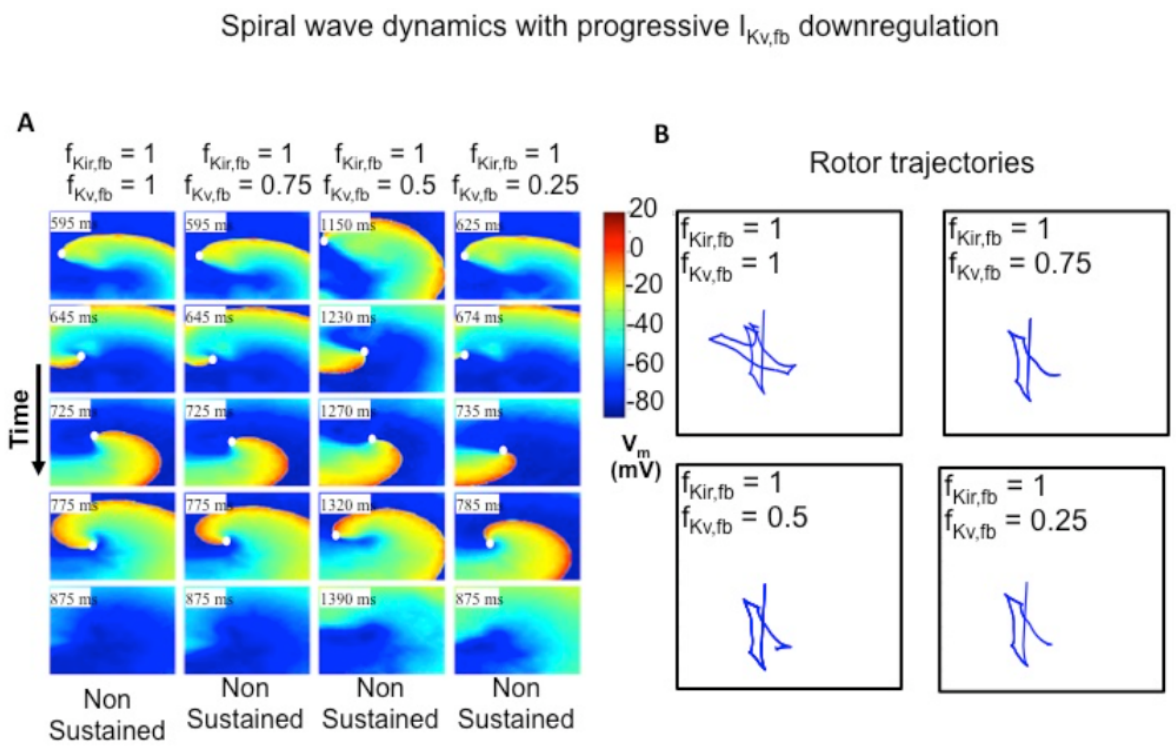

Supplemental Figure 5.5 (A) Spiral-wave dynamics over time for progressive $I_{Kv,fb}$ downregulation for fixed $I_{Kir,fb}$. White dots identify the rotor-tip phase-singularities. In the control condition ($f_{Kir,fb} = f_{Kv,fb} = 1$), the phase-singularity drifts and extinguishes on a boundary. As $I_{Kv,fb}$ is downregulated ($f_{Kv,fb}$ = 0.5 and 0.25), the wavefront fails to depolarize surrounding cardiomyocytes, leading to propagation failure and termination. (B) Rotor trajectory for the corresponding simulations in (A). Qualitatively similar trajectories were observed.

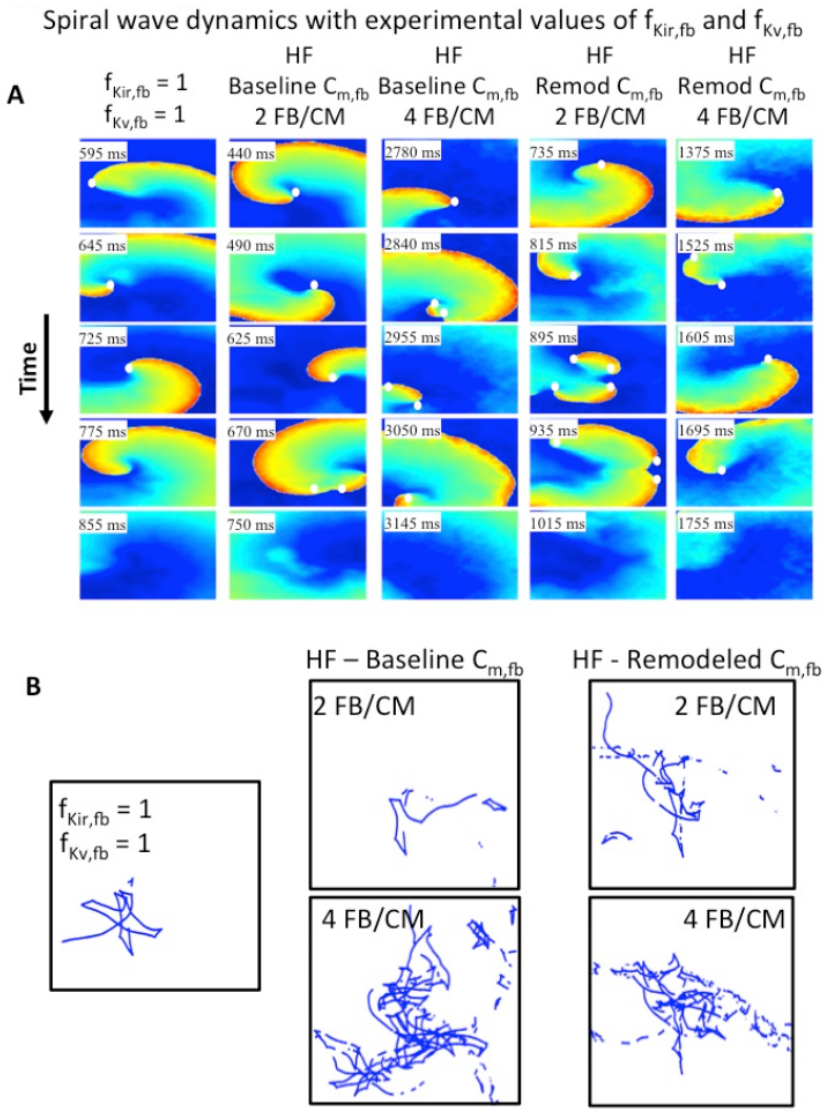

Supplemental Figure 5.6 Spiral-wave dynamics for the control ($f_{Kir,fb} = f_{Kv,fb} = 1$) and HF-induced fibroblast ionic and capacitance remodeling ($f_{Kir,fb} = 1.79$ and $f_{Kv,fb} = 0.56$; $C_{m,fb}$ remodeled = $1.67 \cdot C_{m,fb}$ baseline) using moderate fibroblast density distribution (0.250) with 2 and 4 fibroblasts/cardiomyocyte. HF with 2 fibroblasts/cardiomyocyte led to non-sustained reentry, similar to the control case, however, rotor trajectory complexity was qualitatively increased with remodeled $C_{m,fb}$. Using 4 fibroblasts/cardiomyocyte also led to non-sustained reentry; however, the time to termination was longer compared to control and HF with 2 fibroblasts/cardiomyocyte for both $C_{m,fb}$ settings. (B) Respective rotor trajectories. All cases were non-sustained, but HF with 4 fibroblasts/cardiomyocyte displayed more complex and longer-lasting dynamics.

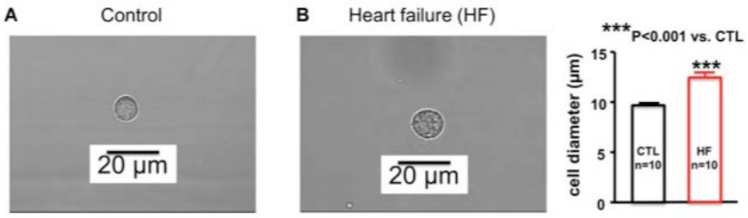

Supplemental Figure 5.7 Size difference between a control (A) and heart failure (B) fibroblast, along with mean cell diameter values for 10 cells of each type. Heart failure increased fibroblast size accounting, at least in part, for the increase in membrane capacitance in heart failure compared to control.

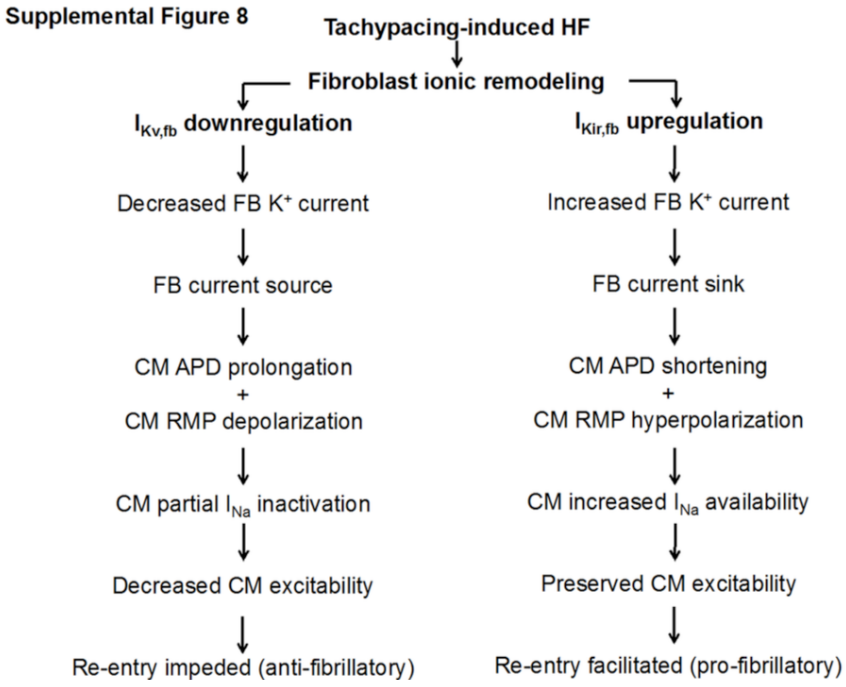

Supplemental Figure 5.8 Summary of electrophysiological effects observed for fibroblast electrical remodeling and consequences for atrial arrhythmogenesis. $I_{Kv,fb}$ downregulation in tachypacing-induced HF leads to decreased fibroblast (FB) repolarizing current, thus making it a source of depolarizing current for the cardiomyocyte (CM). This effect prolongs cardiomyocyte APD and depolarized RMP, thus inducing I_{Na} inactivation, reduced V_{max}, CV and cardiomyocyte excitability and impeding reentry (anti-fibrillatory effect). $I_{Kir,fb}$

was upregulated in tachypacing-induced HF, leading to increased fibroblast repolarizing current and making the fibroblast a current sink for the myocyte. This effect shortened cardiomyocyte APD and hyperpolarizing RMP, increasing I_{Na} availability, maintaining V_{max}, CV and cardiomyocyte excitability at high activation frequencies, thereby facilitating reentry (pro-fibrillatory effect).

	CTL (ms)	HF (ms)
Experimental (Li et al., *Circulation.* 101:2631-2638)		
APD_{90} at 3Hz	138	145
Simulated		
APD_{90} at 3Hz	139	148

Supplemental Table 5.1 Experimental single cell APD_{90} and ERP and matched simulated single cell APD_{90}.

	Experimental		Simulated					
	CTL	HF	CM CTL	CM HF	CM CTL FB CTL	CM CTL FB HF	CM HF FB CTL	CM HF FB HF
FB/CM	-	-	0	0	2	2	2	2
ERP (ms)	131	149	144	188	164	171	189	196

Supplemental Table 5.2 Experimental and simulated ERP for control and remodeled conditions with and without fibrosis.

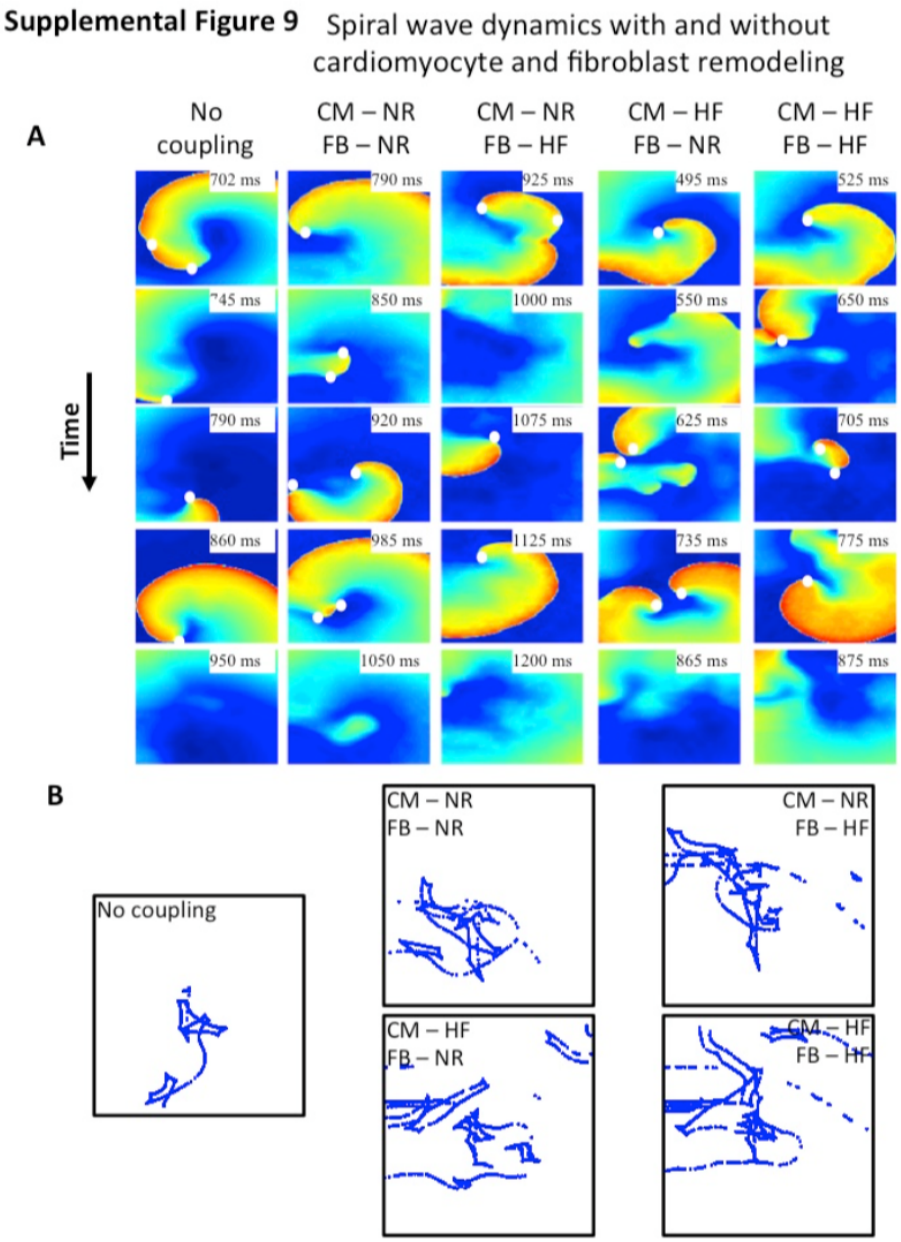

Supplemental Figure 5.9 Effect of the experimentally observed cardiomyocyte and fibroblast ionic and capacitance remodeling on reentry dynamics (A) and rotor trajectories (B). Two-dimensional reentry dynamics with and without cardiomyocyte ionic and capacitance remodeling were qualitatively similar, although termination was slightly faster with the remodeled cardiomyocyte. Fibroblast remodeling tended to prolong the duration of reentry but did not have a significant qualitative effect.

2D time to termination for control, proarrhythmic and antiarrhythmic conditions for variable N_{fb}, G_{gap}, and $C_{m,fb}$

A

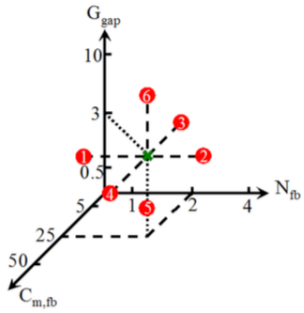

B

#	N_{fb}	G_{gap}	$C_{m,fb}$	a	b	c
		(nS)	(pF)	$f_{Kir,fb}$=1 $f_{Kv,fb}$=1	$f_{Kir,fb}$=10 $f_{Kv,fb}$=1	$f_{Kir,fb}$=1 $f_{Kv,fb}$=0.25
				Time to termination (ms)		
1	1	3	25	943	1439	957
2	4	3	25	451	S	469
3	2	3	5	938	1096	948
4	2	3	50	441	S	464
5	2	0.5	25	933	S	953
6	2	10	25	430	S	440
CTL	2	3	25	1143	S	437

Supplemental Figure 5.10 Effect of varying the number of fibroblasts per cardiomyocyte (N_{fb}), gap junction conductance (G_{gap}) and fibroblast capacitance ($C_{m,fb}$) on spiral-wave dynamics for non-remodeled (a), proarrhythmic (B) and antiarrhythmic (c) conditions. (A) Parameter-space of N_{fb}, G_{gap} and $C_{m,fb}$; the green X represents the default parameter-set used for all simulations in the paper, while the red dots indicate the variations indicated by the red numbers in the table in B. (B) Decreasing N_{fb} attenuated the proarrhythmic effect of $I_{Kir,fb}$-upregulation (#1b vs. CTLb) and antiarrhythmic effect of $I_{Kv,fb}$-downregulation (#1c vs. CTLc). Increasing the N_{fb} (#2) did not have clear effects. Reducing fibroblast-capacitance ($C_{m,fb}$) greatly attenuated effects of fibroblast ion-channel remodeling (#3b and #3c barely changed vs. #3a). Increasing $C_{m,fb}$ (#4) reduced baseline AF-persistence (#4a vs. CTLa) but did not appreciably alter persistence with remodeling (#4b and #4c vs. CTLb and CTLc respectively). Reducing G_{gap} reduced baseline rotor-persistence (#5a vs. CTLa) and virtually eliminated the effects of $I_{Kv,fb}$-downregulation (#5c barely changed vs. #5a), but AF remained sustained with $I_{Kir,fb}$-upregulation (#5b). Increasing G_{gap} did not appreciably alter the effects of ionic remodeling (#6b and #6c vs. CTLb and CTLc respectively).

Chapter 6: Discussion and Conclusion

Cardiac arrhythmias form a clinically important group of disorders. Abnormal heart rhythms are the consequences of pathological electrophysiological changes at the ionic level and myocardial substrate. Our understanding of basic cardiac electrophysiology has evolved tremendously over recent decades, in large part from collaboration between clinicians and scientists. Nevertheless, the highly non-linear nature of the cardiac action potential as well as emergent phenomena in complex geometries pose significant challenges in our ability to probe these systems with traditional experimental methods.

Computational methods are well-established in physical sciences and engineering. Mathematical modeling makes it possible to efficiently study non-linear systems and tackle questions ill-suited for bench experimentation. The application of computational methods to physiology and medicine is relatively recent; there remains an important gap between basic scientists with an expertise in mathematical modeling and clinicians faced with these complex practical problems. There is growing interest in collaborations between clinicians and scientists with complementary skill-sets. For example, it is now possible to reconstruct the cardiac anatomy of patients with complex congenital heart disease on a computer. Engineers, cardiologists and cardiac surgeons can then experiment *in silico* to find the optimal surgical repair strategy, including simulation of blood flow using fluid dynamics equations, in order to improve clinical outcomes (242).

One of the major themes of the thesis was to utilize computational approaches to the study of the consequences and therapeutic opportunities brought about by changes in ion channel properties, in particular as they relate to AF. Atrial fibrillation is a common clinical arrhythmia, reaching almost epidemic levels in the adult population; currently available AADs have limited anti-AF efficacy and significant proarrhythmic side effects. Mathematical modeling is well-suited to study how changes to ion channels properties via pharmacological modulation can be used for therapeutic applications in ways that are complementary to bench experimentation. The research questions discussed in Chapters 2 through 5 showcase clinically-relevant applications of modern computational methods.

Sinus rhythm-maintenance in patients with AF remains a major clinical challenge. The studies presented in this thesis center around a common objective, to utilize advances in basic cardiac electrophysiology to explore novel pharmacological opportunities in antiarrhythmic therapies for AF. Chapters 2 through 4 form a coherent series around the theme of AAD pharmacodynamics optimization for AF. The first of these three studies investigated the effect a NCB's pharmacodynamic properties on its anti-/pro-arrhythmic profile and delineated a range of optimized pharmacodynamic properties for which anti-AF effects were maximal with minimal proarrhythmia. The second study builds on these results by exploring the non-linear effects of addiding KCB to an optimized NCB, as defined in the first paper. Using a combination of experimental and mathematical models, this study identified the mechanisms of synergistic AF-selective antiarrhythmic actions of the NCB/KCB combination. The risk of ventricular arrhythmias associated with traditional KCBs, which target K^+ channels responsible for repolarization of the ventricular action potential is a major issue. As a response to this important clinical limitation of KCB, the third study investigated the role of I_{Kur}, an atrial-specific current, in the repolarization of the atrial action potential. The results of this work are interrelated with the findings presented in Chapters 2 and 3 as the benefits of an optimized NCB in combination with KCB (Chapter 3) can then be expanded to a combination utilizing I_{Kur} (Chapter 4), delivering incremental AF-selective antiarrhythmic effects without ventricular proarrhythmic liability. Finally, the fourth study investigated a complementary and novel antiarrhythmic strategy for AF rhythm-control, that of modulating the ionic currents expressed by cardiac fibroblasts which could in principle be additive to the modulation of cardiomyocyte currents as described in Chapters 2 through 4.

6.1 The Pharmacological Determinants of Na^+-Channel Blocker Atrial Fibrillation-Selectivity

The study presented in Chapter 2 is the first to systematically study the pharmacodynamic determinants of a state-dependent Na^+-channel blocker's antiarrhythmic efficacy and selectivity for AF. Our main findings are

(i) State-dependent Na^+-channel blockers targeting the inactivated state of the channel are optimally AF-selective ; they maximize antiarrhythmic effects while minimizing proarrhythmia.

(ii) The AF-selectivity of an optimized Na^+-channel blocker is mainly from high levels of rate-selectivity with only relatively low levels of atrial-selectivity.

(iii) A state-dependent Na^+-channel blocker AF-selectivity does not increase monotonically with its affinity for the inactivated state of the channel; there exists a narrow range of optimal parameters.

Atrial fibrillation is a complex arrhythmia. However, at the functional level, it is characterized by very rapid and disorganized activation of the atrial myocardium. An ideal AAD for the treatment of AF should have strong antiarrhythmic effects on atrial cardiomyocytes activating at rapid frequencies, such as during AF, while exerting no effect on ventricular cardiomyocytes at physiological activation rates, such as during normal sinus rhythm; we referred to this as *AF-selectivity.* Conceptually, AF-selectivity can be subdivided into the product of *rate-selectivity* and *atrial-selectivity.* Rate-selectivity is the property by which a drug has stronger effects at rapid vs slow activations rates in a given cardiomyocyte type; it is analogous to frequency- or use-dependency. Atrial-selectivity is the property by which a drug has predominant electrophysiological effects on atrial cardiomyocytes vs ventricular cardiomyocytes at a given activation rate. The Na^+ channel changes structural conformation throughout the cardiac cycle; in the simplest model, the channel cycles through a resting (closed channel but available for activation), activated (open and conducting Na^+ ions) and inactivated (closed and refractory to activation). Here, we have proposed the hypothesis that it was theoretically possible to optimize Na^+-channel blocker pharmacological properties to optimize AF-selectivity. In other words, we sought to answer the questions of what binding and unbinding rate-constants to the different states of the Na^+ channel optimize anti-AF efficacy while minimizing proarrhythmia.

Using mathematical models of the canine atrial and ventricular action potential, we were able to demonstrate that AF-selectivity is highly dependent on Na^+ channel pharmacodynamics properties. In other words, blocking the same target, the Na^+ channel, generated different

selectivity profiles as the binding/unbinding rate-constant to the activated and inactivated states of the channel were varied. With our quantitative definition of AF-selectivity, we showed that blockers targeting the inactivated state of the Na^+ channel optimized antiarrhythmic effects while minimizing proarrhythmic side effects.

We were also able to study the relative contribution of rate- vs atrial-selectivity to AF-selectivity, namely that optimization of a Na^+-channel blocker is mainly through its rate-selectivity. This is a relevant observation as (i) it narrows down the potentially highly desirable properties of compounds to combine with an optimized Na^+-channel blocker (i.e., a highly atrial-selective drug) and (ii) highlights a limitation of pure Na^+-channel block, as it is difficult to achieve elevated levels of atrial-selective on the basis of purely functional parameters.

We have also demonstrated that, although inactivated-state blockers are optimally AF-selective, AF-selectivity does not increase monotonically with affinity for the inactivated state. Rather there is a relatively narrow range of parameters for which AF-selectivity is maximal. Hence, the development of a Na^+-channel blocker for AF would not only require that it target preferentially the inactivated state of the channel but would also need to do so with fairly precise pharmacodynamics. This may be why clinically available inactivated-state Na^+-channel blockers have sub-optimal efficacy and safe profiles. This observation also highlights the relationship between the cardiomyocyte's activation frequency, the Na^+-channel blocker pharmacodynamic properties and AF-selectivity. At low levels of inactivated-state affinity, the drug has sufficient time to completely dissociate from the Na^+ channel within the diastolic interval, therefore exerting no antiarrhythmic (or proarrhythmic) effects. As the inactivated-state affinity is increased, block starts to accumulate, preferentially for rapid vs slow activation frequencies (i.e., shorter diastolic intervals); the Na^+-channel blocker now exerts AF- (mainly rate-) selective antiarrhythmic effects. If the inactivated-state affinity is further increased, block starts accumulating at progressively slower activation frequencies leading to a decrease in rate- and AF-selectivity.

This study was the first to propose a quantitative definition for AF-selectivity and to define it as the product of rate- and atrial-selectivity as these properties were most often described in qualitative terms. Quantitation proved to be critical to the systematic study of the

relationship between state-dependent Na^+-channel blocker pharmacodynamics and AF-selectivity; our definitions have since been used by others (243).

Finally, a novel contribution of this paper was that it sought to optimize a Na^+-channel blocker for AF without any *a priori* assumptions of the drug's properties. Most published work in this field at the time of our original publication studied specific drugs with predetermined pharmacodynamic properties (for example, (150) and (244)). This approach is clearly sub-optimal to study the highly non-linear relationship between AF-selectivity and the Na^+-channel blocker binding/unbinding rate-constants, a multi-dimensional optimization problem. Overall, this work highlights the strength of computational methods to tackle complex question which would be extremely challenging to address with the same level of precision in the laboratory.

6.2 The Synergistic Atrial Fibrillation-Selective Effects of Combining Na^+- and K^+-Channel Block

In this study, we sought to investigate the effect of combining an optimized state-dependent Na^+-channel blocker with a K^+-channel blocker on antiarrhythmic efficacy and AF selectivity. Our main findings are

(i) The addition of a K^+-channel blocker to an optimized state-dependent Na^+-channel blocker has synergistic AF-selective effects.

(ii) Potassium-channel block increases the antiarrhythmic efficacy of an optimized Na^+-channel blocker.

This second paper is in direct continuity with the study presented in Chapter 2, in which we addressed the optimization of the pharmacodynamic properties of a Na^+-channel blocker for AF. Here, we looked at what current-block *combination* may have complementary antiarrhythmic effects. The rational for this study is twofold. First, we have demonstrated in Chapter 2 that there exists a limit to the efficacy and selectivity of pure Na^+-channel block; it is therefore relevant to investigate other strategies to further optimize these parameters. Second, multi-channel blockers are empirically more efficacious than single-channel blockers. For example, amiodarone, the most effective clinically-available AAD, modulates almost all the

currents. It then becomes important to understand which ion currents have synergistic, neutral or even antagonist antiarrhythmic effects when blocked in combination.

Using an extension of the mathematical framework developed in Chapter 2, we demonstrated that the addition of an I_{Kr} blocker to an optimized Na^+-channel blocker produced synergistic anti-AF effects. The combination was found to have a four-fold increase in AF-selectivity vs the Na^+-channel blocker alone, mainly through an increase in rate-selectivity. We then replicated these theoretical results in an experimental canine model using pilsicainide, an inactivated-state Na^+-channel blocker, and dofetilide, a selective I_{Kr} blocker, to show that the pilsicainide/dofetilide combination had additive I_{Na}-blocking and antiarrhythmic effects, corroborating our theoretical findings.

Two prior studies had described the effects of combining ranolazine, an activated-state Na^+-channel blocker (126), with amiodarone, a multi-channel class III AAD, or dronedarone, a de-iodinate amiodarone-analogue (149, 150). Both of these studies used an experimental canine model to show that the combination of ranolazine with amiodarone or dronedarone produced stronger V_{max} reduction than either drug alone. The authors suggested that this was the result of concomitant Na^+-channel block in the activated state of the channel by ranolazine as well as in the inactivated state by amiodarone/dronedarone. Our mathematical model offered new insights into the mechanism of synergy between class I (Na^+-channel block) and III (K^+-channel block) antiarrhythmic actions. First, I_{Kr} block prolongs the APD, increasing the time the membrane spends at a depolarized potential per cardiac cycle, delaying recovery of Na^+ channels from their inactivated to resting state (as this transition is voltage-dependent). Second, the I_{Kr} block-induced prolongation of the APD depolarizes the action potential take-off potential, increasing the fraction of Na^+ channels in the inactivated state, thereby increasing functional I_{Na} block in a rate-dependent fashion. Finally, Na^+-channel blocker binding to the channel is voltage-dependent; the longer time the membrane spends at depolarized potentials in the setting of I_{Kr} block potentiates drug binding to the Na^+ channel. Hence, we were able to propose complementary, or perhaps alternative, mechanisms to explain class I and III AADs synergistic effects, other than the block of the Na^+-channel in both the activated and inactivated state, as previously suggested.

Potentially interesting research avenues emanating from the study presented in Chapter 3 includes the investigation of other combinations of channel block on antiarrhythmic efficacy and AF-selectivity. For example, given the mechanisms of Na^+- and K^+-channel block synergism discussed above, it appears plausible to hypothesize that the combination of Na^+- and Ca^{2+}-channel block may have neutral or even antagonistic effects vs pure Na^+-channel block; this would warrant a detailed analysis. Finally, Chapter 3 demonstrated the usefulness of computational approaches to the study of changes to ionic currents and how these relate to electrophysiological observation, which were subsequently corroborated in the animal laboratory.

The rapid component of the delayed-rectifier K^+ current (I_{Kr}; Kv11.1) is largely responsible for phase-3 repolarization of the action potential and is a key determinant of APD under basal conditions. Pharmacological block or inherited loss-of-function mutations in the genes encoding I_{Kr} are associated with APD and an increased risk of malignant ventricular arrhythmias. For example, the long QT syndrome (LQTS) type 2 is caused by a loss-of-function mutation in KCNH2 coding for the alpha subunit of Kv11.1 and is associated with an increased risk of sudden cardiac death. Pharmacological block of I_{Kr} with class III antiarrhythmic drugs such as dofetilide or sotalol is routinely used in clinical practice for the treatment of atrial and ventricular arrhythmias. These drugs can be associated with I_{Kr}-block-mediated QT prolongation and torsade de pointes such that, in some institutions, patients are hospitalized for continuous cardiac rhythm monitoring (telemetry) for drug initiation. A large number of non-cardiac drugs also have clinically significant affinities for I_{Kr} and can also lead to QT prolongation/ventricular arrhythmias. Torsade de pointes induced by I_{Kr}-block generally results from EADs encountering a functionally vulnerable ventricular substrate. EADs result from reactivation of Ca^{2+} channels in the setting of prolonged action potential duration, such as is the case with I_{Kr} block. In the setting of APD heterogeneity, areas of functional block likely create the proarrhythmic milieu necessary for initiation of torsade de pointes.

The simulation experiments presented in this thesis focused on atrial tissue and AF termination by antiarrhythmic drugs. We simulated isolated ventricular cardiomyocytes and used I_{Kr}-block-induced changes in action potential duration as a surrogate for QT prolongation and risk of malignant ventricular arrhythmias. This served as a safety metric in our optimization

of an AF-selective antiarrhythmic drug. In these ventricular simulations, we did not observe behaviors suggestive of torsade de pointes, such as EADs. However, it is important to note that not all mathematical models of ventricular cardiomyocytes exhibit EADs in the setting of APD prolongation as a given model may not have been developed and/or optimized for that purpose. The levels of I_{Kr} block used in these experiments were restricted to levels that would be compatible with clinical use and may therefore have been insufficient to generate EADs. Furthermore, the slow component of the delayed-rectifier K^+ current (I_{Ks}) can often limit the degree of action potential duration prolongation from I_{Kr} block. Patients with I_{Kr}-block-induced torsade de pointes likely have subclinical defects in other repolarizing currents. Finally, we also did not use a multicellular ventricular model and could therefore not observe torsade de pointes per se.

6.3 The Ionic Determinants of I_{Kur} Frequency-Dependent Properties

The paper presented in Chapter 4 sought to update the mathematical formulation for I_{Kur} inactivation dynamics in light of recent experimental data and then use this model to investigate the role of I_{Kur} inactivation and downregulation in action potential dynamics and atrial arrhythmogenesis. Our main findings are

1- We developed an updated mathematical formulation of I_{Kur} inactivation dynamics which closely reproduced experimental data.

2- Contrary to what had been proposed in the published literature, I_{Kur} rate-dependent properties are mediated by its activation properties with minimal contribution from inactivation, under physiological conditions.

3- The contribution of I_{Kur} to action potential repolarization is preserved, or even increased, in the setting of electrical remodeling-induced I_{Kur} downregulation.

In Chapter 2, we demonstrate that optimized Na^+-channel blocker AF-selectivity was mainly from its rate-selectivity; atrial-selectivity was relatively low. In Chapter 3, we extended our findings to show that combined Na^+- and K^+-channel block had synergistic antiarrhythmic

efficacy and AF-selectivity. However, the K^+ current studied in Chapter 3, I_{Kr}, is expressed in atrial *and* ventricular cardiomyocytes; it is one of the main phase-2 and -3 repolarizing currents. Clinically, I_{Kr} block prolongs the QT interval, the electrocardiographic correlate of the APD, which is a risk factor for malignant ventricular arrhythmias, a major limiting factor for successful antiarrhythmic development.

The ultra-rapid delayed-rectifier K^+ current is of particular interest for the development of an AF-selective AAD because it is only functionally expressed in atrial cardiomyocytes. Targeting I_{Kur} would, by definition, be maximally atrial-selective and the ideal complement to rate-selective Na^+-channel block, potentially leading to much improved AF-selectivity levels. However, there are two possible limitations to I_{Kur} as a viable antiarrhythmic target. First, relatively recent experimental data has shown that I_{Kur} inactivates completely at depolarized potentials. Second, I_{Kur} is downregulated in persistent/permanent forms of AF as part of the process of electrical remodeling. Hence, I_{Kur} inactivation and/or downregulation may limit the antiarrhythmic effects of I_{Kur} block.

The study presented in Chapter 4 is the first to implement a realistic mathematical formulation for I_{Kur} inactivation dynamics based on detailed experimental observations. This contribution is significant because it allowed for the first in-depth investigation of the role of I_{Kur} activation and inactivation properties on the action potential repolarization. Using the updated model, we demonstrated that, despite I_{Kur} inactivation at depolarized potentials, inactivation did not play a significant role in action potential repolarization under physiological conditions. These *a priori* contradictory observations can be reconciled by analyzing the kinetic properties of I_{Kur} inactivation. In fact, the channel inactivation gates have slow time-constants ("fast" time-constant $\tau_{ui,f} \sim 0.7$ s and slow time-constant $\tau_{ui,s} \sim 5.6$ s) and relatively depolarized inactivation potentials (-5 mV for the slow inactivation gate and +40 mV for the "fast" inactivation gate). However, under physiological conditions, the atrial action potential spends <50 ms at transmembrane potential positive to I_{Kur} inactivation potential, much too short a period of time for the inactivation gates to close. Hence, I_{Kur} does not inactivate and its dynamics are governed almost exclusively by its activation gate properties.

Most AADs have frequency-dependent actions, meaning that their electrophysiological effects vary with the cardiomyocyte's activation frequency. Sodium-channel blockers are

prototypical *forward use-dependent* agents; their CV/V_{max}-reducing effects are more pronounced at rapid vs slow activation rates. Conversely, K^+-channel blockers display *reverse use-dependent* properties, meaning that their APD-prolonging effects are stronger at slow vs rapid activation frequencies. Clearly, forward used-dependent drugs are much more attractive candidate AADs for the treatment of tachyarrhythmias such as AF, than reverse used-dependent agents; this is a limitation of K^+-channel block as an antiarrhythmic target. Interestingly, recent experimental observations have suggested that I_{Kur}, a K^+ current, block may display *forward* use-dependent properties (172). The ionic mechanisms underlying the rate-dependent effects of I_{Kur} blockade had not been described in detail.

We used our mathematical model with updated inactivation dynamics to investigate this question. We found that I_{Kur} block forward use-dependent effects are the result of functional interactions between the cardiomyocytes repolarizing currents. At slow activation frequencies, the action potential plateau potential is relatively depolarized and I_{Kur} block leads to a marked increase in the plateau potential (i.e., even more depolarized). At these transmembrane potentials, I_{Kr} kinetics are such that it is recruited and generates a repolarizing force sufficient to compensate for the loss of repolarizing current from I_{Kur} block; there is an overall neutral effect on the APD and RP. At rapid activation rates, the action potential plateau potential is at less positive potentials and I_{Kur} block leads to modest further depolarization of the plateau. At these less depolarized transmembrane potentials, I_{Kr} is not recruited to the same extent and the I_{Kur}-block-induced loss of repolarizing current is not compensated by I_{Kr}, leading to prolongation of the APD and RP. This is the proposed mechanism for the forward use-dependent properties of I_{Kur} block, a highly desirable property for an AF-selective (i.e., rate-dependent *and* atrial-selective) AAD.

Finally, we studied the antiarrhythmic efficacy of I_{Kur} in the setting of electrical remodeling. We demonstrated that I_{Kur} block is relatively effective at terminating simulated AF in the absence of electrical remodeling; in the electrically remodeled atrium, I_{Kur} block was found to be much less efficacious. The explanation for I_{Kur} loss of antiarrhythmic efficacy in the setting of electrical remodeling was previously proposed to be from channel downregulation in long-lasting forms of AF. In other words, less electrophysiological effects were expected from blockade of a downregulated current. In Chapter 4, a detailed mathematical investigation of I_{Kur}

dynamics led to an alternative explanation for the lack of antiarrhythmic I_{Kur} block in the remodeled atrium. We found that I_{Kur} block loss of antiarrhythmic efficacy was not due to a decrease in I_{Kur}-block-induced prolongation of the APD. In fact, I_{Kur} prolonged the APD to a similar extent in the remodeled vs non-remodeled cardiomyocyte despite it being downregulated. In other words, the relative contribution of I_{Kur} to the action potential repolarization was preserved, or even increased, in the setting of electrical remodeling because of the concomitant downregulation of other repolarizing currents. However, electrical remodeling led to shortening of the action potential duration in excess of the I_{Kur}-block-induced prolongation, overwhelming the antiarrhythmic effects of I_{Kur} blockade.

The cardiac action potential is the results of the coordinated opening and closing of surface membrane and sarcolemmal ion channels and transporters. The main depolarizing currents in cardiac myocytes are the fast Na^+ (I_{Na}) and L-type Ca^{2+} ($I_{Ca,L}$) currents. K^+ channels carry repolarizing currents and are key regulators of the resting membrane potential and action potential duration. Contrary to the relatively small number of Na^+ and Ca^{2+} channel species, voltage-dependent K^+ channels (Kv) exist in a large number of variants (i.e., I_{Kr}, I_{Ks}, I_{Kur}, I_{to}) (245). Each Kv channel subtype has its characteristic opening and closing dynamic properties and play different physiological functions(245). Dysregulation or dysfunction of specific Kv subtypes are associated with different effects on action potential dynamics and translate to different clinical phenotypes.

Voltage-gated K^+ channels are found in prokaryote and eukaryote organisms (246). From an embryological perspective, the atrial and ventricular myocardium share a common origin from the primitive cardiac tube. The fetal heart forms through the process of looping and septation giving rise to the 4 chambers with similar and contrasting properties adapted to their different physiological functions. For example, despite their common origin, the right and left ventricles are immensely different structures reflecting the chamber-specific expression and suppression of genes. Similarly, there are well-described differences in action potential morphologies in the normal heart, which are also the result of the non-uniform expression of ion channels. For example, there is a gradient in I_{Kr} expression between the LA and RA, which is believed to be relevant in the pathogenesis of AF (247). There are even transmural gradients in ion channel expression as apparent by the different action potential morphologies in the

ventricular endo-, midmyo- and epicardium resulting from the differential expression of repolarizing currents (248). Hence, the chamber-specific expression of different ion channel species is a common finding in the normal heart.

There are a number of atrial-specific K^+ channels in the human heart. The work presented in this thesis does not directly address the question of why these channels were selected through evolution for expression in the atrium and suppressed in human ventricular cardiomyocytes. Other mammalian species, such as rodents, appear to have functional Kv1.5 channels expressed on ventricular cardiomyocytes. A review of the literature did not identify any direct evidence addressing the question of I_{Kur} atrial-specific expression in the human heart. From a functional standpoint, the action potential duration in a given organism needs to be short enough to accommodate tachycardia in the setting of increased metabolic demands but not so short as to support ineffectively rapid rates. The ventricular action potential duration may have been selected to have slightly less aggressive repolarization as this may have provided protection, within limits, against malignant tachycardias. On the other hand, atrial tachyarrhythmias, such as AF, are not associated with the same hemodynamic consequences; as such, atrial repolarization may not have received the same selection pressure. In fact, there are well-characterized differences in morphology between the atrial and ventricular action potential compatible with this hypothesis. Atrial cardiomyocytes have a more positive and overall stronger repolarizing force leading to a shorter action potential duration and a more triangular action potential morphology as compared to ventricular cardiomyocytes.

The transduction of electrical impulses to mechanical contraction is a key physiological function and occurs through the process of excitation-contraction (EC) coupling. Ca^{2+} entry via the Cav1.2 channels ($I_{Ca,L}$) during phase-2 of the action potential triggers the release of Ca^{2+} from the SR through the ryanodine receptor type-2 (RyR2) into the cytosol (Ca^{2+}-induced Ca^{2+}-release; CICR); the 1,4,5-trisphosphate type-2 receptor is a secondary receptor also contributing to CICR (249). Cytosolic Ca^{2+} then binds to troponin C initiating myofilament contraction. Diastolic cytosolic Ca^{2+} concentrations are restored by the diastolic extrusion of Ca^{2+} to the SR via he SR Ca^{2+}-ATPase type-2a (SERCA2a) and to the extracellular space via the NCX

exchanger (250). Ca^{2+} homeostasis is finely-tuned to ensure effective EC coupling on a beat-to-beat basis.

Ca^{2+}-handling abnormalities are known to be responsible for arrhythmic syndromes such as catecholaminergic polymorphic ventricular tachycardia and have also been described in experimental models of AF (251). In humans, DAD-mediated triggered activity has been implicated in the initiation and maintenance of paroxysmal and chronic AF, albeit with different molecular substrates (25). In chronic AF, the NCX-mediated DADs are the results of cytosolic Ca^{2+} overload secondary to CaMKII-dependent RyR2 hyperphosphorylation which in turn increases the channel's open probability (252-254). The pathophysiological consequences of DADs in patients chronic AF is unclear as they may represent an epiphenomenon of the intracellular Ca^{2+} overload state mediating $I_{Ca,L}$ downregulation. Conversely, in paroxysmal AF, RyR2 phosphorylation is unchanged; increased cytosolic Ca^{2+} is mediated by an increase RyR2 channel open probability and expression without a corresponding increasing in counter-regulatory channels(78). DADs have been hypothesized to serve as triggers and/or drivers for paroxysmal AF.

Most available mathematical models, such as the Courtemanche model used in the simulations presented in this thesis, comprise spatially homogeneous cytosolic and sarcolemmal Ca^{2+} pools(113). These models were not optimized to reproduce the recently described, complex intracellular Ca^{2+}-handling dynamics. Recent work by Voigt at al. updated the Grandi model to reproduce the experimentally-observed atrial-specific Ca^{2+} dynamics (78). This sophisticated model was not used in the work presented in this thesis in part because it was not available at the time when we conducted most of our simulations. It is generally accepted that Ca^{2+}-handling abnormalities are potentially important for the initiation of paroxysmal AF episodes; their role in AF maintenance beside that of being a mediator of $I_{Ca,L}$ remodeling is uncertain. Given that most of the papers presented in this thesis had to do with AF maintenance and termination, it is possible that including detailed intracellular Ca^{2+} dynamics may not have significantly changed our results. Moreover, the model developed by Voigt and colleagues is computationally expensive and would have increased the computational time by several orders of magnitude. An exploratory study of the effect of intracellular Ca^{2+}-handling abnormalities on AAD efficacty would certainly be interesting and worthwhile.

6.4 The Effect of Heart Failure-Induced Fibroblast Electrical Remodeling on the Cardiomyocyte Action Potential and Atrial Arrhythmogenesis

In this paper, we sought to investigate a new kind of remodeling, heart failure-induced fibroblast electrical remodeling, on the cardiomyocyte action potential and atrial arrhythmogenesis. Our main findings are

1- Heart failure induced fibroblast ionic remodeling characterized by downregulation of the fibroblast K^+ current $I_{Kv,fb}$ and upregulation of the fibroblast K^+ current $I_{Kir,fb}$.

2- Fibroblast electrical remodeling can have important effects on the cardiomyocyte action potential properties through cardiomyocyte-fibroblast electrical coupling.

3- Downregulation of $I_{Kv,fb}$ had an antiarrhythmic effects whereas $I_{Kir,fb}$ upregulation was found to be proarrhythmic.

Up until recently, cardiac fibroblasts were considered to be electrically inactive component of the cardiac skeleton (209-212) ; this traditional view remains operational in clinical medicine. Under physiological conditions, fibroblasts play an important role in maintenance of the extracellular matrix via a series of auto- and paracrine functions (227, 255, 256). More recently, experimental work demonstrated the presence of functional ionic currents on the fibroblast membrane setting a passive resting membrane potential (223, 225, 227, 228). The two main fibroblast ionic currents are (i) the time- and voltage-dependent K^+ current ($I_{Kv,fb}$) and (ii) an inward-rectifier K^+ current ($I_{Kir,fb}$) (227). The former is tetraethylammonium-sensitive and displays relatively slow activation ($\tau \approx$ 20-32 ms) (229). The latter is highly Ba^{2+}-sensitive current modulated by the extracellular K^+ concentration ; it is responsible for setting the fibroblast resting membrane potential (227).

There is growing experimental data that fibroblasts can interact electrically with the neighboring cardiomyocytes, an phenomenon referred to as cardiomyocyte-fibroblast coupling (214-221). As early as in 1989, Rook and colleagues studied the electrical coupling between

pairs of isolated neonatal rat cardiomyocytes and fibroblasts to show that changes in the potential of fibroblasts could be transmitted to the cardiomyocyte and vice versa (214). They were also able to quantify the conductance of cardiomyocyte-fibroblast pairs to 29 nS, an intermediate value between that of cardiomyocyte-cardiomyocyte coupling (43 nS) and fibroblast-fibroblast connections (22 ns) (214). More recently, Miragoli and colleagues studied the functional effects of cardiomyocyte-fibroblast coupling in cardiomyocytes co-cultured with fibroblasts (218). By varying the ratio of fibroblast to cardiomyocyte, they were able to show a biphasic relationship between CV and said ratio; at low fibroblast:cardiomyocyte ratios, CV was found to be supra-normal whereas at high fibroblast:cardiomyocyte ratios, CV was reduced (218). This effect was shown to be mediated by the modulation of the cardiomyocyte's resting membrane potential by the fibroblast. The existence of cardiomyocyte-fibroblast electrical couple in the live heart is controversial and has not yet been demonstrated (222).

The study presented in Chapter 5 is the first to describe a new kind of remodeling, heart failure-induced fibroblast electrical remodeling. The changes to the cardiomyocyte's ionic currents in AF and heart failure have been well-characterized and incorporated in the conceptual pathophysiological framework of the disease (41, 57, 207, 208). Conversely, fibroblast ionic remodeling had not been previously described and its theoretical implications were unknown. Using bench experiments, we were able to demonstrate heart failure-induced changes in the fibroblast K^+ currents, namely downregulation of $I_{Kv,fb}$ and upregulation of $I_{Kir,fb}$, with the overall effect of hyperpolarizing the fibroblast resting membrane potential.

It is technically challenging to study the potential effects of fibroblast electrical remodeling on the cardiomyocyte action potential properties and atrial arrhythmogenesis. We therefore proceeded to implement the experimentally-observed changes in fibroblast ionic current in a mathematical model of cardiomyocyte-fibroblast coupling. This *in silico* approach has the notable advantage of granting control on all variables of the experiment such as the degree of remodeling, the fibroblast:cardiomyocyte ratio, the cardiomyocyte-fibroblast coupling strength, etc.. We were able to show that the changes to the fibroblast current had differential effects on the cardiomyocytes action potential, the net effect depending on the relative contribution of $I_{Kv,fb}$ downregulation vs $I_{Kir,fb}$ upregulation. On the one hand $I_{Kv,fb}$ downregulation decreased the fibroblast's repolarizing current, depolarizing the fibroblast

resting membrane potential and prolonging its APD; these changes made the fibroblast a *source* of depolarizing current for the cardiomyocyte. Conversely, $I_{Kir,fb}$ upregulation had the opposite effect; it increased the fibroblast repolarizing forces, hyperpolarizing its membrane potential and shortening the APD, making the fibroblast a current *sink* for the cardiomyocyte. When the fibroblast acted as a current sink ($I_{Kir,fb}$ upregulation), we observed a proarrhythmic effect on atrial arrhythmogenesis mediated by fibroblast-mediated hyperpolarization of the cardiomyocyte's resting membrane potential and shortening of its APD. Conversely, when the fibroblast was a current source ($I_{Kv,fb}$ downregulation), we observed an antiarrhythmic effect mediated by prolongation of the cardiomyocyte APD. Again, the overall effect of heart failure-induced fibroblast electrical remodeling depended on the relative contribution of these two opposing forces; however, the proarrhythmic effects dominated over a wide range of $I_{Kir,fb}$ upregulation/$I_{Kv,fb}$ downregulation ratios suggesting that the predominant effect of fibroblast electrical remodeling is likely to be proarrhythmic. This last study also shows the usefulness of combining experimental and computational approaches to gain a better understanding of complex physiological systems. Novel experimental data was translated into a mathematical model to efficiently study the detailed mechanistic implications of these experimental observation.

6.5 Future Directions

The studies presented in Chapters 2 through 5 developed a common theme, that of the application of computational methods to study the effects of changes in the cardiomyocyte ion channel on the action potential and arrhythmogenesis, with a special emphasis on applications to AF. The versatility of mathematical modeling combined with the vastness of the field of cardiac electrophysiology paves the way to a large number of interesting extensions of the work presented in this thesis.

6.5.1 Effect of Electrical and Structural Remodeling on Na^+- and K^+-Channel Block Antiarrhythmic Effects

Despite advances in our understanding of the molecular mechanisms of AF, this very common cardiac arrhythmia remains a major challenge in clinical medicine. At the forefront of the difficulties in AF management is lack of an effective, safe and AF-selective AAD. As described in the Introduction, most currently available AADs are older molecules developed for indications other than AF and, perhaps not surprisingly, have sub-optimal operating characteristic for AF rhythm-control. Computational approaches are well-suited to gain further insight into how to modulate the cardiomyocytes ionic currents in an AF-selective manner.

In Chapter 2, using a detailed mathematical model, we demonstrated that an inactivated-state Na^+-channel blocker is optimally AF-selective; however, anti-AF efficacy was limited with the optimally-AF-selective Na^+-channel block. We then showed in Chapter 3 that the combination of Na^+- and K^+-channel block produced synergistic AF-selective effects, increasing the anti-AF efficacy for any given level of AF-selectivity; however, the K^+ current targeted in this study (I_{Kr}) has significant ventricular proarrhythmic liabilities. In Chapter 4, we showed that the atrial-specific K^+ current I_{Kur} was a viable antiarrhythmic target despite previously voiced concerns in the literature about its inactivation at depolarized potentials. A potential future direction building on these findings would be to study the effect of combined I_{Kur} block (highly atrial-selective) with an optimized Na^+-channel blocker (highly rate-selective) on anti-AF efficacy and AF-selectivity in a geometrically-realistic model of the atria. A few preliminary results of an exploratory study exploring this question are presented below.

The Courtemanche model of the human atrial cardiomyocyte with updated I_{Kur} inactivation was implemented (112, 257). The Hund-Rudy model was used to represent ventricular cardiomyocytes (128). A previously published realistic patient-derived atrial model was utilized to simulated AF (Figure 41) (258, 259) with and without electrical and structural remodeling.

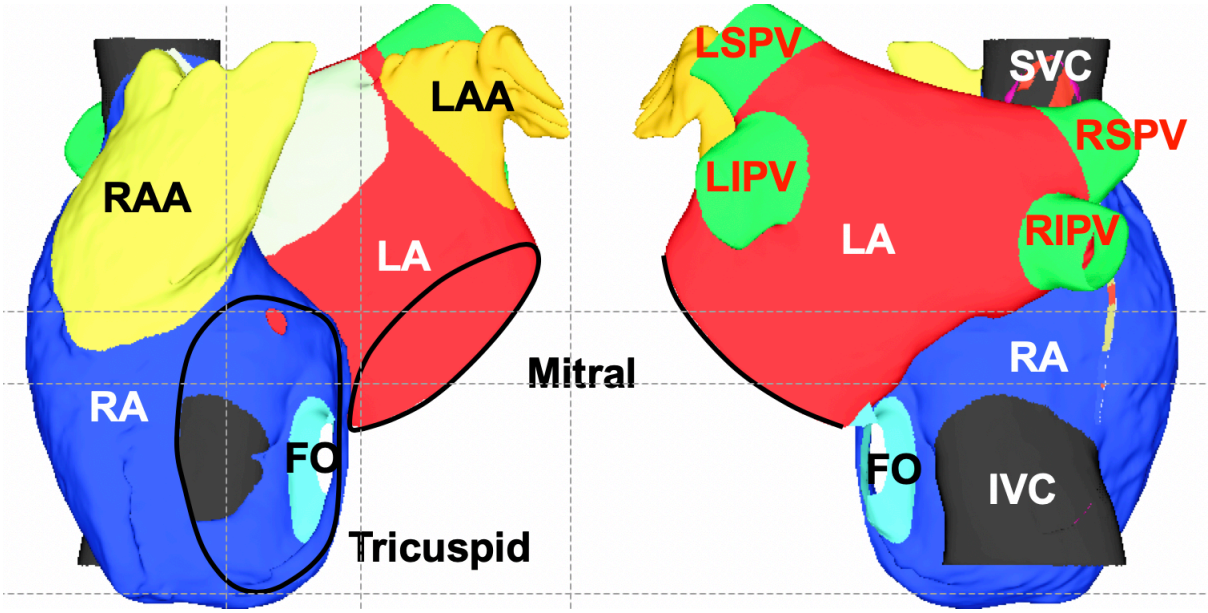

Figure 41. Geometry of the anatomically realistic atrial model. Anterior (left) and posterior (right) views if the anatomically realistic atrial model. Right atrium (RA); left atrium (LA); right atrial appendage (RAA); left atrial appendage (LAA); fossa ovalis (FO); inferior and superior vena cava (IVC and SVC); right (R), left (L), upper (U) and inferior (I) pulmonary veins (PVs). The tricuspid and mitral annuli are also outlined.

6.5.1 Preliminary Results

Optimization of an inactivated-state Na^+-channel blocker. The results presented in Chapters 2 and 3 demonstrated that an inactivated Na^+-channel blocker is optimally AF-selective. Based on those results, we considered the special case of a pure inactivated-state Na^+-channel blocker. These assumptions are mathematically expressed by $B_A = 0$ and $dB_A/dt = 0$, and lead to the following simplified formulation for the time-evolution equations for the Na^+-channel fraction block

$$\frac{dB_I}{dt} = k_I[D](1-h)(1-B_I) - l_I B_I$$

where B_I is the fractional inactivated-state block, k_I is the inactivated-state binding rate-constant, [D] is the drug concentration (60 μM), h is the rapid Na^+-channel inactivation gate and l_I is the inactivated-state unbinding rate-constant. Furthermore, the inactivation gate $h(t)$ can be approximated as a step-function, with $h(t) = \alpha$ for $0 \leq t < \Delta t$ and $h(t) = \beta$ for $\Delta t \leq t < CL$, where

CL is the stimulation cycle length and Δt is a parameter for which $h(\Delta t) = 0.5$ ($\Delta t = 300$ ms for CL = 1000 ms and 245 ms for CL = 250 ms). The equation for B_I then becomes a first-order ordinary differential equation, which can be solved in closed-form. This allowed the optimization of a pure inactivated-state Na^+-channel blocker orders of magnitude faster and with much higher resolution than by running full simulations as selected points in the (k_A, k_I, l_A, l_I) rate-constant parameter-space. The results of this optimization are presented in Figure 42.

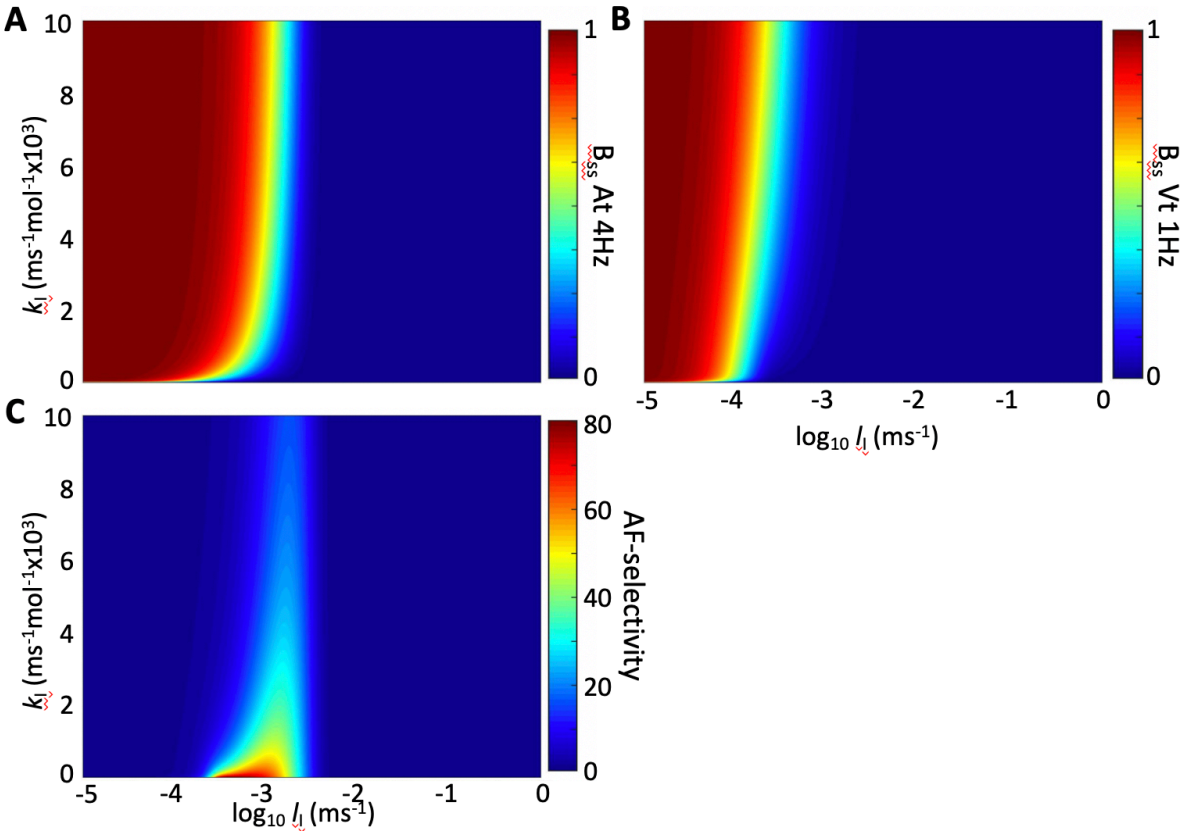

Figure 42. Optimization of a pure inactivated-state Na^+-channel blocker. (A-B) Steady-state I_{Na} block (B_{ss} ; normalized to control value) for an atrial (At) cardiomyocyte paced at 4 Hz (i.e., AF) and a ventricular (Vt) cardiomyocyte paced at 1 Hz (i.e., sinus rhythm) as a function of the binding (k_I) and unbinding (l_I) rate-constants. (C) AF-selectivity defined as B_{ss} At 4 Hz / B_{ss} Vt 1 Hz as a function of k_I and l_I. AF-selectivity is highly dependent on the Na^+-channel blocker's pharmacodynamic properties with an area of maximal selectivity (red). Also note the much higher resolution for the closed-form activation vs the optimization over the entire parameter-space as show in Figure 10.

The effect of electrical and structural remodeling on AF inducibility. Electrical and structural remodeling play a central role in AF pathogenesis. We first sought to confirm that the anatomically-realistic model was capable of reproducing the clinically observed changes in AF inducibility in the remodeled atria. We ran series of simulations in which the pulmonary veins were rapidly stimulated (burst pacing) as a means of inducing AF under different remodeling conditions. The results of this analysis are presented in Figure 43. The model correctly recapitulated the changes in AF inducibility and maintenance in the setting of electrical and structural remodeling.

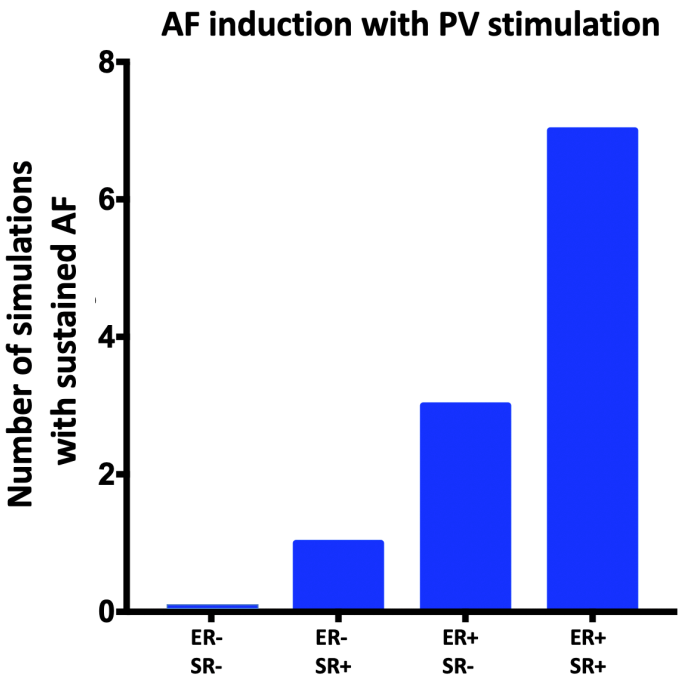

Figure 43. Atrial fibrillation inducibility and maintenance as a function of electrical and structural remodeling. In the control condition (ER-/SR-), the model did not sustain AF. The introduction of electrical (ER+/SR-) or structural (ER-/SR+) remodeling facilitated AF inducibility and maintenance. In the presence of electrical and structural remodeling (ER+/SR+) AF was easily induced and sustained for the duration of the simulation.

Tonic I_{Na} and I_{Kur} block vs remodeling. We then analyzed the effect of tonic channel block (fixed reduction in maximal conductance) on AF dynamics with and without remodeling. The results of this analysis without remodeling (ER-/SR-) are presented in Figure 44. Na^+-channel block was ineffective at block levels <50% (Figure 44A); beyond 50% block, Na^+-

channel blockade was found to be highly effective, reaching 100% termination. Conversely, I_{Kur} block was moderately efficacious, reaching termination rates in the 50%-range at 50% I_{Kur} block; contrary to I_{Na} block, anti-AF efficacy plateaued at 60% termination with maximal I_{Kur} block (Figure 44B). The effects of channel blockade on the average AF cycle length and action potential duration are shown in Figure 44C-D. A representative example of AF termination with I_{Kur} block is shown in Figure 45.

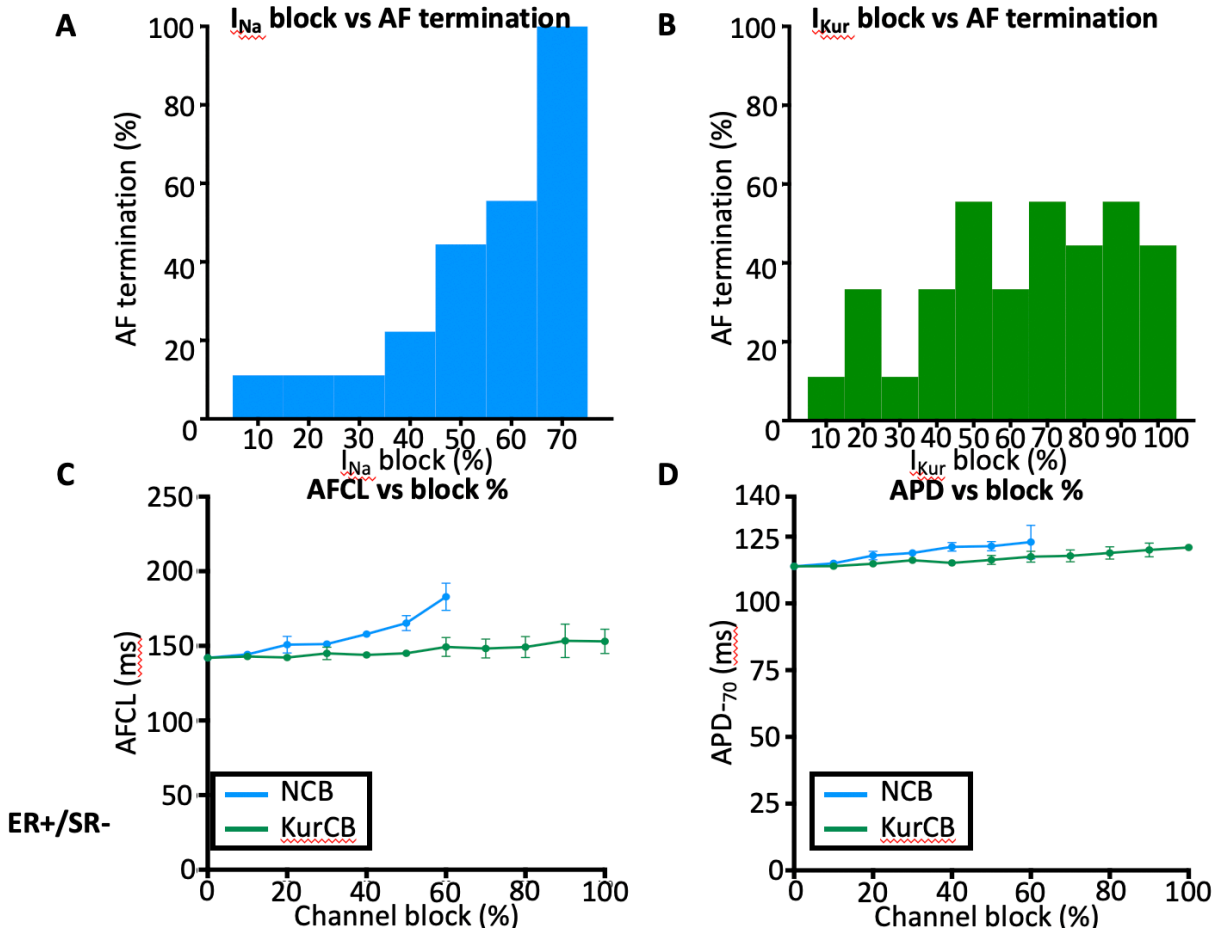

Figure 44. Effects of tonic I_{Na} and I_{Kur} block in the absence of remodeling (ER-/SR-). (A-B) AF termination efficacy as a function of (A) I_{Na} and (B) I_{Kur} block percent. (C-D) Effects on the AF cycle length (AFCL ; C) and action potential at -70 mV (APD_{-70} ; D) as a function I_{Na} (blue) and I_{Kur} (green) block percent.

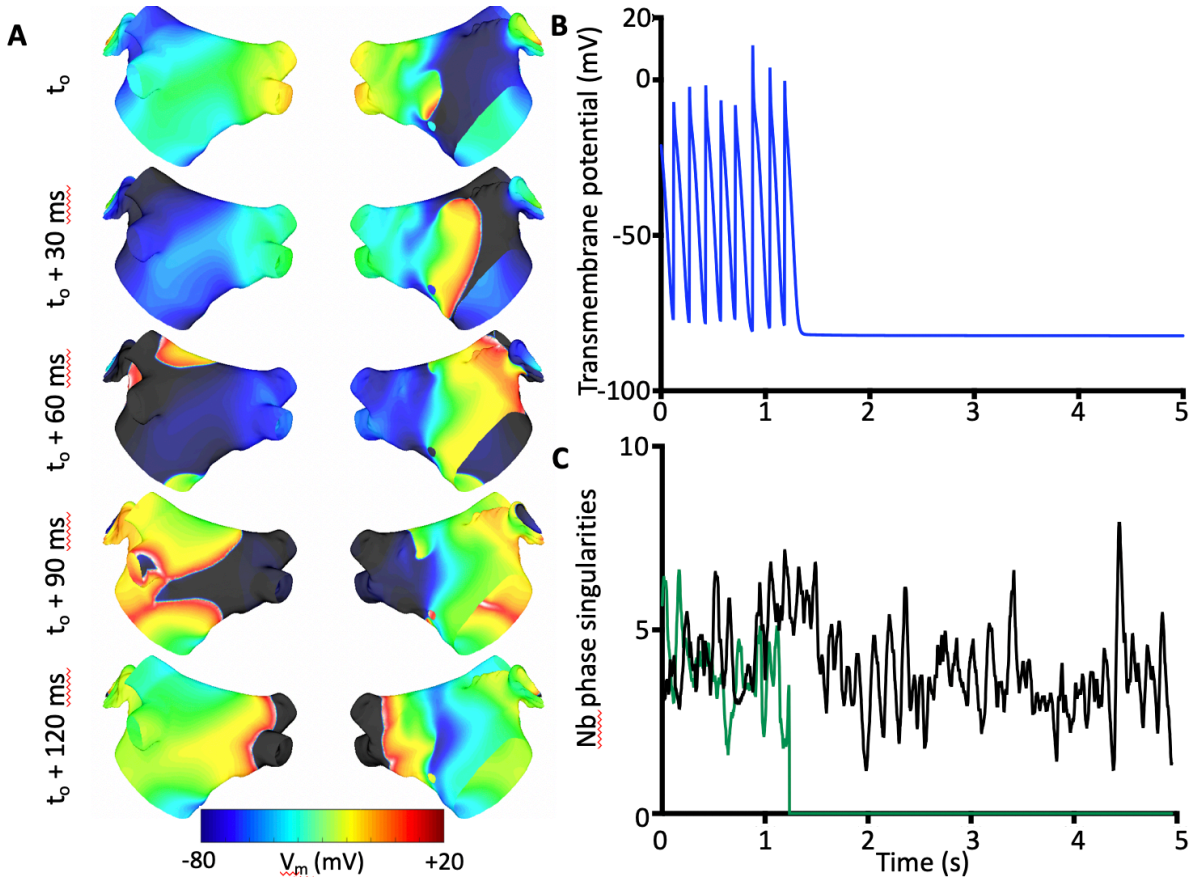

Figure 45. Representative example of AF termination with tonic I_{Kur} block. (A) Snapshots of the left atrial transmembrane potential as a function of time (colorbar at the bottom). Block of I_{Kur} prolongs the action potential duration and increases phase singularity meandering favoring reentry termination. (B) Transmembrane potential of a representative cardiomyocyte on the left atrial posterior wall. (C) Number of phase singularities as a function of time for control (black) and I_{Kur} block (green).

The introduction of electrical and structural remodeling (ER+/SR+) had a major impact on tonic channel block antiarrhythmic efficacy (Figure 46). Na^+-channel block was only midly efficacious up to 70% channel-block, the cardiomyocyte non-excitability threshold (Figure 46), despite a marked effect on the AF cycle length (Figure 46). Even more dramatic was the complete abolition of all of I_{Kur} block's antiarrhythmic efficacy in the ER+/SR+ condition.

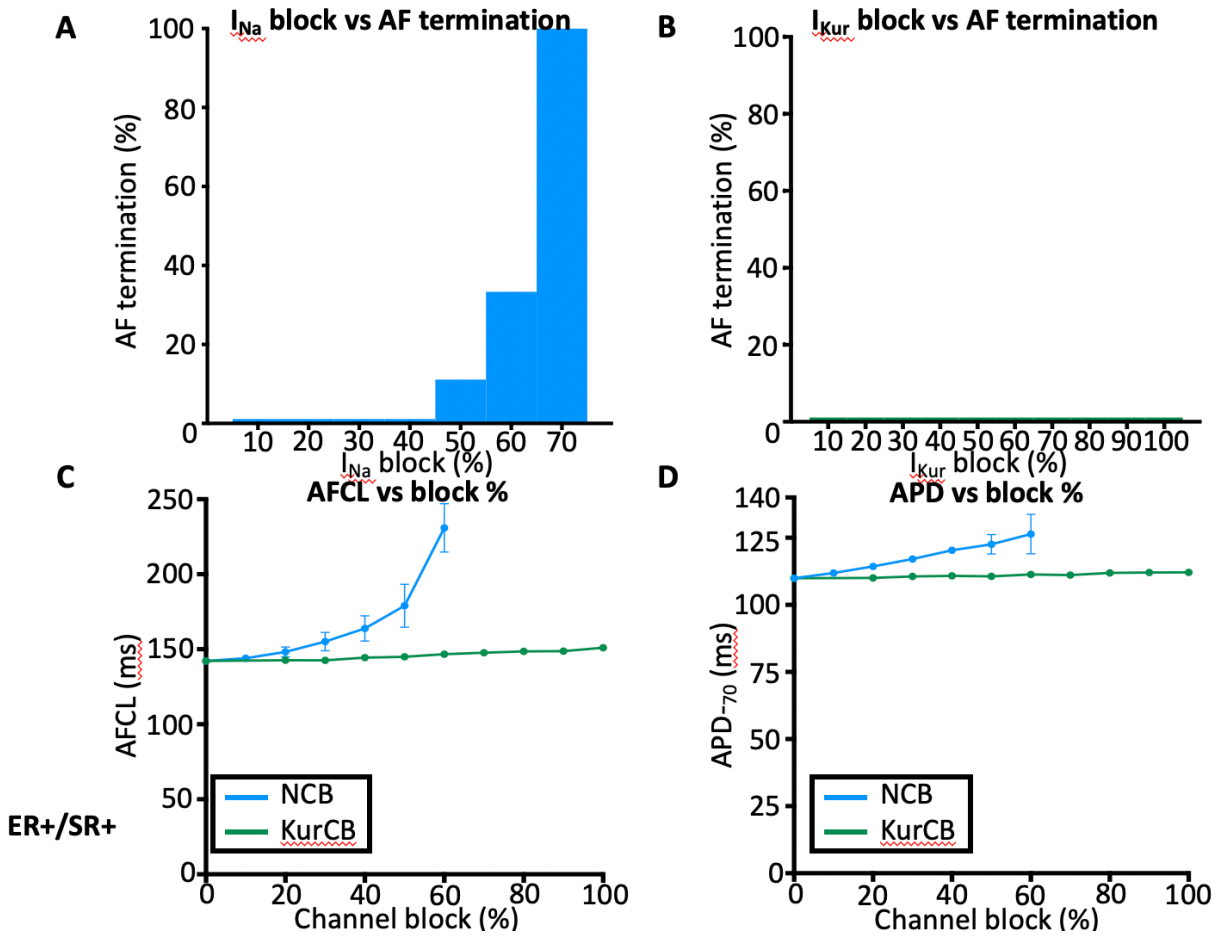

Figure 46. Effect of tonic I_{Na} and I_{Kur} block in the setting of electrical and structural remodeling. (A-B) AF termination efficacy as a function of (A) I_{Na} and (B) I_{Kur} block percent. (C-D) Effects on the AF cycle length (AFCL ; C) and action potential at -70 mV (APD_{-70} ; D) as a function I_{Na} (blue) and I_{Kur} (green) block percent.

State-dependent Na^+-channel block with and without I_{Kur} block. We then investigated the effect of combining an optimized Na^+-channel blocker with I_{Kur} block in the ER-/SR- condition. Using the optimization algorithm, we generated a set of Na^+-channel blockers with progressively higher AF-selectivity. The results of this analysis are presented in Figure 47. The optimized Na^+-channel blocker alone was moderately efficacious for most AF-selectivity levels; the least AF-selective drug was the most effective at terminating AF. The addition of tonic I_{Kur} block significantly increased anti-AF efficacy for any given level of AF-selectivity. Combining I_{Na} and I_{Kur} block is an attractive AF-selective combination as it combines highly rate-selective (I_{Na} block) and atrial-selective (I_{Kur} block) targets.

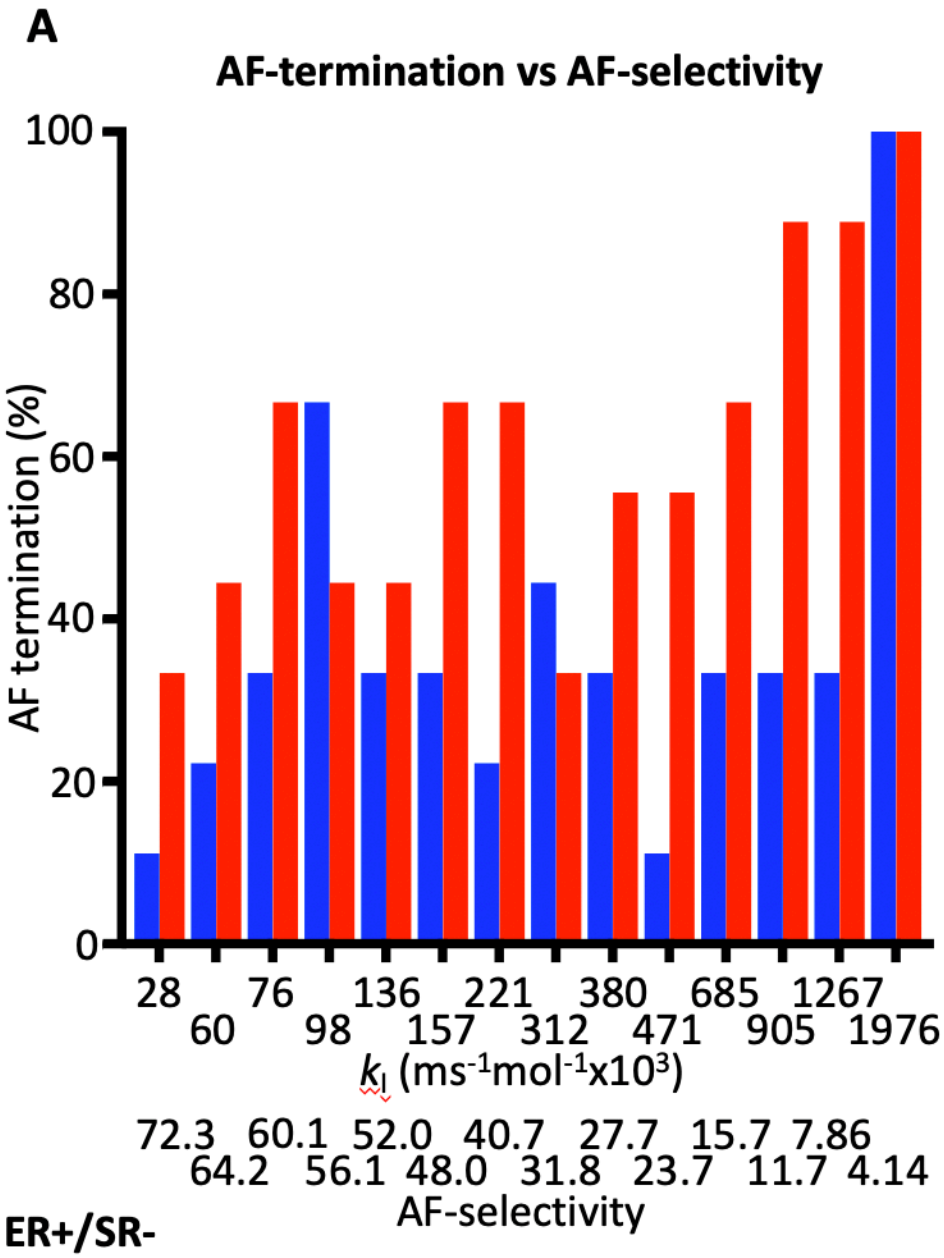

Figure 47. Simulated AF termination as a function of Na^+-channel blocker AF-selectivity without (blue) and with tonic I_{Kur} block (red). The Na^+-channel blocker was moderately efficacious across the range of AF-selectivities ; the least AF-selective drug was the most effective at termating simulated AF. The addition of I_{Kur} block significantly increased anti-AF efficacy for any given level of AF-selectivity.

This exploratory study builds on the work presented in this Thesis to investigate the effects of pharmacological ion channel modulation in an anatomically-realistic atrial model with

and without remodeling. The combination of rate-selective (optimized I_{Na} block) and atrial-selective (I_{Kur} block) targets appears to have synergistic AF-selective antiarrhythmic effects in the non-remodeled atrial; the combination of electrical and structural remodeling significantly diminished anti-AF efficacy. A detailed analysis of this model is required to further refine these findings.

The question of why arrhythmias self-terminate is another major unresolved issue in cardiac electrophysiology. Non-sustained atrial and ventricular arrhythmias are very common. Ambient isolated premature atrial or ventricular depolarizations are ubiquitous and only very rarely trigger sustained arrhythmias, especially in structurally normal hearts. In the cardiac electrophysiology laboratory, it is routine to stimulate the heart with short-coupled extra stimuli looking for inducible atrial and/or ventricular arrhythmias; the majority of programmed electrical stimulation studies do not induce sustained arrhythmias whereas non-sustained runs of tachycardia are relatively common. This suggests that the homeostatic regulatory mechanisms of cardiac electrical function are able to effectively buffer rather large perturbations to the system's steady state. From an evolutionary standpoint, this is perhaps not entirely surprising as variants with easily inducible arrhythmias would be expected to undergo negative selection pressure. An empiric observation in support of this statement is the prevalence of genetic arrhythmogenic cardiomyopathies; mutations with very malignant phenotypes are rare (i.e., Timothy syndrome; mutation in CACNA1C coding for CaV1.2) whereas mutations with milder phenotypes (i.e., Brugada syndrome) are much more prevalent.

The precise pathways by which these regulatory mechanisms operate are, however, complex and incompletely understood. Inherent to the genesis of cardiac arrhythmias are emergent phenomena operating across different scales. A complex interplay between molecular abnormalities, electrical and structural remodeling, organ-level pathology and systemic acute and/or chronic conditions determine sustainability of arrhythmias in general. The question of AF sustenance appears to be particularly complex as the basic mechanisms of AF initiation and maintenance are numerous and different from patient to patient. In other words, AF may be the phenotypic expression of different pathological processes, which themselves may evolve over time. This is somewhat different than, for example, scar-mediated ventricular tachycardia in

which the framework of anatomic re-entry accounts for a large number of experimental and clinical observations.

A systematic answer to this question is beyond the scope of the present thesis. The simulations generated as part of this work were primarily designed to study AF termination by antiarrhythmic drugs. This research theme was selected because of the immediate clinical need for a novel antiarrhythmics with improved safety and efficacy. Nevertheless, the mathematical model used in this thesis could be modified to gain insights into the question of AF self-termination. This is an important and clinically relevant question that may provide insights into the pathophysiology of AF and offer novel therapeutic possibilities. Given the complexity of AF biology, such a specific mathematical model may only be able to address specific components of the larger question, depending of the features included in the model. For example, anatomically realistic models could be used to investigate how the atrial geometry contributes to AF maintenance/self-termination. It is generally accepted that a critical mass of tissue is required to maintain AF and left atril size is clinical risk factor for AF but the complex atrial anatomy may, in it of itself, be a determinant of AF sustainability. Abnormalities in intracellular Ca^{2+}-handling have been shown to play a central role in AF initiation and sophisticated mathematical models incorporating these findings have been developed. However, these have yet to be implemented in geometrically extended and realistic anatomies to gain insight into how these intracellular abnormalities translate into sustained (or non-sustained AF). Atrial fibrosis is another key player in AF pathophysiology; the effect of fibrosis on antiarrhythmic drug efficacy received a preliminary analysis in this section and a similar model could be used to gain further insight into the interplay between fibrosis and AF maintenance.

6.5.2 Novel Approaches to AF-management: High-Frequency Sub-Threshold Stimulation for Mapping of Persistent Atrial Fibrillation

Sinus rhythm-maintenance in patients with persistent AF (persAF) is a major challenge, with 1-year AF-free rates hovering around 50-60% with currently-available therapies (260). Several studies have demonstrated the benefit of pulmonary vein isolation in patients with paroxysmal AF, as the pulmonary veins are the main site for AF triggers in this patient

population. A major unanswered question is what the optimal ablation strategy should be in patients with persAF, as AF in this patient population is often no longer pulmonary vein-dependent. There has been significant interest in identifying AF triggers and drivers in persAF to guide ablation. Several approaches to "mapping" of persAF have been proposed. However, to date, no single method has gained widespread clinical acceptance given the lack of reproducible corroborating evidence of benefit. Hence, trigger/driver mapping for targeted ablation of persAF is a major unmet need in invasive clinical cardiac electrophysiology.

High-frequency sub-threshold stimulation (HFSTS) modifies the electrophysiological properties of excitable cells without eliciting an action potential response. Variations on this form of stimulation are used in clinical neurology to modulate neural networks for the treatment of chronic pain syndromes and Parkinson's disease, for example. In relation to cardiac electrophysiology, early work from the early 1990's demonstrated the feasibility of terminating macro-reentrant arrhythmias such as scar-mediated ventricular tachycardia (261), atrioventricular reentrant tachycardia (262) and atrioventricular nodal reentrant tachycardia (AVNRT) with sub-threshold stimulation (263). Along the same lines, constant (not high-frequency) stimulation has been used to locate the slow-pathway region to guide ablation of AVNRT (264, 265). More recently, kilohertz-range stimulation had been shown to cause reproducible reversible conduction block in a range of experimental models and proposed as a means of delivering low-energy defibrillation (266). The mechanism of tachycardia termination by HFSTS appears to be modulation of the refractory period in a critical part of the reentry circuit (267, 268).

Currently-available mapping strategies identify putative triggers/drivers of persAF but ablation at these sites is not invariably associated with modification or termination of tachycardia. Moreover, extensive ablation in the left atrium (LA) is not benign; the risk of stiff LA syndrome, a condition characterized by pulmonary hypertension due to LA dysfunction in the absence of mitral valve disease, increases with more aggressive ablation strategies.

A potential extension of the work presented in this thesis is the application of mathematical modeling to test the potential value of HFSTS for the mapping of persAF to guide catheter ablation. Conceptually, HFSTS can be used to create localized and reversible conduction block, simulating an ablation lesion, to test whether a site of interest is important for

tachycardia maintenance before delivering ablative energy to the tissue. This would be the first mapping strategy for which evidence of participation to the tachycardia could be obtained prior to ablation.

From a mathematical modeling standpoint, the 3D model presented in Section 6.5.1 could form the basis for further theoretical investigation. Atrial fibrillation could be simulated using various degrees of electrical and structural remodeling to generate different patterns of AF. Then, the effect of HFSTS on different parts of the LA could be investigated in relationship to the AF-driver-sites. Unanswered questions directly accessible to this line of investigation include how does HFSTS interact with atrial fibrillatory activity? Can HFSTS produce stable conduction block during AF? How would application of HFSTS at a driver site affect tachycardia if the driver is functional (rotor) or anatomical (scar-mediated)?

From a clinical standpoint, the technology to deliver HFSTS for persAF mapping is already available but would benefit from a solid theoretical basis to guide clinical application. The development of a wide range of catheters also opens the door to innovative mapping options. For example, decapolar circular catheters could be used to deliver HFSTS to isolate a region of the LA instead of a single point. Then, dissociated activity within that region would potentially indicate a driver site whereas electrical quiescence would be more consistent with a passively-activated site. Such potential application of computational methods to guide invasive clinical electrophysiology would be of great value.

6.5.3 Mathematical Modeling for the Optimization of Stereotatic Body Radioablation Therapy for Refractory Ventricular Tachycardia

Ventricular tachycardiac (VT) and fibrillation (VF) are the leading causes of sudden cardiac death. For patients at risk for malignant ventricular arrhythmias or having survived a tachycardia-mediated cardiac arrest, an implantable cardioverter-defibrillation (ICD) is generally indicated. Although ICDs are life-saving, they do not prevent VT/VF and ICD shocks are associated with worse clinical outcomes (269). Ventricular tachyarrhythmia-suppressive therapies include AADs, which are at best moderately effective (270), and catheter ablation.

Despite significant advances in catheter ablation for VT, the ventricular arrhythmia-recurrence rates after an acutely-successful procedure remain as high as 50%, even in experienced centers (271). A major limitation to VT ablation is the presence of intramural/mid-myocardial circuits or circuits protected by dense scar which are inaccessible to catheter-delivered radiofrequency energy. Moreover, ablation procedures for VT can pose a prohibitive hemodynamic challenge to already-fragile patients. Novel treatment strategies for patients with refractory VT are needed.

Stereotactic radiotherapy, the localized delivery of high-energy ionizing radiation, is standard-of-practice in Radiation Oncology for the non-invasive treatment of solid tumors. In an interestingly translational development, this technology has recently been proposed for the non-invasive ablation of cardiac arrhythmias or stereotactic radioablation therapy (SBRT). In a landmark paper, Cuculich et al. reported on 5 high-risk patients with refractory VT treated with SBRT. The ventricular arrhythmia burden went from a combined 6577 VT episodes pre-treatment to 4 episodes after treatment, a 99.9% reduction with no significant adverse events (272). The average treatment time was <15 minutes vs 3-6 hours for catheter-based VT ablation procedures. More recently, the interim outcomes of SBRT in the 19 patients with refractory VT enrolled in the ENCORE-VT trial have been published, showing similar dramatic reductions in VT burden (273).

The field of SBRT is at its infancy and many unanswered questions remain. A critical component of SBRT delivery is the pre-treatment planning. This is a highly collaborative phase of the treatment in which cardiac electrophysiologists, radiologists and radiation oncologist interact to review the existing electrophysiological maps and imaging studies to “plan” the treatment, that is to determine which part of the heart will be the target for radiation and how to minimize off-target exposure. To date, SBRT planning remains highly empiric, relying on the presumed proarrhythmic site; the effects of treatment are to a large extent uncertain at the time of radiation delivery.

Mathematical modeling could be a highly valuable tool to assist in the planning of SBRT. In fact, the data used for planning of SBRT treatment are static electrophysiological and radiological imaging studies; the dynamic electrophysiological properties of the substrate and the effects of the proposed SBRT are not accessible. Modeling of the ventricular geometry with patient-specific imaging and electrophysiological mapping could provide additional insights

into patients' clinical VT. Perhaps more importantly for successful SBRT, the effects of the proposed radiation protocol could be simulated *in silico* to study how the radiation-induced scar will impact the substrate's propensity to sustain ventricular arrhythmias. This could potentially limit the recurrence of new VT circuits. Along the same lines, computational simulation could be used to delivery more localized radiation, hence further reducing off-target exposure, while retaining antiarrhythmic efficacy, all based on modeling analysis.

6.6 Conclusions

The overarching rationale of this thesis was to apply computational approaches to the understanding of the consequences and opportunities of ion channel properties, especially as they relate to AF. The studies presented here utilized mathematical modeling to address non-linear systems in cardiac electrophysiology in order to tackle questions that would have been very difficult to approach with traditional laboratory-based experimentation. They also showcased how theoretical results can help orient and complement subsequent experimental work (Chapter 3) or, conversely, novel experimental findings can be implemented into mathematical models to investigate potential consequences (Chapters 4 and 5). Atrial fibrillation is the most common arrhythmia in the general population and clinically-available antiarrhythmic therapeutics have sub-optimal operating characteristic. Mathematical modeling is a promising tool to help in studying the complex and non-linear effects of pharmacological modulation of ion channel properties and assist in the development of optimized approaches for the treatment of AF, a major unmet need in clinical in clinical medicine. As computational models increase in sophistication to better represent the cardiomyocyte's electrophysiology, they will almost certainly play an ever-growing role in expanding our understanding of the mechanisms and management of complex arrhythmias.

References

1. Cardiology TFotWGoAotESo. The Sicilian gambit. A new approach to the classification of antiarrhythmic drugs based on their actions on arrhythmogenic mechanisms. Task Force of the Working Group on Arrhythmias of the European Society of Cardiology. Circulation. 1991;84(4):1831-51.
2. Nattel S, Burstein B, Dobrev D. Atrial remodeling and atrial fibrillation: mechanisms and implications. Circulation Arrhythmia and electrophysiology. 2008;1(1):62-73.
3. Nattel S, Quantz MA. Pharmacological response of quinidine induced early afterdepolarisations in canine cardiac Purkinje fibres: insights into underlying ionic mechanisms. Cardiovasc Res. 1988;22(11):808-17.
4. Aguilar M, Nattel S. The pioneering work of George Mines on cardiac arrhythmias: groundbreaking ideas that remain influential in contemporary cardiac electrophysiology. J Physiol. 2016;594(9):2377-86.
5. Allessie MA, Bonke FI, Schopman FJ. Circus movement in rabbit atrial muscle as a mechanism of trachycardia. Circ Res. 1973;33(1):54-62.
6. Allessie MA, Bonke FI, Schopman FJ. Circus movement in rabbit atrial muscle as a mechanism of tachycardia. II. The role of nonuniform recovery of excitability in the occurrence of unidirectional block, as studied with multiple microelectrodes. Circ Res. 1976;39(2):168-77.
7. Allessie MA, Bonke FI, Schopman FJ. Circus movement in rabbit atrial muscle as a mechanism of tachycardia. III. The "leading circle" concept: a new model of circus movement in cardiac tissue without the involvement of an anatomical obstacle. Circ Res. 1977;41(1):9-18.
8. Duytschaever M, Mast F, Killian M, Blaauw Y, Wijffels M, Allessie M. Methods for determining the refractory period and excitable gap during persistent atrial fibrillation in the goat. Circulation. 2001;104(8):957-62.
9. Zaikin AN, Zhabotinsky AM. Concentration wave propagation in two-dimensional liquid-phase self-oscillating system. Nature. 1970;225(5232):535-7.
10. Winfree AT. Spiral waves of chemical activity. Science. 1972;175(4022):634-6.

11. Andrade J, Khairy P, Dobrev D, Nattel S. The clinical profile and pathophysiology of atrial fibrillation: relationships among clinical features, epidemiology, and mechanisms. Circ Res. 2014;114(9):1453-68.

12. Colilla S, Crow A, Petkun W, Singer DE, Simon T, Liu X. Estimates of current and future incidence and prevalence of atrial fibrillation in the U.S. adult population. Am J Cardiol. 2013;112(8):1142-7.

13. Krijthe BP, Kunst A, Benjamin EJ, Lip GY, Franco OH, Hofman A, et al. Projections on the number of individuals with atrial fibrillation in the European Union, from 2000 to 2060. Eur Heart J. 2013;34(35):2746-51.

14. Lip GYH, Brechin CM, Lane DA. The global burden of atrial fibrillation and stroke: a systematic review of the epidemiology of atrial fibrillation in regions outside North America and Europe. Chest. 2012;142(6):1489-98.

15. Lip GY, Fauchier L, Freedman SB, Van Gelder I, Natale A, Gianni C, et al. Atrial fibrillation. Nat Rev Dis Primers. 2016;2:16016.

16. Wang TJ, Larson MG, Levy D, Vasan RS, Leip EP, Wolf PA, et al. Temporal relations of atrial fibrillation and congestive heart failure and their joint influence on mortality: the Framingham Heart Study. Circulation. 2003;107(23):2920-5.

17. Wolf PA, Abbott RD, Kannel WB. Atrial fibrillation as an independent risk factor for stroke: the Framingham Study. Stroke. 1991;22(8):983-8.

18. Cotter PE, Martin PJ, Ring L, Warburton EA, Belham M, Pugh PJ. Incidence of atrial fibrillation detected by implantable loop recorders in unexplained stroke. Neurology. 2013;80(17):1546-50.

19. Bruggenjurgen B, Rossnagel K, Roll S, Andersson FL, Selim D, Muller-Nordhorn J, et al. The impact of atrial fibrillation on the cost of stroke: the berlin acute stroke study. Value Health. 2007;10(2):137-43.

20. Gladstone DJ, Bui E, Fang J, Laupacis A, Lindsay MP, Tu JV, et al. Potentially preventable strokes in high-risk patients with atrial fibrillation who are not adequately anticoagulated. Stroke. 2009;40(1):235-40.

21. Petty GW, Brown RD, Jr., Whisnant JP, Sicks JD, O'Fallon WM, Wiebers DO. Ischemic stroke subtypes : a population-based study of functional outcome, survival, and recurrence. Stroke. 2000;31(5):1062-8.

22. Winter Y, Wolfram C, Schaeg M, Reese JP, Oertel WH, Dodel R, et al. Evaluation of costs and outcome in cardioembolic stroke or TIA. J Neurol. 2009;256(6):954-63.
23. Humphries KH, Jackevicius C, Gong Y, Svensen L, Cox J, Tu JV, et al. Population rates of hospitalization for atrial fibrillation/flutter in Canada. The Canadian journal of cardiology. 2004;20(9):869-76.
24. Benjamin EJ, Wolf PA, D'Agostino RB, Silbershatz H, Kannel WB, Levy D. Impact of atrial fibrillation on the risk of death: the Framingham Heart Study. Circulation. 1998;98(10):946-52.
25. Heijman J, Voigt N, Nattel S, Dobrev D. Cellular and molecular electrophysiology of atrial fibrillation initiation, maintenance, and progression. Circ Res. 2014;114(9):1483-99.
26. Skanes AC, Healey JS, Cairns JA, Dorian P, Gillis AM, McMurtry MS, et al. Focused 2012 update of the Canadian Cardiovascular Society atrial fibrillation guidelines: recommendations for stroke prevention and rate/rhythm control. The Canadian journal of cardiology. 2012;28(2):125-36.
27. Van Gelder IC, Groenveld HF, Crijns HJ, Tuininga YS, Tijssen JG, Alings AM, et al. Lenient versus strict rate control in patients with atrial fibrillation. The New England journal of medicine. 2010;362(15):1363-73.
28. Wyse DG, Waldo AL, DiMarco JP, Domanski MJ, Rosenberg Y, Schron EB, et al. A comparison of rate control and rhythm control in patients with atrial fibrillation. The New England journal of medicine. 2002;347(23):1825-33.
29. Roy D, Talajic M, Nattel S, Wyse DG, Dorian P, Lee KL, et al. Rhythm control versus rate control for atrial fibrillation and heart failure. The New England journal of medicine. 2008;358(25):2667-77.
30. Carlsson J, Miketic S, Windeler J, Cuneo A, Haun S, Micus S, et al. Randomized trial of rate-control versus rhythm-control in persistent atrial fibrillation: the Strategies of Treatment of Atrial Fibrillation (STAF) study. Journal of the American College of Cardiology. 2003;41(10):1690-6.
31. Hohnloser SH, Kuck KH, Lilienthal J. Rhythm or rate control in atrial fibrillation--Pharmacological Intervention in Atrial Fibrillation (PIAF): a randomised trial. Lancet. 2000;356(9244):1789-94.

32. Opolski G, Torbicki A, Kosior DA, Szulc M, Wozakowska-Kaplon B, Kolodziej P, et al. Rate control vs rhythm control in patients with nonvalvular persistent atrial fibrillation: the results of the Polish How to Treat Chronic Atrial Fibrillation (HOT CAFE) Study. Chest. 2004;126(2):476-86.
33. Verma A, Cairns JA, Mitchell LB, Macle L, Stiell IG, Gladstone D, et al. 2014 focused update of the Canadian Cardiovascular Society Guidelines for the management of atrial fibrillation. The Canadian journal of cardiology. 2014;30(10):1114-30.
34. Kirchhof P, Benussi S, Kotecha D, Ahlsson A, Atar D, Casadei B, et al. 2016 ESC Guidelines for the management of atrial fibrillation developed in collaboration with EACTS. Eur Heart J. 2016;37(38):2893-962.
35. Haissaguerre M, Jais P, Shah DC, Takahashi A, Hocini M, Quiniou G, et al. Spontaneous initiation of atrial fibrillation by ectopic beats originating in the pulmonary veins. The New England journal of medicine. 1998;339(10):659-66.
36. Nishida K, Datino T, Macle L, Nattel S. Atrial fibrillation ablation: translating basic mechanistic insights to the patient. Journal of the American College of Cardiology. 2014;64(8):823-31.
37. Verma A, Jiang CY, Betts TR, Chen J, Deisenhofer I, Mantovan R, et al. Approaches to catheter ablation for persistent atrial fibrillation. The New England journal of medicine. 2015;372(19):1812-22.
38. Nattel S, Singh BN. Evolution, mechanisms, and classification of antiarrhythmic drugs: focus on class III actions. Am J Cardiol. 1999;84(9A):11R-9R.
39. Aguilar M, Nattel S. The Past, Present, and Potential Future of Sodium Channel Block as an Atrial Fibrillation Suppressing Strategy. J Cardiovasc Pharmacol. 2015;66(5):432-40.
40. Gold RL, Haffajee CI, Charos G, Sloan K, Baker S, Alpert JS. Amiodarone for refractory atrial fibrillation. Am J Cardiol. 1986;57(1):124-7.
41. Wijffels MC, Kirchhof CJ, Dorland R, Allessie MA. Atrial fibrillation begets atrial fibrillation. A study in awake chronically instrumented goats. Circulation. 1995;92(7):1954-68.
42. Yue L, Feng J, Gaspo R, Li GR, Wang Z, Nattel S. Ionic remodeling underlying action potential changes in a canine model of atrial fibrillation. Circ Res. 1997;81(4):512-25.
43. Yue L, Melnyk P, Gaspo R, Wang Z, Nattel S. Molecular mechanisms underlying ionic remodeling in a dog model of atrial fibrillation. Circ Res. 1999;84(7):776-84.

44. Dobrev D, Graf E, Wettwer E, Himmel HM, Hala O, Doerfel C, et al. Molecular basis of downregulation of G-protein-coupled inward rectifying K(+) current (I(K,ACh) in chronic human atrial fibrillation: decrease in GIRK4 mRNA correlates with reduced I(K,ACh) and muscarinic receptor-mediated shortening of action potentials. Circulation. 2001;104(21):2551-7.

45. Gaborit N, Steenman M, Lamirault G, Le Meur N, Le Bouter S, Lande G, et al. Human atrial ion channel and transporter subunit gene-expression remodeling associated with valvular heart disease and atrial fibrillation. Circulation. 2005;112(4):471-81.

46. Pandit SV, Berenfeld O, Anumonwo JM, Zaritski RM, Kneller J, Nattel S, et al. Ionic determinants of functional reentry in a 2-D model of human atrial cells during simulated chronic atrial fibrillation. Biophys J. 2005;88(6):3806-21.

47. Kneller J, Zou R, Vigmond EJ, Wang Z, Leon LJ, Nattel S. Cholinergic atrial fibrillation in a computer model of a two-dimensional sheet of canine atrial cells with realistic ionic properties. Circ Res. 2002;90(9):E73-87.

48. Cha TJ, Ehrlich JR, Chartier D, Qi XY, Xiao L, Nattel S. Kir3-based inward rectifier potassium current: potential role in atrial tachycardia remodeling effects on atrial repolarization and arrhythmias. Circulation. 2006;113(14):1730-7.

49. Ehrlich JR, Cha TJ, Zhang L, Chartier D, Villeneuve L, Hebert TE, et al. Characterization of a hyperpolarization-activated time-dependent potassium current in canine cardiomyocytes from pulmonary vein myocardial sleeves and left atrium. J Physiol. 2004;557(Pt 2):583-97.

50. Voigt N, Maguy A, Yeh YH, Qi X, Ravens U, Dobrev D, et al. Changes in I K, ACh single-channel activity with atrial tachycardia remodelling in canine atrial cardiomyocytes. Cardiovasc Res. 2008;77(1):35-43.

51. Bosch RF, Zeng X, Grammer JB, Popovic K, Mewis C, Kuhlkamp V. Ionic mechanisms of electrical remodeling in human atrial fibrillation. Cardiovasc Res. 1999;44(1):121-31.

52. Grammer JB, Bosch RF, Kuhlkamp V, Seipel L. Molecular remodeling of Kv4.3 potassium channels in human atrial fibrillation. J Cardiovasc Electrophysiol. 2000;11(6):626-33.

53. Workman AJ, Kane KA, Rankin AC. The contribution of ionic currents to changes in refractoriness of human atrial myocytes associated with chronic atrial fibrillation. Cardiovasc Res. 2001;52(2):226-35.

54. Brandt MC, Priebe L, Bohle T, Sudkamp M, Beuckelmann DJ. The ultrarapid and the transient outward K(+) current in human atrial fibrillation. Their possible role in postoperative atrial fibrillation. J Mol Cell Cardiol. 2000;32(10):1885-96.

55. Van Wagoner DR, Pond AL, McCarthy PM, Trimmer JS, Nerbonne JM. Outward K+ current densities and Kv1.5 expression are reduced in chronic human atrial fibrillation. Circ Res. 1997;80(6):772-81.

56. Nattel S, Maguy A, Le Bouter S, Yeh YH. Arrhythmogenic ion-channel remodeling in the heart: heart failure, myocardial infarction, and atrial fibrillation. Physiol Rev. 2007;87(2):425-56.

57. Li D, Fareh S, Leung TK, Nattel S. Promotion of atrial fibrillation by heart failure in dogs: atrial remodeling of a different sort. Circulation. 1999;100(1):87-95.

58. Nattel S, Harada M. Atrial remodeling and atrial fibrillation: recent advances and translational perspectives. Journal of the American College of Cardiology. 2014;63(22):2335-45.

59. Harada M, Van Wagoner DR, Nattel S. Role of inflammation in atrial fibrillation pathophysiology and management. Circ J. 2015;79(3):495-502.

60. Rudolph V, Andrie RP, Rudolph TK, Friedrichs K, Klinke A, Hirsch-Hoffmann B, et al. Myeloperoxidase acts as a profibrotic mediator of atrial fibrillation. Nat Med. 2010;16(4):470-4.

61. Wu N, Xu B, Xiang Y, Wu L, Zhang Y, Ma X, et al. Association of inflammatory factors with occurrence and recurrence of atrial fibrillation: a meta-analysis. Int J Cardiol. 2013;169(1):62-72.

62. Li J, Solus J, Chen Q, Rho YH, Milne G, Stein CM, et al. Role of inflammation and oxidative stress in atrial fibrillation. Heart Rhythm. 2010;7(4):438-44.

63. Pinto A, Tuttolomondo A, Casuccio A, Di Raimondo D, Di Sciacca R, Arnao V, et al. Immuno-inflammatory predictors of stroke at follow-up in patients with chronic non-valvular atrial fibrillation (NVAF). Clin Sci (Lond). 2009;116(10):781-9.

64. Liuba I, Ahlmroth H, Jonasson L, Englund A, Jonsson A, Safstrom K, et al. Source of inflammatory markers in patients with atrial fibrillation. Europace. 2008;10(7):848-53.
65. Cardin S, Li D, Thorin-Trescases N, Leung TK, Thorin E, Nattel S. Evolution of the atrial fibrillation substrate in experimental congestive heart failure: angiotensin-dependent and -independent pathways. Cardiovasc Res. 2003;60(2):315-25.
66. Goette A, Staack T, Rocken C, Arndt M, Geller JC, Huth C, et al. Increased expression of extracellular signal-regulated kinase and angiotensin-converting enzyme in human atria during atrial fibrillation. Journal of the American College of Cardiology. 2000;35(6):1669-77.
67. Reil JC, Hohl M, Selejan S, Lipp P, Drautz F, Kazakow A, et al. Aldosterone promotes atrial fibrillation. Eur Heart J. 2012;33(16):2098-108.
68. Reil JC, Tauchnitz M, Tian Q, Hohl M, Linz D, Oberhofer M, et al. Hyperaldosteronism induces left atrial systolic and diastolic dysfunction. Am J Physiol Heart Circ Physiol. 2016;311(4):H1014-H23.
69. Nattel S, Dobrev D. Controversies About Atrial Fibrillation Mechanisms: Aiming for Order in Chaos and Whether it Matters. Circ Res. 2017;120(9):1396-8.
70. F. HB, Jr BJT. Antiarrhythmic drugs. In: R. DJ, editor. Drill's Pharmacology in Medicine. 4th edition ed. New York: McGraw-Hill; 1971. p. 824-52.
71. Singh BN, Vaughan Williams EM. A third class of anti-arrhythmic action. Effects on atrial and ventricular intracellular potentials, and other pharmacological actions on cardiac muscle, of MJ 1999 and AH 3474. Br J Pharmacol. 1970;39(4):675-87.
72. Singh BN. A fourth class of anti-dysrhythmic action? Effect of verapamil on ouabain toxicity, on atrial and ventricular intracellular potentials, and on other features of cardiac function. Cardiovasc Res. 1972;6(2):109-19.
73. Campbell TJ. Kinetics of onset of rate-dependent effects of Class I antiarrhythmic drugs are important in determining their effects on refractoriness in guinea-pig ventricle, and provide a theoretical basis for their subclassification. Cardiovasc Res. 1983;17(6):344-52.
74. Echt DS, Liebson PR, Mitchell LB, Peters RW, Obias-Manno D, Barker AH, et al. Mortality and morbidity in patients receiving encainide, flecainide, or placebo. The Cardiac Arrhythmia Suppression Trial. The New England journal of medicine. 1991;324(12):781-8.

75. Group IR. International mexiletine and placebo antiarrhythmic coronary trial: I. Report on arrhythmia and other findings. Impact Research Group. Journal of the American College of Cardiology. 1984;4(6):1148-63.
76. Waldo AL, Camm AJ, deRuyter H, Friedman PL, MacNeil DJ, Pauls JF, et al. Effect of d-sotalol on mortality in patients with left ventricular dysfunction after recent and remote myocardial infarction. The SWORD Investigators. Survival With Oral d-Sotalol. Lancet. 1996;348(9019):7-12.
77. Qi XY, Diness JG, Brundel BJ, Zhou XB, Naud P, Wu CT, et al. Role of small-conductance calcium-activated potassium channels in atrial electrophysiology and fibrillation in the dog. Circulation. 2014;129(4):430-40.
78. Voigt N, Heijman J, Wang Q, Chiang DY, Li N, Karck M, et al. Cellular and molecular mechanisms of atrial arrhythmogenesis in patients with paroxysmal atrial fibrillation. Circulation. 2014;129(2):145-56.
79. Pascale LR, Bernstein LM, Schoolman HM, Foley EF. Intravenous procaine amide in the treatment of cardiac arrhythmias. Am Heart J. 1954;48(1):110-22.
80. Halpern SW, Ellrodt G, Singh BN, Mandel WJ. Efficacy of intravenous procainamide infusion in converting atrial fibrillation to sinus rhythm. Relation to left atrial size. Br Heart J. 1980;44(5):589-95.
81. Fenster PE, Comess KA, Marsh R, Katzenberg C, Hager WD. Conversion of atrial fibrillation to sinus rhythm by acute intravenous procainamide infusion. Am Heart J. 1983;106(3):501-4.
82. Vandenbosch R, Lisin N, Andriange M, Gach J, Carlier J. [Clinical experimentation with intravenously administered disopyramide]. Acta Cardiol. 1975;30(4):267-78.
83. Gavaghan TP, Feneley MP, Campbell TJ, Morgan JJ. Atrial tachyarrhythmias after cardiac surgery: results of disopyramide therapy. Aust N Z J Med. 1985;15(1):27-32.
84. Karlson BW, Torstensson I, Abjorn C, Jansson SO, Peterson LE. Disopyramide in the maintenance of sinus rhythm after electroconversion of atrial fibrillation. A placebo-controlled one-year follow-up study. Eur Heart J. 1988;9(3):284-90.
85. Juul-Moller S, Edvardsson N, Rehnqvist-Ahlberg N. Sotalol versus quinidine for the maintenance of sinus rhythm after direct current conversion of atrial fibrillation. Circulation. 1990;82(6):1932-9.

86. Borgeat A, Goy JJ, Maendly R, Kaufmann U, Grbic M, Sigwart U. Flecainide versus quinidine for conversion of atrial fibrillation to sinus rhythm. Am J Cardiol. 1986;58(6):496-8.
87. Byrne-Quinn E, Wing AJ. Maintenance of sinus rhythm after DC reversion of atrial fibrilllation. A double-blind controlled trial of long-acting quinidine bisulphate. Br Heart J. 1970;32(3):370-6.
88. Hillestad L, Bjerkelund C, Dale J, Maltau J, Storstein O. Quinidine in maintenance of sinus rhythm after electroconversion of chronic atrial fibrillation. A controlled clinical study. Br Heart J. 1971;33(4):518-21.
89. Hartel G, Louhija A, Konttinen A. Disopyramide in the prevention of recurrence of atrial fibrillation after electroconversion. Clin Pharmacol Ther. 1974;15(6):551-5.
90. Lloyd EA, Gersh BJ, Forman R. The efficacy of quinidine and disopyramide in the maintenance of sinus rhythm after electroconversion from atrial fibrillation. A double-blind study comparing quinidine, disopyramide and placebo. S Afr Med J. 1984;65(10):367-9.
91. Sodermark T, Jonsson B, Olsson A, Oro L, Wallin H, Edhag O, et al. Effect of quinidine on maintaining sinus rhythm after conversion of atrial fibrillation or flutter. A multicentre study from Stockholm. Br Heart J. 1975;37(5):486-92.
92. Coplen SE, Antman EM, Berlin JA, Hewitt P, Chalmers TC. Efficacy and safety of quinidine therapy for maintenance of sinus rhythm after cardioversion. A meta-analysis of randomized control trials. Circulation. 1990;82(4):1106-16.
93. Naccarelli GV, Dorian P, Hohnloser SH, Coumel P. Prospective comparison of flecainide versus quinidine for the treatment of paroxysmal atrial fibrillation/flutter. The Flecainide Multicenter Atrial Fibrillation Study Group. Am J Cardiol. 1996;77(3):53A-9A.
94. Suttorp MJ, Kingma JH, Lie AHL, Mast EG. Intravenous flecainide versus verapamil for acute conversion of paroxysmal atrial fibrillation or flutter to sinus rhythm. Am J Cardiol. 1989;63(11):693-6.
95. Crozier IG, Ikram H, Kenealy M, Levy L. Flecainide acetate for conversion of acute supraventricular tachycardia to sinus rhythm. Am J Cardiol. 1987;59(6):607-9.
96. Crijns HJ, van Wijk LM, van Gilst WH, Kingma JH, van Gelder IC, Lie KI. Acute conversion of atrial fibrillation to sinus rhythm: clinical efficacy of flecainide acetate. Comparison of two regimens. Eur Heart J. 1988;9(6):634-8.

97. Berns E, Rinkenberger RL, Jeang MK, Dougherty AH, Jenkins M, Naccarelli GV. Efficacy and safety of flecainide acetate for atrial tachycardia or fibrillation. Am J Cardiol. 1987;59(15):1337-41.

98. Anderson JL, Jolivette DM, Fredell PA. Summary of efficacy and safety of flecainide for supraventricular arrhythmias. Am J Cardiol. 1988;62(6):62D-6D.

99. Goy JJ, Kaufmann U, Kappenberger L, Sigwart U. Restoration of sinus rhythm with flecainide in patients with atrial fibrillation. Am J Cardiol. 1988;62(6):38D-40D.

100. Alboni P, Botto GL, Baldi N, Luzi M, Russo V, Gianfranchi L, et al. Outpatient treatment of recent-onset atrial fibrillation with the "pill-in-the-pocket" approach. The New England journal of medicine. 2004;351(23):2384-91.

101. Nabar A, Rodriguez LM, Timmermans C, van Mechelen R, Wellens HJ. Class IC antiarrhythmic drug induced atrial flutter: electrocardiographic and electrophysiological findings and their importance for long term outcome after right atrial isthmus ablation. Heart. 2001;85(4):424-9.

102. Niederer SA, Lumens J, Trayanova NA. Computational models in cardiology. Nat Rev Cardiol. 2019;16(2):100-11.

103. Courtemanche M, Winfree AT. Re-entrant rotating waves in a Beeler-Reuter based model of two-dimensional cardiac electrical activity. Int J Bifurcat Chaos. 1991;1:431-44.

104. Holden AV, Panfilov AV. Spatiotemporal chaos in a model of cardia electrical activity. Int J Bifurcat Chaos. 1991;1:219-25.

105. Davidenko JM, Pertsov AV, Salomonsz R, Baxter W, Jalife J. Stationary and drifting spiral waves of excitation in isolated cardiac muscle. Nature. 1992;355(6358):349-51.

106. Arevalo HJ, Vadakkumpadan F, Guallar E, Jebb A, Malamas P, Wu KC, et al. Arrhythmia risk stratification of patients after myocardial infarction using personalized heart models. Nat Commun. 2016;7:11437.

107. Bayer JD, Roney CH, Pashaei A, Jais P, Vigmond EJ. Novel Radiofrequency Ablation Strategies for Terminating Atrial Fibrillation in the Left Atrium: A Simulation Study. Front Physiol. 2016;7:108.

108. Hodgkin AL, Huxley AF. A quantitative description of membrane current and its application to conduction and excitation in nerve. J Physiol. 1952;117(4):500-44.

109. Lascano EC, Said M, Vittone L, Mattiazzi A, Mundina-Weilenmann C, Negroni JA. Role of CaMKII in post acidosis arrhythmias: a simulation study using a human myocyte model. J Mol Cell Cardiol. 2013;60:172-83.

110. Heijman J, Volders PG, Westra RL, Rudy Y. Local control of beta-adrenergic stimulation: Effects on ventricular myocyte electrophysiology and Ca(2+)-transient. J Mol Cell Cardiol. 2011;50(5):863-71.

111. Fink M, Niederer SA, Cherry EM, Fenton FH, Koivumaki JT, Seemann G, et al. Cardiac cell modelling: observations from the heart of the cardiac physiome project. Progress in biophysics and molecular biology. 2011;104(1-3):2-21.

112. Courtemanche M, Ramirez RJ, Nattel S. Ionic mechanisms underlying human atrial action potential properties: insights from a mathematical model. Am J Physiol. 1998;275(1 Pt 2):H301-21.

113. Heijman J, Erfanian Abdoust P, Voigt N, Nattel S, Dobrev D. Computational models of atrial cellular electrophysiology and calcium handling, and their role in atrial fibrillation. J Physiol. 2016;594(3):537-53.

114. Hondeghem LM, Katzung BG. Antiarrhythmic agents: the modulated receptor mechanism of action of sodium and calcium channel-blocking drugs. Annu Rev Pharmacol Toxicol. 1984;24:387-423.

115. Hondeghem LM, Katzung BG. Time- and voltage-dependent interactions of antiarrhythmic drugs with cardiac sodium channels. Biochim Biophys Acta. 1977;472(3-4):373-98.

116. Hille B. Local anesthetics: hydrophilic and hydrophobic pathways for the drug-receptor reaction. J Gen Physiol. 1977;69(4):497-515.

117. Starmer CF, Grant AO, Strauss HC. Mechanisms of use-dependent block of sodium channels in excitable membranes by local anesthetics. Biophys J. 1984;46(1):15-27.

118. Nattel S. New ideas about atrial fibrillation 50 years on. Nature. 2002;415(6868):219-26.

119. Ehrlich JR, Nattel S. Novel approaches for pharmacological management of atrial fibrillation. Drugs. 2009;69(7):757-74.

120. Nattel S, Carlsson L. Innovative approaches to anti-arrhythmic drug therapy. Nat Rev Drug Discov. 2006;5(12):1034-49.

121. de Denus S, Sanoski CA, Carlsson J, Opolski G, Spinler SA. Rate vs rhythm control in patients with atrial fibrillation: a meta-analysis. Arch Intern Med. 2005;165(3):258-62.
122. Wijffels MC, Dorland R, Mast F, Allessie MA. Widening of the excitable gap during pharmacological cardioversion of atrial fibrillation in the goat: effects of cibenzoline, hydroquinidine, flecainide, and d-sotalol. Circulation. 2000;102(2):260-7.
123. Kawase A, Ikeda T, Nakazawa K, Ashihara T, Namba T, Kubota T, et al. Widening of the excitable gap and enlargement of the core of reentry during atrial fibrillation with a pure sodium channel blocker in canine atria. Circulation. 2003;107(6):905-10.
124. Kneller J, Kalifa J, Zou R, Zaitsev AV, Warren M, Berenfeld O, et al. Mechanisms of atrial fibrillation termination by pure sodium channel blockade in an ionically-realistic mathematical model. Circ Res. 2005;96(5):e35-47.
125. Burashnikov A, Di Diego JM, Zygmunt AC, Belardinelli L, Antzelevitch C. Atrium-selective sodium channel block as a strategy for suppression of atrial fibrillation: differences in sodium channel inactivation between atria and ventricles and the role of ranolazine. Circulation. 2007;116(13):1449-57.
126. Zygmunt AC, Nesterenko VV, Rajamani S, Hu D, Barajas-Martinez H, Belardinelli L, et al. Mechanisms of atrial-selective block of Na(+) channels by ranolazine: I. Experimental analysis of the use-dependent block. Am J Physiol Heart Circ Physiol. 2011;301(4):H1606-14.
127. Ramirez RJ, Nattel S, Courtemanche M. Mathematical analysis of canine atrial action potentials: rate, regional factors, and electrical remodeling. Am J Physiol Heart Circ Physiol. 2000;279(4):H1767-85.
128. Hund TJ, Rudy Y. Rate dependence and regulation of action potential and calcium transient in a canine cardiac ventricular cell model. Circulation. 2004;110(20):3168-74.
129. Cardona K, Trenor B, Molto G, Martinez M, Ferrero JM, Jr., Starmer F, et al. Exploring the role of pH in modulating the effects of lidocaine in virtual ischemic tissue. Am J Physiol Heart Circ Physiol. 2010;299(5):H1615-24.
130. Villemaire C, Savard P, Talajic M, Nattel S. A quantitative analysis of use-dependent ventricular conduction slowing by procainamide in anesthetized dogs. Circulation. 1992;85(6):2255-66.

131. Moreno JD, Zhu ZI, Yang PC, Bankston JR, Jeng MT, Kang C, et al. A computational model to predict the effects of class I anti-arrhythmic drugs on ventricular rhythms. Sci Transl Med. 2011;3(98):98ra83.
132. Starmer CF, Lastra AA, Nesterenko VV, Grant AO. Proarrhythmic response to sodium channel blockade. Theoretical model and numerical experiments. Circulation. 1991;84(3):1364-77.
133. Starmer CF, Colatsky TJ, Grant AO. What happens when cardiac Na channels lose their function? 1--numerical studies of the vulnerable period in tissue expressing mutant channels. Cardiovasc Res. 2003;57(1):82-91.
134. Starmer CF. How antiarrhythmic drugs increase the rate of sudden cardiac death. Int J Bifurcat Chaos. 2002;12:1953-68.
135. Comtois P, Sakabe M, Vigmond EJ, Munoz M, Texier A, Shiroshita-Takeshita A, et al. Mechanisms of atrial fibrillation termination by rapidly unbinding Na+ channel blockers: insights from mathematical models and experimental correlates. Am J Physiol Heart Circ Physiol. 2008;295(4):H1489-504.
136. Ravens U. Novel pharmacological approaches for antiarrhythmic therapy. Naunyn Schmiedebergs Arch Pharmacol. 2010;381(3):187-93.
137. Nattel S, Kneller J, Zou R, Leon LJ. Mechanisms of termination of atrial fibrillation by Class I antiarrhythmic drugs: evidence from clinical, experimental, and mathematical modeling studies. J Cardiovasc Electrophysiol. 2003;14(10 Suppl):S133-9.
138. Cabo C, Pertsov AM, Davidenko JM, Baxter WT, Gray RA, Jalife J. Vortex shedding as a precursor of turbulent electrical activity in cardiac muscle. Biophys J. 1996;70(3):1105-11.
139. Burashnikov A, Di Diego JM, Zygmunt AC, Belardinelli L, Antzelevitch C. Atrial-selective sodium channel block as a strategy for suppression of atrial fibrillation. Ann N Y Acad Sci. 2008;1123:105-12.
140. Farkas AS, Nattel S. Minimizing repolarization-related proarrhythmic risk in drug development and clinical practice. Drugs. 2010;70(5):573-603.
141. Nesterenko VV, Zygmunt AC, Rajamani S, Belardinelli L, Antzelevitch C. Mechanisms of atrial-selective block of Na(+) channels by ranolazine: II. Insights from a mathematical model. Am J Physiol Heart Circ Physiol. 2011;301(4):H1615-24.

142. Burashnikov A, Antzelevitch C. New pharmacological strategies for the treatment of atrial fibrillation. Ann Noninvasive Electrocardiol. 2009;14(3):290-300.
143. Balser JR. The cardiac sodium channel: gating function and molecular pharmacology. J Mol Cell Cardiol. 2001;33(4):599-613.
144. Comtois P, Nattel S. Impact of tissue geometry on simulated cholinergic atrial fibrillation: a modeling study. Chaos. 2011;21(1):013108.
145. Kneller J, Ramirez RJ, Chartier D, Courtemanche M, Nattel S. Time-dependent transients in an ionically based mathematical model of the canine atrial action potential. Am J Physiol Heart Circ Physiol. 2002;282(4):H1437-51.
146. Liu S, Rasmusson RL. Hodgkin-Huxley and partially coupled inactivation models yield different voltage dependence of block. Am J Physiol. 1997;272(4 Pt 2):H2013-22.
147. Pratt CM, Moye LA. The cardiac arrhythmia suppression trial. Casting suppression in a different light. Circulation. 1995;91(1):245-7.
148. Zimetbaum P. Antiarrhythmic drug therapy for atrial fibrillation. Circulation. 2012;125(2):381-9.
149. Burashnikov A, Sicouri S, Di Diego JM, Belardinelli L, Antzelevitch C. Synergistic effect of the combination of ranolazine and dronedarone to suppress atrial fibrillation. Journal of the American College of Cardiology. 2010;56(15):1216-24.
150. Sicouri S, Burashnikov A, Belardinelli L, Antzelevitch C. Synergistic electrophysiologic and antiarrhythmic effects of the combination of ranolazine and chronic amiodarone in canine atria. Circulation Arrhythmia and electrophysiology. 2010;3(1):88-95.
151. Kowey P, Reiffel JA, Camm AJ, Zereba W, Prokopczuk EK, Zeng D, et al., editors. The effect of the combination of ranolazine and low dose dronedarone on atrial fibrillation burden in patients with paroxysmal atrial fibrillation (HARMONY trial). Abstract LB03-05. Heart Rhythm Scientific Sessions; 2014; San Francisco, CA.
152. Aguilar-Shardonofsky M, Vigmond EJ, Nattel S, Comtois P. In silico optimization of atrial fibrillation-selective sodium channel blocker pharmacodynamics. Biophys J. 2012;102(5):951-60.
153. Yamashita T, Murakawa Y, Sezaki K, Hayami N, Inoue M, Fukui E, et al. Uniqueness of pilsicainide in class Ic antiarrhythmics. Jpn Heart J. 1998;39(3):389-97.

154. Antman EM, Beamer AD, Cantillon C, McGowan N, Goldman L, Friedman PL. Long-term oral propafenone therapy for suppression of refractory symptomatic atrial fibrillation and atrial flutter. Journal of the American College of Cardiology. 1988;12(4):1005-11.

155. Singh S, Zoble RG, Yellen L, Brodsky MA, Feld GK, Berk M, et al. Efficacy and safety of oral dofetilide in converting to and maintaining sinus rhythm in patients with chronic atrial fibrillation or atrial flutter: the symptomatic atrial fibrillation investigative research on dofetilide (SAFIRE-D) study. Circulation. 2000;102(19):2385-90.

156. Li D, Zhang L, Kneller J, Nattel S. Potential ionic mechanism for repolarization differences between canine right and left atrium. Circ Res. 2001;88(11):1168-75.

157. Fukuda K, Watanabe J, Yagi T, Wakayama Y, Nakano M, Kondo M, et al. A sodium channel blocker, pilsicainide, produces atrial post-repolarization refractoriness through the reduction of sodium channel availability. Tohoku J Exp Med. 2011;225(1):35-42.

158. Hattori Y, Hidaka T, Aisaka K, Satoh F, Ishihara T. Effect of SUN 1165, a new potent antiarrhythmic agent, on the kinetics of rate-dependent block of Na channels and ventricular conduction of extrasystoles. J Cardiovasc Pharmacol. 1988;11(4):407-12.

159. Hattori Y, Inomata N. Modes of the Na channel blocking action of pilsicainide, a new antiarrhythmic agent, in cardiac cells. Jpn J Pharmacol. 1992;58(4):365-73.

160. Takahara A, Takeda K, Tsuneoka Y, Hagiwara M, Namekata I, Tanaka H. Electrophysiological effects of the class Ic antiarrhythmic drug pilsicainide on the guinea-pig pulmonary vein myocardium. J Pharmacol Sci. 2012;118(4):506-11.

161. Kanki H, Mitamura H, Takatsuki S, Sueyoshi K, Shinagawa K, Sato T, et al. Postrepolarization refractoriness as a potential anti-atrial fibrillation mechanism of pilsicainide, a pure sodium channel blocker with slow recovery kinetics. Cardiovasc Drugs Ther. 1998;12(5):475-82.

162. Yatani A, Akaike N. Effects of a new antiarrhythmic compound SUN 1165 [N-(2,6-dimethylphenyl)-8-pyrrolizidineacetamide hydrochloride] on the sodium currents in isolated single rat ventricular cells. Naunyn Schmiedebergs Arch Pharmacol. 1984;326(2):163-8.

163. Gwilt M, Arrowsmith JE, Blackburn KJ, Burges RA, Cross PE, Dalrymple HW, et al. UK-68,798: a novel, potent and highly selective class III antiarrhythmic agent which blocks potassium channels in cardiac cells. J Pharmacol Exp Ther. 1991;256(1):318-24.

164. Tande PM, Bjornstad H, Yang T, Refsum H. Rate-dependent class III antiarrhythmic action, negative chronotropy, and positive inotropy of a novel Ik blocking drug, UK-68,798: potent in guinea pig but no effect in rat myocardium. J Cardiovasc Pharmacol. 1990;16(3):401-10.

165. Ravens U, Wettwer E. Ultra-rapid delayed rectifier channels: molecular basis and therapeutic implications. Cardiovasc Res. 2011;89(4):776-85.

166. Dobrev D, Carlsson L, Nattel S. Novel molecular targets for atrial fibrillation therapy. Nat Rev Drug Discov. 2012;11(4):275-91.

167. Qi D, Yang Z, Robinson VM, Li J, Gao C, Guo D, et al. Heterogeneous distribution of INa-L determines interregional differences in rate adaptation of repolarization. Heart Rhythm. 2015;12(6):1295-303.

168. Cohen CJ, Bean BP, Tsien RW. Maximal upstroke velocity as an index of available sodium conductance. Comparison of maximal upstroke velocity and voltage clamp measurements of sodium current in rabbit Purkinje fibers. Circ Res. 1984;54(6):636-51.

169. Yang T, Chun YW, Stroud DM, Mosley JD, Knollmann BC, Hong C, et al. Screening for acute IKr block is insufficient to detect torsades de pointes liability: role of late sodium current. Circulation. 2014;130(3):224-34.

170. Wang Z, Fermini B, Nattel S. Sustained depolarization-induced outward current in human atrial myocytes. Evidence for a novel delayed rectifier K+ current similar to Kv1.5 cloned channel currents. Circ Res. 1993;73(6):1061-76.

171. Feng J, Xu D, Wang Z, Nattel S. Ultrarapid delayed rectifier current inactivation in human atrial myocytes: properties and consequences. Am J Physiol. 1998;275(5 Pt 2):H1717-25.

172. Ford J, Milnes J, El Haou S, Wettwer E, Loose S, Matschke K, et al. The positive frequency-dependent electrophysiological effects of the IKur inhibitor XEN-D0103 are desirable for the treatment of atrial fibrillation. Heart Rhythm. 2016;13(2):555-64.

173. Vigmond EJ, Hughes M, Plank G, Leon LJ. Computational tools for modeling electrical activity in cardiac tissue. J Electrocardiol. 2003;36 Suppl:69-74.

174. Courtemanche M, Ramirez RJ, Nattel S. Ionic targets for drug therapy and atrial fibrillation-induced electrical remodeling: insights from a mathematical model. Cardiovasc Res. 1999;42(2):477-89.

175. Feng J, Wible B, Li GR, Wang Z, Nattel S. Antisense oligodeoxynucleotides directed against Kv1.5 mRNA specifically inhibit ultrarapid delayed rectifier K+ current in cultured adult human atrial myocytes. Circ Res. 1997;80(4):572-9.
176. Amos GJ, Wettwer E, Metzger F, Li Q, Himmel HM, Ravens U. Differences between outward currents of human atrial and subepicardial ventricular myocytes. J Physiol. 1996;491 (Pt 1):31-50.
177. Firek L, Giles WR. Outward currents underlying repolarization in human atrial myocytes. Cardiovasc Res. 1995;30(1):31-8.
178. Koidl B, Flaschberger P, Schaffer P, Pelzmann B, Bernhart E, Machler H, et al. Effects of the class III antiarrhythmic drug ambasilide on outward currents in human atrial myocytes. Naunyn Schmiedebergs Arch Pharmacol. 1996;353(2):226-32.
179. Philipson LH, Hice RE, Schaefer K, LaMendola J, Bell GI, Nelson DJ, et al. Sequence and functional expression in Xenopus oocytes of a human insulinoma and islet potassium channel. Proc Natl Acad Sci U S A. 1991;88(1):53-7.
180. Snyders DJ, Tamkun MM, Bennett PB. A rapidly activating and slowly inactivating potassium channel cloned from human heart. Functional analysis after stable mammalian cell culture expression. J Gen Physiol. 1993;101(4):513-43.
181. Zaza A. Control of the cardiac action potential: The role of repolarization dynamics. J Mol Cell Cardiol. 2010;48(1):106-11.
182. Banyasz T, Horvath B, Virag L, Barandi L, Szentandrassy N, Harmati G, et al. Reverse rate dependency is an intrinsic property of canine cardiac preparations. Cardiovasc Res. 2009;84(2):237-44.
183. Cummins MA, Dalal PJ, Bugana M, Severi S, Sobie EA. Comprehensive analyses of ventricular myocyte models identify targets exhibiting favorable rate dependence. PLoS Comput Biol. 2014;10(3):e1003543.
184. Blaauw Y, Gogelein H, Tieleman RG, van Hunnik A, Schotten U, Allessie MA. "Early" class III drugs for the treatment of atrial fibrillation: efficacy and atrial selectivity of AVE0118 in remodeled atria of the goat. Circulation. 2004;110(13):1717-24.
185. Dorian P, Pinter A, Mangat I, Korley V, Cvitkovic SS, Beatch GN. The effect of vernakalant (RSD1235), an investigational antiarrhythmic agent, on atrial electrophysiology in humans. J Cardiovasc Pharmacol. 2007;50(1):35-40.

186. Fedida D, Orth PM, Chen JY, Lin S, Plouvier B, Jung G, et al. The mechanism of atrial antiarrhythmic action of RSD1235. J Cardiovasc Electrophysiol. 2005;16(11):1227-38.
187. Knobloch K, Brendel J, Peukert S, Rosenstein B, Busch AE, Wirth KJ. Electrophysiological and antiarrhythmic effects of the novel I(Kur) channel blockers, S9947 and S20951, on left vs. right pig atrium in vivo in comparison with the I(Kr) blockers dofetilide, azimilide, d,l-sotalol and ibutilide. Naunyn Schmiedebergs Arch Pharmacol. 2002;366(5):482-7.
188. Scholz EP, Carrillo-Bustamante P, Fischer F, Wilhelms M, Zitron E, Dossel O, et al. Rotor termination is critically dependent on kinetic properties of I kur inhibitors in an in silico model of chronic atrial fibrillation. PLoS One. 2013;8(12):e83179.
189. Roy D, Pratt CM, Torp-Pedersen C, Wyse DG, Toft E, Juul-Moller S, et al. Vernakalant hydrochloride for rapid conversion of atrial fibrillation: a phase 3, randomized, placebo-controlled trial. Circulation. 2008;117(12):1518-25.
190. van Hunnik A, Lau DH, Zeemering S, Kuiper M, Verheule S, Schotten U. Antiarrhythmic effect of vernakalant in electrically remodeled goat atria is caused by slowing of conduction and prolongation of postrepolarization refractoriness. Heart Rhythm. 2016;13(4):964-72.
191. Lagrutta A, Wang J, Fermini B, Salata JJ. Novel, potent inhibitors of human Kv1.5 K+ channels and ultrarapidly activating delayed rectifier potassium current. J Pharmacol Exp Ther. 2006;317(3):1054-63.
192. Choi BH, Choi JS, Jeong SW, Hahn SJ, Yoon SH, Jo YH, et al. Direct block by bisindolylmaleimide of rat Kv1.5 expressed in Chinese hamster ovary cells. J Pharmacol Exp Ther. 2000;293(2):634-40.
193. Delpon E, Valenzuela C, Gay P, Franqueza L, Snyders DJ, Tamargo J. Block of human cardiac Kv1.5 channels by loratadine: voltage-, time- and use-dependent block at concentrations above therapeutic levels. Cardiovasc Res. 1997;35(2):341-50.
194. Valenzuela C, Delpon E, Franqueza L, Gay P, Perez O, Tamargo J, et al. Class III antiarrhythmic effects of zatebradine. Time-, state-, use-, and voltage-dependent block of hKv1.5 channels. Circulation. 1996;94(3):562-70.

195. Tsujimae K, Suzuki S, Murakami S, Kurachi Y. Frequency-dependent effects of various IKr blockers on cardiac action potential duration in a human atrial model. Am J Physiol Heart Circ Physiol. 2007;293(1):H660-9.
196. Ford J, Milnes J, Wettwer E, Christ T, Rogers M, Sutton K, et al. Human electrophysiological and pharmacological properties of XEN-D0101: a novel atrial-selective Kv1.5/IKur inhibitor. J Cardiovasc Pharmacol. 2013;61(5):408-15.
197. Burashnikov A, Antzelevitch C. Can inhibition of IKur promote atrial fibrillation? Heart Rhythm. 2008;5(9):1304-9.
198. Yue L, Wang Z, Rindt H, Nattel S. Molecular evidence for a role of Shaw (Kv3) potassium channel subunits in potassium currents of dog atrium. J Physiol. 2000;527 Pt 3:467-78.
199. Pavri BB, Greenberg HE, Kraft WK, Lazarus N, Lynch JJ, Salata JJ, et al. MK-0448, a specific Kv1.5 inhibitor: safety, pharmacokinetics, and pharmacodynamic electrophysiology in experimental animal models and humans. Circulation Arrhythmia and electrophysiology. 2012;5(6):1193-201.
200. Christophersen IE, Olesen MS, Liang B, Andersen MN, Larsen AP, Nielsen JB, et al. Genetic variation in KCNA5: impact on the atrial-specific potassium current IKur in patients with lone atrial fibrillation. Eur Heart J. 2013;34(20):1517-25.
201. Hayashi K, Konno T, Tada H, Tani S, Liu L, Fujino N, et al. Functional Characterization of Rare Variants Implicated in Susceptibility to Lone Atrial Fibrillation. Circulation Arrhythmia and electrophysiology. 2015;8(5):1095-104.
202. Olson TM, Alekseev AE, Liu XK, Park S, Zingman LV, Bienengraeber M, et al. Kv1.5 channelopathy due to KCNA5 loss-of-function mutation causes human atrial fibrillation. Hum Mol Genet. 2006;15(14):2185-91.
203. Yang T, Yang P, Roden DM, Darbar D. Novel KCNA5 mutation implicates tyrosine kinase signaling in human atrial fibrillation. Heart Rhythm. 2010;7(9):1246-52.
204. Aguilar M, Xiong F, Qi XY, Comtois P, Nattel S. Potassium Channel Blockade Enhances Atrial Fibrillation-Selective Antiarrhythmic Effects of Optimized State-Dependent Sodium Channel Blockade. Circulation. 2015;132(23):2203-11.
205. Li GR, Feng J, Wang Z, Fermini B, Nattel S. Adrenergic modulation of ultrarapid delayed rectifier K+ current in human atrial myocytes. Circ Res. 1996;78(5):903-15.

206. Almquist J, Wallman M, Jacobson I, Jirstrand M. Modeling the effect of Kv1.5 block on the canine action potential. Biophys J. 2010;99(9):2726-36.
207. Wijffels MC, Kirchhof CJ, Dorland R, Power J, Allessie MA. Electrical remodeling due to atrial fibrillation in chronically instrumented conscious goats: roles of neurohumoral changes, ischemia, atrial stretch, and high rate of electrical activation. Circulation. 1997;96(10):3710-20.
208. Sun H, Chartier D, Leblanc N, Nattel S. Intracellular calcium changes and tachycardia-induced contractile dysfunction in canine atrial myocytes. Cardiovasc Res. 2001;49(4):751-61.
209. Carver W, Nagpal ML, Nachtigal M, Borg TK, Terracio L. Collagen expression in mechanically stimulated cardiac fibroblasts. Circ Res. 1991;69(1):116-22.
210. Kawara T, Derksen R, de Groot JR, Coronel R, Tasseron S, Linnenbank AC, et al. Activation delay after premature stimulation in chronically diseased human myocardium relates to the architecture of interstitial fibrosis. Circulation. 2001;104(25):3069-75.
211. Spach MS, Heidlage JF, Dolber PC, Barr RC. Mechanism of origin of conduction disturbances in aging human atrial bundles: experimental and model study. Heart Rhythm. 2007;4(2):175-85.
212. Tanaka K, Zlochiver S, Vikstrom KL, Yamazaki M, Moreno J, Klos M, et al. Spatial distribution of fibrosis governs fibrillation wave dynamics in the posterior left atrium during heart failure. Circ Res. 2007;101(8):839-47.
213. Yue L, Xie J, Nattel S. Molecular determinants of cardiac fibroblast electrical function and therapeutic implications for atrial fibrillation. Cardiovasc Res. 2011;89(4):744-53.
214. Rook MB, Jongsma HJ, de Jonge B. Single channel currents of homo- and heterologous gap junctions between cardiac fibroblasts and myocytes. Pflugers Arch. 1989;414(1):95-8.
215. Rook MB, van Ginneken AC, de Jonge B, el Aoumari A, Gros D, Jongsma HJ. Differences in gap junction channels between cardiac myocytes, fibroblasts, and heterologous pairs. Am J Physiol. 1992;263(5 Pt 1):C959-77.
216. Gaudesius G, Miragoli M, Thomas SP, Rohr S. Coupling of cardiac electrical activity over extended distances by fibroblasts of cardiac origin. Circ Res. 2003;93(5):421-8.
217. Camelliti P, Green CR, LeGrice I, Kohl P. Fibroblast network in rabbit sinoatrial node: structural and functional identification of homogeneous and heterogeneous cell coupling. Circ Res. 2004;94(6):828-35.

218. Miragoli M, Gaudesius G, Rohr S. Electrotonic modulation of cardiac impulse conduction by myofibroblasts. Circ Res. 2006;98(6):801-10.
219. Zlochiver S, Munoz V, Vikstrom KL, Taffet SM, Berenfeld O, Jalife J. Electrotonic myofibroblast-to-myocyte coupling increases propensity to reentrant arrhythmias in two-dimensional cardiac monolayers. Biophys J. 2008;95(9):4469-80.
220. Jacquemet V, Henriquez CS. Loading effect of fibroblast-myocyte coupling on resting potential, impulse propagation, and repolarization: insights from a microstructure model. Am J Physiol Heart Circ Physiol. 2008;294(5):H2040-52.
221. MacCannell KA, Bazzazi H, Chilton L, Shibukawa Y, Clark RB, Giles WR. A mathematical model of electrotonic interactions between ventricular myocytes and fibroblasts. Biophys J. 2007;92(11):4121-32.
222. Wakili R, Voigt N, Kaab S, Dobrev D, Nattel S. Recent advances in the molecular pathophysiology of atrial fibrillation. J Clin Invest. 2011;121(8):2955-68.
223. Dawson K, Wu CT, Qi XY, Nattel S. Congestive heart failure effects on atrial fibroblast phenotype: differences between freshly-isolated and cultured cells. PLoS One. 2012;7(12):e52032.
224. Ashihara T, Haraguchi R, Nakazawa K, Namba T, Ikeda T, Nakazawa Y, et al. The role of fibroblasts in complex fractionated electrograms during persistent/permanent atrial fibrillation: implications for electrogram-based catheter ablation. Circ Res. 2012;110(2):275-84.
225. Wu CT, Qi XY, Huang H, Naud P, Dawson K, Yeh YH, et al. Disease and region-related cardiac fibroblast potassium current variations and potential functional significance. Cardiovasc Res. 2014;102(3):487-96.
226. Xie Y, Garfinkel A, Camelliti P, Kohl P, Weiss JN, Qu Z. Effects of fibroblast-myocyte coupling on cardiac conduction and vulnerability to reentry: A computational study. Heart Rhythm. 2009;6(11):1641-9.
227. Chilton L, Ohya S, Freed D, George E, Drobic V, Shibukawa Y, et al. K+ currents regulate the resting membrane potential, proliferation, and contractile responses in ventricular fibroblasts and myofibroblasts. Am J Physiol Heart Circ Physiol. 2005;288(6):H2931-9.
228. Li GR, Sun HY, Chen JB, Zhou Y, Tse HF, Lau CP. Characterization of multiple ion channels in cultured human cardiac fibroblasts. PLoS One. 2009;4(10):e7307.

229. Shibukawa Y, Chilton EL, Maccannell KA, Clark RB, Giles WR. K+ currents activated by depolarization in cardiac fibroblasts. Biophys J. 2005;88(6):3924-35.
230. Vasquez C, Mohandas P, Louie KL, Benamer N, Bapat AC, Morley GE. Enhanced fibroblast-myocyte interactions in response to cardiac injury. Circ Res. 2010;107(8):1011-20.
231. Sachse FB, Moreno AP, Seemann G, Abildskov JA. A model of electrical conduction in cardiac tissue including fibroblasts. Ann Biomed Eng. 2009;37(5):874-89.
232. Xie Y, Garfinkel A, Weiss JN, Qu Z. Cardiac alternans induced by fibroblast-myocyte coupling: mechanistic insights from computational models. Am J Physiol Heart Circ Physiol. 2009;297(2):H775-84.
233. McDowell KS, Arevalo HJ, Maleckar MM, Trayanova NA. Susceptibility to arrhythmia in the infarcted heart depends on myofibroblast density. Biophys J. 2011;101(6):1307-15.
234. Li D, Melnyk P, Feng J, Wang Z, Petrecca K, Shrier A, et al. Effects of experimental heart failure on atrial cellular and ionic electrophysiology. Circulation. 2000;101(22):2631-8.
235. Tamargo J, Caballero R, Gomez R, Valenzuela C, Delpon E. Pharmacology of cardiac potassium channels. Cardiovasc Res. 2004;62(1):9-33.
236. Zheng ZJ, Croft JB, Giles WH, Mensah GA. Sudden cardiac death in the United States, 1989 to 1998. Circulation. 2001;104(18):2158-63.
237. Josephson ME. Josephson's Clinical Cardiac Electrophysiology: Techniques and Interpretations. 4th ed. Philadelphia: Wolters Kluwer; 2008 June 17 2008. 912 p.
238. Feld Y, Melamed-Frank M, Kehat I, Tal D, Marom S, Gepstein L. Electrophysiological modulation of cardiomyocytic tissue by transfected fibroblasts expressing potassium channels: a novel strategy to manipulate excitability. Circulation. 2002;105(4):522-9.
239. Benamer N, Vasquez C, Mahoney VM, Steinhardt MJ, Coetzee WA, Morley GE. Fibroblast KATP currents modulate myocyte electrophysiology in infarcted hearts. Am J Physiol Heart Circ Physiol. 2013;304(9):H1231-9.
240. Kohl P, Camelliti P. Cardiac myocyte-nonmyocyte electrotonic coupling: implications for ventricular arrhythmogenesis. Heart Rhythm. 2007;4(2):233-5.
241. Burstein B, Libby E, Calderone A, Nattel S. Differential behaviors of atrial versus ventricular fibroblasts: a potential role for platelet-derived growth factor in atrial-ventricular remodeling differences. Circulation. 2008;117(13):1630-41.

242. Grant EK, Olivieri LJ. The Role of 3-D Heart Models in Planning and Executing Interventional Procedures. The Canadian journal of cardiology. 2017;33(9):1074-81.
243. Ni H, Whittaker DG, Wang W, Giles WR, Narayan SM, Zhang H. Synergistic Anti-arrhythmic Effects in Human Atria with Combined Use of Sodium Blockers and Acacetin. Front Physiol. 2017;8:946.
244. Varela M, Colman MA, Hancox JC, Aslanidi OV. Atrial Heterogeneity Generates Re-entrant Substrate during Atrial Fibrillation and Anti-arrhythmic Drug Action: Mechanistic Insights from Canine Atrial Models. PLoS Comput Biol. 2016;12(12):e1005245.
245. Grandi E, Sanguinetti MC, Bartos DC, Bers DM, Chen-Izu Y, Chiamvimonvat N, et al. Potassium channels in the heart: structure, function and regulation. J Physiol. 2017;595(7):2209-28.
246. Nerbonne JM. Molecular basis of functional voltage-gated K+ channel diversity in the mammalian myocardium. J Physiol. 2000;525 Pt 2:285-98.
247. Voigt N, Trausch A, Knaut M, Matschke K, Varro A, Van Wagoner DR, et al. Left-to-right atrial inward rectifier potassium current gradients in patients with paroxysmal versus chronic atrial fibrillation. Circulation Arrhythmia and electrophysiology. 2010;3(5):472-80.
248. Antzelevitch C. M cells in the human heart. Circ Res. 2010;106(5):815-7.
249. Landstrom AP, Dobrev D, Wehrens XHT. Calcium Signaling and Cardiac Arrhythmias. Circ Res. 2017;120(12):1969-93.
250. Zima AV, Blatter LA. Inositol-1,4,5-trisphosphate-dependent Ca(2+) signalling in cat atrial excitation-contraction coupling and arrhythmias. J Physiol. 2004;555(Pt 3):607-15.
251. Sood S, Chelu MG, van Oort RJ, Skapura D, Santonastasi M, Dobrev D, et al. Intracellular calcium leak due to FKBP12.6 deficiency in mice facilitates the inducibility of atrial fibrillation. Heart Rhythm. 2008;5(7):1047-54.
252. Hove-Madsen L, Llach A, Bayes-Genis A, Roura S, Rodriguez Font E, Aris A, et al. Atrial fibrillation is associated with increased spontaneous calcium release from the sarcoplasmic reticulum in human atrial myocytes. Circulation. 2004;110(11):1358-63.
253. Neef S, Dybkova N, Sossalla S, Ort KR, Fluschnik N, Neumann K, et al. CaMKII-dependent diastolic SR Ca2+ leak and elevated diastolic Ca2+ levels in right atrial myocardium of patients with atrial fibrillation. Circ Res. 2010;106(6):1134-44.

254. Voigt N, Li N, Wang Q, Wang W, Trafford AW, Abu-Taha I, et al. Enhanced sarcoplasmic reticulum Ca2+ leak and increased Na+-Ca2+ exchanger function underlie delayed afterdepolarizations in patients with chronic atrial fibrillation. Circulation. 2012;125(17):2059-70.

255. Brilla CG, Maisch B, Zhou G, Weber KT. Hormonal regulation of cardiac fibroblast function. Eur Heart J. 1995;16 Suppl C:45-50.

256. Ellmers LJ, Knowles JW, Kim HS, Smithies O, Maeda N, Cameron VA. Ventricular expression of natriuretic peptides in Npr1(-/-) mice with cardiac hypertrophy and fibrosis. Am J Physiol Heart Circ Physiol. 2002;283(2):H707-14.

257. Aguilar M, Feng J, Vigmond E, Comtois P, Nattel S. Rate-Dependent Role of IKur in Human Atrial Repolarization and Atrial Fibrillation Maintenance. Biophys J. 2017;112(9):1997-2010.

258. Labarthe S, Bayer J, Coudiere Y, Henry J, Cochet H, Jais P, et al. A bilayer model of human atria: mathematical background, construction, and assessment. Europace. 2014;16 Suppl 4:iv21-iv9.

259. Labarthe S, Coudiere Y, Henry J, Cochet H. A semi-automatic method to construct atrial fibre structures: a tool for atrial simulations. Comput Cardiol. 2012:881-4.

260. Packer DL, Mark DB, Robb RA, Monahan KH, Bahnson TD, Poole JE, et al. Effect of Catheter Ablation vs Antiarrhythmic Drug Therapy on Mortality, Stroke, Bleeding, and Cardiac Arrest Among Patients With Atrial Fibrillation: The CABANA Randomized Clinical Trial. JAMA. 2019.

261. Shenasa M, Cardinal R, Kus T, Savard P, Fromer M, Page P. Termination of sustained ventricular tachycardia by ultrarapid subthreshold stimulation in humans. Circulation. 1988;78(5 Pt 1):1135-43.

262. Gang ES, Peter T, Nalos PC, Meesmann M, Karagueuzian HS, Mandel WJ, et al. Subthreshold atrial pacing in patients with a left-sided accessory pathway: an effective new method for terminating reciprocating tachycardia. Journal of the American College of Cardiology. 1988;11(3):515-21.

263. Fromer M, Shenasa M. Ultrarapid subthreshold stimulation for termination of atrioventricular node reentrant tachycardia. Journal of the American College of Cardiology. 1992;20(4):879-83.

264. Willems S, Weiss C, Hofmann T, Rickers C, Meinertz T. Subthreshold stimulation in the region of the slow pathway during atrioventricular node reentrant tachycardia: correlation with effect of radiofrequency catheter ablation. Journal of the American College of Cardiology. 1997;29(2):408-15.

265. Willems S, Rostock T, Shenasa M, Weiss C, Risius T, Ventura R, et al. Sub-threshold stimulation in variants of atrioventricular nodal re-entrant tachycardia: electrophysiological effects and impact for guidance of slow pathway ablation. Eur Heart J. 2004;25(14):1249-56.

266. Tandri H, Weinberg SH, Chang KC, Zhu R, Trayanova NA, Tung L, et al. Reversible cardiac conduction block and defibrillation with high-frequency electric field. Sci Transl Med. 2011;3(102):102ra96.

267. Lewis T, Drudy A. Revised views of the refractory period in relation to drugs reputed to prolong it, and in relation to circus movement. Heart. 1926;13:95-100.

268. Drudy A, Love W. The supposed lengthening of the absolute refractoy period of the frog's ventricular muscle by veratanine. Heart. 1926;13:77-85.

269. Poole JE, Johnson GW, Hellkamp AS, Anderson J, Callans DJ, Raitt MH, et al. Prognostic importance of defibrillator shocks in patients with heart failure. The New England journal of medicine. 2008;359(10):1009-17.

270. Connolly SJ, Dorian P, Roberts RS, Gent M, Bailin S, Fain ES, et al. Comparison of beta-blockers, amiodarone plus beta-blockers, or sotalol for prevention of shocks from implantable cardioverter defibrillators: the OPTIC Study: a randomized trial. JAMA. 2006;295(2):165-71.

271. Sapp JL, Wells GA, Parkash R, Stevenson WG, Blier L, Sarrazin JF, et al. Ventricular Tachycardia Ablation versus Escalation of Antiarrhythmic Drugs. The New England journal of medicine. 2016;375(2):111-21.

272. Cuculich PS, Schill MR, Kashani R, Mutic S, Lang A, Cooper D, et al. Noninvasive Cardiac Radiation for Ablation of Ventricular Tachycardia. The New England journal of medicine. 2017;377(24):2325-36.

273. Robinson CG, Samson PP, Moore KMS, Hugo GD, Knutson N, Mutic S, et al. Phase I/II Trial of Electrophysiology-Guided Noninvasive Cardiac Radioablation for Ventricular Tachycardia. Circulation. 2019;139(3):313-21.